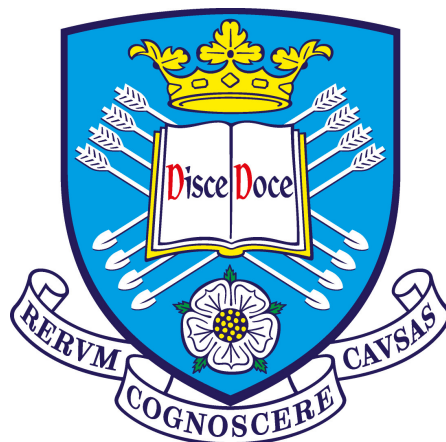


How fast do white dwarfs accrete from their low mass companion stars?

James F. Wild

Department of Physics & Astronomy
The University of Sheffield



*A dissertation submitted in candidature for the degree of
Doctor of Philosophy at the University of Sheffield*

June 2022

“

After all my time here, I've yet to
see any problem, however
complicated, which when you
looked at it the right way didn't
become still more complicated.

”

— Poul Anderson

Contents

1	Background, context, and motivation	1
1.1	Roche geometry	3
1.2	Accretion in CVs	5
1.3	CV variability and subtypes	7
1.3.1	Brown dwarf donors	7
1.3.2	Magnetic CVs	7
1.3.3	Helium-rich CVs	8
1.3.4	Classical Novae	8
1.3.5	Dwarf Novae	9
1.3.6	SU UMa stars	10
1.3.7	Novalike systems	11
1.4	CV formation	12
1.5	CV evolution	14
1.5.1	The classical picture of CV evolution	15
1.5.2	The effect of mass transfer on the binary	15
1.5.3	Period evolution and key population features	17
1.5.4	Problems with the classical picture	21
1.5.5	The missing AML problem	21
1.5.6	Consequential AML	24
1.5.7	A review of modern magnetic braking theories	27
1.6	This work	37
2	Observations and observational techniques	39
2.1	Instruments	40
2.1.1	HiPERCAM	40
2.1.2	ULTRACAM	42
2.1.3	ULTRASPEC	42
2.2	Data reduction	43
2.3	Photometric calibration	46
2.3.1	Calculating atmospheric extinction coefficients	47
2.3.2	Transformations between filter systems	47
2.3.3	Calculating comparison star magnitudes	52
2.3.4	Producing a flux-calibrated target light curve	52

2.4 Catalogue of observations	54
3 Modelling techniques and methodology	64
3.1 Parameter optimisation of many variables	65
3.1.1 Bayesian analysis	66
3.1.2 MCMC optimisation	66
3.1.3 The bisection method	70
3.2 Finding an orbital ephemeris	71
3.2.1 Finding eclipse times	71
3.2.2 Computing period	72
3.3 Modelling CV eclipse light curves	74
3.3.1 Phase-folded eclipse modelling	76
3.3.2 Post-processing the eclipse model	80
3.3.3 Capturing flickering with Gaussian Processes	82
3.3.4 Hierarchical model structure	86
3.4 Evolutionary modelling	88
3.4.1 MESA configuration for low-mass M dwarfs	89
3.4.2 Modelling star spots in MESA	93
3.4.3 Optimising mass loss rate to donor observations	98
3.4.4 Determining AML rate from system parameters	98
4 Three CVs with peculiar white dwarf colours	100
4.1 Prior observations	101
4.2 Eclipse modelling	102
4.3 White dwarf atmosphere fits	116
4.4 System Parameters	122
4.5 Implications of results	123
4.5.1 Is it correct to assume an unobscured white dwarf?	123
4.5.2 The hot white dwarf of SSSJ0522–3505	125
4.6 Summarising remarks	127
5 Eclipse modelling results of 12 CVs	128
5.1 Results	131
5.1.1 ASASSN-14hq	133
5.1.2 ASASSN-14kb	137
5.1.3 ASASSN-15pb	140
5.1.4 ASASSN-17fo	144
5.1.5 AY For	149
5.1.6 CSS090102	154
5.1.7 CSS090419	157
5.1.8 CSS090622	161
5.1.9 MASOT0014	165
5.1.10 OGLE82	170
5.1.11 SDSS J0748	174

5.1.12	SDSS J1524	179
5.2	Comparing observations with model donor tracks	187
5.2.1	A preliminary look at AML in CVs	190
6	Inferring mass loss rate from donor properties	194
6.1	Reproducing the canonical CV donor tracks	195
6.2	For what range of masses can mass loss rates be extracted?	198
6.3	Tuning star spot parameters to observations	202
6.4	Inferred mass and angular momentum loss rates from CV donors .	204
6.4.1	Systematic issues with mass loss estimation	204
6.5	Inferring mass loss from white dwarf properties	208
7	Discussion	212
7.1	Mass loss rate correlations	216
7.2	Measured angular momentum loss	221
7.3	A closer look at CAML	224
8	Conclusion and future work	227
A	Appendix	240
A.1	Eclipse modelled CV sample	241

List of Figures

1.1	A schematic of the structure of a CV, not to scale. The black dashed line outlines each Roche lobe. The dark blue circle is the white dwarf and is surrounded by its accretion disc. The lower red teardrop is the secondary star, and is connected to the donor via the mass stream. The light blue spot where the mass stream meets the disc is the bright spot impact region.	2
1.2	Showing the Roche potential in the neighbourhood of the binary system, with the more massive primary star on the left. Darker regions are lower potentials, lighter regions are higher potentials. The red line illustrates the Roche lobes.	4
1.3	Reproduced from Southworth et al. (2015) , Figure 14. The orbital period distribution of RKCat (Ritter, H. & Kolb, U., 2003) CVs identified by the SDSS (white histogram) and of the subset of these which are eclipsing (grey histogram). The light grey shaded region illustrates the period gap at 2.1 - 3.1 hours. The periods have been collected into histogram bins which are of equal size in log space.	18
1.4	Reproduced from Knigge et al. (2011) . Black markers are data from superhumpers, Red markers are data from eclipsers. Crosses denote candidate period bouncer CVs, Squares are short-period CVs, and Circles are long period CVs. Open symbols are omitted from their analysis due to lying in the period gap. The Dashed Black lines are their ‘standard’, naïve model, and the Solid Red line includes an empirically determined excess AML source, scaled to gravitational wave braking. In the top panel, the Vertical black line signifies the observed period minimum, with the grey region as the FWHM of the period spike as measured in Gänsicke et al. (2009)	23

1.5	Reproduced from Figure 2 and Figure 3 of Schreiber et al. (2016). Black squares are observed CVs, and cyan dots are predicted CV populations. <i>Top</i> is for a fully conservative CV model, the <i>middle panel</i> is for the classical non-conservative model, and the <i>bottom panel</i> is the eCAML results. The $M_{wd} > 1.44M_{\odot}$ regions are forbidden, as these white dwarfs exceed the Chandrasekhar limit.	28
1.6	Figure taken from Matt et al. (2015). Red crosses are observations of the ONC (<i>top</i>) and Praesepe (<i>bottom</i>) cluster stars. Black diamonds are synthetic cluster stars. In the bottom panel, the solid green line is the theoretical asymptotic spin rate of unsaturated stars and the dotted blue line delimits magnetically saturated and unsaturated stars.	32
1.7	Example comparison between synthetic and observed cluster populations taken from Garraffo et al. (2018a). Red points are observations of M37, which has its age measured at $\sim 346 - 550$ Myrs. Blue points are the probability distribution of the synthetic cluster population from Garraffo et al. (2018a).	35
1.8	Showing the AML rates, \dot{J} , of three magnetic braking prescriptions, applied to the masses, radii, and spin periods of the ‘standard’ CV donor track of Knigge et al. (2011). The vertical shaded region shows the period gap, corresponding to the mass at which Knigge et al. (2011) enforces the period gap to occur. Green lines show the Rappaport et al. (1983) magnetic braking prescription, which is the default used in MESA (Paxton et al., 2015). The red line shows the Matt et al. (2015) prescription, and the blue line shows the Garraffo et al. (2018a) prescription.	36
2.1	Taken from Dhillon et al. (2021). Transmission profiles of the as-built HiPERCAM dichroic beam-splitters (dashed black lines), the HiPERCAM standard SDSS filters (dotted lines), and the HiPERCAM Super SDSS filters (solid lines).	41
2.2	Illustrating the effect of omitting negative values on the average of a distribution. The black line is a Gaussian distribution with an average of 5 and a standard deviation of 7. The vertical dashed line shows the ‘true’ average of 5 ADU, and the vertical solid line shows the average given by an ADC that reports negative electron counts as 0.	44
2.3	The differences in photometric throughput in terms of registered ADU, for SDSS filter system (dotted lines), and ULTRACAM Super SDSS filters, for ULTRACAM mounted on the NTT (solid lines). Blue: u bands, Green: g bands, Red: r bands, Black: i bands. Both throughputs include atmospheric extinction of $\chi = 1.3$.	48

2.4	The difference between the classic SDSS photometric system, and the ULTRACAM SuperSDSS filters on the NTT, as a function of SDSS colours, are calculated for model atmospheres. Red points are Koester white dwarf models, black points are Phoenix main sequence model atmospheres, and the blue line is the best fit straight line to the combination of both datasets. When applying colour corrections, the highlighted relations were used.	50
2.5	As Figure 2.4	51
3.1	Reproduced from Goodman & Weare (2010) , showing the concept of a stretch move proposal. The proposed next step for j is given by choosing a random position on the line joining the last step on chain j , X_j , and the last chain on another walker chosen at random, X_k . The proposed step is shown by the star, Y . Grey dots with no outlines illustrate the other walkers in the ensemble, but are unused.	68
3.2	Showing an example eclipse light curve, folded about the period of the eclipse. The solid black line shows the brightness of the system varying over time. The blue solid lines show the white dwarf ingress (left) and egress (right). The red dashed lines show the ingress (left) and egress (right) of the bright spot. The pre-eclipse hump is the grey shaded region	77
3.3	Showing a schematic of the bright spot model. The lower dashed line joins the centres of the white dwarf and donor stars, and the upper dashed line runs parallel to it, intersecting the bright spot location. The straight red line is one half of the flux-emitting strip and has a profile exponent Y , and the arrow shows the direction of light emission, at an angle θ_{yaw} from the normal.	79
3.4	Reproduced from McAllister (2017) . Two variables, $t_{1,2}$, are described by a joint Gaussian distribution. Blue ellipses trace lines of equal probability of drawing a sample. Solid black Gaussians along each axis show the probability distributions of each variable, and the dashed black Gaussian along the y-axis shows the probability distribution of t_2 , given a fixed value of t_1 , which is shown by the vertical dashed line	83
3.5	The hierarchical structure of the light curve model. Parameters are inherited downwards, to produce an eclipse at the ‘leaves’ of the tree, e.g. Eclipse 3 inherits the parameters of Band 2, which in turn inherits the Core parameters. $F_{wd,RS}$ represent the fluxes of the white dwarf and donor star, and U_{LD} is the limb darkening coefficient of the white dwarf.	87

3.6	Showing the radius inflation of default MESA models over the Brown relation, i.e. $(R_{\text{MESA}} - R_{\text{brown}})/R_{\text{brown}}$. The horizontal dashed line is the target radius inflation for MESA models, of 4.5% over the Brown relation. Crosses correspond to MESA models at an age of 2 Gyrs.	94
3.7	Showing how model radius varies as a function of spot coverage for a $0.15M_{\odot}$ star. Here, spots are perfectly black ($x_{\text{spot}} \equiv 0$), and the radius is extracted at 2 Gyrs. Evaluated MESA models are shown as black crosses , and joined by a black line to guide the eye.	97
4.1	ASASSN-17jf light curve models. <i>Top:</i> grey points are the observed flux, and note that the photometric system is the SDSS as per §2.3.4; black line is the observed flux, with the mean Gaussian process sample subtracted; the dark blue line is the mean light curve model, and the blue band is the standard deviation on this in the MCMC chain. The components of the model are also shown: the light blue line is the white dwarf flux, green line is the bright spot, orange line is the disc, and the red line is the donor. <i>Bottom:</i> The residuals between the data and model are plotted as the black line , with grey error bars. The Gaussian process 1-sigma region is shown as a red band	103
4.2	ASASSN-17jf light curve models (cont.)	104
4.3	ASASSN-17jf light curve models (cont.)	105
4.4	ASASSN-16kr light curve models. Symbols are the same as Figure 4.1106	
4.5	ASASSN-16kr light curve models (cont.)	107
4.6	ASASSN-16kr light curve models (cont.)	108
4.7	ASASSN-16kr light curve models (cont.)	109
4.8	ASASSN-16kr light curve models (cont.)	110
4.9	ASASSN-16kr light curve models (cont.)	111
4.10	ASASSN-16kr light curve models (cont.)	112
4.11	SSSJ0522–3505 light curve models. Symbols are the same as Figure 4.1	113
4.12	SSSJ0522–3505 light curve models (cont.)	114
4.13	SSSJ0522–3505 light curve models (cont.)	115
4.14	The white dwarf model atmosphere fits for ASASSN-17jf. Green circle : Best fit with uniform prior on $\log(g)$. Red circle : Best fit with the prior $\log(g) = 8.10 \pm 0.04$. The observations are shown as the black point and error bars . Solid black lines are white dwarf model cooling tracks, increasing in $\log(g)$ to the left. Red dashed lines are isothermal tracks for different $\log(g)$	118
4.15	The white dwarf model atmosphere fits for ASASSN-16kr. The red circle is the best fit with a prior of $\log(g) = 8.52 \pm 0.02$. Symbols are the same as Figure 4.14.	119

4.16	The white dwarf model atmosphere fits for SSSJ0522–3505. The red circle is the best fit with a prior of $\log(g) = 8.28 \pm 0.04$. Symbols are the same as Figure 4.14.	120
4.17	The result of fitting white dwarf model atmospheres to each photometric band independently. Blue solid line : u' band, Green solid line : g' band, Red solid line : r' band. The joint distribution between all bands is characterised in each case by the best fit Gaussian (magenta dashed lines). <i>Top</i> : ASASSN-17jf, joint $T_{\text{eff}} = 8330 \pm 780$ K; <i>Middle</i> : ASASSN-16kr, joint $T_{\text{eff}} = 12150 \pm 300$ K; <i>Bottom</i> : SSSJ0522–3505, joint $T_{\text{eff}} = 33300 \pm 5200$ K.	121
4.18	Donor evolution tracks compared with these observations – note that both axes are scaled logarithmically. Solid black line : the standard donor sequence from Knigge et al. (2011), solid red line : the ‘optimal’ donor track from Knigge et al. (2011). The three systems characterised in this chapter are shown as blue crosses	124
5.1	ASASSN-14hq light curve models. Symbols are the same as Figure 4.1. Data are the result of binning the following nights: 2016/11/9, 2016/11/11, 2017/3/19, 2017/3/21.	134
5.2	ASASSN-14hq light curve models (cont.). Data are the result of binning the following nights: 2018/1/23, 2018/1/25, both 2018/1/28 observations, 2018/1/30.	135
5.3	ASASSN-14hq observed white dwarf fluxes, compared to the best-fit model atmosphere.	136
5.4	ASASSN-14kb light curve models. Symbols are the same as Figure 4.1	138
5.5	ASASSN-14kb observed white dwarf fluxes, compared to the best-fit model atmosphere.	139
5.6	ASASSN-15pb light curve models. Symbols are the same as Figure 4.1. u' , g' , and r' data are the result of binning together all observations.	141
5.7	ASASSN-15pb light curve models (cont.)	142
5.8	ASASSN-15pb observed white dwarf fluxes, compared to the best-fit model atmosphere.	143
5.9	ASASSN-17fo light curve models. Symbols are the same as Figure 4.1	145
5.10	ASASSN-17fo light curve models (cont.)	146
5.11	ASASSN-17fo light curve models (cont.)	147
5.12	ASASSN-17fo observed white dwarf fluxes, compared to the best-fit model atmosphere.	148
5.13	AY For light curve models. Symbols are the same as Figure 4.1	150
5.14	AY For light curve models (cont.)	151
5.15	AY For light curve models (cont.)	152
5.16	AY For observed white dwarf fluxes, compared to the best-fit model atmosphere.	153

5.17	CSS090102 light curve models. Symbols are the same as Figure 4.1. Data are the results of binning all available eclipses.	155
5.18	CSS090102 observed white dwarf fluxes, compared to the best-fit model atmosphere.	156
5.19	CSS090419 light curve models. Symbols are the same as Figure 4.1. Data are the results of binning all available eclipses.	158
5.20	CSS090419 light curve models (cont.). Data are the results of bin- ning all available eclipses.	159
5.21	CSS090419 observed white dwarf fluxes, compared to the best-fit model atmosphere.	160
5.22	CSS090622 light curve models. Symbols are the same as Figure 4.1. Data are the result of binning together the three eclipses of 2014/8/5.	162
5.23	CSS090622 light curve models (cont.). Data are the result of bin- ning together the eclipses of 2014/8/8, 2014/8/9, 2014/8/11.	163
5.24	CSS090622 observed white dwarf fluxes, compared to the best-fit model atmosphere.	164
5.25	MAS0014 light curve models. Symbols are the same as Figure 4.1.	166
5.26	MAS0014 light curve models (cont.)	167
5.27	MAS0014 light curve models (cont.). Data are the result of binning together the eclipses of 2016/8/25 and 2016/8/26.	168
5.28	MAS0014 observed white dwarf fluxes, compared to the best-fit model atmosphere.	169
5.29	OGLE82 light curve models. Symbols are the same as Figure 4.1	171
5.30	OGLE82 light curve models (cont.)	172
5.31	OGLE82 observed white dwarf fluxes, compared to the best-fit model atmosphere.	173
5.32	SDSS J0748 light curve models. Symbols are the same as Figure 4.1.	175
5.33	SDSS J0748 light curve models (cont.). Data are the result of bin- ning the following eclipses: both eclipses of 2017/2/14, 2017/2/24, 2017/3/20, 2018/12/17.	176
5.34	SDSS J0748 light curve models (cont.). Data are the result of combining the eclipse of 2018/2/4 with the two r' band eclipses observed on 2018/12/17.	177
5.35	SDSS J0748 observed white dwarf fluxes, compared to the best-fit model atmosphere.	178
5.36	SDSS J1524 light curve models. Symbols are the same as Figure 4.1.	180
5.37	SDSS J1524 light curve models (cont.). Binned data are the re- sult of combining eclipses from 2011/5/28, 2011/5/31, 2011/6/2, 2013/7/13, 2013/7/21, 2013/7/30, and, in the case of the g' band, 2014/3/3.	181

5.38	SDSS J1524 light curve models (cont.). Data labelled ‘bin A’ are a combination of the eclipses from the nights of Binned data are the result of combining eclipses from 2011/5/28, 2011/5/31, 2011/6/2, 2013/7/13, 2013/7/21, and 2013/7/30. Data labelled ‘bin B’ are the combination of 2012/4/29, 2012/4/29, and 2013/8/5.	182
5.39	SDSS J1524 light curve models (cont.). Data are the combination of 2012/4/29, 2012/4/29, and 2013/8/5.	183
5.40	SDSS1524 observed white dwarf fluxes, compared to the best-fit model atmosphere.	184
5.41	Showing how eclipse modelled observations compare with evolutionary models in the short period regime. The solid blue line is the ‘standard’ Knigge et al. (2011) donor track with only gravitational braking below the period gap, and the solid green line is the ‘optimal’ track with $2.47\times$ amplified gravitational braking. Data points are scaled based on their white dwarf masses. The magenta crosses are the 3 CVs with peculiar colours from Chapter 4, black circles are the 12 systems of Chapter 5, gold upright triangles are data from McAllister et al. (2019), grey squares are from Savoury et al. (2011), and the brown inverted triangles are the supplementary systems from Gänsicke et al. (2010); McAllister et al. (2015); McAllister et al. (2017a); McAllister et al. (2017b). . .	188
5.42	Showing how the modelled observations compare with the average white dwarf mass found by Pala et al. (2020), $0.83\pm0.17M_\odot$, which is shown by the red dashed line and red shaded area . Data symbols are similar to Figure 5.41, and the data points are similarly scaled to aid understanding of the correlation between datum size and M_{wd}	189
5.43	The relation between the two body masses, and the period excess, P_{ex} is shown. The observed data are keyed the same as Figure 5.41, and the solid red line shows the best-fit solution to the data. Shaded red regions show successively lower confidence intervals of the fit, with the darkest region being 1σ confidence, and the lightest region being 3σ confidence. The lines of best fit have the forms: $P_{\text{ex}} = -(4.07 \pm 0.83)M_{\text{donor}}/M_\odot + (0.32 \pm 0.06)$ and $P_{\text{ex}}/\text{hours} = -(1.62 \pm 0.27)M_{\text{wd}}/M_\odot + (1.34 \pm 0.21)$	193
6.1	Showing how well MESA can reproduce the canonical Knigge et al. (2011) donor tracks. Solid lines are MESA tracks, and dotted lines are the Knigge et al. (2011) tracks. Black lines have only gravitational braking below the period gap, and red lines gave gravitational braking at $2.47\times$ strength below the period gap. . .	197
6.2	Showing how the two timescales, τ_{KH} and $\tau_{\dot{M}}$ vary with donor mass below the period gap in CV donors, as modelled by MESA (Paxton et al., 2015; Pala et al., 2017).	199

- 7.1 *Top*: Plotting the Period - M_{donor} relationship for the systems for which the white dwarf mass was determined. The MESA donor tracks are also plotted; the **blue dashed line** shows the purely gravitational wave driven model, and the **green dashed line** shows the model with gravitational braking amplified by a factor of 2.47. The symbols denote the source of the data: **circles** are the systems from Chapter 5, **upright triangles** are data from [McAllister et al. \(2019\)](#), **squares** are from [Savoury et al. \(2011\)](#), and the **inverted triangle** is the supplementary system from [McAllister et al. \(2017b\)](#). *Bottom*: Comparing the mass loss rates inferred from the donor properties (**red data**) with those inferred from the white dwarf properties (**black data**). Symbols are similar to the top panel. 215
- 7.2 Reproduced from [Pala et al. \(2021\)](#), Figure 13. The subset of modelled systems, with $P < 3\text{hr}$ are shown. **Circles** and **stars** are pre- and post-period bounce systems derived by [Pala et al. \(2021\)](#), and **diamonds** and **pentagons** are pre- and post-period bounce systems taken from the literature. *Left*: The T_{eff} is plotted against M_{wd} , and no correlation can be seen. *Right*: $\log\langle\dot{M}\rangle$ is plotted against M_{wd} , though now the data are correlated along the white dwarf mass-radius relationship outlined by [Pala et al. \(2021\)](#), $M_{\text{wd}} \propto R_{\text{wd}}^2$, shown by the **black line**. 218
- 7.3 Showing the correlation between the white dwarf mass and mass loss rate. The **black circles** are the systems from Chapter 5 and have their system names labelled, **gold upright triangles** are data from [McAllister et al. \(2019\)](#), **grey squares** are from [Savoury et al. \(2011\)](#), and the **brown inverted triangle** is the supplementary system from [McAllister et al. \(2017b\)](#). The **red line** shows the best fit to the data, with the **shaded red region** showing the coverage of the uncertainty in the line parameters. The darkest region is 1σ , the middle region is 2σ , and the lightest region shows 3σ . The best fit line has the form $\log(\dot{M}, M_{\odot} \text{ yr}^{-1}) = (-2.62 \pm 0.60)(M_{\text{wd}}, M_{\odot}) - (8.18 \pm 0.44)$. Also shown as the **dashed green line** is the mass loss expected corresponding to a typical CV white dwarf T_{eff} , following the relationship described in Equation 7.2 . . . 219
- 7.4 Showing the donor masses and mass loss rates. Observations are styled similarly to Figure 7.3. The **dashed blue line** shows the value predicted by the ‘standard’ MESA CV model, and the **dashed green line** is the ‘optimal’ MESA CV track. 220
- 7.5 Showing the correlation between the donor mass and angular momentum loss rate, \dot{J} . Observations are keyed similarly to Figure 7.3, though here the **dashed blue line** shows perfect agreement between observations and gravitational angular momentum loss. The **dashed green line** shows the $2.47 \times$ donor track. 222

7.6	Showing the correlation between the white dwarf mass and angular momentum loss rate, \dot{J} . Observations are keyed similarly to Figure 7.3, and the best fit line has the form $(\dot{J}_{\text{obs}} - \dot{J}_{\text{MESA}})$, $J = (-8.3 \pm 1.6) \times 10^{27} (M_{\text{wd}}, M_{\odot}) + (6.9 \pm 1.3) \times 10^{27}$	223
7.7	Showing the observed quantities relevant to Equation 7.4 and the best-fit value of C for short period CVs, based on donor properties. Symbols are as in Figure 7.3, and the dashed blue line shows the relationship for $C = 0.35$	225
7.8	Showing the calculated values of ν for each short period CV in this sample. Symbols are as in Figure 7.3, though note that for clarity the error bars here are partially transparent. The dashed black line shows the eCAML prescription for $\nu = 0.35/M_{\text{wd}}$, and the red dashed line shows $\nu = 0.59/M_{\text{wd}}$	226

List of Tables

2.1	ULTRACAM colour term best fit lines from Figure 2.4. The data are modelled by equations of the form $(u' - u_{\text{sup}}) = \phi + c_u(u' - g')$, with c_u being the relevant colour gradient.	50
2.2	HiPERCAM colour term best fit lines from Figure 2.5. The data are modelled by equations of the form $(u' - u_{\text{sup}}) = \phi + c_u(u' - g')$, with c_u being the relevant colour gradient.	51
2.3	Acronyms used in the observation summaries.	54
2.4	Observations taken for ASASSN-14hq. Mid-eclipse times and cycle numbers are calculated following the method detailed in §3.2.	55
2.5	Observations taken for ASASSN-14kb.	55
2.6	Observations taken for ASASSN-15pb.	56
2.7	Observations taken for ASASSN-16kr. Eclipses marked with a binning ID of ‘-’ were fit as an individual eclipse, and not combined with any other data.	56
2.8	Observations taken for ASASSN-17fo.	57
2.9	Observations taken for ASASSN-17jf.	57
2.10	Observations taken for AY For.	57
2.11	Observations taken for CSS090102.	58
2.12	Observations taken for CSS090419.	58
2.13	Observations taken for CSS090622.	59
2.14	Observations taken for MASTER OT J001400.25-561735.0.	59
2.15	Observations taken for OGLE82.	60
2.16	Observations taken for SDSS J0748. Here, ‘N’ denotes eclipses that were used to refine ephemeris, but not used in the phase-folded eclipse modelling.	61
2.17	Observations taken for CRTS SSSJ0522–3505 J052210-350530. Mid-eclipse times and cycle numbers are calculated following the method detailed in §3.2.	62
2.18	Observations taken for SDSS J152419.33+220920.0. Note that the observations showed some color-dependent variability, so were binned with a different grouping.	63
3.1	The various symbols used in this chapter, and their meanings. . .	75

4.1	Summary of observational information for the 3 CVs of this chapter.	101
4.2	The system parameters found for the three CVs with peculiar white dwarf colours. Here, the reported π is the posterior distribution from fitting the white dwarf fluxes, c.f. §3.3.2.	123
5.1	Summary of observational information for the 12 CVs of this chapter.	131
5.2	The system parameters found for the CVs analysed here. The reported parallax, π , is the posterior distribution from fitting the white dwarf fluxes, c.f. §3.3.2.	185
5.3	Table 5.2, continued.	186
6.1	The inferred \dot{M} for eclipse-modelled CVs. For the Source column, ‘W22’ are from Chapter 5, ‘M19’ are systems modelled by McAllister et al. (2019) , ‘M17b’ is from McAllister et al. (2017b) , ‘S11’ are from Savoury et al. (2011)	205
6.2	The inferred AML rates for the CVs in this sample. \dot{J}_{total} is calculated from the inferred \dot{M} , and \dot{J}_{GR} is the calculated gravitational AML rate. Sources are keyed the same as Table 6.1.	206
6.3	The \dot{M} found using the white dwarf properties for each system with a \dot{M} measurement from donor properties. Sources are keyed the same as Table 6.1	210
6.4	Table 6.3, continued	211
A.1	The system parameters found for the 12 CVs analysed in Chapter 5. The reported parallax, π , is the posterior distribution from fitting the white dwarf fluxes, c.f. §3.3.2.	242
A.2	Table A.1, continued.	243
A.3	Table A.1, continued.	244
A.4	The system parameters found for the three CVs with peculiar white dwarf colours. Here, the reported π is the posterior distribution from fitting the white dwarf fluxes, c.f. §3.3.2.	245
A.5	System parameters for 15 eclipsing systems from McAllister et al. (2019) .	246
A.6	Table A.5, continued.	247
A.7	Table A.5, continued.	248
A.8	System parameters derived by Savoury et al. (2011) .	249
A.9	Table A.8, continued	250
A.10	Table A.8, continued	251
A.11	System parameters from assorted other sources: McAllister et al. (2015) (M15), McAllister et al. (2017a) (M17a), McAllister et al. (2017b) (M17b), Gänsicke et al. (2010) (C10), Shafter & Holland (2003) (S03),	252

Declaration

I declare that, unless otherwise stated, the work presented in this thesis is my own. No part of this thesis has been accepted or is currently being submitted for any other qualification at the University of Sheffield or elsewhere.

Some of this work is adapted from a prior publication – Chapter 4 is published as [Wild et al. \(2021\)](#) in the Monthly Notices of the Royal Astronomical Society under the title *System parameters of three short period cataclysmic variable stars* by Wild, Littlefair, Ashley, Breedt, Brown, Dhillon, Dyer, Green, Kerry, Marsh, Parsons, and Sahman.

Acknowledgments

First, thank you to Stuart Littlefair. This thesis and the work that went into it has only been possible with your guidance and help. Big thanks also go to the rest of the white dwarf group at Sheffield for lending their ears and knowledge over the years. You helped more than you know, but amongst other things thanks to Vik Dhillon and Dave Sahman for teaching me how to use telescopes, Martin Dyer for his sage wisdom and wonderful company, and Steven Parsons and Alex Brown for making the latter parts of this thesis possible at all. Thank you to Paul Kerry, for setting the bar for good tech support to such an impossibly high level. Finally, thank you to my wife, Charlotte. You know exactly what this work has meant to me, and the value of the love and support you've given me can't be understated.

I would like to acknowledge the Science and Technology Facilities Council (STFC) for providing the funding for my PhD, and the Isaac Newton Group (ING) of la Palma and the National Astronomical Research Institute of Thailand (NARIT) for the use of their telescopes in this work. A further thanks to the European Southern Observatory, for the opportunity to use their instruments to aid the work of others.

I can't forget to thank the fellow PhD students that have come and gone through the years, and given me such excellent company. In no particular order, thank you to Liam, Johnny, James, Christina, Emma, Lydia, Umar, Rebecca, Alex, Luke, George, and Summer, for all the good times. To my family, thank you for all the time you've spent listening to me witter on about my research – Mum and Dad, by brother Ted, my second parents in Mike and Angie, and Alex and Kathleen. Your patience and inexhaustible words of encouragement have been deeply helpful.

Summary

Cataclysmic variables are a type of close, interacting binary system, with a white dwarf primary and an M dwarf donor star that is in contact with its Roche lobe. As such, the outer layers of the M dwarf are gradually accreted onto the white dwarf, driven by angular momentum loss. Mass transfer and angular momentum loss dominates the evolution of these systems.

I characterise 15 new eclipsing cataclysmic variable stars, finding component masses and radii, and orbital separations by modelling their light curves in multiple filters. These characterisations conform to the results of previous similar works, tracking the canonical donor evolutionary sequence.

I develop a method to infer mass loss and angular momentum loss rates from donor properties. Stars are inflated by mass loss, and by replicating a donor star with the stellar evolutionary code, MESA, I can infer the mass loss rate the star is subjected to and calculate the corresponding angular momentum loss rate. I apply this method to the newly extended sample of eclipse-modelled cataclysmic variables, and report my findings.

The field of research around cataclysmic variables has struggled with an unknown contribution to angular momentum losses in the short period (< 2.5 hours) regime for some time. This is seen in population synthesis models and evolutionary models, though discriminating between differing explanations for these excess losses has been somewhat challenging. By comparing existing prescriptions for magnetic braking and consequential angular momentum loss (specifically, extra angular momentum loss resulting from successive nova eruptions) with observed mass loss and angular momentum loss rates, I present preliminary evidence in favour of nova eruptions being the dominant source of excess angular momentum losses. These findings are limited primarily by the poorly understood and poorly characterised M dwarf mass-radius relationship, a problem likely to be mitigated with the release of Gaia DR3.

Chapter 1

Background, context, and motivation

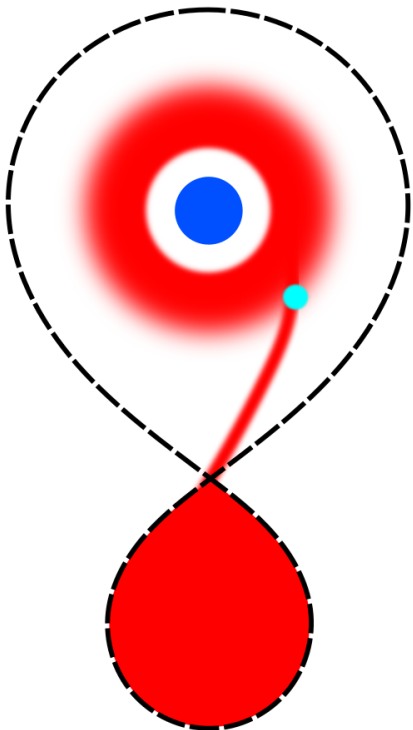


Figure 1.1: A schematic of the structure of a CV, not to scale. The **black dashed line** outlines each Roche lobe. The **dark blue circle** is the white dwarf and is surrounded by its accretion disc. The **lower red teardrop** is the secondary star, and is connected to the donor via the mass stream. The **light blue spot** where the mass stream meets the disc is the bright spot impact region.

Cataclysmic Variable (CV) systems consist of a white dwarf primary, and a lower mass red dwarf secondary star. The two are in extremely close proximity, such that the outer layers of the secondary are gradually accreted onto the white dwarf; this mass transfer process affects the evolution of both stars, in particular the donor, and is the main driving mechanism for the evolution of the system as a whole. The mass transfer also gives rise to two more observable features of a CV: an accretion disc around the white dwarf, and a shock-heated bright spot region where accreted donor material impacts the outer rim of the disc (Warner, 1995; Hellier, 2001). Figure 1.1 shows a schematic of this structure.

Systems actively undergoing mass transfer are important to our understand-

ing of stellar evolution. A diversity of stars will experience a mass transfer phase, and losing mass strongly influences a star’s evolutionary path and must be accounted for (e.g. [Renzini 1981](#); [Smith 2014](#) for single stars, or [Hurley et al. 2002](#) for binaries). Of such systems, CVs in particular are interesting as modelling their eclipse light curves can yield precise, independent measures of both stars’ mass and radius ([Wood & Crawford, 1986](#); [Littlefair et al., 2008](#); [Savoury et al., 2011](#)). Further, since the donor stars’ evolution is dominated by its mass loss, CVs provide a window into binary evolution ([Knigge, 2006](#)). The mass loss itself is driven by poorly-understood mechanisms, classically attributed to stellar magnetism and gravitational waves, that can also be probed using CV observation and modelling.

Since CVs can have directly observed orbital separations, stellar masses, and radii, they gain additional powerful diagnostics, in addition to parameters accessible with more general techniques such as spectroscopic analysis. The ability to thoroughly characterise CVs makes them an excellent test-bed for binary modelling, and the complex processes that contribute to their evolution. Unfortunately, whilst reasonably accurate semi-empirical modelling of most of the CV evolutionary track and population distribution has been possible for more than a decade (e.g. [Knigge et al. 2011](#); [Paxton et al. 2015](#)), the field has yet to produce physically motivated theoretical models capable of accurately reproducing either the CV population distribution or complete evolutionary track, indicating some shortfalls in our understanding ([Schreiber et al., 2015](#); [Schreiber et al., 2016](#)). Of most significance to this work is the problem of missing Angular Momentum Loss (AML), where CVs with low mass donor stars appear to be losing angular momentum much faster than our models predict ([Schreiber et al., 2016](#)). This first chapter will summarise the current understanding of CV formation and evolution, with a focus on the issues with CV evolutionary models.

1.1 Roche geometry

Before discussing the formation, structure, and evolution of CVs, it is first critical to understand Roche lobes. In a two-body orbital system, the Roche potential of a point is an effective potential in the non-inertial, co-rotating frame of reference. It is given by the sum of the gravitational potential energies due to the two masses, and the potential energy arising from centrifugal force. This can be described

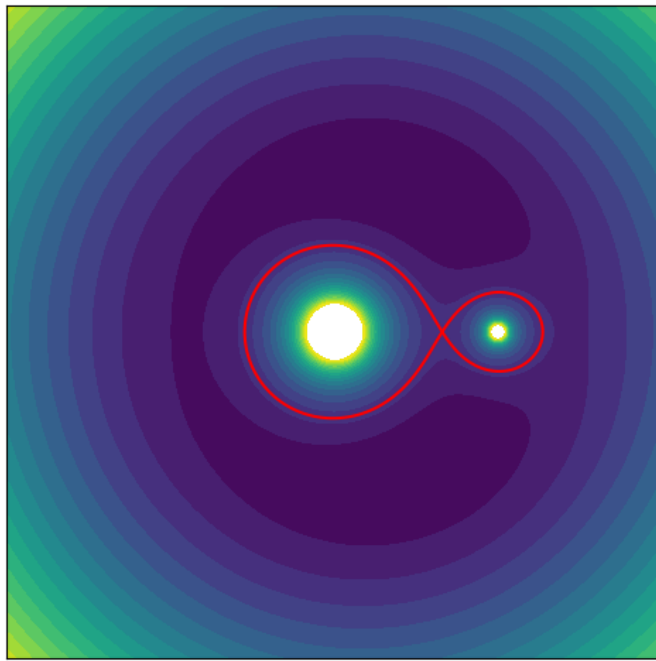


Figure 1.2: Showing the Roche potential in the neighbourhood of the binary system, with the more massive primary star on the left. Darker regions are lower potentials, lighter regions are higher potentials. The **red line** illustrates the Roche lobes.

mathematically for each position vector:

$$\phi = -\frac{GM_1}{|\mathbf{r} - \mathbf{r}_1|} - \frac{GM_2}{|\mathbf{r} - \mathbf{r}_2|} - \frac{1}{2}(\boldsymbol{\Omega} \times \mathbf{r})^2 \quad (1.1)$$

Where ϕ is the Roche potential, G is the gravitational constant, \mathbf{r} is the position vector being considered relative to the centre of mass, and $\boldsymbol{\Omega}$ is the angular momentum vector of the binary. $M_{1,2}$ and $\mathbf{r}_{1,2}$ are the masses and position vectors of the two orbiting bodies, measured from the centre of mass. Figure 1.2 shows this graphically.

There are five key locations in the Roche potential, called Lagrange points. The first Lagrange point, L_1 , is the point at which a small (co-rotating) mass is attracted both equally and oppositely by both bodies, and their effects are cancelled out. The line of constant potential that passes through L_1 gives two teardrops joined at the tips, and the teardrop encapsulating an object is known as its Roche lobe. Matter that lies beyond the Roche lobe is no longer gravitationally bound to that body, and will leave the surface of the object. If the matter crosses into the other object's Roche lobe, the material will fall onto that body, otherwise

the material will be ejected. Ejected material will no longer be in a stable orbit, and will go on to either be ejected from the system entirely, or find a new higher orbit where the two-body effects are negligible.

The shape of the Roche lobes are non-trivial to calculate, and must be done numerically. However, approximations exist for the volume-equivalent radius of a Roche lobe (that is, the radius of a sphere of equivalent volume). Most commonly used is the [Eggleton \(1983\)](#) approximation,

$$\frac{R_L}{a} = \frac{0.49q^{2/3}}{0.6q^{2/3} + \ln(1 + q^{1/3})} \quad (1.2)$$

where a is the orbital separation, and q is the mass ratio of the system, M_2/M_1 . This formula is accurate to within $\lesssim 1\%$ for all values of q . In CVs, where the secondary star is completely filling its Roche lobe, R_L makes for a reasonable approximation for the secondary stars' radius though note that the lobe is non-spherical, as can be seen in Figure 1.2.

1.2 Accretion in CVs

Accretion physics is important to the appearance and behaviour of a CV. Whilst it is summarised here, more in-depth descriptions can be found in [Warner \(1995\)](#); [Hellier \(2001\)](#); [Ritter \(2010a\)](#).

When the donor star overfills its Roche lobe, matter is ejected from its surface at thermal velocities, $\sim 10\text{km s}^{-1}$ for a 5000K M dwarf, which is small compared to the orbital velocity of the system (M dwarf velocities of $\sim 400 - 500\text{ km s}^{-1}$ are common in the observations reported in Chapters 4 and 5). Since the ejected material is effectively stationary as it leaves the donor, it falls along a ballistic trajectory towards the white dwarf primary and forms an accretion disc around it.

Disc material gradually loses angular momentum and gravitational potential energy due to its viscosity, which acts over time to concentrate the majority of the disc's angular momentum in the minority of the disc's mass, ejecting some material at high velocities at the expense of moving the remainder closer to the white dwarf. This viscosity partially arises from friction within the fluid of the disc but the main source is thought to be from turbulence – random eddy currents moving material to different radii. This form of turbulence in a thin disc was

formalised in the alpha disc model by [Shakura & Sunyaev \(1973\)](#), where viscosity, ν , is related to scale height, H , and the speed of sound, c_s , by a free parameter, α .

$$\nu = \alpha c_s H \quad (1.3)$$

Since turbulent eddies cannot be larger than H or have velocities greater than c_s , $c_s H$ forms the upper limit of ν , and α is limited in this model to values between 0 and 1. In typical CV accretion discs (i.e. quiescent discs, see §1.3.5), α takes values from $\sim 0.01 - 0.05$ ([Hellier, 2001](#)).

Material that enters the disc must lose gravitational potential energy before it can be accreted to the white dwarf surface. Approximately half of this energy is lost thermally, through radiating accretion light, and the other half is converted to the kinetic energy necessary to maintain orbit about the white dwarf at lower altitudes. This low orbit has typical velocities roughly an order of magnitude higher than the rotational velocity of the white dwarf, so for material to settle on the stars' surface it must dissipate a large amount of kinetic energy. A region between the inner edge of the disc and the surface of the white dwarf where this deceleration occurs is called the boundary layer, and can be a significant contributor to the total brightness of a CV.

As the white dwarf is accreting material onto its surface, one might expect it to grow in mass over time, and possibly even detonate as a type Ia supernova when it crosses the $1.4M_\odot$ Chandrasekhar limit. This postulation is supported by the white dwarfs in CVs being significantly more massive than their singleton counterparts ([Zorotovic et al., 2011](#)), but were this the case one would expect there to be a relationship between age and white dwarf mass. [McAllister et al. \(2019\)](#) searched for this relationship, but found no correlation between the two, indicating that the white dwarfs in CVs do not grow over time, and are unlikely to reach the Chandrasekhar limit. Growth is thought to be limited by the accreted material cyclically detonating, in events called Classical Novae outlined in §1.3.4 ([Wijnen et al., 2015; Sparks & Sion, 2021](#)). Serial detonation is even invoked as a potential source of AML, dubbed Consequential AML (CAML), that is described in §1.5.6.

1.3 CV variability and subtypes

Several subtypes of CV exist that can lie significantly outside the normal evolutionary tracks, contain exotic components, or undergo outbursts. In addition, it is common for CVs to display a significant short term, stochastic variability, known as flickering. This quasi-random noise is not fully understood, but is known to be localised to the vicinity of the white dwarf or bright spot (Horne & Stiening, 1985; Bruch et al., 1996; Bruch, 2000), though does not appear to lie directly on it. Here I briefly describe the various subtypes of CVs, though note that only quiescent CVs are suitable for analysis in this work.

1.3.1 Brown dwarf donors

The formation channel of CVs does not require that the secondary star meets any minimum mass requirement, and it is theoretically possible to form a CV with a substellar brown dwarf donor (Politano, 2002, 2004). Because the donor is so small, these systems can form well below the theoretical minimum period (see §1.5.3), between 46 minutes and 2.5 hours (Politano, 2004). CVs are observed with extremely short orbital periods, but observational evidence of these hosting brown dwarfs is rare. However, some tentative candidates do exist, for example in SDSS J150722.30+523039.8 (initially Littlefair et al. 2007, though contested by Uthas et al. 2011)

1.3.2 Magnetic CVs

It is possible for white dwarfs to have very strong magnetic fields, in the region of tens to hundreds of megagauss. Such white dwarfs are called polars and are an interesting field of study in their own right, but when a polar is accreting material from a donor star the system is designated as an AM Her star and the intense magnetic field strength alters the CV in a two main ways. The strong field lines of the polar mean that the hot, charged photosphere material transferred to the primary cannot form an accretion disc and instead falls directly onto the surface of the white dwarf. The impacting material forms a bright spot on the white dwarf surface, which is usually bright enough to be visible from Earth. In addition, the strong field lines force the white dwarf to become tidally locked to the donor star.

There is also a subclass of magnetic CVs with weaker field strengths of a few megagauss, known as DQ Her stars. In these systems, the white dwarf is not tidally locked, and a partial disc can exist.

1.3.3 Helium-rich CVs

A small number of CV donors are helium-rich, with much smaller radii than their hydrogen-rich counterparts; these can be semi-degenerate helium stars, the cores of highly evolved main sequence stars, or a second white dwarf. As a CV donor must be in contact with its Roche lobe, such systems are far more compact than usual, with orbital periods $\lesssim 65$ minutes. Such systems are AM CVn stars, after the prototypical system AM Canum Venaticorum. For further discussion on AM CVn stars, see [Solheim \(2010\)](#).

1.3.4 Classical Novae

The white dwarf in a CV is almost constantly accreting matter onto its surface. Over time this surface layer can build up, and is placed under immense pressure by the gravity of the white dwarf. Eventually, pressures rise enough to force material at the boundary to become degenerate, and once hot enough this boundary layer can begin nuclear fusion. Since the accreted material is degenerate, it cannot expand in response to the energy injected by fusion and heats further, leading to more and more fusion and culminating in a complete detonation of the accreted material on the white dwarf's surface ([Warner, 1995](#)). This detonation heats the material enough to lift degeneracy, and the accreted material is blown from the surface. These are recognised by a significant brightening of the system of between 6 and 19 magnitudes, lasting anywhere from a few days, to several months.

Once a system has experienced a classical nova, it is classified as a CNe system. ([Warner, 1995](#)). However, theory suggests that all CVs experience classical novae many times over their lifetimes. The required amount of accreted material for the nova to occur depends on the white dwarf mass, but lies between $3 \times 10^{-5} M_{\odot}$ of hydrogen for a $1.3M_{\odot}$ white dwarf, and $5 \times 10^{-3} M_{\odot}$ for a $0.6M_{\odot}$ white dwarf ([Hellier, 2001](#)). Typical CV accretion rates are around $10^{-9} M_{\odot} \text{ yr}^{-1}$ for long period systems, and $10^{-10} M_{\odot} \text{ yr}^{-1}$ for short period systems ([Hellier, 2001](#); [Pala et al., 2021](#)), suggesting classical novae recur every few million years, or every few tens of thousands of years at most.

The amount of material retained by the white dwarf is likely negligible. Both population synthesis (Wijnen et al., 2015) and observations (McAllister et al., 2017a) indicate no evidence of mass growth over time for the white dwarfs in CVs, and hence that the expulsion of the accreted material in a classical nova is complete.

A final note is that some CVs show multiple classical novae in relatively quick succession (Schaefer, 2010). These Recurrent Novae (RNe) are distinguished by having more than one observed nova event recorded. As good quality data only exist for the last few centuries, this enforces a soft limit on recurrence interval of a few hundred years, though recent efforts have been made to search ancient records for candidate events (Hoffmann & Vogt, 2022). Only a handful of confirmed RNe are known; the variable star index (Watson et al., 2006) only contains 12 systems classified as RNe.

1.3.5 Dwarf Novae

CVs also undergo less extreme brightening events, called dwarf nova outbursts. These brighten the system by between 2 and 5 magnitudes (Warner, 1995) and are more brief than typical CNe, lasting less than ~ 20 days. However, in contrast to CNe, they have recurrence times much more in line with human timescales, ranging from a few days to some decades. This is due to the fundamental difference in the physical origin of the two phenomena. Dwarf nova outbursts do not originate directly from either star in the system, but rather from the accretion disc around the white dwarf. Such outbursts are well-described by the disc instability model (Cannizzo, 1993; Dubus et al., 2018).

Initially, the disc is in a cooler, “low” state with low temperature, low surface density, and low viscosity. Material in the disc moves inwards due to friction from turbulence (see §1.2) which is relatively weak in the low viscosity material, so radial movement of disc material is slow.

If the accretion rate of donor material exceeds the rate material falls onto the surface of the white dwarf, then a build-up of matter begins in the outer regions of the disc, raising the density and temperature. Eventually, this annulus reaches $\sim 7000K$, at which point hydrogen becomes partially ionised and a rapid further increase in temperature is triggered as the material becomes optically thick and heat is trapped in the disc. In addition, as the temperature and density rise, so does c_s , and following Equation 1.3, so does viscosity, even assuming constant

α . In fact, α *rises* during outburst, to $\alpha \sim 0.1 - 0.5$ ([Hellier, 2001](#)). This hot, luminous, “high” state is again stable, and the disc is said to be in outburst.

Now that the disc is more viscous, material is moved inwards more readily. The infall rate onto the white dwarf is significantly increased, and is now higher than the mass transfer rate, so the disc is drained onto the surface of the white dwarf. As it does so, the surface density and temperature begin to fall, and eventually protons and electrons recombine into hydrogen. Recombination is an exothermic process, but the release of energy is outweighed by the material once again becoming optically thin and allowing radiation to more easily escape the disc. The disc then quickly cools back down to the quiescent, “low” state, returning to a low surface density, and the cycle can repeat. For a more in-depth consideration of this model, refer to discussions by [Cannizzo \(1993\)](#), [Osaki \(1996\)](#), and [Hameury \(2002\)](#).

Three types of dwarf novae exist, which exhibit somewhat different behaviour than what is outlined above. The first of which are SS Cyg stars, distinguished by very consistent amplitudes across outbursts, though there is variation in length, shape, and recurrence time.

Z Cam stars exhibit standstills, events where the system enters outburst, peaks in brightness, then begins to dim. However, rather than returning to its quiescent magnitude, the brightness is maintained $\sim 1 - 1.5$ magnitudes below peak brightness for a long period of time, typically between a few days, and a few years ([Simonsen et al., 2014](#)).

The third subtype are SU UMa stars. These systems are known for their more complex behaviour, exhibiting superoutbursts and superhumping, and are described in §1.3.6

1.3.6 SU UMa stars

SU UMa stars are distinguished by exhibiting superoutbursts, similar to the regular dwarf nova outbursts that the star still undergoes, but with greater amplitudes and durations, and longer recurrence times. These outbursts are triggered by the disc radius growing to such an extent that it begins to be tidally perturbed by the donor star, and becomes elliptical. This can only take place when the donor star is less than $\sim 1/3$ the white dwarf mass, so only short period systems see these superoutbursts. ([Hellier, 2001](#)). SU UMa stars are known for their superhumps, which also arises from the disc eccentricity. The tidal interaction between the

disc and the donor produces an area of increased luminosity at the edge of the disc between the white dwarf and the donor (Warner & O'Donoghue, 1988). As the disc is elliptical, the distance between this disc edge and the donor varies over the course of an orbit, causing variation in brightness as the donor moves around the disc. These fluctuations are the superhumps, and are useful as they provide a diagnostic to the mass ratio for the system as the (Patterson, 1998, 2001; Patterson et al., 2005).

Because of the strong influence of the donor, the disc is subject to precession, with a precession rate slightly longer than the orbital period. The superhump period, P_{hump} is then a combination of the orbital period, P_{orb} , and the precessional period P_{pr} ,

$$\frac{1}{P_{\text{hump}}} = \frac{1}{P_{\text{orb}}} - \frac{1}{P_{\text{pr}}} \quad (1.4)$$

and whilst P_{pr} is difficult to observe, both P_{orb} and P_{hump} can be readily observed with photometry. Since the precession period is dependant on the mass ratio and the disc radius, by finding the superhump period of eclipsing CVs an empirical relationship can be found between the superhump excess, ϵ , and the mass ratio of a CV, where:

$$\epsilon = \frac{P_{\text{hump}} - P_{\text{orb}}}{P_{\text{orb}}} \quad (1.5)$$

and several papers exist discussing and calibrating this relationship, see McAllister et al. (2019) and Kato (2022) for some recent calibrations and a good starting point for more information.

1.3.7 Novalike systems

The disc instability model applies to CVs with mass transfer rates that are high enough to exceed the infall rate onto the CV during the “low” state, but low enough that the “high” state can drive a net loss of mass from the disc. However, a subset of CVs have mass transfer rates high enough to sustain the high state and maintain a permanent outburst mode. Such systems are called novalikes.

Most novalike CVs show little variation besides the stochastic flickering seen in most CVs, though a small number known as VY Scl stars do occasionally enter “low” states and dip in brightness by several magnitudes. Livio & Pringle (1994) propose that this is triggered by a starspot rotating into the L1 point causing a fall in mass transfer rate. This fall is because the stellar surface in a starspot is lower than at the unspotted surface, causing the donor to temporarily disconnect

from the L1 point whilst the L1 is covered with a spot. A competing theory from [Wu et al. \(1995\)](#) proposes that the fall in brightness is caused by the irradiation of the donor stars' atmosphere driving mass transfer, and that when this irradiation becomes blocked in some way, the mass transfer rate falls enough for the disc to enter the low state for a short time.

1.4 CV formation

The formation of a CV begins with a binary system forming at a distance of $\sim 100R_\odot$. Crucially, the stars differ significantly in mass, one typically being $< 1M_\odot$ and the other $> 1M_\odot$ ([Ritter, 2012](#)). The lifespan of a star falls as its mass increases, so the larger star evolves faster than its companion, increasing in radius as it does so. Eventually, the primary fills its Roche lobe, usually when it ascends to the red giant branch. Once the outer layers of the primary contact the Roche lobe, the L₁ point forms a locus for mass to move from the massive, evolved star onto the less evolved secondary star.

As mass moves away from the primary, and away from the centre of mass of the system, it gains angular momentum. However, because angular momentum is conserved within the binary this is offset by a drop in separation, and the radius of the Roche Lobe, R_L , contracts following Equation 1.2. More matter is now outside the primary Roche lobe, encouraging further mass transfer and hence further reduction in orbital separation ([Ritter, 2010b](#)).

With this positive feedback loop, the primary can quickly transfer its whole envelope. The process is very rapid – so rapid that models have been unable to properly resolve it, but is probably $\sim 10^2 - 10^3$ years in duration ([Ritter, 2012](#)). With this influx of mass, the secondary star grows and the accreted matter forms a thick, bloated, deeply convective envelope on the star. The increased radius of the secondary brings the two bodies into contact ([Ritter, 2010b](#)) and the stars enter a common envelope phase of evolution. See [Paczynski \(1976\)](#) for an original reference on common envelope evolution, or [Ivanova et al. \(2020\)](#) for a recent review of the topic. For detail on this phase as it relates to CVs, see [Taam et al. \(1978\)](#); [Webbink \(1984\)](#); [Zorotovic & Schreiber \(2010\)](#); [Passy et al. \(2011\)](#).

The common envelope phase transfers much of the secondary stars' angular momentum to the shared envelope, though the mechanism for this is poorly understood ([De Marco et al., 2011](#)). If the common envelope is substantial enough,

all the energy can be removed from the orbit and the two stars will merge. If it is not substantial enough, the entire common envelope is unbound from the stars before a merger occurs, and the stars are left in a more compact orbit than when the common envelope phase began. CV systems are the product of the latter scenario - the common envelope is ejected via a strong wind, leaving the remnant core of the primary as a white dwarf, and a low mass secondary companion M dwarf still on the main sequence.

The common envelope phase can be parametrised with the energies involved, namely the gravitational binding energy of the envelope, U_{bind} , and the change in the angular momentum contained in the orbit before and after the common envelope phase, ΔU_{orb} , as the common envelope efficiency parameter, α .

$$\alpha = \frac{U_{\text{bind}}}{\Delta U_{\text{orb}}} \quad (1.6)$$

This is known as the α formalism ([De Marco et al., 2011](#)), and is a good illustration of how poorly the field understands CE evolution. α should be a metric that can be predicted with models, but this has proven very challenging and several competing frameworks exist ([Ivanova et al., 2020](#)).

The energy needed to liberate the envelope is expected to come from the orbit of the binary, but some systems have been observed and characterised with $\alpha > 1$, suggesting that other sources, like the thermal output of the stars, can contribute to the envelope ejection ([De Marco et al., 2011](#); [Ivanova et al., 2013](#)). Common envelope evolution remains a very difficult problem to solve, and only approximate models currently exist ([Ivanova et al., 2020](#)), but the following scenario is generally accepted as likely in the case of CVs.

For proto-CVs, α has been loosely estimated to be $\sim 0.2 - 0.6$ ([Politano & Weiler, 2007](#)), and some evidence exists for lower q systems having larger α ([Passy, 2013](#)). The ejecta carries with it angular momentum, causing orbital separation to quickly fall from $\sim 100R_\odot$ to a few R_\odot ([Politano & Weiler, 2007](#)). Following the common-envelope phase, angular momentum is shed through magnetic braking and gravitational wave braking until the donor comes into contact with its Roche lobe, a process that takes $\sim 1 - 2$ Gyrs. Mass transfer can then resume, though this time in the more stable secondary-to-primary direction. The system is now a CV, and its evolution from here will be dominated by AML and mass transfer, detailed in §1.5.1.

Early population studies expect that under this formation process up to 50%

of CVs should host a helium white dwarf (Politano, 1996), though to date this has been difficult to test. Zorotovic & Schreiber (2010) examined a sample of post-common envelope binaries and found only $13 \pm 7\%$ of the sample to be expected to evolve into a CV containing a helium white dwarf. However, no confirmed helium white dwarfs have been observed in CVs.

1.5 CV evolution

Once the system emerges from the common envelope phase, AML causes the orbit to tighten until the less massive red dwarf secondary fills its Roche lobe. Converse to during formation, mass transfer is now moving matter closer to the system’s centre of mass, imparting angular momentum to the secondary as it does so. This causes the orbit to widen, and increases R_L . Hence, mass transfer now acts to decrease further transfer (Ritter, 2010b), rather than exacerbate it.

To maintain mass transfer some mechanism is necessary to shed angular momentum and bring the secondary back in contact with its Roche lobe. Canonically, two mechanisms are thought to drive this; gravitational wave braking, and magnetic braking (Knigge, 2006; Knigge et al., 2011). AML drives the two bodies closer together and triggers mass transfer, and mass loss from the donor drives it to retreat from the white dwarf primary. These two processes find equilibrium when the donor is just barely overflowing its Roche lobe, and the angular momentum gained by the donor from mass transfer is offset by the AML from the system. The mass transfer timescale of the donor is much shorter than its nuclear timescale, so mass loss dominates its evolution and gives rise to a single, unified CV evolutionary path.

There is a further complicating factor to consider; whilst the secondary is losing mass, it is not in thermodynamic equilibrium. The outer layers are being lost, which reduces the pressure on the core and so reduces the rate of fusion. Below masses of $\sim 0.2M_\odot$, the thermal timescale is comparable to the mass loss timescale (this is later demonstrated in §3.4), so the star is unable to cool and contract to its equilibrium radius. This leaves the star hotter than it would be under zero mass loss, and its radius increases proportionally to the mass loss rate (Knigge, 2006; Knigge et al., 2011).

1.5.1 The classical picture of CV evolution

When two bodies orbit each other in space, the periodic warping of space-time produces gravitational waves ([Einstein, 1918](#)) and these waves carry energy away from the system, robbing it of angular momentum and reducing the orbital radius ([Paczynski, 1967](#)). In CVs, the rate of momentum loss from gravitational waves is small, so long timescales are needed to significantly alter the orbital period. Both population synthesis models and evolutionary models of CVs do not match the observed population distribution with gravitational braking alone, and magnetic braking is thought to make up the deficit (e.g. [Kolb \(1993\)](#); [Kolb & de Kool \(1993\)](#); [Davis et al. \(2008\)](#); [Garrallo et al. \(2018b\)](#)). A quantitative description of the some magnetic braking models are given in §1.5.7. Before discussing the braking mechanisms in CVs, it is important to review the classical understanding of CV evolution

1.5.2 The effect of mass transfer on the binary

When mass moves from the donor to the white dwarf primary, the redistribution of matter within the system must take place whilst conserving angular momentum. The total angular momentum of the binary, J , is given by,

$$J = M_1 a_1 v_1 + M_2 a_2 v_2 = M_1 a_1 \frac{2\pi a_1}{P_{orb}} + M_2 a_2 \frac{2\pi a_2}{P_{orb}} \quad (1.7)$$

where the distance from each star to the centre of mass is $a_{1,2}$, and the velocity of each star is $v_{1,2}$. The binary separation between the stars is $a = a_1 + a_2$, and the ratio between the stars' distances to the centre of mass is the inverse of their mass ratio, i.e. $\frac{a_2}{a_1} = \frac{M_1}{M_2}$. By substituting P_{orb} for Kepler's 3rd law, a simple equation for J can be constructed,

$$J = M_1 M_2 \left(\frac{G a}{M_1 + M_2} \right)^{1/2} \quad (1.8)$$

Now, by taking the natural log of both sides and differentiating with respect to time, the following relation between the derivatives is found.

$$\frac{\dot{a}}{a} = 2 \frac{\dot{J}}{J} + \frac{(\dot{M}_1 + \dot{M}_2)}{M_1 + M_2} + 2 \frac{\dot{M}_1}{M_1} + 2 \frac{\dot{M}_2}{M_2} \quad (1.9)$$

For the specific case where the total system mass is fully conserved, $\dot{M} = 0$, $\dot{M}_1 = -\dot{M}_2$, and $\dot{J} \equiv 0$ allows the above to be simplified,

$$\frac{\dot{a}}{a} = 2\frac{\dot{M}_1}{M_1} + 2\frac{\dot{M}_2}{M_2} = 2(q-1)\frac{\dot{M}_2}{M_2} \quad (1.10)$$

or by similarly differentiating the logarithm of $P_{orb}^2 \propto a^3$,

$$\frac{\dot{P}_{orb}}{P_{orb}} = \frac{3}{2}\frac{\dot{a}}{a} = 3(q-1)\frac{\dot{M}_2}{M_2} \quad (1.11)$$

Equations 1.10 and 1.11 tell us how the binary responds to mass transfer. As mass is lost from the secondary, \dot{M}_2 is negative and systems with $q > 1$ will have their orbits contract, whilst systems with $q < 1$ will have their orbits widen in response to mass transfer.

The effect of mass transfer on the Roche lobe is important to CVs, and must be considered. A simpler, more easily manipulated alternative to the Eggleton R_L approximation (Equation 1.2) from (Paczynski, 1971),

$$\frac{R_L}{a} = 0.462 \frac{q}{1+q}^{1/3} \quad (1.12)$$

although this only holds between $0 < q < 0.8$ and is accurate to 2%. Taking the logarithm, differentiating with respect to time, and substituting Equation 1.10,

$$\frac{\dot{R}_L}{R_L} = \frac{\dot{a}}{a} + \frac{\dot{M}_2}{3M_2} = \left(2q - \frac{5}{3}\right)\frac{\dot{M}_2}{M_2} \quad (1.13)$$

However, this reveals the flaw in assuming fully conservative mass transfer ($\dot{M} \equiv 0$, $\dot{J} \equiv 0$), as this implies that for $q < 5/6$, R_L will increase in response to mass transfer. This is not compatible with continuous mass transfer without some mechanism driving the stars closer together again (such as the nuclear expansion of an evolved donor ascending the red giant branch, as during the CV formation), and as most CVs are observed with $q < 5/6$ and do not possess such a mechanism.

Finally, the stability criteria for mass transfer can be evaluated using the equations above. The maximum stable value of q can be found by considering the mass-radius exponent of the donor (ξ), and its Roche lobe (ξ_L). For the donor, ξ

can be found by simply differentiating the general equation $R \propto M^\xi$.

$$\xi = \frac{d \ln R_2}{d \ln M_2} \quad (1.14)$$

Similarly, by using Equation 1.13,

$$\xi_L = \frac{d \ln R_L}{d \ln M_2} = 2q - \frac{5}{3} \quad (1.15)$$

For stable mass transfer, the response of the Roche lobe must be less than the response of the donor, $\xi > \xi_L$. This ensures that mass loss causes the star to contract more than the Roche lobe contracts, and gives the following stability criterion,

$$q < \frac{1}{2}\xi + \frac{5}{6} \quad (1.16)$$

for which a theoretical value of ξ can be used to find the maximum q . For a low mass, main sequence star ($M < 0.8M_\odot$), $\xi \simeq 0.8$ (Knigge et al., 2011) and $q < 1.23$. Below $M_2 \lesssim 0.43M_\odot$, the star becomes deeply convective and ξ falls sharply to $\xi = -1/3$ (Paczynski, 1965; Rappaport et al., 1982), and $q \lesssim 2/3$.

1.5.3 Period evolution and key population features

The orbital period of a CV can be measured by tracking either their spectroscopic radial velocities (e.g. Gänsicke et al. 2009), or the timings of repeating features in their light curves (e.g. Littlefair et al. 2008). Once this has been done for a large enough sample (Southworth et al., 2015), a histogram of the periods can be plotted. This plot, shown in fig. 1.3, has three immediately obvious features:

- a long period cutoff, as the number of systems taper off after ~ 12 hrs
- a period gap at $\sim 2 - 3$ hrs
- a period minimum at ~ 1 hour, with a pile-up of systems just above it.

Each of these features are discussed in turn.

The period maximum

There are three constraints on a CV pertinent to the maximum allowable period. The mass ratio, $q = \frac{M_{\text{donor}}}{M_{\text{wd}}}$, must be low enough for thermally stable mass transfer

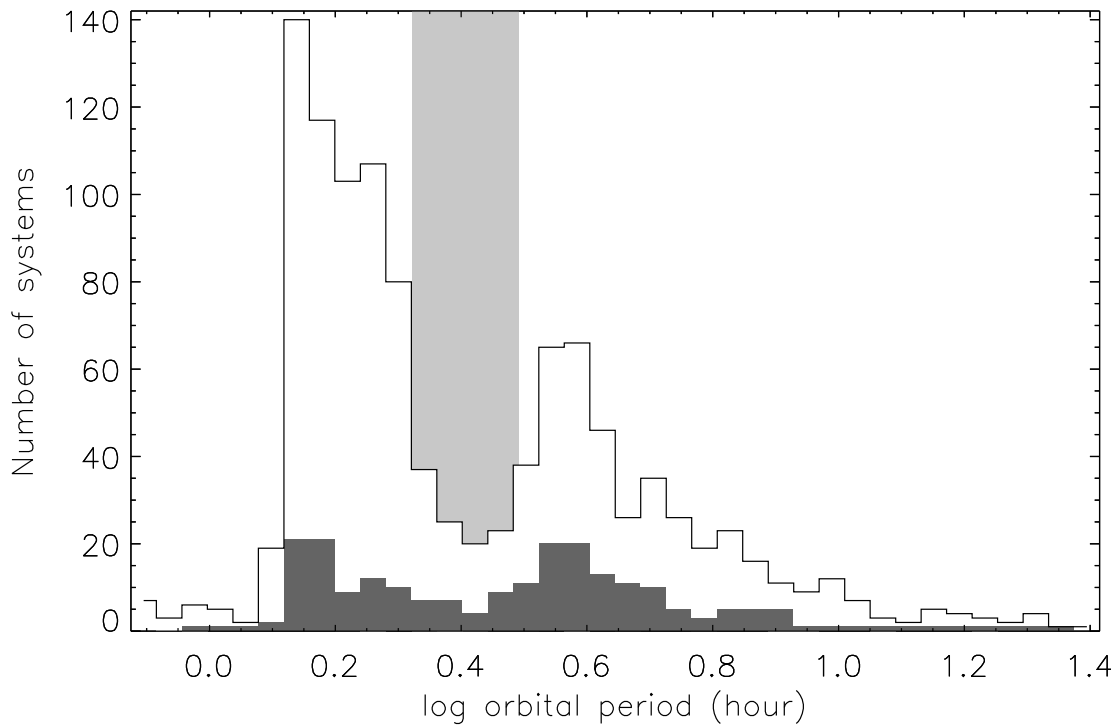


Figure 1.3: Reproduced from [Southworth et al. \(2015\)](#), Figure 14. The orbital period distribution of RKCat ([Ritter, H. & Kolb, U., 2003](#)) CVs identified by the SDSS (**white histogram**) and of the subset of these which are eclipsing (**grey histogram**). The **light grey shaded region** illustrates the period gap at 2.1 - 3.1 hours. The periods have been collected into histogram bins which are of equal size in log space.

($q < 1.23$ from §1.5.2, here approximated as $q = 1.0$), the donor radius must be approximately equal to the Roche radius, and maximum mass of a white dwarf is well known to be limited to $\leq 1.4M_{\odot}$ before triggering thermonuclear runaway (Schönberg & Chandrasekhar, 1942).

Now, to find the theoretical period maximum, one must simply find the period corresponding to the largest possible donor star. Warner (1995) shows that the average density, ρ_{av} , for objects that fill their R_L follows a robust relationship;

$$\frac{\rho_{av}}{\rho_{\odot}} = 75.9P_{orb}^{-2}(h) \quad (1.17)$$

Knigge et al. (2011) derived a connection between CV secondary mass and radius, M_2 & R_L . This can be manipulated to produce a mass-period relationship,

$$\rho_{av} = \frac{3M_2}{4\pi R_L^3} \simeq 75.9P(h)^{-2} \quad (1.18)$$

$$\frac{R_L}{R_{\odot}} = C \cdot \left(\frac{M_2}{D \cdot M_{\odot}} \right)^{\alpha} \quad (1.19)$$

where C and D are constants for a particular regime, i.e., short-period, long-period, or period bouncer, and α is the mass-radius index (Knigge, 2011). Combining the above gives a pleasingly simple relationship.

$$M_2^{(1-3\alpha)} \propto P^{-2} \quad (1.20)$$

For long-period CVs, $\alpha = 0.67 \pm 0.04$ (Knigge et al., 2011), and equation 1.20 becomes $M_2^{1.01} \propto P^2$, and larger secondary masses require longer periods. The theoretical maximum secondary mass of $1.4M_{\odot}$ corresponds to a period of ~ 12 hrs, though in reality these higher mass donors are rarer and the frequency of CVs at these higher periods begins to drop much earlier, at ~ 6 hrs (Gänsicke et al., 2009).

The period gap

Between periods of around 2-3 hours, there is a dramatic fall in the number of CVs detected and volume-limited samples indicate that this is a real effect and not a selection bias (Kolb et al., 1998; Pala et al., 2020). The origin of this gap in the period distribution is something of an open problem.

Models indicate that long period systems ($P > 3$ h) have far higher mass loss

rates than short period systems ($P < 2\text{h}$) (Ritter, 1985). This suggests a significant change in braking mechanisms between the two regimes. Recall that the donor star is inflated by mass loss (§1.5). If the cutoff of angular momentum loss is sharp, i.e. magnetic braking suddenly ceases, the donor is allowed to contract to its equilibrium radius and disconnects from its Roche lobe, shutting off mass transfer. The system is still subject to gravitational radiation, however, so gradually continues to evolve towards shorter periods. Once the secondary reconnects with its Roche lobe, mass transfer resumes and the system again presents itself as a CV, emerging from the period gap at a $\sim 2\text{hr}$ period (Kolb, 2002).

The disruption of magnetic braking was proposed early on to explain the period gap (Rappaport et al., 1983; Spruit & Ritter, 1983), and relatively shortly after Kolb & de Kool (1993) showed more quantitatively that a sub-class of purely gravitational braking CV systems does not reproduce the observed population. The classical evolutionary path of CVs has involved the secondary becoming fully convective which was thought to disrupt the magnetic field and so cease magnetic braking (Knigge et al., 2011). Davis et al. (2008) used population synthesis to demonstrate that, if the period gap is caused by disrupted magnetic braking, this may affect the mass function of quiescent CVs that are moving through the gap. They expect an excess of non-transferring CVs over low mass post-common envelope CVs that emerge from the common envelope phase directly into the period gap. These should form at a predictable rate across q , but due to the slow crossing of quiescent CVs the latter ‘pile up’ in the gap - a detectable effect observed by Zorotovic et al. (2011).

The period minimum, and period bouncer systems

The period minimum was first predicted by Rappaport et al. (1982), and can be understood by considering the two governing timescales affecting the secondary. For donors with masses above $\sim 0.1M_{\odot}$, the donor is contracting in response to mass loss. As this proceeds, both the Kelvin-Helmholtz (a.k.a. thermal) timescale, τ_{KH} , and mass transfer timescale, $\tau_{\dot{M}}$, are increasing (the latter due to \dot{M}_2/M_2 rising as the period shrinks). However, τ_{KH} rises faster, and at a period of ~ 80 minutes (Ritter & Kolb, 1998; McAllister et al., 2019), τ_{KH} exceeds $\tau_{\dot{M}}$, causing the donor to lose mass adiabatically and expand rather than contract in response to mass loss. This allows the donor to remain in contact with its Roche Lobe when mass loss raises it to a higher orbit, and the system evolves to

longer periods over time.

More quantitatively, as the components of a short period CV move closer together and the donor falls in mass, τ_{KH} and τ_M become more out of balance, corresponding to α in equation 1.20 decreasing ([Knigge, 2011](#)). A main-sequence star will have $\alpha \sim 1$, but a secondary subjected to fast, adiabatic mass loss will have $\alpha \simeq -1/3$. Looking at the gradient of equation 1.20, the existence of a period minimum can be easily seen.

$$\frac{\dot{P}}{P} = \frac{(3\alpha - 1)}{2} \frac{\dot{M}_2}{M_2} \quad (1.21)$$

When $\alpha \leq 1/3$, a negative \dot{M} will produce a *positive* change in P , and the donor begins to retreat from the white dwarf ([Rezzolla et al., 2001](#)).

This has been confirmed by [Knigge et al. \(2011\)](#), who found that for period bouncer CVs, $\alpha = 0.21^{+0.05}_{-0.10}$, giving the following empirical version of equation 1.20 in the post-period minimum regime.

$$M_2 \propto P^{-5.4} \quad (1.22)$$

1.5.4 Problems with the classical picture

A solid knowledge of exactly how and why CVs lose angular momentum has remained surprisingly elusive for several decades now. Early theories established gravitational waves and magnetic braking as the two main sources of AML, but attempts to quantify this with evolutionary models and population synthesis models consistently fall short. Gravitational losses are well understood, and have been independently observed and studied, but the sources and consequences of magnetic braking are not so easy.

1.5.5 The missing AML problem

The evolution of CVs is driven by the donor stars. The orbital period is determined by the mass-radius relationship of the donor under mass loss, and the decay of the orbit should simply result directly from the two braking mechanisms (gravitational and magnetic). Figure 1.4 shows the relationship between the donor mass and orbital period, and the single unified CV track can be seen in the observations. CV evolution models can be built to try and reproduce this track,

and indeed at long periods, our understanding of those mechanisms seem robust enough to produce models that satisfy observations. The period gap can, with some manual tweaks, also be reproduced with some accuracy. Unfortunately, at short periods ($\lesssim 2$ hours), the data begin to diverge from models (Knigge, 2006; Knigge et al., 2011).

Section 1.5 describes how the donor’s mass-radius relation is altered by the presence of continued mass loss. The donor is larger than a singleton of the same mass, as the mass loss timescale is comparable to the thermal timescale and the donor is not quite able to maintain thermal equilibrium (Knigge et al., 2011). The degree of this inflation increases with more rapid mass loss. As mass loss is driven by AML, it follows that a CV donor that has stronger AML will have a larger radius, and therefore sit at a longer period than a CV with weaker AML, altering the gradient of the tracks in Figure 1.4 at periods of $\lesssim 3$ hours. In this way, the shape of the tracks in Figure 1.4 is a diagnostic of the form of AML experienced by a CV across its lifetime (Knigge et al., 2011).

Knigge et al. (2011) used observations of donor masses and radii and attempted to recreate the donor evolutionary sequence. An unknown additional source of AML was added to their models, simply scaled relative to gravitational braking. This unknown contribution to AML is motivated by the disagreement between data and the model that omits this source. Knigge et al. (2011) find that the best-fit model to their data uses an excess braking below the period gap that is $1.47 \times j_{GR}$, where j_{GR} is the AML due to gravitational waves. Figure 1.4 is reproduced from their work, and shows the significant improvement in agreement with data.

Pala et al. (2017) used the effective temperatures of the white dwarfs to probe CV evolution. The white dwarf temperature can be enhanced by accretion, so a hotter white dwarf suggests a higher mass transfer rate. This is sensitive to changes in \dot{M} on relatively short timescales ($\sim 10^4$ yrs), but still provides a valuable insight. Pala et al. (2017) compare their white dwarf temperatures (and therefore mass transfer rates and AML rates) to MESA CV evolutionary tracks, and find that their observed temperatures are poorly described by only gravitational AML, but are more well described by models that includes excess AML equivalent to gravitational losses, i.e. double-strength gravitational AML.

The disagreement between theory and observation at short periods indicates that our understanding of AML in this regime is lacking, and a few proposals to

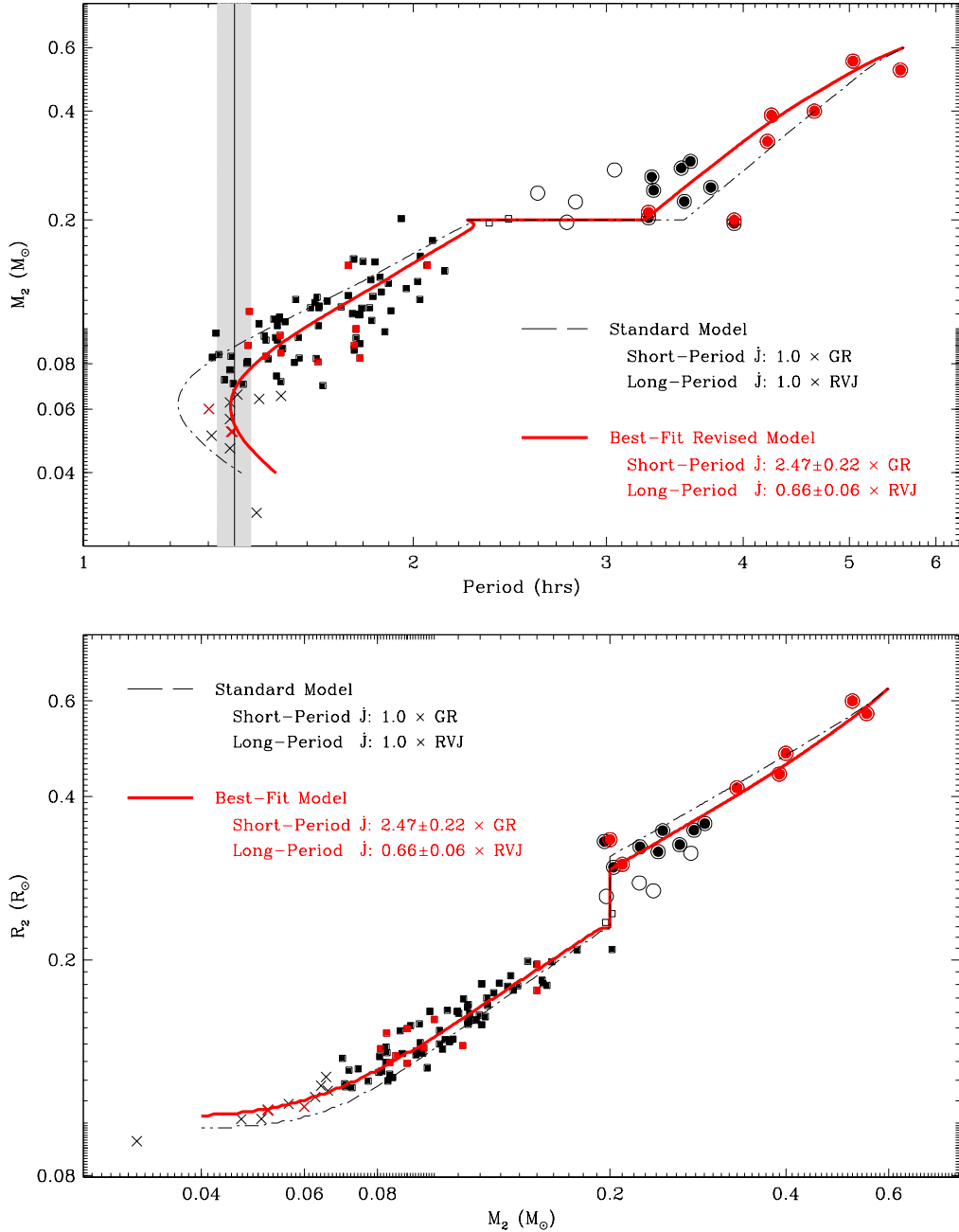


Figure 1.4: Reproduced from Knigge et al. (2011). **Black** markers are data from superhumpers, **Red** markers are data from eclipsers. **Crosses** denote candidate period bouncer CVs, **Squares** are short-period CVs, and **Circles** are long period CVs. **Open symbols** are omitted from their analysis due to lying in the period gap. The **Dashed Black lines** are their ‘standard’, naïve model, and the **Solid Red line** includes an empirically determined excess AML source, scaled to gravitational wave braking. In the top panel, the **Vertical black line** signifies the observed period minimum, with the grey region as the FWHM of the period spike as measured in Gänsicke et al. (2009).

rectify this have been suggested.

The obvious solution to the problem of missing AML is that we simply do not understand magnetic braking well enough to say that it fully disappears below the period gap. The donor may retain a residual magnetic field strong enough to drive some weaker form of magnetic braking that remains after the bulk of magnetic braking ceases, a.k.a. residual magnetic braking.

The period gap is frequently attributed to a fall in magnetic braking when the donor becomes fully convective, due to a large reduction in magnetic field strength. However, observations of field M dwarfs of similar masses, with convective envelopes, are seen with key tracers of magnetism. Specifically, X-ray observations find that the coronal magnetic energy dissipation of fully convective stars is similar to non-convective stars (Wright & Drake, 2016), and Zeeman-Doppler imaging of rapidly rotating M dwarfs indicate that magnetic fields remain strong, whilst the complexity of surface magnetic fields increases alongside rotation rate (e.g. Petit et al. 2003; Donati & Landstreet 2009; Marsden et al. 2011; Waite et al. 2011, 2015). Together, these observations strongly indicate that the disrupted magnetic braking model commonly accepted is ill-motivated, and may be more closely tied to field complexity than field strength (Garraffo et al., 2018b). If the gap is indeed driven by a sudden increase in field complexity, then it is reasonable to assume that magnetic braking may remain significant after the system emerges from the period gap.

Magnetic braking is not the only possible explanation for excess AML, and another strong candidate is consequential AML. This mechanism is discussed below.

1.5.6 Consequential AML

Consequential AML (CAML) is an additional source of momentum loss, originally motivated physically as a second source of magnetic wind emanating from the inner regions of the white dwarf accretion disc (King & Kolb, 1995; Schenker et al., 1998). In more modern considerations of CAML, the excess loss is explained as nova events temporarily immersing the system in a viscous medium, causing drag on the two bodies and reducing their orbital separation (Schreiber et al., 2016). In each case, this AML is “consequential”, in the sense that they rely on either a pre-existing disc to be present or the white dwarf to be accreting enough mass to trigger novae, and the CAML disappears in the absence of existing AML.

By modelling CV evolution including this process, several issues of older CV population synthesis and evolutionary models can be solved at once ([Schreiber et al., 2016](#)). These issues are:

1. the observed mass of CV white dwarfs is systematically higher than singleton white dwarfs (e.g. [McAllister et al. 2019](#); [Pala et al. 2020](#));
2. since the short period regime has much lower AML rates, CVs should spend most of their time below the period gap, and $\sim 99\%$ of CVs are expected to be short period ([Kolb, 1993](#)), but observations see a less severe imbalance between long (17%) and short (83%) period systems ([Pala et al., 2020](#));
3. under purely gravitational losses, the period minimum was first calculated at ~ 67 minutes ([Kolb & Baraffe, 1999](#)), but is observed at ~ 79 minutes ([McAllister et al., 2019](#));
4. the space density of CVs is roughly 1-2 orders of magnitude lower than population synthesis models predict.

The introduction of a modified, empirically calibrated CAML produces models that do not suffer from these issues, making a compelling case for its use – though it is unsurprising that observations can be matched by the introduction of an unrestricted free parameter.

The maximum dynamically stable mass transfer rate of a CV is a function of q , related via the adiabatic mass-radius exponent, ξ_{ad} , and the mass-radius exponent of the Roche radius, ξ_L . Where the two intersect forms a threshold beyond which runaway mass transfer (much like the pre-CV common envelope phase) is triggered, and most likely results in a merger between the two bodies. Similarly to the derivation in §1.5.2,

$$\xi_{ad} = \frac{\mathrm{dln}(R_2)}{\mathrm{dln}(M_2)}_{ad} = \frac{\mathrm{dln}(R_L)}{\mathrm{dln}(M_2)} = \xi_L \quad (1.23)$$

where ξ_{ad} for convective stars is $-1/3$. Recalling the Eggleton approximation for the Roche radius, Equation 1.2, we can find $\xi_{ad}(q)$ ([Schreiber et al., 2016](#)) in the absence of CAML,

$$\xi_{ad} = \frac{2}{3} \frac{\ln(1 + q^{1/3}) - \frac{1}{2} \frac{q^{1/3}}{1+q^{1/3}}}{0.6q^{2/3} + \ln(1 + q^{1/3})} (1 + q) + 2(q - 1) = -1/3 \quad (1.24)$$

Solving this equation gives a critical maximum value of $q \lesssim 0.634$. However, under CAML, extra sources of \dot{J} are introduced. For example, under the classical non-conservative construction, \dot{J}_{CAML} is due to nova ejecta carrying angular momentum away from the system as it leaves, contributing

$$\frac{\dot{J}_{CAML}}{J} = \nu \frac{\dot{M}_2}{M_2} \quad (1.25)$$

Here, $\nu = M_2^2/(M_1(M_1 + M_2))$ and encapsulates the assumption that the angular momentum carried by ejected nova material is equal angular momentum to the white dwarf. The right hand side of Equation 1.23 is then altered by the increased AML rate.

$$\xi_{ad} = \frac{2}{3} \left(\frac{\ln(1 + q^{1/3}) - \frac{1}{2} \frac{q^{1/3}}{1+q^{1/3}}}{0.6q^{2/3} + \ln(1 + q^{1/3})} \right) + 2\nu + \frac{M_2}{M_1 + M_2} - 2 \quad (1.26)$$

The effect of this altered form of ξ_{ad} is that CVs with higher mass ratios are stable. Binary population synthesis models by [Schreiber et al. \(2016\)](#) demonstrate that this model is not compatible with observations, producing *more* CVs with low mass donors than the non-CAML model and actually performing worse than models that don't include this version of CAML. However, by altering the form of ν so that it is no longer tied to the white dwarf's angular momentum, a much better agreement with observations can be reached. This is the empirical CAML model, or eCAML.

ν is altered to a simple function of the white dwarf primary mass,

$$\nu(M_1) = \frac{C}{M_1} \quad (1.27)$$

where C is an arbitrary constant chosen to best reflect observations, and ([Schreiber et al., 2016](#)) adopt values of $C = 0.3\text{--}0.4$. The inverse relationship of more CAML at lower white dwarf masses is motivated by lower mass systems ejecting nova material at a lower velocity, meaning the binary is immersed in a friction-generating medium for longer and imparting more energy into the ejecta.

With eCAML, the dynamically unstable region is expanded. This has the important effect of making CVs with low-mass white dwarfs prone to dynamically unstable mass transfer (see §1.5.2), removing them from the CV population – this simultaneously answers the question of CV white dwarfs being more massive than

expected, and also vastly lowers the space density ([Belloni et al., 2018](#)). Finally, the majority of systems that are now dynamically unstable are short-period CVs, so the observed period distribution is significantly better reproduced. Figure 1.5 is reproduced from [Schreiber et al. \(2016\)](#), and shows the three dynamically unstable regions graphically.

Some observational evidence for eCAML has recently been uncovered by [Pala et al. \(2021\)](#), where an inverse correlation between white dwarf mass and mass loss rate was observed. This is in line with Equation 1.27. Also, low mass ($< 0.5M_{\odot}$) helium-core white dwarfs are expected to be formed in binaries, but are frequently observed as singletons. The merger scenario under eCAML provides a neat explanation for this ([Zorotovic & Schreiber, 2017](#)). In addition, [Sparks & Sion \(2021\)](#) observed the spectra of CV donors and found significant non-solar abundances, indicating that after nova outbursts, some of the nova-processed material is retained in the system long enough to be accreted onto the donor, and is supportive both of lower mass white dwarfs having a lower eCAML contribution, and of the donor being immersed in nova material long enough to accrete significant amounts of it.

1.5.7 A review of modern magnetic braking theories

The M dwarf secondary of a CV will emanate some wind, made up of charged ions, and have some magnetic field which co-rotates with the star. Consider a blob of charged wind material, moving with some sideways velocity in the plane of the orbit, almost certainly slower than the magnetic field lines. The blob will interact with the field and be accelerated to co-rotate with them. This higher velocity causes it to move outwards, to a higher orbit, where the field lines are moving even faster, accelerating the blob more. As the wind material is accelerated, it exerts a drag force on the magnetic field of the donor and slows its rotation rate. The close proximity of the binary means that tidal effects are strong, and the donor is spun up again by robbing the orbit of angular momentum, reducing the binary separation and hardening the binary ([Verbunt & Zwaan, 1981](#)).

As an aside, [Wickramasinghe et al. \(1996\)](#) presented theoretical motivation that the white dwarfs in CVs can have too strong a magnetic field to allow magnetic braking. Open field lines are necessary for wind to escape the system, so too strong a white dwarf magnetic field can trap the ionised gas in-system, suppressing the wind of the secondary. Evidence for AML suppression under strong

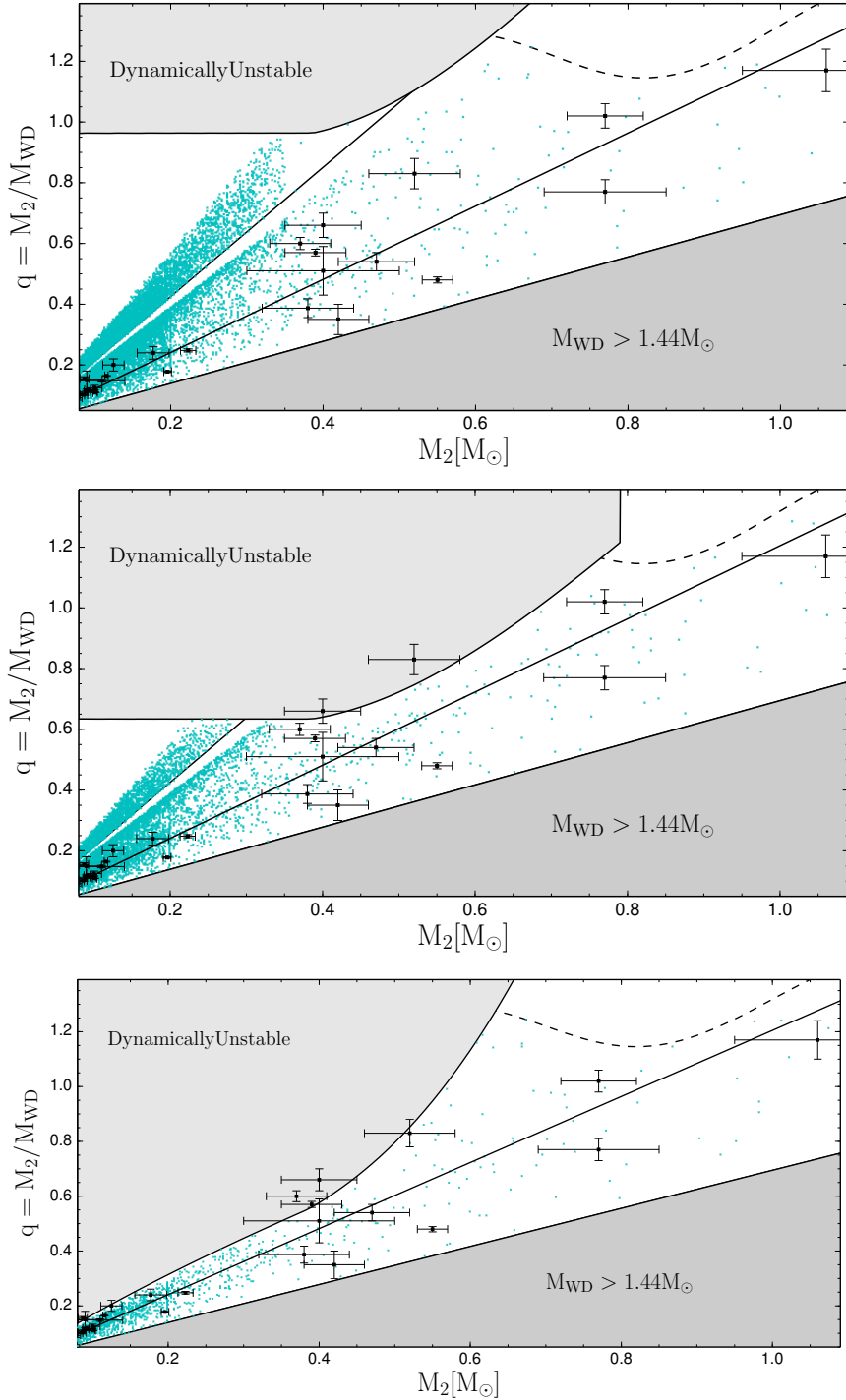


Figure 1.5: Reproduced from Figure 2 and Figure 3 of Schreiber et al. (2016). **Black squares** are observed CVs, and **cyan dots** are predicted CV populations. *Top* is for a fully conservative CV model, the *middle panel* is for the classical non-conservative model, and the *bottom panel* is the eCAML results. The $M_{\text{wd}} > 1.44M_\odot$ regions are forbidden, as these white dwarfs exceed the Chandrasekhar limit.

magnetic fields has been found in binary population synthesis models that focus on magnetic CVs ([Belloni et al., 2020](#)). The models that include magnetic wind suppression under a strong white dwarf magnetic field result in a better fit to key CV observables – specifically the orbital period distribution, white dwarf temperature distribution, and space density.

When building a magnetic braking model, assumptions must be made about the effects of the magnetic field strength and field geometry, as well as how the wind speed scales with the donor’s mass, radius, and rotation rate. The adopted values for these free parameters are tuned to match open cluster data, as open clusters can have their ages determined, and the masses, radii, and rotation rates of the stars contained in them observed (e.g. [Matt et al. 2015](#); [Garraffo et al. 2018a](#)). The CV community is able to use these findings to inform CV models. However, the parameter space covered by open cluster data does not cover the parameter space occupied by CVs. Rotation rate is a key variable in magnetic braking prescriptions, but the typical CV rotational period is on the order of a few hours, and singleton M dwarfs are considered extremely fast rotators with periods of a day – a difference of an order of magnitude. Observations of singletons simply do not reach to the extremely low mass, rapid rotations that are frequently seen in CVs, so we are forced to rely on extrapolation and theory.

This carries with it some major practical issues. One is that whilst the broad effects of magnetic fields is relatively easy to intuit, quantitative physical understanding the mechanics and origins of stellar magnetic fields is difficult, involving fluid dynamics, considering interactions with the accretion disc, and magnetism acting on complex systems, which quickly becomes prohibitive to model and is usually handled with one of a variety of recipes. [Knigge et al. \(2011\)](#) contains a detailed compilation of some older approaches, but the decade since has seen a few newer methodologies emerge. Here, two recent magnetic braking prescriptions are described in moderate detail: the [Matt et al. \(2015\)](#) prescription, and the [Garraffo et al. \(2018a\)](#) prescription. For a more complete, detailed summary of the modern understanding of M dwarf magnetic fields refer to [Kochukhov \(2021\)](#).

Matt prescription for magnetic torque

In [Matt et al. \(2015\)](#), an empirical prescription is derived that relates the torque felt by a low mass main sequence star to that stars’ mass, radius, and Rossby number, Ro . Ro is a fluid dynamics term for the ratio between the inertial

and Coriolis force terms of the Navier-Stokes equations. A small Ro indicates a system dominated by Coriolis effects, and a large Ro indicates that centrifugal and inertial forces dominate. The Ro of a main sequence star can be calculated from its rotation period, P_{rot} , and the convective turnover timescale, τ_{cz} .

$$Ro = \frac{P_{rot}}{\tau_{cz}} \quad (1.28)$$

Through Ro , the effectiveness of magnetic braking is tied to rotation, which is extremely fast in CVs, and stellar mass and age, which affect τ_{cz} .

[Matt et al. \(2015\)](#) make use of observations of stars with masses between $0.15 - 1.3M_\odot$ and ages of $\sim 10^{6-9}$ yrs, that have had their rotation periods measured. This dataset is used to calibrate a theoretically motivated empirical prescription for magnetic braking. There is some evidence for a saturation of magnetic activity below a critical Rossby value (a.k.a. above a critical rotational period) ([Reiners et al., 2009](#)), where magnetic activity seems to no longer respond to changes in rotation. [Matt et al. \(2015\)](#) therefore adopt two relationships for torque, T , modulated by an empirical value, p ,

$$T = -T_0 \left(\frac{\tau_{cz}}{\tau_{cz,\odot}} \right)^p \left(\frac{\Omega_*}{\Omega_\odot} \right)^{p+1} \quad (1.29)$$

for the unsaturated regime, and

$$T = -T_0 \chi^p \left(\frac{\Omega_*}{\Omega_\odot} \right) \quad (1.30)$$

in the saturated regime. In both cases, p is assigned as $p = 2$ in order to agree with the most common literature spin-scaling prescription, $T \propto \Omega_*^3$. χ is the inverse critical Ro for saturation, for which [Matt et al. \(2015\)](#) adopt a value of 10. The rotation rates of the donor and the Sun are $\Omega_{*,\odot}$ respectively, and T_0 is given by a function of mass and radius,

$$T_0 = 9.5 \times 10^{30} \text{erg} \left(\frac{R_*}{R_\odot} \right) \left(\frac{M_*}{M_\odot} \right) \quad (1.31)$$

The authors take observations of two clusters, the ~ 5 Myr old ONC cluster and the ~ 580 Myr old Praesepe cluster, and use the first as initial conditions and the second as target distribution to reproduce. Figure 1.6 is taken from [Matt et al. \(2015\)](#), and compares the initial and final conditions of their synthetic

cluster model compared to these two boundary conditions. During the first few tens of Myrs of this model, the stars in the synthetic cluster are spun up as they contract, lowering their periods by factors of $\sim 5 - 10$. After this initial phase, which is much shorter than the spin down timescales, the more long-term spin evolution begins.

The agreement between the synthetic cluster and the Praesepe cluster at 574 Myrs is impressive. Above $\sim 0.8M_{\odot}$, stars converge on a single narrow mass - period track just as is seen in the observations, and the large scatter below $\sim 0.8M_{\odot}$ is also reproduced. Also, just as is seen in the cluster observations of Praesepe, the fastest rotators are those with the lowest masses. Both of these features arise from the transition from saturated braking, to unsaturated braking (Matt et al., 2015).

At formation, almost all stars experience saturated magnetic braking. The single narrow track arises from higher mass stars spinning down faster than lower mass stars, moving them off the much less efficient saturated braking regime sooner. The pile-up of systems then produces the narrow track. The mass dependency of this track comes from the fact that spin-down timescale in the saturated regime is shorter for higher mass stars. The broad population of low mass rapid rotators is a direct result of the broad initial conditions, which span an order of magnitude themselves, and the longer spin-down time of lower mass stars in the saturated regime allowing them to remain at high rotation rates for longer.

However, this model does fail in a few key respects. In the bottom panel of Figure 1.6, a small population of very slow rotators can be seen at $\sim 0.4M_{\odot}$. The slower rotation rates of these stars suggests an alternative spin-down mechanism. The inverse problem is seen at $\sim 0.7M_{\odot}$, where a handful of stars are seen rotating *faster* than predicted by any of the synthetic cluster stars, suggesting that magnetic braking is not as effective in their case. More importantly for the CV field, the parameter space of CVs is completely uncovered, as CVs have rotation periods of < 0.2 days, and the systems that this work concerns have periods of $\lesssim 0.07$ days. Whilst this would firmly place CVs in the saturated regime, there is evidence of a ‘supersaturated’ regime at extreme rotation periods that may be relevant to CV donors (James et al., 2000; Wright et al., 2011; Argiroff et al., 2016). This possibility is also noted by Gossage et al. (2021) when outlining best practice use of this prescription in the stellar evolution code MESA, though the subject is not a settled matter and competing evidence for the *lack* of supersaturation has

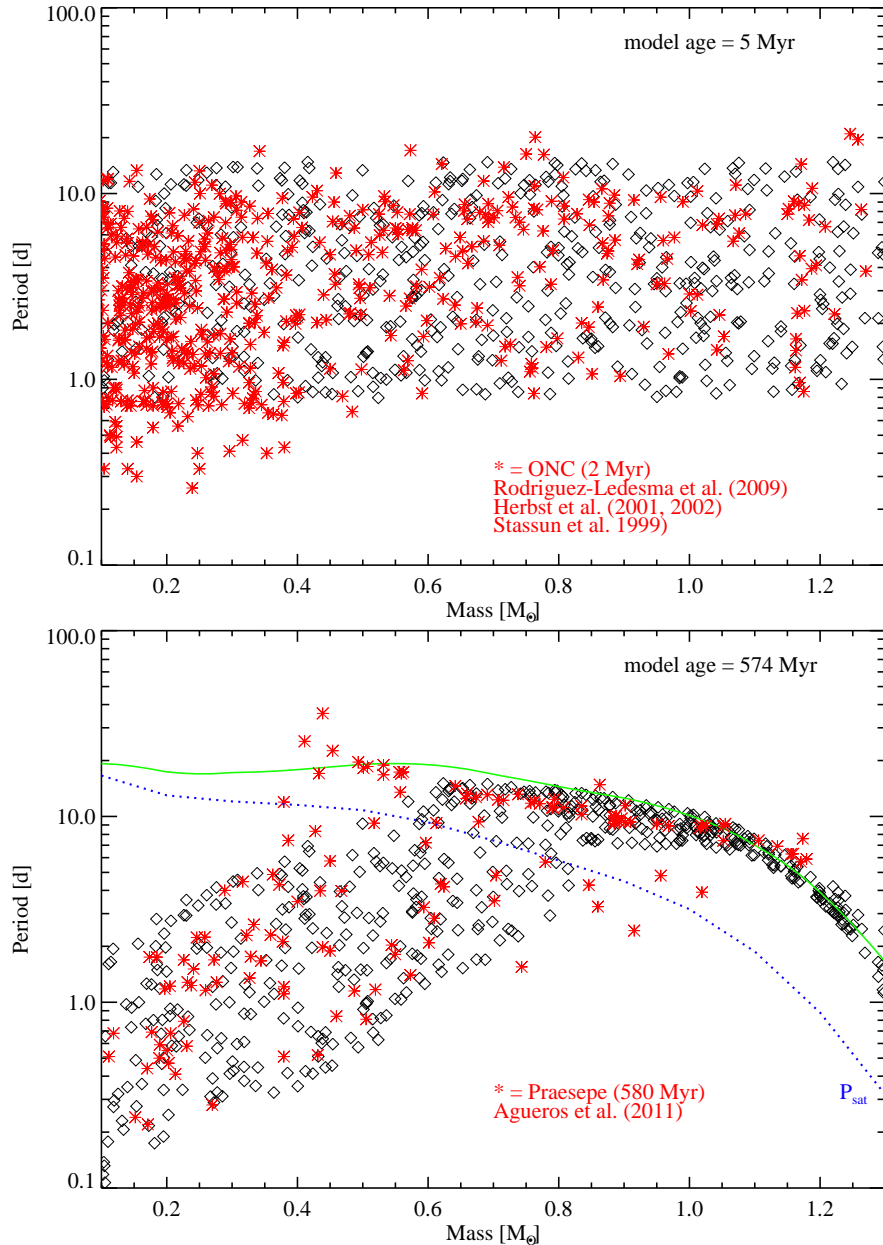


Figure 1.6: Figure taken from Matt et al. (2015). **Red crosses** are observations of the ONC (*top*) and Praesepe (*bottom*) cluster stars. **Black diamonds** are synthetic cluster stars. In the bottom panel, the **solid green line** is the theoretical asymptotic spin rate of unsaturated stars and the **dotted blue line** delimits magnetically saturated and unsaturated stars.

been reported by [Jeffries et al. \(2011\)](#).

Garraffo prescription for magnetic torque

The [Garraffo et al. \(2018a\)](#) model considers the morphology of the magnetic field to also be important to the strength of magnetic braking, based on the work by [Garraffo et al. \(2015\)](#). The primary justification for this inclusion is observations of open clusters of a known age, where a bimodality is seen in the rotation rates of stars of similar masses. Some stars appear to be fast rotators, and some are slow rotators, and there is a dEarth of systems between the two. Previous attempts to model this bimodality have relied on an unexplained transition between an efficient braking state, and an inefficient braking state ([Spada et al., 2011; Reiners & Mohanty, 2012; Gallet & Bouvier, 2013](#)), and [Garraffo et al. \(2018a\)](#) expand on this by offering a shift in magnetic field morphology as the underlying trigger.

Their formalisation of this is based on two assumptions. They assume that stars with a dipolar magnetic field follow a known spin-down law, with a mass dependence reflecting τ_{cz} ([Skumanich, 1972](#)). Second, they assume that there is some relationship between field morphology and stellar spin rate. Specifically, that stars rotating more rapidly have more complex magnetic fields. This is formalised via an AML rate, \dot{J} ,

$$\dot{J} = \dot{J}_{\text{dipole}} Q_J(n) \quad (1.32)$$

where \dot{J}_{dipole} is the dipole loss under the Skumanich law, $\dot{J}_{\text{dipole}} \propto \Omega^3 \tau_{\text{cz}}$. Q_J is a modulating factor that encapsulates the field complexity at the stellar surface, and is controlled by the complexity factor, n , which is a function of Ro . [Garraffo et al. \(2016\)](#) derive an equation for Q_J , based on fitting the results of magnetohydrodynamic simulations with varying field complexities.

$$Q_J(n) = 4.05e^{-1.4n} + \frac{n - 1}{60Bn} \quad (1.33)$$

Where B is the magnetic field strength at the stellar surface. As the second term is only significant for $n > 7$, [Garraffo et al. \(2018a\)](#) consider $n = 7$ as the maximum complexity, and consider only the first term of this relation. This is the equivalent of the saturation of magnetic braking, but here is contingent on field complexity rather than Ro .

[Garraffo et al. \(2018a\)](#) suggest the following relation between Ro and n ,

$$n = 1 + \frac{x}{Ro} + (y \cdot Ro) \quad (1.34)$$

where x and y are free parameters, chosen to fit observations of open clusters. The three terms reflect three aspects of the magnetic braking model - the minimum complexity is defined as $n \equiv 1$, the first factor encodes stars with small Ro having large n (e.g. young, fast rotators), and the third term gives stars with large Ro similarly large n to explain the observed population of old rapid rotators that appear to have experienced minimal spin-down ([van Saders et al., 2016](#)). This prescription explains the AML of a star as purely a function of Ro .

Similar to [Matt et al. \(2015\)](#), [Garraffo et al. \(2018a\)](#) run a population synthesis model to compare to observations using initial conditions taken from the 13 Myr old h Persei cluster ([Moraux et al., 2013](#)), but the authors show that differences between alternative initial conditions do not survive longer than 200 Myrs. Observations of stellar rotation periods and colour from several clusters with known ages are then compared to the synthetic population.

The resulting distribution does recover the Skumanich bifurcation observed in open clusters, reproducing the fast and slow rotating populations and the gap between them, though the large uncertainty in the age of the cluster does introduce some discrepancy. In addition, the synthetic cluster does not consider the effects of close binary stars, which will affect the spin-down rate through tidal effects. However, this effect is ignored by the author, as there is evidence that the binary fraction in open clusters is low ([Meibom et al., 2007](#)). The mass dependency of this track is also reproduced by the model, and Figure 1.7.

The [Garraffo et al. \(2018a\)](#) prescription is simpler in concept than the [Matt et al. \(2015\)](#) prescription, and both prescriptions perform well. However, neither formulation covers the parameter space of CV donors, and both are semi-empirical with some arbitrary decisions made in order to fit open cluster data. This makes both approaches highly vulnerable to extrapolation errors and difficult to trust in the context of CV evolution, especially in the short period regime.

Comparisons to the Rappaport, Verbundt and Joss model

The differences between these prescriptions in the case of CV evolution can be examined by applying them to a donor evolutionary track, and [Knigge et al.](#)

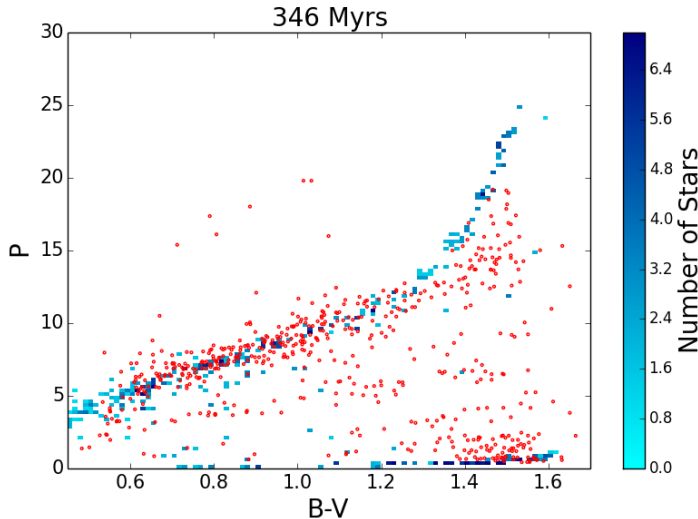


Figure 1.7: Example comparison between synthetic and observed cluster populations taken from [Garraffo et al. \(2018a\)](#). **Red points** are observations of M37, which has its age measured at $\sim 346 - 550$ Myrs. **Blue points** are the probability distribution of the synthetic cluster population from [Garraffo et al. \(2018a\)](#).

[\(2011\)](#) has constructed a donor sequence using their own models that reasonably accurately reproduces observations. The masses, radii, and periods along the sequence are given, so the would-be effects of the magnetic braking prescriptions described above can be calculated. In addition to the two previously discussed prescriptions, the default MESA ([Paxton et al., 2015](#)) magnetic braking prescription ([Rappaport et al., 1983](#)) is included. This prescription includes a magnetic braking index, γ ,

$$\dot{J} = -3.8 \times 10^{-30} M R_{\odot}^4 \left(\frac{R}{R_{\odot}} \right)^{\gamma} \omega^3 \text{ dyn cm} \quad (1.35)$$

Note that in the specific case of CVs, period and radius are synonymous with one another due to the requirement that the donor is in contact with the Roche lobe, and is tidally locked.

Figure 1.8 shows how the [Matt et al. \(2015\)](#) magnetic braking prescription compares to the [Garraffo et al. \(2018a\)](#) and MESA [Rappaport et al. \(1983\)](#) magnetic braking prescriptions. Most prescriptions see a discontinuity at $0.2M_{\odot}$, where [Knigge et al. \(2011\)](#) imposes the magnetic braking cutoff and the donor

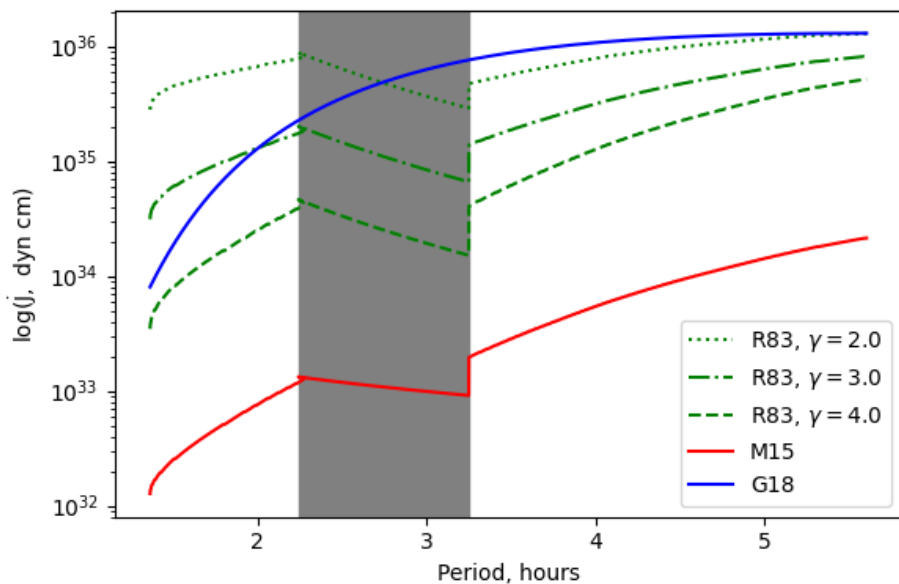


Figure 1.8: Showing the AML rates, \dot{J} , of three magnetic braking prescriptions, applied to the masses, radii, and spin periods of the ‘standard’ CV donor track of Knigge et al. (2011). The **vertical shaded region** shows the period gap, corresponding to the mass at which Knigge et al. (2011) enforces the period gap to occur. **Green lines** show the Rappaport et al. (1983) magnetic braking prescription, which is the default used in MESA (Paxton et al., 2015). The **red line** shows the Matt et al. (2015) prescription, and the **blue line** shows the Garraffo et al. (2018a) prescription.

contracts to its equilibrium radius.

The differences between the three prescriptions is clear in both the overall strength of the prescriptions, but also in how they evolve with mass. All the prescriptions shown decrease at lower masses, but at different rates. In the context of CV evolution, a different dropoff rates of magnetic braking would alter the shape of the donor mass-radius sequence, so observations of CV donors should be able to allow us to evaluate the effectiveness of different braking prescriptions.

Note that the AML from magnetic braking predicted by [Matt et al. \(2015\)](#) is ~ 2 orders of magnitude lower than the braking commonly required to calculate CV evolution. This is a consequence of tuning their braking model's free parameters to open cluster rotation rates, and the effects of this under-estimation is explored by [Andronov et al. \(2003\)](#). This problem is avoided in the case of [Garraffo et al. \(2018a,b\)](#), by using different values of their free parameters for open cluster stars and CVs.

1.6 This work

The primary focus of this work is in expanding the sample of well-characterised CV donors, which remains small (less than 40 systems in total). Whilst this sample is augmented by the large number of donors characterised using the superhump excess technique (§1.3.6), eclipse modelled systems are preferable due to the small number of robust assumptions that need to be made. The specific focus is on characterising systems with short periods, and therefore low mass donors, in an attempt to increase the number of well characterised CVs below the period gap. I characterise an additional 15 CV systems with periods of $\lesssim 2.5$ hours.

The secondary goal is then to take this larger sample, and make comparisons to CV evolutionary models below the period gap. By comparing observed data with the modelled donor masses and radii, the long-term baseline AML rate can be inferred for a given system. As these short-period systems are expected to only evolve under gravitational braking, but are known to experience some excess AML above this, various empirical prescriptions for excess AML as functions of the CV system parameters can be built and serve as a diagnostic for the physical motivation of the excess AML.

Chapter 2 catalogues the observations used in this work, and Chapter 3 describes the modelling approach and analysis techniques used to process the obser-

vations. Chapter 4 details the analysis of three CVs below the period gap, which are given closer examination due to issues with their characterisation. Chapter 5 then applies the same methodology to a further 12 CVs, which were not subject to any serious issues. Chapter 6 infers mass loss rates and angular momentum loss rates for the eclipse modelled CV population, the results of which are then explored in Chapter 7. Finally, Chapter 8 summarises the work presented here.

Chapter 2

Observations and observational techniques

The work of this thesis has made use of three instruments: ULTRASPEC, ULTRACAM, and HiPERCAM. These are time-series photometric imaging cameras, capable of taking high-cadence images of the night sky in one, three, or five colours, respectively. The observed eclipses typically span around 30 minutes and observations need to measure flux changes on timescales of a few seconds to resolve the eclipse. Crucially, HiPERCAM and ULTRACAM make their multi-colour images simultaneously, which removes the possibility of changes in brightness in the disc or bright spot polluting the white dwarf colour measurement, making them ideal instruments for this analysis.

2.1 Instruments

The cameras used were mounted on several telescopes across the decade of our observations. These were the Gran Telescopio de Canarias (GTC) on La Palma (with HiPERCAM), the Thai National Telescope (TNT) with ULTRASPEC, the New Technology Telescope (NTT) in Chilé (with ULTRACAM). Prior to 2016, ULTRACAM was hosted on the William Herschel Telescope (WHT), on La Palma. Section 2.4 details what instrument/telescope combination was used for each observation used in this thesis.

2.1.1 HiPERCAM

HiPERCAM is a quintuple-beam optical imaging camera that saw first light on the WHT in 2017, and is sensitive to wavelengths from 320 – 1060nm (Dhillon et al., 2021). HiPERCAM uses a system of ‘Super SDSS’ filters (u_{sup} , g_{sup} , r_{sup} , i_{sup} , z_{sup}), designed to match the classic SDSS band cutoff wavelengths (Fukugita et al., 1996), but allow a higher throughput and so give a more sensitive instrument. This instrument has a series of dichroic beam-splitters, that sequentially pick off the u_{sup} , g_{sup} , r_{sup} , i_{sup} , z_{sup} bands and funnel each into dedicated cameras that use highly sensitive, low readout noise, Charge-Coupled Devices (CCDs) as detectors. However, this improvement in sensitivity is not constant across the bands, shown in Figure 2.1, resulting in a small difference between colours observed with HiPERCAM and the SDSS. Unfortunately, as magnitudes for standard stars are often reported in the classic SDSS photometric system, some work was necessary to color-correct the HiPERCAM observations, which is described in detail in §2.3.2.

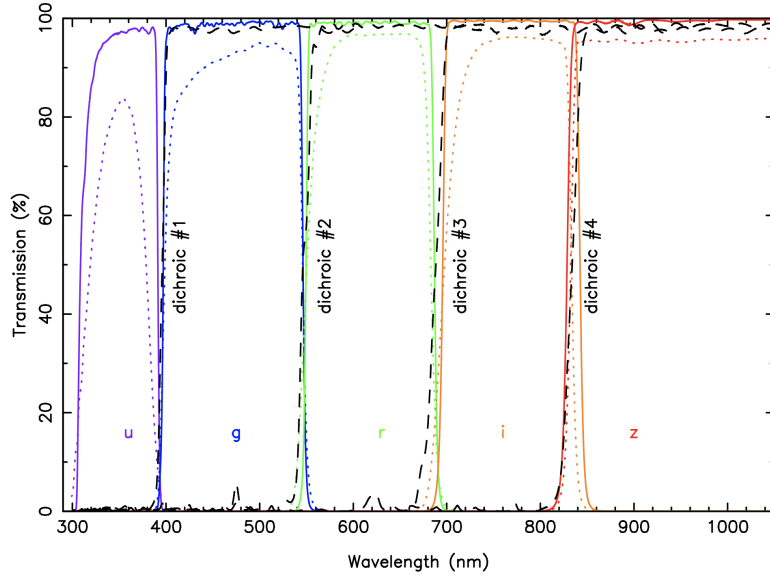


Figure 2.1: Taken from Dhillon et al. (2021). Transmission profiles of the as-built HiPERCAM dichroic beam-splitters (**dashed black lines**), the HiPERCAM standard SDSS filters (**dotted lines**), and the HiPERCAM Super SDSS filters (**solid lines**).

On the GTC, HiPERCAM is capable of detecting sources down to $g_{\text{sup}} \sim 23$ in exposures of only a second, and can achieve $g_{\text{sup}} \sim 28$ with an hour of exposure. This allows observations of fainter CVs than previous studies (e.g. McAllister 2017), and helps target CVs at short periods with faint, low mass donors. Unfortunately, while HiPERCAM was used to observe eclipses for some systems, no HiPERCAM observations were modelled for this thesis, with observed systems either being in outburst, or not having observable bright spot features, which are essential for modelling.

HiPERCAM is capable of incredibly fast frame rates of up to $\sim 1000\text{Hz}$, though this capability was not used for this work. However, as part of the effort to achieve this frame rate by reducing dead-time between frames HiPERCAM is capable of exposing a frame while *simultaneously* reading out the previous image. This is achieved by masking half of the CCD, and only exposing with one half. When a frame is finished exposing, the electrons are shuttled across to the masked side (a rapid process, 6.8 – 7.8 ms) and can be read out during the next exposure time. HiPERCAM has four sets of readout electronics that operate in tandem. This virtual elimination of dead-time is a significant benefit when resolving the large, rapid changes in flux during the ingresses and egresses of CV eclipses.

2.1.2 ULTRACAM

ULTRACAM is a three-beam optical imager sensitive to wavelengths between $\sim 300 - 1100\text{nm}$, and is the direct predecessor to HiPERCAM (Dhillon et al., 2007). It is similarly built for high-speed photometric studies, but is not capable of the extreme framerates of HiPERCAM, limited to framerates of $\lesssim 500\text{Hz}$. ULTRACAM uses the same frame transfer readout technique to HiPERCAM, though uses only two CCDs.

ULTRACAM was originally commissioned with SDSS-like u' , g' , r' , i' , z' filters, that match the SDSS closely and did not necessitate colour-term corrections. However, in February 2019 ULTRACAM was upgraded to use the same Super SDSS photometric system used by HiPERCAM. When necessary, observations were translated to the classic SDSS system as described in §2.3.2. Observing an object with ULTRACAM in more than three bands requires multiple observing runs, and manually swapping filters.

2.1.3 ULTRASPEC

ULTRASPEC was occasionally used to supplement ULTRACAM and HiPERCAM observations. ULTRASPEC was originally commissioned as a spectrographic cousin of ULTRACAM, using again a frame transfer design, with an electron-multiplying CCD (Dhillon et al., 2014). After a brief proof-of-concept trial as a photometric imager in June 2009, ULTRASPEC was modified to a full-time imaging instrument and mounted on the 2.4m TNT in November 2013, and is now operated by the National Astronomical Research Institute of Thailand (NARIT).

This is a single-colour instrument that uses the u' , g' , r' , i' , z' filters, in addition to a wide-band KG5 filter that is approximately equivalent to $u' + g' + r'$. It is also the slowest of the three cameras, but is still capable of high framerates up to $\sim 200\text{Hz}$. However, as ULTRASPEC on the NTT is a somewhat less in-demand instrument than either HiPERCAM or ULTRACAM, it proved useful in two significant respects - to gauge the viability of CV systems before dedicating more valuable HiPERCAM and ULTRACAM observing time (e.g. testing the visibility of eclipse features, checking if a CV is undergoing an outburst), and in acquiring or refining measurements of orbital period.

2.2 Data reduction

All three cameras use CCD detectors, which are a staple of ground-based astronomy due to their high sensitivity, and low noise. CCDs are made up of a large grid of photosensitive pixels, which release electrons proportionally to the number of photons that fall on them. This signal is then moved pixel-by-pixel into the readout electronics, which is essentially a capacitor that has its voltage measured to determine the number of electrons that were released. This voltage is converted to electron counts with an Analog-to-Digital Converter (ADC), that outputs the corresponding integer number of electrons to the input charge, in Analog-to-Digital Units (ADU). To extract time-series photometric information from the raw image files, the HiPERCAM data reduction pipeline was used¹.

The analysis of this data uses flux-calibrated relative photometry, in which a reference star in the same image as the target is extracted and used as a known-constant flux source. Then, by using the ADU flux ratio between these two sources as the observable, effects from changes in weather, altitude, and seeing conditions are compensated for, since these variations are assumed to affect both the target and reference star equally. By multiplying the ADU ratio between the target and reference stars by the flux in mJy of the reference star, the photometry can be calibrated and produce a light curve of the target star.

Bias frames

The readout electronics of a CCD are not perfect, and contribute a small amount of gaussian noise to each pixel, called readout noise. The ADC is only capable of recording *positive integer values*, and rounds negative pixel counts to 0. To illustrate why this is an issue, take the exaggerated example of a readout noise of $7e^-/\text{px}$ on a region of the CCD that is stimulated by $5e^-/\text{px}$. If negative values are limited to 0, the effect is to increase the average, and Figure 2.2 illustrates the effect of discarding negative counts. This will have a small corrupting effect on low-signal areas of the CCD, significantly corrupting the sky background signal that must be subtracted from the source signal (§2.2). Without proper bias correction, a similar corruption also occurs for the flat field images described below.

To prevent corruption, a small bias voltage is applied to each pixel, raising

¹Available <https://cygnus.astro.warwick.ac.uk/phsaap/hipercam/docs/html/>

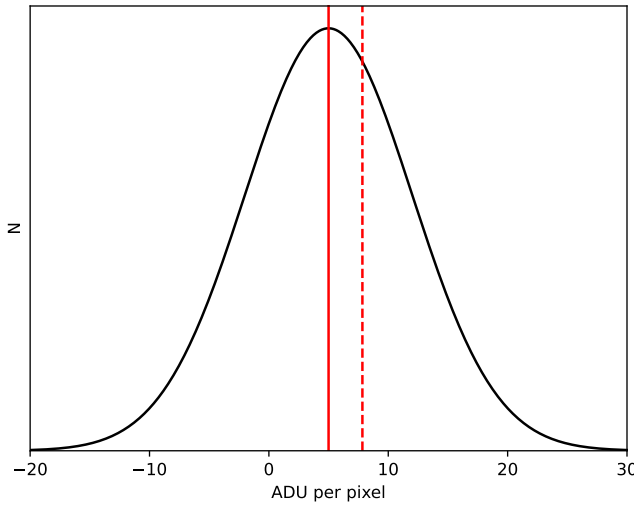


Figure 2.2: Illustrating the effect of omitting negative values on the average of a distribution. The **black line** is a Gaussian distribution with an average of 5 and a standard deviation of 7. The **vertical dashed line** shows the ‘true’ average of 5 ADU, and the **vertical solid line** shows the average given by an ADC that reports negative electron counts as 0.

the null detection value away from zero and preventing noise from giving negative readings. To then remove this bias voltage from observations, zero second exposures of a masked detector are taken to characterise the bias voltage for each pixel, and are subtracted off each subsequent exposure. These are known as bias frames, and because the structure of the bias is subtly altered by different instrument setups, a new bias frame is taken when instrument options such as binning pixels together when reading them out, or only reading out partial images, are altered.

Flat fielding

The response of each pixel to photons is similar, but not exactly equal. In addition, the optics of the telescope are not perfect and throughput varies across the field of view, a.k.a vignetting. Dust and imperfections in the telescope optics can also introduce variation across the image, and must also be accounted for.

These effects mean that each exposure the instrument takes is convolved with a constant flat-field response pattern.

In order to characterise and remove the flat-field pattern, an exposure is taken

of an image that is known to be uniform in brightness, which will have the flat-field pattern imprinted on it. The twilight sky forms a highly uniform field in optical bands, so was used as this flat source.

Residual stellar light should still be removed, so to completely eliminate stars from the flat field observation, many exposures are taken while the telescope is being nudged by a small amount every few seconds. Since the stars move pixels between each exposure, calculating the median frame will remove stars from the image, leaving behind only the uniform sky observation imprinted with the flat-field response pattern. The flat field images are bias corrected to give the final flat image. Then, by dividing each subsequent exposure by the flat image, non-uniformity in the detector response can be corrected in future images.

Aperture photometry

While stars are theoretically point sources, they are observed through the atmosphere and the optics of the telescope, which act to spread the light from a star, usually by a few arcseconds even under the best conditions. This spreads light from a star over several pixels. As such, to find the total flux of a star the contributions from all pixels containing the stars' flux must be summed together, ideally subtracting all flux contributed by non-stellar sources. The HiPERCAM pipeline has two methods for this: ‘normal’ extraction and ‘optimal’ extraction.

The sky background is not perfectly black and in both extraction methods must be removed from the extracted flux of a source. This is done by taking an annulus about each source, and assuming it is solely made up of sky background light (in the case of a nearby object, portions of the annulus can be masked in software and not counted in the sky background). The inner edge of the annulus is selected to be far enough from the source that none of the target's light is present, and the outer edge is limited by the need to avoid contamination from other sources, and large annuli starting to become sensitive to sky variations across the image. The average sky signal per pixel is then calculated, and subtracted to isolate the source flux.

Under normal extraction, the user specifies one or more ‘reference’ stars, and one or more ‘target’ stars. The pixel ADU counts around the reference stars as a function of their radial distance to the peak flux are characterised with a Gaussian or Moffat profile. The Full-Width at Half Maximum (FWHM) of this distribution fit is calculated, and all pixels within $x \times \text{FWHM}$ of the peak flux are summed

to give the extracted flux of a source, cutting off some fraction of the wings of the flux distribution. Here x is a user-defined parameter, and while in theory a large value of x would be desirable to capture all flux from a source, adding extra pixels increases the readout noise of the detection, and suffers from diminishing returns due to the small amounts of flux contained in the wings. Also, as the same fraction of light from each source should be lost from both the target sources and reference sources, cutting out these wings should not alter the flux ratio between sources, and the flux ratio is the relevant quantity under relative photometry (see §2.3).

In many cases, it is preferable to use the ‘optimal’ extraction method, described by [Naylor \(1998\)](#). Here, a weight is taken into account when summing the flux contributions of each pixel based on the *expected* contribution to the overall flux. This can give an improvement of $\sim 10\%$ to the signal-to-noise ratio, especially in faint sources as less weight is given to pixels at the wings of the flux profile, where readout noise and error from the sky background are more significant. However, in brighter stars with an already high signal-to-noise ratio the improvement is offset by the potential systematic error introduced by any divergence from the model profile fit used. As such, the optimal extraction method is generally used for faint stars, and normal extraction is used for bright stars.

2.3 Photometric calibration

A comparison star in the same frame as the target is used to account for seeing and transparency variations over an observation, and standard stars from [Smith et al. \(2002\)](#) were used to transform the light curves from ADU to the SDSS $u'g'r'i'z'$ photometric system. At the core of the photometric calibrations is the following expression of the apparent magnitude in some band, m_{app} , of a target,

$$m_{app} = m_{inst} + \chi k_{ext} + m_{zp} + C_{inst} c_m \quad (2.1)$$

where m_{inst} is the instrumental magnitude, $-2.5\log(\text{ADU}/\text{time})$, χ is the airmass of the observation and k_{ext} is the atmospheric extinction coefficient in the relevant band. m_{zp} is the zero point offset of the instrument, calculated from photometric standard stars, ideally taken on the night of an observation. c_m is the colour term correction between the response curve of the instrument, and the target photometric system, and C_{inst} is a diagnostic instrumental colour. Each of these

terms must be properly handled, and are discussed in turn.

2.3.1 Calculating atmospheric extinction coefficients

Atmospheric extinction was calculated using the longest continuous observation available within a reasonable time from target observations.

To calculate the atmospheric extinction coefficients, aperture photometry was extracted for five sources in these long observations, and the instrumental magnitude, m_{inst} , vs airmass, χ , was fit with a straight line for each source. The gradients of these lines are the atmospheric extinction coefficients, k_{ext} , for the relevant band, and the y-intercept is the instrumental magnitude of that object above the atmosphere, $m_{\text{inst},0}$:

$$m_{\text{inst}} = m_{\text{inst},0} + \chi k_{\text{ext}} \quad (2.2)$$

2.3.2 Transformations between filter systems

ULTRACAM and HiPERCAM use an SDSS-*like* filter system with higher efficiency bandpasses, referred to as Super SDSS. There are three relevant photometric systems:

- SDSS filters, u', g', r', i', z' ;
- ULTRACAM/ULTRASPEC SDSS-like, $u_{\text{reg}}, g_{\text{reg}}, r_{\text{reg}}, i_{\text{reg}}, z_{\text{reg}}$;
- HiPERCAM/ULTRACAM Super SDSS, $u_{\text{sup}}, g_{\text{sup}}, r_{\text{sup}}, i_{\text{sup}}, z_{\text{sup}}$.

Note that I have no z band observations, so the z band is omitted hereafter. I aim to place our photometry in the SDSS $u'g'r'i'$ system, as this is the system later used by the white dwarf atmospheric models, and allows data from different instruments to be either binned together, or modelled simultaneously c.f. §3.3.4. The $u_{\text{reg}}, g_{\text{reg}}, r_{\text{reg}}, i_{\text{reg}}$ filters were sufficiently similar to standard SDSS filters that the uncorrected magnitudes of standard reference stars from [Smith et al. \(2002\)](#) could be used to calibrate absolute photometry without issue. However, with the new filters, there was concern that the different shape of the sensitivity curves, particularly in the u' band, differ enough from the SDSS filters to cause issues with our photometric calibration. Figure 2.3 illustrates the change in throughput between the SDSS photometric system, and the Super SDSS filters, on ULTRACAM on the NTT.

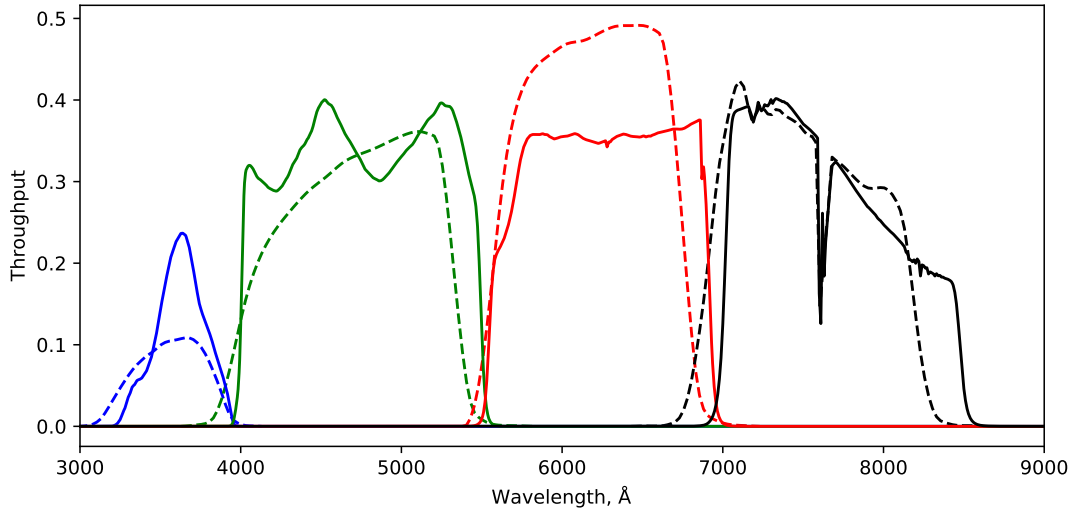


Figure 2.3: The differences in photometric throughput in terms of registered ADU, for SDSS filter system (**dotted lines**), and ULTRACAM Super SDSS filters, for ULTRACAM mounted on the NTT (**solid lines**). Blue: u bands, Green: g bands, Red: r bands, Black: i bands. Both throughputs include atmospheric extinction of $\chi = 1.3$.

To perform the colour corrections, Equation 2.2 for the magnitude of a star was used with the addition of a colour term. Using the g' band as an example:

$$g' = g_{\text{inst}} + \chi k_{\text{ext}} + g_{\text{zp}} + c_{g,\text{sup}}(g' - r') \quad (2.3)$$

where g_{zp} is the zero point, $g_{\text{inst}} = -2.5\log(\text{ADU}_{\text{exp}}/t_{\text{exp}})$ for an exposure time of t_{exp} , and $c_{g,\text{sup}}$ is the colour term correction gradient. In theory, the atmospheric extinction term also has some colour dependency, as extinction varies with wavelength. However, the effect is negligible between these photometric systems, so it is omitted.

In order to compute the colour term correction gradients, the optical path of each system was simulated using the `pysynphot` package, with measured throughputs of all ULTRACAM and HiPERCAM components in the optical path. Pre-computed stellar models from Dotter (2016) and Choi et al. (2016) were used to generate the T_{eff} and $\log(g)$ values of an 8.5 Gyr isochrone for main sequence stars with masses from 0.1 to $3 M_{\odot}$, spanning from $\log(g) = 3.73 \rightarrow 5.17$, and $T_{\text{eff}} = 2900\text{K} \rightarrow 10,300\text{K}$. The Phoenix model atmospheres (Allard et al., 2012) were used to generate model spectra of each mass, which were then folded through each optical path to calculate an AB magnitude. In addition, white dwarf models

with $\log(g) = 8.5$ were similarly processed (Koester, 2010; Tremblay & Bergeron, 2009), to assess the impact of the different spectral shape on the resulting colour terms.

The colour terms between the SDSS and Super SDSS systems were then synthesised, e.g., $g' - g_{\text{sup}}$, on ULTRACAM and HiPERCAM for each model atmosphere. These data were plotted against synthesised SDSS colours, i.e. $(u' - g')$, $(g' - r')$, $(g' - i')$, and a straight line was fit to the colour relationship for the combined dataset of both white dwarf and main sequence stars. In the example case of $g' - g_{\text{sup}}$, this would be

$$g' - g_{\text{sup}} = g_{\text{zp}} + c_{g,\text{sup}}(g' - r')$$

These relationships are shown for HiPERCAM in Figure 2.4 for all four Super SDSS filters used to observe these CVs, and Table 2.1 and Table 2.2 contain the coefficients of each colour term correction for both HiPERCAM and ULTRACAM. When processing ULTRACAM data, $(u' - g')$ was used to correct u magnitudes, $(g' - r')$ was used to correct g and r magnitudes, $(g' - i')$ was used to correct the i band. These colour corrections are not generally the same for main sequence stars and white dwarfs, though the colours of the CVs presented in this work are all such that the discrepancy is on the order of a few percent, and is considered negligible.

Table 2.1: ULTRACAM colour term best fit lines from Figure 2.4. The data are modelled by equations of the form $(u' - u_{\text{sup}}) = \phi + c_u(u' - g')$, with c_u being the relevant colour gradient.

Correction	Diagnostic	ϕ	c
$(u' - u_{\text{sup}})$	$(u' - g')$	0.003	0.036
	$(g' - r')$	0.033	0.063
	$(g' - i')$	0.038	0.044
$(g' - g_{\text{sup}})$	$(u' - g')$	-0.001	0.014
	$(g' - r')$	0.010	0.027
	$(g' - i')$	0.012	0.018
$(r' - r_{\text{sup}})$	$(u' - g')$	-0.017	0.016
	$(g' - r')$	-0.004	0.032
	$(g' - i')$	-0.002	0.022
$(i' - i_{\text{sup}})$	$(u' - g')$	-0.031	0.020
	$(g' - r')$	-0.015	0.040
	$(g' - i')$	-0.012	0.028

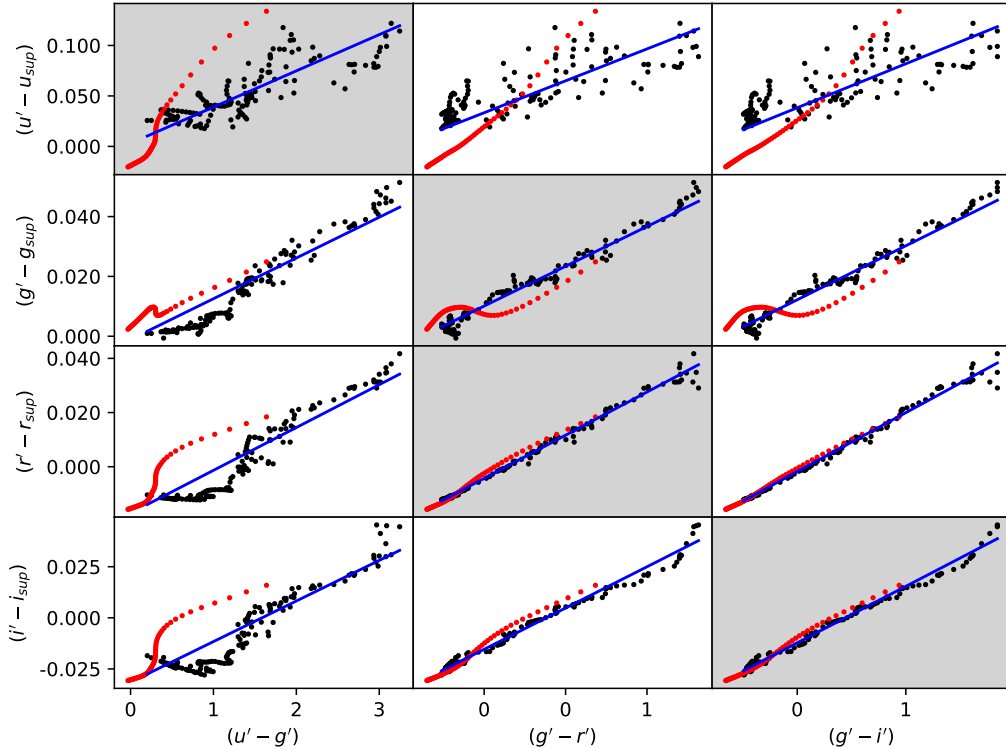


Figure 2.4: The difference between the classic SDSS photometric system, and the ULTRACAM SuperSDSS filters on the NTT, as a function of SDSS colours, are calculated for model atmospheres. **Red points** are Koester white dwarf models, **black points** are Phoenix main sequence model atmospheres, and the **blue line** is the best fit straight line to the combination of both datasets. When applying colour corrections, the highlighted relations were used.

Table 2.2: HiPERCAM colour term best fit lines from Figure 2.5. The data are modelled by equations of the form $(u' - u_{\text{sup}}) = \phi + c_u(u' - g')$, with c_u being the relevant colour gradient.

Correction	Diagnostic	ϕ	c
$u' - u_{\text{sup}}$	$(u' - g')$	0.096	0.054
	$(g' - r')$	0.150	0.029
	$(g' - i')$	0.152	0.022
$g' - g_{\text{sup}}$	$(u' - g')$	0.008	0.023
	$(g' - r')$	0.010	0.045
	$(g' - i')$	0.014	0.031
$r' - r_{\text{sup}}$	$(u' - g')$	0.000	0.001
	$(g' - r')$	0.001	0.003
	$(g' - i')$	0.001	0.002
$i' - i_{\text{sup}}$	$(u' - g')$	0.033	0.022
	$(g' - r')$	0.016	0.044
	$(g' - i')$	0.012	0.030

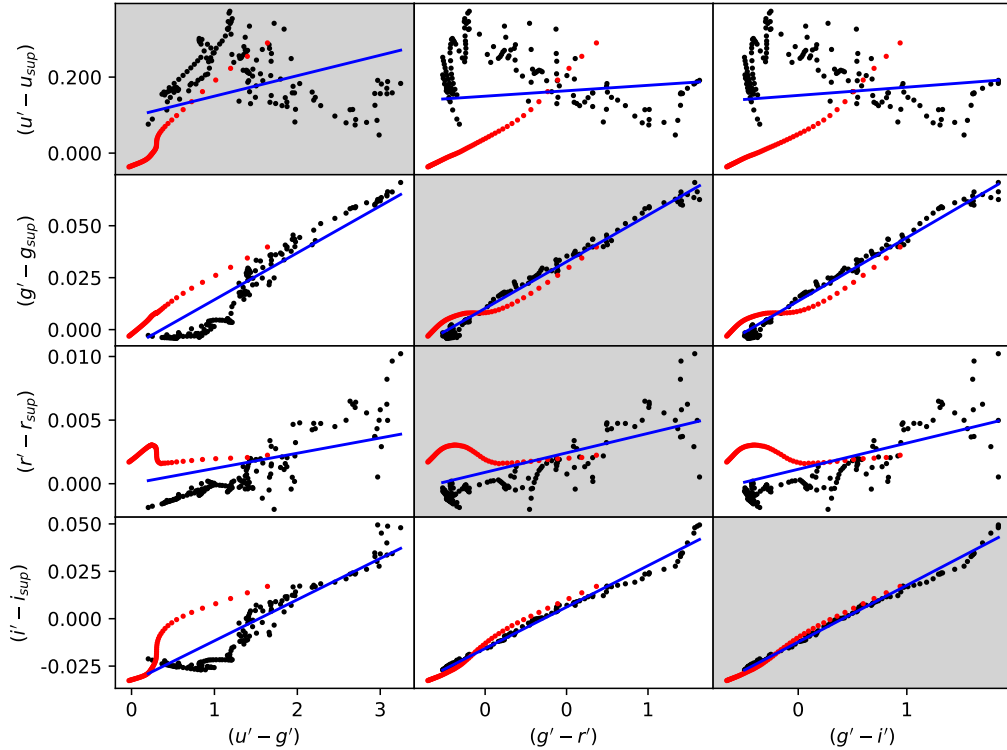


Figure 2.5: As Figure 2.4

2.3.3 Calculating comparison star magnitudes

The comparison stars in the target frame often do not have known brightnesses in the SDSS photometric system, and so this must be determined by observation. The network of SDSS photometric standards provided by Smith et al. (2002) are used as calibrating objects, with robust, accurate known magnitudes. By observing a flux standard during clear conditions, the comparison stars' magnitude can then be calculated from a similarly clear observation. Equation 2.2 was used to calculate the zero points of the telescope/instrument combination in each band from a standard star observation.

The comparison star magnitudes were then calculated from observations. Since the colour term corrections are dependent on SDSS colours, an iterative approach was used to converge on these values. SDSS magnitudes are related to the instrumental magnitudes by:

$$\begin{aligned} u' &= u_{\text{inst},0} + u_{\text{zp}} + c_{u,\text{sup}}(u' - g') \\ g' &= g_{\text{inst},0} + g_{\text{zp}} + c_{g,\text{sup}}(g' - r') \\ r' &= r_{\text{inst},0} + r_{\text{zp}} + c_{r,\text{sup}}(g' - r') \\ i' &= i_{\text{inst},0} + i_{\text{zp}} + c_{i,\text{sup}}(g' - i') \end{aligned}$$

Initially, u', g', r', i' magnitudes are set equal to the instrumental magnitudes, and a new set of u', g', r', i' magnitudes are calculated. The new values are then used to repeat the calculation until a new iteration produces no change, typically after ~ 4 loops.

2.3.4 Producing a flux-calibrated target light curve

Finally, the target light curves can be calculated. Broadly, this encompasses two processes: the target star light curve must be corrected for transparency variations, and then converted from ADU counts to calibrated flux. As the aim is to produce a flux-calibrated light curve in the SDSS photometric system, from observations using a significantly different photometric system, the simple ADU ratio between the target and comparison is insufficient. Consider the target star

g' magnitude and flux, g^t, F^t , and comparison star g' magnitude and flux, g^c, F^c :

$$\begin{aligned} g^t &= g_{\text{inst},0}^t + g_{\text{zp}} + c_{\text{g,sup}}(g' - r')^t \\ g^c &= g_{\text{inst},0}^c + g_{\text{zp}} + c_{\text{g,sup}}(g' - r')^c \end{aligned}$$

since,

$$g^t - g^c = -2.5 \log\left(\frac{F^t}{F^c}\right)$$

we can write

$$\begin{aligned} \frac{F^t}{F^c} &= 10^{-0.4(g_{\text{inst},0}^t - g_{\text{inst},0}^c)} \cdot 10^{-0.4c_{\text{g,sup}}((g' - r')^t - (g' - r')^c)} \\ \frac{F^t}{F^c} &= \frac{\text{ADU}^t}{\text{ADU}^c} \cdot K^{t,c} \end{aligned}$$

where $K^{t,c} = 10^{-0.4c_{\text{g,sup}}((g' - r')^t - (g' - r')^c)}$. This accounts for differences in wavelength response between the two systems when calculating the flux ratio, and is applied to each frame. The $(g' - r')^t$ magnitudes are calculated using a sigma-clipped mean instrumental magnitudes computed from all frames in the observation. In practice, the factor $K^{t,c}$ varies from $\sim 1.0 - 1.1$ for our observations.

While developing this correction method, some verification tests were performed. ASASSN-16kr was observed in both the standard SDSS filters in 2018, and the super SDSS filters in 2019. This presented an opportunity to compare the corrected 2019 data with the fluxes observed in 2018. Additionally, both ASASSN-16kr and SSSJ0522–3505 use multiple standard stars across observations, which should agree if the calibration has been done correctly. Finally, AY For provided a case where the SDSS magnitudes of the comparison stars were known *a priori*, as the field has been observed in the Pan-STARRS survey. The calibrated comparison star magnitudes using the technique provided here are within 2% of the Pan-STARRS magnitudes, indicating a reasonable calibration. In all cases, the flux-calibrated light curves were similar and the white dwarf colours consistent, suggesting that this method of flux calibration is indeed accurate.

I add a 3% systematic error in quadrature to the white dwarf fluxes when fitting for the effective temperature. This is a practice established by [McAllister et al. \(2019\)](#), to account for systematic error in flux calibration and modelling.

2.4 Catalogue of observations

The observations analysed in this work span the full decade from 2011, through to 2021, and have been taken from multiple sites as the instruments move from telescope to telescope. To aid with the readability, a key is provided in Table 2.3 of the acronyms used for instruments and telescopes.

When optimising the eclipse model to the data, some systems had their eclipses binned together where appropriate to reduce the complexity of the parameter space. These tables also detail which data were combined, and where no binning ID is given the eclipse is fit individually.

Acronym	Expansion
NTT	New Technology Telescope
TNT	Thai National Telescope
WHT	William Herschel Telescope
UCAM	ULTRACAM
USPEC	ULTRASPEC

Table 2.3: Acronyms used in the observation summaries.

Table 2.4: Observations taken for ASASSN-14hq. Mid-eclipse times and cycle numbers are calculated following the method detailed in §3.2.

Instrument	Telescope	Date	Observation start TDB	Observation end TDB	Filter(s)	T_{ecl}	Cycle No.	Binning ID
						MJD		
UCAM	NTT	2016/11/9	06:06	06:45	$u_{\text{reg}}, g_{\text{reg}}, r_{\text{reg}}$	57701.27137(1)	0	A
UCAM	NTT	2016/11/11	06:22	06:49	$u_{\text{reg}}, g_{\text{reg}}, r_{\text{reg}}$	57703.27826(1)	27	A
UCAM	NTT	2017/3/19	02:25	03:09	$u_{\text{reg}}, g_{\text{reg}}, r_{\text{reg}}$	57831.12065(1)	1747	A
UCAM	NTT	2017/3/21	23:59	00:44	$u_{\text{reg}}, g_{\text{reg}}, r_{\text{reg}}$	57834.01942(1)	1786	A
UCAM	NTT	2018/1/23	00:55	01:48	$u_{\text{sup}}, g_{\text{sup}}, r_{\text{sup}}$	58141.06425(1)	5917	B
UCAM	NTT	2018/1/25	01:19	01:57	$u_{\text{sup}}, g_{\text{sup}}, r_{\text{sup}}$	58143.07107(2)	5944	B
UCAM	NTT	2018/1/28	02:28	03:05	$u_{\text{sup}}, g_{\text{sup}}, r_{\text{sup}}$	58146.11846(2)	5985	B
UCAM	NTT	2018/1/28	04:09	04:49	$u_{\text{sup}}, g_{\text{sup}}, r_{\text{sup}}$	58146.19283(2)	5986	B
UCAM	NTT	2018/1/30	01:04	01:29	$u_{\text{sup}}, g_{\text{sup}}, r_{\text{sup}}$	58148.05102(3)	6011	B

Table 2.5: Observations taken for ASASSN-14kb.

Instrument	Telescope	Date	Observation start TDB	Observation end TDB	Filter(s)	T_{ecl}	Cycle No.	Binning ID
						MJD		
UCAM	NTT	2018/1/20	01:01	01:32	$u_{\text{sup}}, g_{\text{sup}}, r_{\text{sup}}$	58138.05257(1)	-75	A
UCAM	NTT	2018/1/23	05:25	06:24	$u_{\text{sup}}, g_{\text{sup}}, r_{\text{sup}}$	58141.25354(1)	-28	A
UCAM	NTT	2018/1/25	03:12	04:11	$u_{\text{sup}}, g_{\text{sup}}, r_{\text{sup}}$	58143.16050(1)	0	A
UCAM	NTT	2018/1/26	02:06	02:56	$u_{\text{sup}}, g_{\text{sup}}, r_{\text{sup}}$	58144.11398(2)	14	A

Table 2.6: Observations taken for ASASSN-15pb.

Instrument	Telescope	Date	Observation	Observation	Filter(s)	T_{ecl}	Cycle No.	Binning
			start	end				ID
			TDB	TDB		MJD		
UCAM	NTT	2016/8/20	23:33	00:37	$u_{\text{reg}}, g_{\text{reg}}, i_{\text{reg}}$	57621.01182(3)	-55	A
UCAM	NTT	2016/8/22	02:37	03:25	$u_{\text{reg}}, g_{\text{reg}}, r_{\text{reg}}$	57622.13130(5)	-43	A
UCAM	NTT	2016/8/22	04:39	05:39	$u_{\text{reg}}, g_{\text{reg}}, r_{\text{reg}}$	57622.22458(4)	-42	A
UCAM	NTT	2016/8/23	01:02	01:50	$u_{\text{reg}}, g_{\text{reg}}, r_{\text{reg}}$	57623.06421(2)	-33	A
UCAM	NTT	2016/8/25	04:44	05:19	$u_{\text{reg}}, g_{\text{reg}}, r_{\text{reg}}$	57625.20988(2)	-10	A
UCAM	NTT	2016/8/26	02:56	03:39	$u_{\text{reg}}, g_{\text{reg}}, r_{\text{reg}}$	57626.14278(2)	0	A

Table 2.7: Observations taken for ASASSN-16kr. Eclipses marked with a binning ID of ‘-’ were fit as an individual eclipse, and not combined with any other data.

Instrument	Telescope	Date	Observation	Observation	Filter(s)	T_{ecl}	Cycle No.	Binning
			start	end				ID
			TDB	TDB		MJD		
UCAM	NTT	2018/10/13	02:34	03:15	$u_{\text{reg}}, g_{\text{reg}}, r_{\text{reg}}$	58404.131217(3)	-3774	-
UCAM	NTT	2018/10/16	04:25	04:59	$u_{\text{reg}}, g_{\text{reg}}, r_{\text{reg}}$	58407.1955(2)	-3724	-
UCAM	NTT	2018/10/17	02:24	04:26	$u_{\text{reg}}, g_{\text{reg}}, r_{\text{reg}}$	58408.114806(4), 58408.176(1)	-3709, -3708	-
UCAM	NTT	2019/09/27	23:56	00:27	$u_{\text{sup}}, g_{\text{sup}}, r_{\text{sup}}$	58754.012610(3)	1935	-
UCAM	NTT	2019/09/29	00:48	01:37	$u_{\text{sup}}, g_{\text{sup}}, r_{\text{sup}}$	58755.054468(3)	1952	-
UCAM	NTT	2019/09/30	03:21	04:48	$u_{\text{sup}}, g_{\text{sup}}, r_{\text{sup}}$	58756.157613(4)	1970	-

Table 2.8: Observations taken for ASASSN-17fo.

Instrument	Telescope	Date	Observation start TDB	Observation end TDB	Filter(s)	T_{ecl}	Cycle No.	Binning ID
								MJD
UCAM	NTT	2018/1/24	05:55	06:19	$u_{\text{sup}}, g_{\text{sup}}, r_{\text{sup}}$	58142.25819(1)	-16	-
UCAM	NTT	2018/1/25	05:10	05:55	$u_{\text{sup}}, g_{\text{sup}}, r_{\text{sup}}$	58143.24296(1)	0	-
UCAM	NTT	2018/1/26	06:34	07:03	$u_{\text{sup}}, g_{\text{sup}}, r_{\text{sup}}$	58144.28927(2)	17	-

Table 2.9: Observations taken for ASASSN-17jf.

Instrument	Telescope	Date	Observation start TDB	Observation end TDB	Filter(s)	T_{ecl}	Cycle No.	Binning ID
								MJD
UCAM	NTT	2019/09/28	01:41	03:04	$u_{\text{sup}}, g_{\text{sup}}, r_{\text{sup}}$	58754.12003(2)	-42	-
UCAM	NTT	2019/09/30	02:16	02:46	$u_{\text{sup}}, g_{\text{sup}}, r_{\text{sup}}$	58756.10769(1)	-7	-
UCAM	NTT	2019/10/01	04:08	04:38	$u_{\text{sup}}, g_{\text{sup}}, r_{\text{sup}}$	58757.18671(1)	12	-

Table 2.10: Observations taken for AY For.

Instrument	Telescope	Date	Observation start TDB	Observation end TDB	Filter(s)	T_{ecl}	Cycle No.	Binning ID
								MJD
UCAM	NTT	2016/11/09	01:57	03:02	$u_{\text{reg}}, g_{\text{reg}}, r_{\text{reg}}$	57701.10964(1)	-0	-
UCAM	NTT	2016/11/10	03:09	03:53	$u_{\text{reg}}, g_{\text{reg}}, r_{\text{reg}}$	57702.15423(1)	14	-
UCAM	NTT	2016/11/11	02:34	03:12	$u_{\text{reg}}, g_{\text{reg}}, r_{\text{reg}}$	57703.12424(1)	27	-

Table 2.11: Observations taken for CSS090102.

Instrument	Telescope	Date	Observation start TDB	Observation end TDB	Filter(s)	T_{ecl}	Cycle No.	Binning ID
						MJD		
UCAM	WHT	2011/5/30	23:30	23:49	$u_{\text{reg}}, g_{\text{reg}}, r_{\text{reg}}$	55711.98538(2)	-3705	A
UCAM	WHT	2011/6/2	00:23	01:38	$u_{\text{reg}}, g_{\text{reg}}, r_{\text{reg}}$	55714.04408(2)	-3672	A
UCAM	WHT	2011/6/2	01:38	02:41	$u_{\text{reg}}, g_{\text{reg}}, r_{\text{reg}}$	55714.10647(2)	-3671	A
UCAM	WHT	2012/1/17	02:28	03:18	$u_{\text{reg}}, g_{\text{reg}}, r_{\text{reg}}$	55943.12147(4)	0	A
UCAM	WHT	2012/1/17	05:16	06:11	$u_{\text{reg}}, g_{\text{reg}}, r_{\text{reg}}$	55943.24624(2)	2	A
UCAM	WHT	2014/8/4	21:01	21:58	$u_{\text{reg}}, g_{\text{reg}}, r_{\text{reg}}$	56873.90433(4)	14920	A

Table 2.12: Observations taken for CSS090419.

Instrument	Telescope	Date	Observation start TDB	Observation end TDB	Filter(s)	T_{ecl}	Cycle No.	Binning ID
						MJD		
UCAM	WHT	2013/25/7	21:41	22:38	$u_{\text{reg}}, g_{\text{reg}}, i_{\text{reg}}$	56498.92854(2)	0	A
UCAM	WHT	2013/26/7	21:05	22:00	$u_{\text{reg}}, g_{\text{reg}}, r_{\text{reg}}$	56499.90935(3)	13	A
UCAM	WHT	2013/28/7	22:12	23:02	$u_{\text{reg}}, g_{\text{reg}}, i_{\text{reg}}$	56501.94632(7)	40	A
UCAM	WHT	2013/4/8	21:00	21:30	$u_{\text{reg}}, g_{\text{reg}}, r_{\text{reg}}$	56508.88704(3)	132	A
UCAM	WHT	2013/4/8	22:55	23:21	$u_{\text{reg}}, g_{\text{reg}}, r_{\text{reg}}$	56508.96244(3)	133	A
UCAM	WHT	2014/3/8	20:59	21:50	$u_{\text{reg}}, g_{\text{reg}}, r_{\text{reg}}$	56872.89819(3)	4957	A
UCAM	NTT	2021/9/7	03:26	04:00	$u_{\text{sup}}, g_{\text{sup}}, i_{\text{sup}}$	59404.15373(6)	38509	A
UCAM	NTT	2021/10/7	04:30	05:10	$u_{\text{sup}}, g_{\text{sup}}, i_{\text{sup}}$	59405.21005(7)	38523	A

Table 2.13: Observations taken for CSS090622.

Instrument	Telescope	Date	Observation start TDB	Observation end TDB	Filter(s)	T_{ecl}	Cycle No.	Binning ID
						MJD		
UCAM	WHT	2014/8/5	02:31	03:20	$u_{\text{reg}}, g_{\text{reg}}, r_{\text{reg}}$	56874.13102(5)	-1	A
UCAM	WHT	2014/8/5	04:34	04:58	$u_{\text{reg}}, g_{\text{reg}}, r_{\text{reg}}$	56874.20195(5)	0	A
UCAM	WHT	2014/8/5	23:07	23:43	$u_{\text{reg}}, g_{\text{reg}}, r_{\text{reg}}$	56874.98217(5)	11	A
UCAM	WHT	2014/8/8	22:31	23:10	$u_{\text{reg}}, g_{\text{reg}}, i_{\text{reg}}$	56877.96120(5)	53	B
UCAM	WHT	2014/8/9	03:43	04:22	$u_{\text{reg}}, g_{\text{reg}}, i_{\text{reg}}$	56878.17399(5)	56	B
UCAM	WHT	2014/8/11	04:50	05:37	$u_{\text{reg}}, g_{\text{reg}}, i_{\text{reg}}$	56880.23094(5)	85	B

Table 2.14: Observations taken for MASTER OT J001400.25-561735.0.

Instrument	Telescope	Date	Observation start TDB	Observation end TDB	Filter(s)	T_{ecl}	Cycle No.	Binning ID
						MJD		
UCAM	NTT	2016/8/25	05:28	07:36	$u_{\text{reg}}, g_{\text{reg}}, r_{\text{reg}}$	57625.29674(4)	-11	A
UCAM	NTT	2016/8/26	01:26	02:22	$u_{\text{reg}}, g_{\text{reg}}, r_{\text{reg}}$	57626.08356(7)	0	A
UCAM	NTT	2016/11/8	02:39	03:04	$u_{\text{reg}}, g_{\text{reg}}, r_{\text{reg}}$	57700.116579(7)	1035	-
UCAM	NTT	2017/6/12	10:07	10:30	$u_{\text{reg}}, g_{\text{reg}}, r_{\text{reg}}$	57916.42174(1)	4059	-

Table 2.15: Observations taken for OGLE82.

Instrument	Telescope	Date	Observation start TDB	Observation end TDB	Filter(s)	T_{ecl}	Cycle No.	Binning ID
						MJD		
UCAM	NTT	2016/8/21	23:47	00:50	$u_{\text{sup}}, g_{\text{sup}}, r_{\text{sup}}$	57622.02757(1)	-14	-
UCAM	NTT	2016/8/23	00:26	00:59	$u_{\text{sup}}, g_{\text{sup}}, r_{\text{sup}}$	57623.03460(1)	0	-

Table 2.16: Observations taken for SDSS J0748. Here, ‘N’ denotes eclipses that were used to refine ephemeris, but not used in the phase-folded eclipse modelling.

Instrument	Telescope	Date	Observation	Observation	Filter(s)	T_{ecl}	Cycle No.	Binning ID
			start TDB	end TDB				
USPEC	TNT	2017/1/14	20:28	20:58	$KG5$	57767.87085(2)	-699	N
USPEC	TNT	2017/1/17	14:14	14:42	$KG5$	57770.61147(4)	-652	N
USPEC	TNT	2017/1/22	18:32	19:15	$KG5$	57775.80116(2)	-563	N
USPEC	TNT	2017/2/14	12:48	13:05	$KG5$	57798.54248(2)	-173	N
USPEC	TNT	2017/2/14	13:55	14:27	g_{reg}	57798.60079(3)	-172	A
USPEC	TNT	2017/2/15	12:24	12:54	g_{reg}	57799.53377(3)	-156	N
USPEC	TNT	2017/2/24	14:11	15:20	r_{reg}	57808.63030(3)	0	A
UCAM	NTT	2017/3/20	23:39	00:43	$u_{\text{reg}}, g_{\text{reg}}, r_{\text{reg}}$	57833.00433(3)	418	A
USPEC	TNT	2017/12/12	15:20	16:01	r_{reg}	58099.66090(2)	4991	N
USPEC	TNT	2018/2/1	17:21	17:53	$KG5$	58150.74140(3)	5867	N
USPEC	TNT	2018/2/4	18:12	18:40	r_{reg}	58153.77358(1)	5919	B
USPEC	TNT	2018/2/5	17:59	18:27	r_{reg}	58154.76487(3)	5936	-
USPEC	TNT	2018/2/7	15:55	16:48	g_{reg}	58156.68913(2)	5969	-
USPEC	TNT	2018/12/16	22:10	22:50	g_{reg}	58468.94496(5)	11324	-
USPEC	TNT	2018/12/17	16:31	16:55	u_{reg}	58469.70301(5)	11337	A
USPEC	TNT	2018/12/17	19:16	19:45	$KG5$	58469.81963(6)	11339	N
USPEC	TNT	2018/12/17	20:38	21:08	r_{reg}	58469.87794(5)	11340	B
USPEC	TNT	2018/12/17	22:04	22:37	r_{reg}	58469.93625(4)	11341	B

Table 2.17: Observations taken for CRTS SSSJ0522–3505 J052210-350530. Mid-eclipse times and cycle numbers are calculated following the method detailed in §3.2.

Instrument	Telescope	Date	Observation	Observation	Filter(s)	T_{ecl}	Cycle No.	Binning
			start	end				ID
			TDB	TDB				MJD
UCAM	NTT	2019/09/29	08:12	09:00	$u_{\text{sup}}, g_{\text{sup}}, r_{\text{sup}}$	58755.36436(6)	-710	-
UCAM	NTT	2019/10/01	08:01	08:43	$u_{\text{sup}}, g_{\text{sup}}, r_{\text{sup}}$	58757.35456(1)	-678	-
UCAM	NTT	2020/01/29	04:07	05:02	$u_{\text{sup}}, g_{\text{sup}}, i_{\text{sup}}$	58877.20128(5)	1249	-

Table 2.18: Observations taken for SDSS J152419.33+220920.0. Note that the observations showed some color-dependent variability, so were binned with a different grouping.

Instrument	Telescope	Date	Observation start TDB	Observation end TDB	Filter(s)	T_{ecl}	Cycle No.	Binning ID
						MJD		
UCAM	NTT	2011/5/28	03:34	04:10	$u_{\text{reg}}, g_{\text{reg}}, r_{\text{reg}}$	55709.16440(1)	-11907	A
UCAM	NTT	2011/5/31	02:05	02:45	$u_{\text{reg}}, g_{\text{reg}}, r_{\text{reg}}$	55712.10374(1)	-11862	A
UCAM	NTT	2011/6/2	02:48	04:50	$u_{\text{reg}}, g_{\text{reg}}, r_{\text{reg}}$	55714.12865(1)	-11831	A
UCAM	WHT	2012/4/29	03:11	03:38	$u_{\text{reg}}, g_{\text{reg}}, r_{\text{reg}}$	56046.14373(1)	-6748	B
UCAM	WHT	2012/4/29	23:08	00:07	$u_{\text{reg}}, g_{\text{reg}}, r_{\text{reg}}$	56046.99290(1)	-6735	B
UCAM	WHT	2013/7/13	21:30	22:09	$u_{\text{reg}}, g_{\text{reg}}, i_{\text{reg}}$	56486.91456(1)	0	A
UCAM	WHT	2013/7/21	20:49	21:30	$u_{\text{reg}}, g_{\text{reg}}, i_{\text{reg}}$	56494.88342(1)	122	A
UCAM	WHT	2013/7/30	21:01	21:50	$u_{\text{reg}}, g_{\text{reg}}, i_{\text{reg}}$	56503.89743(1)	260	A
UCAM	WHT	2013/8/5	22:50	23:51	$u_{\text{reg}}, g_{\text{reg}}, r_{\text{reg}}$	56509.97209(1)	353	B
UCAM	WHT	2014/3/3	05:47	06:23	$u_{\text{reg}}, g_{\text{reg}}, r_{\text{reg}}$	56719.25331(1)	3557	g A, r & u fit individually
UCAM	WHT	2014/8/2	22:58	23:39	$u_{\text{reg}}, g_{\text{reg}}, r_{\text{reg}}$	56871.96768(1)	5895	-

Chapter 3

Modelling techniques and methodology

This chapter describes in detail the two modelling techniques used for this thesis: the characterisation of a CV using multi-band eclipse modelling, and using MESA models to infer the long-term mass loss rate of a system from its donor properties. The MESA modelling was done in collaboration with Meridith Joyce¹ and Marc Pinsonneault², whom I thank for their contributions to building the MESA configuration for M dwarfs, and in designing the star spot implementation.

Since the models used in this analysis are computationally expensive and require large parameter spaces, the choice of fitting algorithm is important. The majority of the parameter optimisation done in this work uses a type of Markov Chain Monte Carlo (MCMC) technique, and this is described in detail in §3.1, before discussing the models themselves.

3.1 Parameter optimisation of many variables

Frequently in science, a model must have its input parameters fit to data. For models with few input parameters and well-behaved evaluation metrics (i.e. model likelihood varies smoothly with input parameters), optimisation is relatively easy, but this is often not the case; for example the eclipse modelling portion of this work (§3.3.1) has a noisy likelihood landscape, and requires 18 parameters for a single eclipse. Fitting a full dataset of multiple eclipses frequently involves fitting 100+ parameters. To make matters worse, the eclipse model is fairly expensive to compute in large numbers, making a full exploration of the parameter space impractical.

The MCMC method is now a well-established tool in astronomy. It is robust, efficient when used properly, and yields the probability distribution of the variables being optimised even when the distributions are not well-described by simple functions. This has led to MCMC often being the method of choice when fitting models. This section provides a working knowledge of MCMC, but for an in-depth introduction and review of the technique and its various sub-types see [Sharma \(2017\)](#).

¹Space Telescope Science Institute: Baltimore, MD, US

²Ohio State University, OH, US

3.1.1 Bayesian analysis

Bayesian inference uses known, ‘prior’ knowledge combined with new information, ‘data’, to derive a better understanding - the ‘posterior’ knowledge - of a model. This somewhat self-evident intuition is formalised as Bayes’ Theorem, which calculates the posterior probability, $p(\theta|D, I)$ a set of model parameters, θ , given some observed data, D , and background information, I .

$$p(\theta|D, I) = \frac{\mathcal{L}(D|\theta, I) \cdot q(\theta|I)}{p(D|I)} \quad (3.1)$$

Here, $\mathcal{L}(D|\theta, I)$ is the probability of the observed data, given a model and prior information, so is called the likelihood of the data. $q(\theta|I)$ is the probability of the model being valid, given some prior information, so is called the prior distribution. Finally, $p(D|I)$, or the probability of observing the data, given the previously known information, is also called the ‘Evidence’, and acts as a normalisation factor. Using this vocabulary, Equation 3.1 can be written as:

$$\text{Posterior} = \frac{\text{Likelihood} \times \text{Prior}}{\text{Evidence}} \quad (3.2)$$

In Bayesian inference, the goal is to find the posterior distribution of the parameters of a model, given some data and any prior information.

3.1.2 MCMC optimisation

The MCMC technique is a class of tools developed to approximate the posterior distribution in Equation 3.1. Analytical calculations of the posterior are predicated on knowing the analytical forms of the likelihood, prior and evidence, which is often not known.

An MCMC sampler, as the name suggests, is a combination of a Monte Carlo method, a class of algorithms that rely on random sampling to find a result, and a Markov chain, a mathematical system that transitions between states according to probabilistic rules (Foreman-Mackey et al., 2013). An MCMC randomly samples the prior distributions of the model variables (the Monte Carlo half of the algorithm), evaluates their \mathcal{L} and q , and either accepts them onto its chain of sampled points or not, depending on if they meet a set of conditions (the Markov chain half of the algorithm). If the \mathcal{L} of the proposed set of variables is higher than the \mathcal{L} of the last set on the chain, the proposed set of variables is accepted.

If \mathcal{L} is lower, the algorithm randomly accepts or rejects the proposed step. Conveniently, \mathcal{L} is usually related to the χ^2 metric by $\mathcal{L} \propto \exp(-\chi^2/2)$, so a change in \mathcal{L} is often relatively easy to compute. The method by which a new set of parameters is proposed, and acceptance decided in the event of a decrease in \mathcal{L} is the sampling method, and several choices exist for different types of problems. The sampling method used here is the affine invariant sampling method with parallel tempering, described below.

By giving a finite chance to accept a ‘worse’ set of parameters, the chain is, in theory, allowed to explore and sample the entire possible parameter space without becoming trapped in local minima, though this requires an infinitely long chain. However, as the sampler preferentially accepts positions with higher \mathcal{L} , as the length of the chain increases the distribution of samples on the MCMC chain approaches the ‘true’ distribution of the posterior.

Affine invariant ensemble sampling

The affine invariant ensemble method of sampling was developed by [Goodman & Weare \(2010\)](#), and makes use of many ‘walkers’ sampling the parameter space in tandem. Each walker functions as an individual MCMC chain, and the walkers interact by proposing steps based on the current states of other walkers. A new parameter vector for walker k is proposed via a ‘stretch move’; another walker, j is chosen at random, and the last position vectors on each chain, $\theta_{j,N}$ and $\theta_{k,N}$, are used to propose a new position, Θ_k , that lies somewhere on the line connecting the two position vectors.

$$\Theta_k = \theta_j + z \cdot (\theta_k - \theta_j) \quad (3.3)$$

The variable z determines the location of the new vector on the line, and is randomly drawn from a probability distribution $g(z)$,

$$g(z) \propto \begin{cases} \frac{1}{\sqrt{z}}, & \frac{1}{2} \leq z \leq 2 \\ 0, & \text{Otherwise} \end{cases} \quad (3.4)$$

The choice of $g(z)$ favours a consolidation of the walkers, and aids convergence on regions of high \mathcal{L} . A schematic of this stretch move concept is shown in Figure 3.1.

Then, Θ_k is either accepted or rejected from the chain depending on the current state of the chain. Recall that if the proposed $\mathcal{L}_{N+1} > \mathcal{L}_N$, i.e. the likelihood

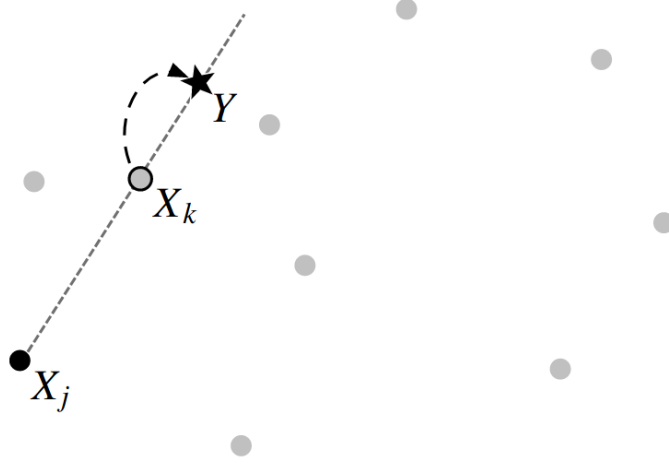


Figure 3.1: Reproduced from Goodman & Weare (2010), showing the concept of a stretch move proposal. The proposed next step for j is given by choosing a random position on the line joining the last step on chain j , X_j , and the last chain on another walker chosen at random, X_k . The proposed step is shown by the star, Y . Grey dots with no outlines illustrate the other walkers in the ensemble, but are unused.

has improved, the sample is immediately accepted. However, if $\mathcal{L}_{N+1} < \mathcal{L}_N$, the acceptance is determined by the transition probability, $P(\Theta_k|\theta_{k,N})$, defined as

$$P(\Theta_k|\theta_{k,N}) = \alpha(\Theta_k|\theta_{k,N}) \cdot q(\Theta_k|\theta_{k,N}) \quad (3.5)$$

where $\alpha(\Theta_k|\theta_{k,N})$ is the acceptance probability,

$$\alpha(\Theta_k|\theta_{k,N}) = \min\left(1, z^{n-1} \frac{\mathcal{L}(\Theta_k)}{\mathcal{L}(\theta_{k,N})}\right) \quad (3.6)$$

for a model with n dimensions. A random number, u , is drawn from a uniform distribution from 0 to 1, and if $u < \alpha(\Theta_k|\theta_{k,N})$, the proposed position is accepted. This quantifies two aspects of the sampler: the larger the drop in the probability that a new Θ_k describes observation, the *less likely* the algorithm is to accept Θ_k onto the chain; and larger stretch moves are more likely to be accepted. At each step in the MCMC, every walker has a new position proposed this way.

The affine invariant ensemble sampler benefits significantly from having the walkers in the ensemble interact, as they can communicate to other walkers regions of high \mathcal{L} even between walkers in different local minima. Further, the sampler

has a higher likelihood to accept dispersing steps than consolidating steps, so walkers are only likely to gather in deep minima, increasing exploration except in the case of a significantly higher likelihood. This improves the ensemble's ability to both locate the global minimum, and to sample non-spherical probability distributions (a task that can be difficult for simpler sampling techniques). Further, this algorithm is able to have the proposal and evaluation of new steps in every chain performed *simultaneously*, significantly improving computation time; a typical rule-of-thumb is to use $2n$ walkers for n parameters being optimised (Goodman & Weare, 2010), and since the number of walkers is almost always larger than the number of available threads, increased evaluation time scales well with more threaded computation.

Parallel tempering

Parallel tempering is an additional element of an MCMC sampler that helps in more fully exploring the parameter space in more complex models, while also being more capable of characterising posterior distributions in the case of complex correlations between parameters (Earl & Deem, 2005).

In metallurgy, a metal can be toughened by relieving its internal stresses through tempering, a treatment in which a metal is first heated to a high temperature, then slowly cooled. While the metal is at a high temperature, impurities are able to diffuse throughout the crystal structure of the metal and explore possible crystallisation locations. As the metal slowly cools, impurity atoms are gradually more and more attracted to areas of the crystal that exert less stress on the material, until the metal is fully cooled and the majority of atoms have found areas of local minima in stress potential.

The ensemble MCMC can take analogy from this ‘hot’ exploration phase and ‘cool’ settling phase (Earl & Deem, 2005). This is done by running several parallel ensembles, that each have a different ‘temperature’ between 1 and ∞ . Each ensemble samples a modified posterior, that follows $\pi_T(\Theta)$;

$$\pi_T(\Theta) = [\mathcal{L}(\Theta)^{\frac{1}{T}}]q(\Theta) \quad (3.7)$$

As $T \rightarrow \infty$, the chain samples the prior with no respect to how well Θ describes the data. This hot chain is analogous to the diffusive atoms with much higher thermal energy than the stress potential of the metal, and is free to randomly

explore available parameter space without being restricted by the \mathcal{L} function, potentially finding regions of high likelihood far from the initial conditions and communicating these regions back to cooler ensembles. Cooler temperatures are analogous to the cooling metal – drawn increasingly strongly towards regions of high likelihood. The cold case of $T \equiv 1$ behaves equivalently to a normal ensemble sampler.

Note that because hotter walkers are less sensitive to \mathcal{L} , their posterior no longer accurately reflects the ‘true’ distribution. If a parameter is described by a Gaussian distribution with a standard deviation, σ , the tempered \mathcal{L} will have a standard deviation of $\sigma\sqrt{T}$.

When running a parallel tempered MCMC, the values used in the software are $\beta = 1/T$, for which I choose between 3 and 5 evenly spaced values of β between 0 and 1. The number of temperatures used depends on the evaluation time; since parallel tempering runs multiple full ensembles in tandem, in models with very large numbers of parameters it becomes highly desirable to use as few temperatures as possible. However, the penalty in computation time per step comes with the benefit of a dramatically improved ability to locate the global minimum, especially in complex parameter space.

3.1.3 The bisection method

When searching for the root of a simple model, i.e. one with a single input parameter, x , and a single output metric, y , that either monotonically increases or decreases with x , I use the bisection method. This requires relatively few evaluations to find the root of a function, i.e. $y(x_0) = 0$. If two values of y are known to have opposite signs, e.g. $y_1(x_1)$ is positive and $y_2(x_2)$ is negative, it can be deduced that x_0 lies between x_1 and x_2 . Then, by repeatedly evaluating midpoint between the two values of x known to be closest to x_0 , the algorithm will tend towards $x_1 \sim x_2 \sim x_0$. In practice, the optimisation terminates when $y(x_1) - y(x_2)$ is within some tolerance. Step-by-step, this proceeds as follows:

1. First, evaluate the upper and lower limits of x , x_{low} and x_{high} , to ensure that one returns a negative y , and one returns a positive y
2. Evaluate $y(x_{\text{mid}})$, where $x_{\text{mid}} = 0.5(x_{\text{low}} + x_{\text{high}})$.
3. If x_{mid} has the same sign as x_{high} , assign $x_{\text{high}} = x_{\text{mid}}$, or vice-versa for x_{low} .

4. Check if the difference between $y(x_{\text{low}})$ and $y(x_{\text{high}})$ is within tolerance. If it is, terminate the optimisation. Otherwise, repeat the process.

3.2 Finding an orbital ephemeris

Crucial to both observing and modelling an eclipse is a good knowledge of the orbital ephemeris. This is described by the equation

$$T_{\text{ecl}} = T_0 + P_{\text{orb}}E \quad (3.8)$$

where T_{ecl} is the time of mid-eclipse, T_0 is the mid-eclipse time of the zeroth eclipse, and E is the eclipse number. Accurately calculating T_{ecl} is important to scheduling observations of a system, and P_{orb} is a crucial to the eclipse modelling.

As observations are often separated by several months or even years, an error in P_{orb} of even ~ 0.1 seconds can accumulate to give significantly inaccurate predicted eclipse times. This need for precision also requires the definition of *where* a time is recorded from, as the delay introduced by the light travel time from one side of the Earth's orbit to the other can significantly offset an observed time. All eclipse times presented in this thesis are given in the Barycentric Modified Julian Date (BMJD), which is the time of eclipse as measured from the centre of mass of the solar system. Note that this is different to the heliocentric MJD often seen in the literature, and where heliocentric literature values are used, they are converted to BMJD. Two timescales are relevant: UTC, in which a clock ticks at the rate of an Earth-bound observer; and TDB, in which a clock ticks at the rate of an observer at the barycentre of the solar system. Literature values, and the clocks in the observing cameras, use UTC time. This is converted to TDB during photometric calibration, for consistency with the BMJD times used.

3.2.1 Finding eclipse times

When finding an eclipse time, simply taking a time of minimum light is insufficient for the systems in this work. This is because it is common for CV eclipses to have very flat eclipse minima, and because CV eclipses have a fairly complex structure. Rather, finding the mid-eclipse time is done by looking at the numerical derivative of an eclipse. First, an eclipse is smoothed to remove short term fluctuations, partly those due to noise but also to mitigate the short term flickering often seen

in CVs. This initial smoothing is done by applying a median filter to the data. Then, the numerical derivative is calculated and smoothed again, this time with a ‘boxcar’ convolution (a.k.a. a moving average). Properly filtered, the dominant remaining features of the numerical derivative are the ingresses and egresses of the white dwarf and bright spot. The white dwarf ingress and egress are, in theory, symmetrical – the ingress should be a sharp, negative spike, and egress should be a sharp, positive spike. As the two should be the same shape, a double-Gaussian is fit to the derivative, using manually chosen initial conditions. In this model, two Gaussians share a width, σ , and have their mid-points equidistant from a central point. The magnitude of their heights are shared, but with opposite signs;

$$\begin{aligned} T_{1,2} &= T_{\text{ecl}} \pm \Delta T \\ h_{1,2} &= \pm h \end{aligned}$$

where $T_{1,2}$ are the respective midpoints of the two Gaussians, $h_{1,2}$ are their respective heights, and $2\Delta T$ is the distance between the two Gaussians. The derivative is then fit with these four free parameters (T_{ecl} , h , ΔT , σ) using an MCMC with wide, uniform priors of appropriate ranges, to give the T_{ecl} .

3.2.2 Computing period

To find a rough initial ephemeris of a system, at least two eclipse observations with known E are necessary. Given no prior knowledge of P_{orb} and T_0 , this can be done by simply observing the system for several hours, until two consecutive eclipses are seen. This gives a rough measure of P_{orb} , but can be significantly refined with longer baseline observations. For each observed T_{ecl} , E could unambiguously be determined, either from observing consecutive eclipses or from previously reported literature values. Where literature values were used to calculate a value of E , the result never deviated from an integer by more than 0.25 and were rounded to the nearest whole number.

An MCMC algorithm was used to fit a straight line model to the independent variable E and dependent variable T_{ecl} , with a gradient P and intercept T_0 ; i.e. model values of T'_{ecl} were generated from the set of E and a proposed (P, T_0) pair, and $(T_{\text{ecl}} - T'_{\text{ecl}})$ was minimised. Again, wide uniform priors were used for P and T_0 , based on initial values.

The model also accounts for potential systematic differences in timing accuracy

between instruments by having variable error scale factors applied to all eclipses observed with a specific instrument. For example, the timing reported for eclipses observed with ULTRACAM may be systematically offset from reality, and the errors associated with those observations might need to be larger than reported to be consistent with data from other instruments. The prior distribution assumed for these error factors was log-uniform ranging from 0.01 to 5, which favours the smallest error-multiplying factor consistent with the data.

Finally, the values of E for each eclipse were offset to minimise the covariance between T_0 and P . Consider a predicted eclipse time for E . The uncertainty on T_{ecl} in Equation 3.8 can be written as,

$$\sigma_{T_{\text{ecl}}}^2 = \sigma_{T_0}^2 + 2\sigma_{T_0}\sigma_P E + \sigma_P^2 E^2 \quad (3.9)$$

from the standard error propagation formula. To evaluate an alternative set of E' , E can be offset by some integer, N , with $E' = E - N$. By substituting this into equation 3.9, expanding out the brackets, and consolidating some terms, $\sigma_{T_{\text{ecl}}}^2$ becomes,

$$\sigma_{T_{\text{ecl}}}^2 = \sigma_{T_0}^2 + 2\sigma_{T_0}\sigma_P(E' + N) + \sigma_P^2(E' + N)^2$$

To minimise the cross-correlation between P and T_0 , the second term of the above equation should be minimised. This is achieved by setting $N = -(\sigma_{T_0}\sigma_P)/(\sigma_P^2)$, and re-fitting the ephemeris. Then, the above becomes:

$$\sigma_{T_{\text{ecl}}}^2 = \sigma_{T_0}^4 + (\sigma_P E')^2 \quad (3.10)$$

with no cross correlation, in theory. In practice, as E must be rounded to an integer, some residual cross-correlation persists, but is minimised.

3.3 Modelling CV eclipse light curves

To determine the system parameters for the CVs in this study, the eclipse light-curves were modelled. This method is more frequently applicable in CVs than the more traditional approach of using spectroscopic eclipsing binaries, since the donor star is rarely directly visible. Compared to using the superhump period excess to estimate the mass ratio (Patterson et al., 2005; Knigge, 2006), light curve modelling requires few assumptions. However, it does require reasonably precise alignment of the system and so is not possible for a large fraction of CVs.

CV eclipse modelling was first developed by Wood & Crawford (1986), and has been refined significantly over the last decade (Savoury et al., 2011; Littlefair et al., 2014; McAllister et al., 2017a, 2019). The code used for this modelling, however, is the publicly available `lfit_python` software³, based on the `lcurve`⁴ code authored by Tom Marsh. The method relies on four assumptions, namely that: (1) the stream of mass flowing from the donor to the white dwarf follows a ballistic trajectory, (2) the white dwarf obeys a theoretical mass-radius relationship, (3) the white dwarf is unobscured by the accretion disc or other sources of intra-system material, and (4) the donor exactly fills its Roche lobe. Most of these assumptions are considered robust, though the visibility of the white dwarf has been called into question by Spark & O'Donoghue (2015). The white dwarf mass-radius relationship was recently tested by Parsons et al. (2017), and found to be a reasonable assumption. Assuming that the mass stream following a ballistic trajectory appears to be a reasonable assumption, as the thermal velocity of the donor surface is orders of magnitude lower than the orbital velocity of the two stars. However, the most convincing argument to the validity of these assumptions are comparative studies, showing good consistency between eclipse modelling and other techniques (Tulloch et al., 2009; Copperwheat et al., 2012; Savoury et al., 2012; Sion & Godon, 2022).

The rough outline of the modelling process is described here, but is detailed fully in §3.3.1. Throughout, symbols are typically used when referring to model and system parameters, and a key is provided in Table 3.1. Radii are found by assuming that the secondary star completely fills its Roche lobe, which is required for mass transfer and ensures that the donor radius is solely a function of mass ratio, q , and orbital separation, a , c.f. Equation 1.2. The white dwarf eclipse

³Available at https://github.com/StuartLittlefair/lfit_python

⁴Available at <https://cygnus.astro.warwick.ac.uk/phsaap/software/>

Table 3.1: The various symbols used in this chapter, and their meanings.

Symbol	Parameter
F_{wd} , donor, disc,bs	White dwarf, donor star, disc, and bright spot fluxes
T_{eff}	White dwarf effective temperature
$\log(g)$	White dwarf surface gravity
$M_{\text{wd}}, R_{\text{wd}}$	White dwarf mass and radius
$M_{\text{donor}}, R_{\text{donor}}$	Donor star mass and radius
q	Mass ratio
a	Orbital separation
x_{l1}	Distance from the white dwarf to the L_1 point
i	Inclination
$\Delta\phi$	White dwarf eclipse width in units of phase
R_{disc}	Accretion disc radius
b	Disc surface profile exponent
$\theta_{\text{yaw}}, \theta_{\text{tilt}}, \theta_{\text{az}}$	Bright spot yaw, tilt, azimuth
S	Bright spot length scale
Y, Z	Bright spot profile exponents
u_{ld}	White dwarf limb darkening coefficient
ϕ_0	An eclipse phase offset
π	Parallax
E(B-V)	Interstellar extinction

width is set by the width of the donor, a , inclination, i , and q ([Bailey, 1979](#)).

Assuming that the mass stream between the two stars follows a ballistic trajectory puts the stream on a calculable path, determined by q ([Lubow & Shu, 1975](#)). This allows the location of the bright spot to be fixed in space, as the point at which this path intersects the outer edge of the accretion disc. Therefore, the phase of the bright spot ingress and egress is a function of q , i , $\Delta\phi$, and disc radius. By assuming that the white dwarf is unobscured, the duration of white dwarf ingress and egress are dependent on the white dwarf radius and inclination.

Four components of the eclipse model are the four component fluxes, F_{wd} , F_{donor} , F_{disc} , F_{bs} . As the white dwarf is assumed to follow a known mass-radius relationship, by fitting the observed white dwarf colours with a temperature, gravity, distance and interstellar extinction, the temperature and radius of the white dwarf yield a mass. The donor mass is then a simple product of the white dwarf mass, and q . The final result of modelling are then the following system parameters:

- white dwarf and donor masses

- white dwarf and donor radii
- orbital separation
- orbital velocity of the white dwarf and donor
- inclination
- white dwarf effective temperature and surface gravity
- distance

Practically, the modelling actually takes place in two phases, which are each described in detail. First the phase-folded eclipse is modelled under the above assumptions using proxy variables, then the resulting proxy variables are converted to physical parameters once observations are well-described by an eclipse model. This proxy variable fitting is done for the sake of computational efficiency.

Note that this model requires simultaneously fitting many variables simultaneously, thus finding the best-fitting parameters to observed data is complex. The technique used is described in §3.3.4.

3.3.1 Phase-folded eclipse modelling

Recall that the light from a CV originates from four distinct objects in the system. The white dwarf and donor star, the accretion disc about the white dwarf, and the bright spot impact region (hereafter simply ‘the bright spot’), where transferred material impacts the outer rim of the accretion disc and liberates significant amounts of energy. Notably the bright spot emits flux directionally, so beaming must also be accounted for in the model. The anatomy of a CV eclipse light curve is a sequence of five events that usually occur in the following order:

1. a pre-eclipse hump is often seen as the bright spot rotates to point at the observer
2. The white dwarf becomes obscured by the donor
3. The bright spot becomes obscured by the donor
4. The white dwarf emerges from behind the donor
5. The bright spot emerges from behind the donor

Figure 3.2 shows a typical light curve, with these events noted.

A single eclipse is described by 18 parameters:

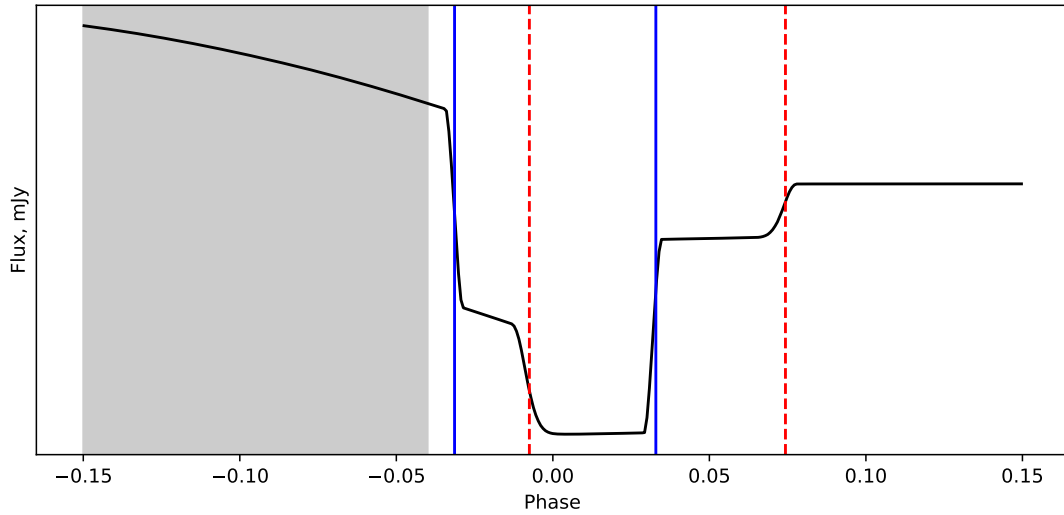


Figure 3.2: Showing an example eclipse light curve, folded about the period of the eclipse. The **solid black line** shows the brightness of the system varying over time. The **blue solid lines** show the white dwarf ingress (left) and egress (right). The **red dashed lines** show the ingress (left) and egress (right) of the bright spot. The pre-eclipse hump is the **grey shaded region**

- White dwarf, donor star, disc, and bright spot fluxes, $F_{\text{wd}, \text{donor}, \text{disc,bs}}$
- Mass ratio, q
- White dwarf eclipse width in units of phase, $\Delta\phi$
- Scaled white dwarf radius, R_{wd}/x_{l1}
- White dwarf limb darkening coefficient, u_{ld}
- Scaled outer disc radius, R_{disc}/x_{l1}
- Disc surface profile exponent, b
- Seven parameters describing the bright spot
- An eclipse phase offset, ϕ_0

The seven bright spot parameters are not physically motivated, but describe a flexible empirical bright spot model designed to capture a large range of bright spot eclipse morphologies.

The white dwarf

The white dwarf is modelled as a luminous disc, with a total surface brightness F_{wd} and a radius of R_{wd}/x_{l1} . It is subject to limb darkening, using a linear

prescription:

$$\frac{I_l}{I_0} = 1 - u_{\text{ld}}(1 - \cos\beta) \quad (3.11)$$

where I_0 is the intensity at the centre of the disc, and I_l is the intensity at a limb. β is the angle between the line normal to the surface of the white dwarf, and the observer's line of sight. However, the observations are not precise enough to constrain u_{ld} , so a Gaussian prior derived from the white dwarf T_{eff} and $\log(g)$ is used.

The donor star

The secondary star does not become obscured during an eclipse, but there is still some variation in its brightness. The donor is not spherical, so a small ellipsoidal variation is seen as it rotates to expose more or less of its surface to the observer. As a result, the donor is modelled as a limb darkened, and gravity darkened disc with total surface brightness F_{donor} , and a modulation to describe the changing observable surface area.

The accretion disc

The accretion disc is modelled as a series of annular rings about the white dwarf, extending out to R_{disc}/x_{l1} and with a total surface brightness of F_{disc} . The intensity of each annulus decreases with distance from the white dwarf, following an exponential formula, $I_i \propto R^{-b}$ for ring i at distance R from the white dwarf. As b is a free parameter in the model, the disc brightness can be made more or less centrally concentrated to match observations. As the bright spot location is determined by q and R_{disc}/x_{l1} , the phases of bright spot ingress and egress provide a valuable constraint for R_{disc}/x_{l1} .

The bright spot

The bright spot model is not physically motivated, but rather is chosen to be able to reproduce a large range of bright spot eclipses. It is modelled as a strip of flux extending from the edge of the disc, with a defined brightness profile and overall flux. The strip intensity falls off exponentially, described by the equation

$$I_X \propto \left(\frac{X}{S}\right)^Y \cdot \exp\left[-\left(\frac{X}{S}\right)^Z\right] \quad (3.12)$$

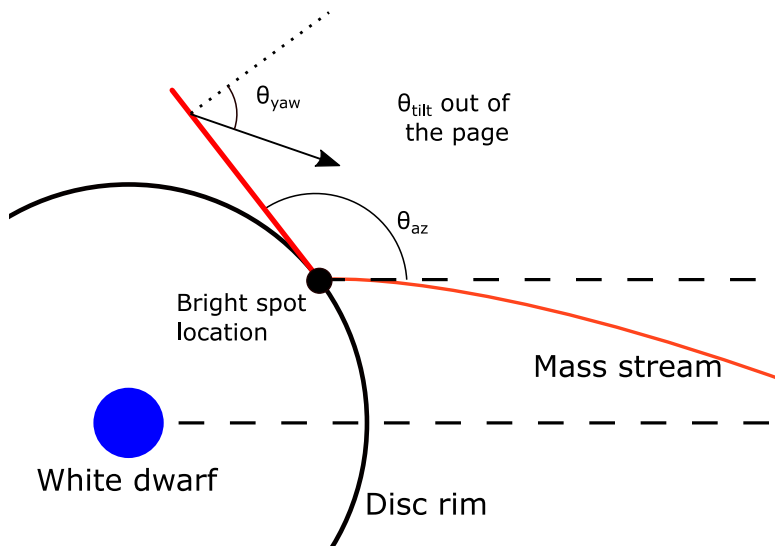


Figure 3.3: Showing a schematic of the bright spot model. The **lower dashed line** joins the centres of the white dwarf and donor stars, and the **upper dashed line** runs parallel to it, intersecting the bright spot location. The **straight red line** is one half of the flux-emitting strip and has a profile exponent Y , and the **arrow** shows the direction of light emission, at an angle θ_{yaw} from the normal.

where I_X is the intensity of the strip a distance X along it, and S is the scale of the bright spot. Y and Z are the profile exponents.

The bright spot is known to emit light directionally, at a beaming angle, θ_{yaw} , from the normal to the strip in the plane of the disc, and an angle θ_{tilt} from the plane of the disc. Some fraction of the light is beamed, and the rest, f_{is} , is emitted isotropically from the strip. This geometry is shown in Figure 3.3

Lower values of q will cause the ballistic stream to take a wider arc towards the white dwarf, moving the intersection point with the disc. The angle between the bright spot and disc edge is defined by θ_{az} , the angle between the strip and the line of sight of the observer.

As the bright spot is the most complex component of the model, there is an option to simplify it in software for systems with faint bright spot features that cannot be properly resolved. This mode is called the ‘simple’ bright spot model, and fixes θ_{tilt} at 90° , θ_{yaw} at 0° , and the strip exponents X and Y to 1 and 2, respectively. By removing these four degrees of freedom, better and faster characterisation of the eclipse is possible.

Choice of priors

The choice of prior is important in Bayesian inference, but I have very little prior knowledge on a system. The prior distributions used were generally uniform and span the numerically allowed range⁵, with a few exceptions.

As it is unconstrained by data, u_{ld} initially uses a Gaussian prior centred on 0.3 with a width of 0.1. Once a constraint on T_{eff} is known, a more accurate value of u_{ld} can be calculated and used for future fitting. The bright spot scale draws from a log-uniform prior between 0 and 0.2, which favours smaller values, and θ_{az} is forbidden from values that would cause the bright spot strip to deviate from a tangent to the disc by $> 80^\circ$. Finally, some combinations of parameters are forbidden in the model. The values of q and $\Delta\phi$ must be such that $i \leq 90^\circ$ for an eclipse to occur, and the disc radius is constrained by the maximum radius before precession becomes a significant effect, $R_{\text{disc}}/a < 0.46$ (Hellier, 2001).

3.3.2 Post-processing the eclipse model

The eclipse modelling uses proxy variables, so some processing must be done to convert them to physical values. This is done in two steps. First, a white dwarf temperature and surface gravity are fit to the white dwarf fluxes. Then, the white dwarf temperature and orbital period are combined with the best-fit eclipse model parameters to convert the scaled distances to metres, and mass ratio to the masses of each star.

Fitting white dwarf colours

By modelling the eclipse in multiple bands, at least three observations of white dwarf flux are available. The DA white dwarf cooling model from Bergeron et al. (1995)⁶ is fit to these flux observations. These cooling models yield the absolute magnitude of the white dwarf in each band, M , for a given effective temperature, T_{eff} and surface gravity, $\log(g)$. This absolute magnitude is then easily translated to an apparent magnitude, m , given a system parallax, π , and interstellar extinction coefficient, $E(B - V)$,

$$m = M - 5 \log(\pi, \text{ arcsec}) - 5 \quad (3.13)$$

⁵e.g. angles are limited to be between 0 and 2π , and fluxes range from 0 to the peak flux of the eclipses.

⁶Available at <http://www.astro.umontreal.ca/~bergeron/CoolingModels>

To optimise these four parameters, an affine-invariant MCMC with three levels of parallel tempering was used, c.f. §3.1.2. for priors, uniform T_{eff} and $\log(g)$ distributions were used that span the range set by the model cooling tracks. $E(B - V)$ used a uniform distribution between 0, and the maximum IRSa measurement for the relevant sky coordinates⁷, and the parallax prior was chosen to match the Gaia measurement of the system (Lindegren et al., 2018; Luri et al., 2018; Gaia Collaboration et al., 2016, 2018).

Conversion of proxy variables to physical parameters

The eclipse model proxy variables are then converted to real values. Five input variables are needed: T_{eff} , P_{orb} , q , $\Delta\phi$, and R_{wd}/x_{l1} .

A measure of the white dwarf radius, R_{wd} , can be found using Kepler's 3rd law and making the substitutions $r = R_{\text{wd}}/a$ and $q = M_{\text{donor}}/M_{\text{wd}}$.

$$P_{\text{orb}}^2 = \frac{4\pi^2 a^3}{G(M_{\text{wd}} + M_{\text{donor}})} \quad (3.14)$$

$$= \frac{4\pi^2 R_{\text{wd}}^3}{GM_{\text{wd}}(1+q)r^3} \quad (3.15)$$

$$R_{\text{wd}}^3 = \frac{P_{\text{orb}}^2 r^3 GM_{\text{wd}}(1+q)}{4\pi^2} \quad (3.16)$$

r can be found from R_{wd}/x_{l1} by calculating x_{l1}/a , which itself is a function only of q .

Finding R_{wd} this way requires the white dwarf mass. Fortunately, for a given T_{eff} (which is known from the colour fits, §3.3.2), white dwarfs follow tight theoretical mass-radius relationships (Parsons et al., 2017), that can be employed to find the unique M_{wd} , R_{wd} pair that satisfies both Equation 3.16 and the theoretical mass-radius relationship. Specifically, a proposed theoretical mass-radius pair is chosen from a model relationship and a value of $R_{\text{wd,calc}}$ is calculated from Equation 3.16. If this matches the theoretical value, the mass is valid. Otherwise, the proposed mass is altered accordingly and a new mass-radius pair is checked again until the two agree.

Three white dwarf mass-radius relations were used. First, a solution was searched for using the Wood (1995) models, spanning masses of $0.4 - 1.0 M_{\odot}$. The Wood (1995) models are preferred, as they use a thicker hydrogen layer

⁷ Available at <https://irsa.ipac.caltech.edu/applications/DUST/>

that is more appropriate for the accreting CV white dwarfs. If no solution could be found, the [Panei et al. \(2000\)](#) models were searched, spanning masses from $0.4 - 1.2M_{\odot}$. Both of these mass-radius relationships account for the white dwarf T_{eff} . If no solution has been found with these two tracks, the [Hamada & Salpeter \(1961\)](#) 0 Kelvin mass-radius relation is checked for solutions. This track spans the largest range in mass, from $0.14 - 1.44M_{\odot}$. If no solution is found with the [Hamada & Salpeter \(1961\)](#) tracks, the model is considered invalid, though this did not occur for any system in this thesis.

Then, the inclination is calculated. $\Delta\phi$ is solely a function of q , and i . Therefore, the eclipse model values of $\Delta\phi$ and q are used to calculate the system inclination - this is done by proposing candidate values of i , and comparing the calculated $\Delta\phi_{\text{calc}}(q, i)$ with the modelled $\Delta\phi$, and adjusting i as needed until the two agree.

Now, three quantities are known; i , M_{wd} , and R_{wd} . As previously mentioned, R_{donor} is assumed to be the Roche radius, from Equation 1.2, and M_{donor} is found simply by $(q \cdot M_{\text{wd}})$. a is calculated from the two component masses and P_{orb} , using Kepler's laws. Finally, the orbital velocities, $K_{\text{wd}, \text{donor}}$ respectively, of the two stars are calculated using Kepler's laws.

$$K_{\text{wd}} = \frac{2\pi a \sin i}{P_{\text{orb}}} \frac{q}{1+q} \quad (3.17)$$

$$K_{\text{donor}} = K_{\text{wd}} \cdot \frac{M_{\text{wd}}}{R_{\text{wd}}} \quad (3.18)$$

3.3.3 Capturing flickering with Gaussian Processes

CVs almost always display some amount of stochastic variability, known as flickering. Rather than attempting to model this physically, it is instead treated as correlated noise and characterised with a Gaussian process (GP). The application of GPs to capturing flickering was established by [McAllister et al. \(2017a\)](#) based on work by [Roberts et al. \(2012\)](#) and [Gibson et al. \(2012\)](#). The utility of this addition to the eclipse modelling step is a significant improvement in the accuracy of parameter posteriors, as the GP can be used to subtract flickering from the observations while leaving the key light curve features that modelling aims to reproduce, demonstrated by [McAllister et al. \(2017a\)](#).

This section is aimed at giving a working knowledge of GPs in the context of characterising flickering, and for more in-depth discussion the reader is directed

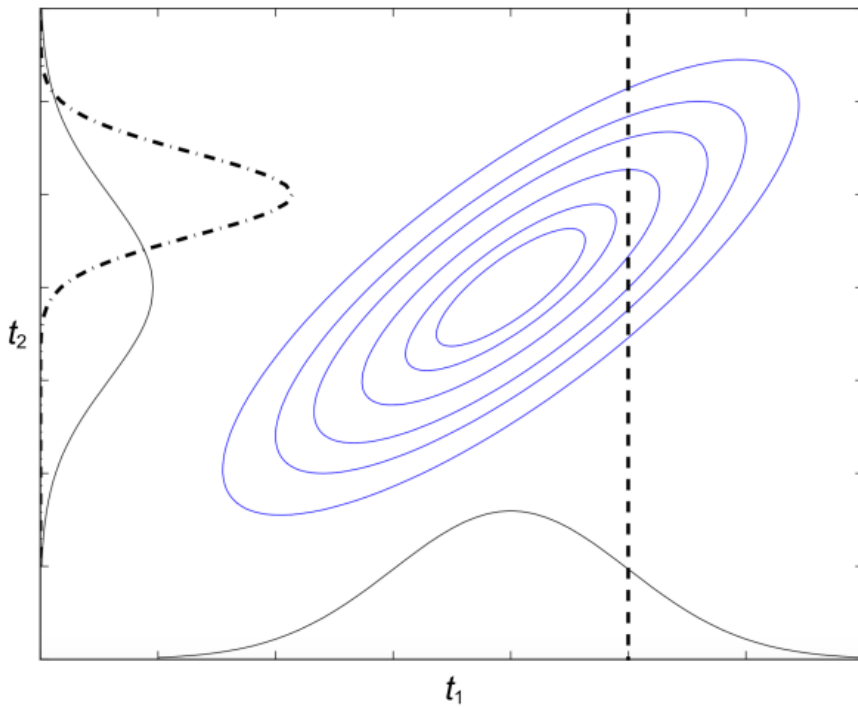


Figure 3.4: Reproduced from [McAllister \(2017\)](#). Two variables, $t_{1,2}$, are described by a joint Gaussian distribution. **Blue ellipses** trace lines of equal probability of drawing a sample. **Solid black Gaussians** along each axis show the probability distributions of each variable, and the **dashed black Gaussian** along the y-axis shows the probability distribution of t_2 , given a fixed value of t_1 , which is shown by the **vertical dashed line**.

towards these works. The mathematics below omits error in flux for legibility, but closely similar derivations are possible that include error when calculating the likelihood of a data set.

Gaussian Process background

GPs are a statistical method that can be adapted to produce a series of correlated points across a time (or space) axis, the distribution of which is described by a Gaussian function. The points are related to one another by a joint distribution; to illustrate what a joint distribution is, take the example to two variables t_1, t_2 , shown graphically in Figure 3.4. Each is normally distributed about a central value, but higher values of t_1 are more likely to be produced alongside higher values of t_2 . Thus, knowing the value of t_1 can inform the likely value of t_2 , written as $P(t_1|t_2)$.

By describing a time-series dataset as an arbitrarily large number of variables

with a joint distribution between them, the probability of a point being described by a GP, *given the rest of the data*, can be computed. Similarly, the likelihood of an entire data set being described by a GP is also calculable. This principle is the basis of time-series GPs, and allows them to be used when evaluating the goodness-of-fit of a model.

A GP distribution is defined simply by two functions, a mean function, $\mu(t)$, and a covariance function, $k(t_i, t_j)$.

$$y(t) \sim \mathcal{GP}(\mu(t) \cdot k(t_i, t_j)) \quad (3.19)$$

where $t_{i,j}$ are the times of two data points, and are not necessarily adjacent. In this context, the set of \mathbf{y} is a set of observed fluxes at times \mathbf{t} . The distribution of \mathbf{y} is then represented by the joint distribution of $P(\mathbf{y}|\mathbf{t})$, following a multivariate Gaussian, \mathcal{N} ,

$$P(\mathbf{y}|\mathbf{t}) = \mathcal{N}(\mu(\mathbf{t}), \mathbf{K}) \quad (3.20)$$

Where \mathbf{K} is the covariance matrix of the multivariate Gaussian, and fully describes how the distribution of each element of \mathbf{t} is affected by each other element, forming an $n \times n$ matrix for n data in \mathbf{t} .

$$\mathbf{K} = \begin{pmatrix} k(t_1, t_1) & k(t_1, t_2) & \cdots & k(t_1, t_n) \\ k(t_2, t_1) & k(t_2, t_2) & \cdots & k(t_2, t_n) \\ \cdots & \cdots & \cdots & \cdots \\ k(t_n, t_1) & k(t_n, t_2) & \cdots & k(t_n, t_n) \end{pmatrix} \quad (3.21)$$

Computing a covariance matrix

In practice, as \mathbf{t} becomes a larger set and n increases, computing the $n \times n$ matrix \mathbf{K} becomes impractical. Instead, a kernel is defined that gives analytical functions that approximate each $k(t_i, t_j)$, and the choice of kernel defines the type of correlation between data.

When modelling flickering, a Matern-3/2 kernel is used, which produces a covariance matrix that correlates nearby values more strongly than those further away in time. The kernel has a ‘memory’ timescale, λ , and an amplitude, α , that can be tuned to a data set. This replaces $k(t_i, t_j)$ with $\alpha \cdot k_M(r^2)$, where $k_M(r^2)$ is defined as

$$k_M(r^2) = (1 + \sqrt{3r^2}) \cdot \exp(-\sqrt{3r^2}) . \quad (3.22)$$

Here, r^2 is a pseudo-radius, and is a function of the distance between the two $t_{i,j}$ being considered. Generally, since the Gaussian process technique is applicable to parameter *vectors*, this is written as

$$r^2 = (\mathbf{t}_i - \mathbf{t}_j)^\top \cdot \Lambda^{-1} \cdot (\mathbf{t}_i - \mathbf{t}_j) \quad (3.23)$$

Note that the choice of the matrix Λ defines how other data in a set affect other data, and can be any square matrix of the same width as \mathbf{t} . For the GP used in this work, a simple Λ is used which has λ along the diagonal and 0 elsewhere, making λ a kernel scale parameter. In this model each t_i is a single time value, making Λ a 1×1 matrix with values of λ along the ‘diagonal’ – functionally, $r^2 = \lambda \cdot (t_i - t_j)^2$.

Evaluating a model fit with a Gaussian process

Finally, the \mathcal{L} of a set of \mathbf{y}, \mathbf{t} can be calculated given a GP, i.e. $\mathcal{L}(\mathbf{y}|\alpha, \lambda, \mathbf{t})$, analogous to $P(\mathbf{y}|\mathbf{t})$ (Rasmussen & Williams, 2006). This is the pertinent step to the modelling, as the likelihood function of the data is replaced with the likelihood of the GP. When evaluating a proposed Θ in the MCMC, rather than using $\mathcal{L} \propto \exp(-\chi^2/2)$ the likelihood function is replaced with the likelihood of the residuals after observed fluxes have had the eclipse modelled fluxes subtracted, i.e. $\mathbf{y}_{\text{res}} = \mathbf{y}_{\text{obs}} - \mathbf{y}_{\text{model}}$, given an (α, λ) pair. This is expressed more clearly algebraically, as

$$\mathcal{L} = P(\mathbf{y}_{\text{res}}|\mathbf{t}, \alpha, \lambda) = \frac{1}{(2\pi)^{n/2} |\mathbf{K}|^{1/2}} \exp \left(-\frac{1}{2} \mathbf{y}_{\text{res}}^\top \mathbf{K}^{-1} \mathbf{y}_{\text{res}} \right) \quad (3.24)$$

One final factor must be accounted for. Flickering appears to be localised to the region of space near the white dwarf, and often reduces in amplitude substantially during the white dwarf eclipse (McAllister et al., 2017a). To capture this in the GP, two kernels are used: one external to the white dwarf eclipse, and one internal to the white dwarf eclipse. Each shares a value of λ , but has its own freely variable α , α_{out} and α_{in} .

Overall, the GP adds three new parameters to the eclipse model: $\alpha_{\text{out,in}}$ and λ , which are optimised alongside the eclipse parameters themselves. $\alpha_{\text{out,in}}$ use wide, log-uniform priors to prioritise smaller amplitudes. λ uses a narrower log-uniform prior, chosen to prevent the timescale from either exceeding the duration of the eclipse, or becoming shorter than the time resolution between data points.

The slightly more complex parameter space that must now be explored, and more computationally expensive evaluation of \mathcal{L} , is made up for in a significantly better characterisation of lower quality eclipses ([McAllister et al., 2017a](#)).

3.3.4 Hierarchical model structure

In this thesis, the light curve fitting model used by [McAllister et al. \(2019\)](#) is extended, adopting a hierarchical approach to reduce model complexity.

Changes in the disc radius and brightness profile, and bright spot parameters can mean that the same CV has a significantly different eclipse light curve at different times, often making it difficult to justify averaging together many eclipses, as features can become smeared out and uninformative. In the worst-case scenario, all 18 parameters would be independently variable for each eclipse, in each band. However, by sharing some parameters between eclipses and bands, this large number of free parameters is slightly reduced, and the posterior of some parameters can be informed by multiple eclipses. [McAllister et al. \(2017a\)](#) share q , R_{wd}/x_{l1} , and $\Delta\phi$ between eclipses, and I broaden that concept by organising the model into a hierarchical structure, a schematic of which is shown in Figure 3.5.

The top level of the model provides the core parameters, which are unchanging between all observing bands and constant across our observations: q , R_{wd}/a , and $\Delta\phi$. I assume the white dwarf and donor fluxes do not change on the timescale of our observations, and so these variables, along with the limb darkening coefficient of the white dwarf, are shared between all eclipses observed with the same filters. The bottom level holds parameters that can vary quickly enough to change between eclipses, i.e. parameters describing the accretion disc and bright spot. By handling parameters this way, I maximise the amount of data informing important variables. I also somewhat reduce the number of free parameters, which aids in model fitting, but the chief justification for the hierarchical approach is that it ensures consistency between eclipses - something not guaranteed when fitting eclipses individually.

Where possible, data were also binned together. Ideally, this has three beneficial effects: the number of eclipses, and therefore the number of parameters, is reduced; binning increases the signal-to-noise ratio of the data; and as the flickering component is not consistent between eclipses, should reduce the degree of flickering present in the data. However, as CV eclipses often have variable bright

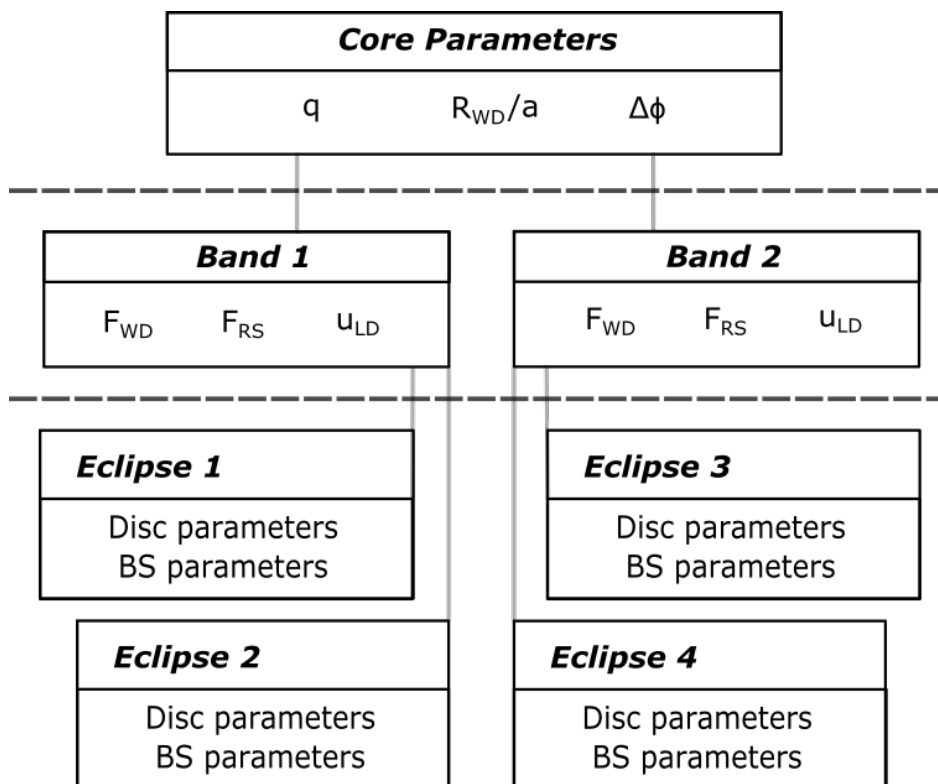


Figure 3.5: The hierarchical structure of the light curve model. Parameters are inherited downwards, to produce an eclipse at the ‘leaves’ of the tree, e.g. Eclipse 3 inherits the parameters of Band 2, which in turn inherits the Core parameters. $F_{wd,RS}$ represent the fluxes of the white dwarf and donor star, and U_{LD} is the limb darkening coefficient of the white dwarf.

spot and disc contributions, it is frequently not reasonable to combine eclipses. Varying bright spot and eclipse features will become smeared out when binned, corrupting crucial elements of the eclipse. This smearing effect is also subtly present, even in data that appear consistent. As a bin width must be chosen that will not precisely align with the integration times of the photometric data, binning will always introduce a small blurring of timing data, and whilst this is a small effect, it can significantly alter the white dwarf ingress and egress features. Therefore, binning is only done when data are sufficiently similar, and is treated with caution.

3.4 Evolutionary modelling

Once armed with a robust sample of CVs donor masses and radii, evolutionary modelling is able to refine our understanding even further. In §1.5, I motivated how the donor star inflates in response to mass loss, and how the degree of this inflation is related to the severity of the mass loss. If the radius of an equivalent star in the absence of mass loss is known, and the observed radius of a CV donor can be reproduced by stellar structure models with the introduction of some amount of mass loss, the long-term average mass loss rate can be inferred.

The stellar evolution code used is the MESA codebase ([Paxton et al., 2011, 2013; Paxton et al., 2015, 2019](#)), a one-dimensional stellar evolution model. MESA is highly flexible, due to its use of various ‘modules’, wherein each module supplies code with an element of the physics of the star. These are configurable with relatively simple input files, and can be customised to extend MESA with new physics not contained in the core codebase. Regarding CV modelling in particular, there is *a priori* cause for confidence; largely default MESA configurations are capable of modelling CV donor tracks with impressive accuracy, even reproducing the period gap by a shutdown of magnetic braking triggered by the donor becoming fully convective ([Paxton et al., 2015](#)). §6.1 also demonstrates this capability, and shows that with some small modifications the agreement between the evolutionary tracks produced by MESA and [Knigge et al. \(2011\)](#) can be improved further.

Note that all MESA models for this thesis were run using version 21.12.1 of the MESA codebase, and use the configuration detailed in §3.4.1, unless specified otherwise.

To extract mass loss rates, I will go through three steps. Firstly, I demonstrate how the radius of a zero- \dot{M} singleton model of a given mass can be tuned to match the M dwarf mass-radius relationship given by [Brown et al. \(2022\)](#) by introducing star spots. Secondly, I explore the range of donor masses for which the radius is insensitive to mass loss history – donors within this mass range can be used to find the secular mass loss rate. Finally, I outline the method by which I search for mass loss rates that produce stellar models matching CV donor observations.

3.4.1 MESA configuration for low-mass M dwarfs

Broadly speaking, when computing a stellar evolution model one must simply input models of physical processes, describe some initial conditions, and allow the stellar model to evolve over time. Unfortunately, the physics of stars is not completely understood, and the processes that affect a star’s evolution significantly differ depending on its conditions. Whilst some core physics is fixed, MESA provides many options for which prescriptions to use for a particular process, or even which processes to consider at all. MESA has default configuration values that are reasonable for some common stellar conditions, but some tuning of the model physics is a necessary step for any rigorous modelling. As such, some tailoring of configuration files must be done in order to produce accurate donor models.

Parameters that are not discussed below are left as the MESA default. Notably left as default is the metallicity of the donor stars; robust measurements of donor metallicity are challenging, though some recent attempts have yielded results ([Harrison, 2016, 2018](#)). However, these are prone to systematic error, and refer to a small sample size. All MESA models presented here use the default MESA metallicity, $Z = 0.02$ (`initial_z = 0.02d0`), $Y = 0.28$ (`initial_y = 0.28d0`).

Model initialisation

Whilst MESA allows for beginning a MESA run with a precomputed stellar model, the models in this analysis all generate their stars from a pre-main sequence cloud of gas before each run. This ensures that each model is computed from the very beginning with the correct physics, and is set by the command `create_pre_main_sequence_model = .true.`

Nuclear processing

Computing the equilibrium reaction rates of nuclear burning in a star is non-trivial, as the different species being consumed and produced form a complex network of interactions. The products of one reaction are often the reagents of another, and with many options for reaction paths and hard-to-calculate reaction rates, this is prohibitive (and often inaccurate) to compute on the fly. Rather, a pre-calculated or empirical reaction network is used.

MESA has several options for the reaction network available in its core code-base. By default, the `basic` network considers the reactions of the staple elements of most stellar cores: hydrogen-1, helium-3, carbon-12, nitrogen-14, oxygen-16, neon-20, and magnesium-24. However, we use the more complete reaction network given by `pp_and_cno_extras`. This is a combination of two other networks, `pp_extras` and `cno_extras`. `pp_extras` is preferred, as it more accurately represents nuclear reactions in young stars (Murphy et al., 2021), and `cno_extras` more fully considers the reaction chains the CNO cycle, specifically at high temperatures (Paxton et al., 2011). To enable this, the lines `change_net = .true., new_net_name = 'pp_and_cno_extras.net'` are added to the configuration file.

In addition, the JINA Reaclib reaction rate library (Cyburt et al., 2010) is used: `set_rates_preference = .true., new_rates_preference = 2`

Opacity tables

MESA uses two opacities: radiative opacity and conductive opacity, with options to select which opacity sources to use and when to use them. I use the opacities calculated for Asplund et al. (2009) solar abundances by setting the following flags:

- `kap_file_prefix = 'a09'`
- `kap_lowT_prefix = 'lowT_fa05_a09p'`
- `kap_CO_prefix = 'a09_co'`

Note that MESA uses separate opacity tables for high (`kap_file_prefix`) and low (`kap_lowT_prefix`) temperatures, and I set both to the appropriate tables for Asplund et al. (2009). For completeness, I also set the higher temperature, hydrogen-poor/metal-rich opacity table to the Asplund et al. (2009) (`kap_CO_prefix`), though

the stars modelled here are all low temperature M dwarfs and this does not affect these specific results.

Surface boundary lookup tables

When solving the four differential equations necessary to produce an internally consistent stellar model, i.e. how the radius, pressure, luminosity, and temperature vary with mass, some boundary conditions are required. The boundary conditions for radius and luminosity are self-evident: $R(M = 0) = 0$, and $L(M = 0) = 0$. Unfortunately, such simple fixed central values are not available for the temperature and pressure, so the boundary condition at the surface of the star is used instead. This requires defining the location of the surface of the star. This is done by setting a value of optical depth, τ , to use as the base of the stellar atmosphere.

A basic approach is to set the pressure and temperature to 0 at the stellar surface, i.e. $P(M = M_\tau) = 0$, $T(M = M_\tau) = 0$, but this is a poor approximation. A far more accurate approximation is to pre-calculate model stellar atmospheres, which then give values of P, T as a function of τ , $\log(g)$, and luminosity. Different choices of atmosphere table results in different surface temperatures and pressures, which can alter the mass-radius relation for the resulting models.

For these MESA models, the `tau_10` grid was used, which interpolates the PHOENIX (Hauschildt et al., 1999, 2001) and Castelli & Kurucz (2004) stellar atmospheres (which assume solar metallicity) at $\tau = 10$ for the base of the atmosphere (Paxton et al., 2010, 2011). Note that none of the atmosphere tables available in MESA accurately reproduce observations of M dwarfs across the range of donor masses required. In fact, of the available tables, the `tau_10` gives some of the less accurate modelled mass-radius relations for low mass stars. However, this atmosphere grid was chosen as it produces stars that are *consistently* smaller than required for stars with $M < 0.3M_\odot$, a deficit that is compensated for in §6.3, using the method described in §3.4.2. In this way, rather than relying on the atmosphere table to produce the correct stellar radii, the radius can be manually adjusted to match observations.

Mixing length theory

Mixing length theory is concerned with the convective boundary, where rising material dissipates its heat, reverses trajectory, and begins to sink. Models that

treat a convective layer as a hard boundary between convective and non-convective material are less able to describe observations than models that allow for some degree of overshooting of rising material past the theoretical convective boundary, before dispersing its energy ([Prandtl, 1925](#)). This is often justified physically by a rising packet of material having some momentum that must be dissipated before reversing direction ([Bradshaw, 1974](#)).

By reducing the degree of overshooting, the efficiency with which energy is transported from the inner regions of the star is similarly reduced, increasing $R(L)$. We decrease the default MESA overshooting of $2\times$ the pressure scale height of the convective boundary, to $1.95\times$ this scale height: `mixing_length_alpha = 1.95`. In addition, we use the [Heney et al. \(1965\)](#) MLT formulation, and the following overshooting formalism new to MESA v21.12.1:

- `overshoot_scheme(:) = 'exponential'`
- `overshoot_zone_type(:)= 'any'`
- `overshoot_zone_loc(:)= 'any'`
- `overshoot_bdy_loc(:) = 'any'`

[Model convergence and grid fidelity](#)

Finally, two numerical options were enabled. The first is the MESA ‘gold’ tolerances, which enforces tight tolerances on energy conservation. If, after computing a time step, the sum of the energies of each model cell does not closely match the known total energy of the star, the step is rejected and re-attempted, resulting in more accurate models ([Paxton et al., 2019](#)).

Second, we apply the `okay_to_reduce_gradT_excess = .true.` flag, which enables the `MLT++` treatment of convection of §7.2 of [Paxton et al. \(2013\)](#). When the stellar envelope is superadiabatic and its atmosphere is radiation-dominated, the convective velocities can approach the speed of sound of the stellar envelope. This forces MESA to take extremely short time steps to try and resolve convection, and makes such envelopes prohibitive to model. The `okay_to_reduce_gradT_excess` flag allows MESA to reduce the severity of the temperature gradient, making the star less superadiabatic, and less prone to small time steps. This is important to the star spot corrections, as it allows them to be numerically stable for a larger range of spot parameters.

3.4.2 Modelling star spots in MESA

A general problem in the modelling of low mass stars is an under-estimation of their radii (López-Morales & Ribas, 2005), and MESA is no exception. Recently, Brown et al. (2022) characterised a sample of ~ 15000 M dwarfs with Gaia parallaxes, radii, and 2MASS K_S measurements from Morrell & Naylor (2019) with a 5th order polynomial, $R(M)$, referred to as the Brown relation. Notably, this relation shifts to the theoretical Baraffe et al. (2015) tracks at $M < 0.121M_\odot$, as the data become increasingly sparse at such low masses. We use this semi-empirical mass-radius relation as the baseline ‘zero mass loss’ benchmark radius for comparison against models.

The difference between singleton MESA models with no mass loss and the Brown relation is shown in Figure 3.6, but the goal is not to reproduce the Brown relation exactly; CV donors are filling their Roche lobes, so are non-spherical. To partially account for this effect, Knigge et al. (2011) introduces a 4.5% radius inflation over isolated stars, and I mirror this approach. Thus, the target radius inflation in Figure 3.6 is 4.5%. However, it must be emphasised that the non-spherical Roche geometry is not solely a geometric effect – the breakdown of spherical symmetry means that the gravitational potential of the star is no longer similar to a point mass, which fundamentally alters the structure of the star near the surface where the effects are largest and increases the stellar radius (Renvoizé et al., 2002). The effects are not captured by this radius correction. However, for the purposes of this work, they can be considered negligible.

To artificially inflate the MESA models to account for the discrepancy with empirical mass radius relationships, and the additional inflation caused by departures from spherical symmetry, I introduce star spots into MESA. Star spots are magnetic phenomena, where the magnetic pressure from concentrations of magnetic field lines provides partial pressure support to the photospheric material, and since spots must remain in pressure equilibrium with the spotted surface, the temperature in a spotted region is reduced by ideal gas laws. As a consequence, the cooler spotted regions emit less black body radiation, inhibiting energy flux out of the stellar interior, and inflating the star.

The star spot model

As MESA is a one-dimensional code and star spots are a two-dimensional phenomenon, spots are modelled using the formulation given by Somers & Pinson-

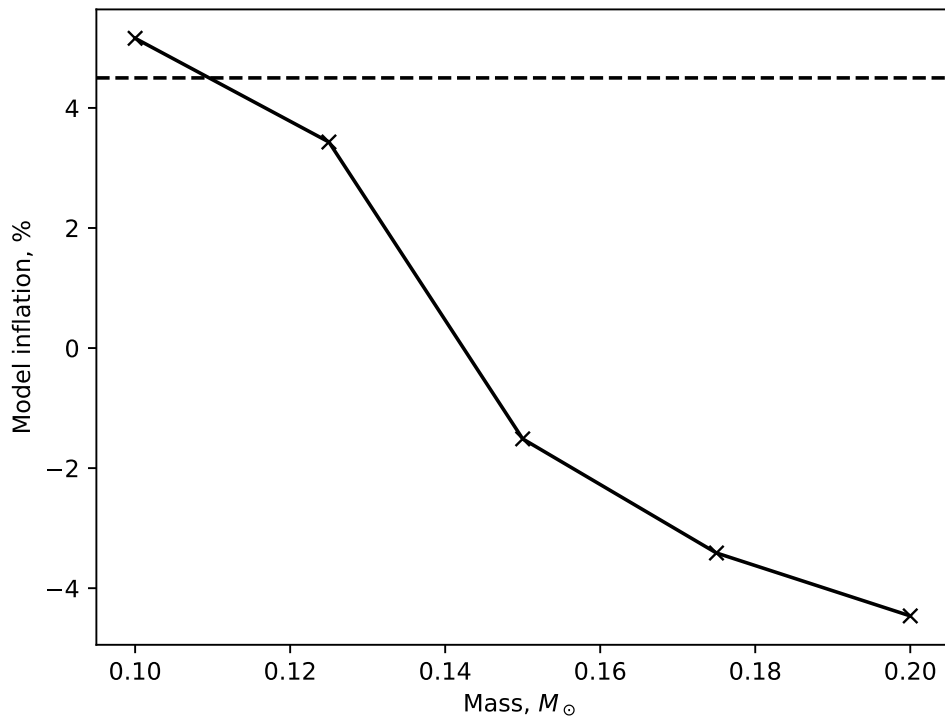


Figure 3.6: Showing the radius inflation of default MESA models over the Brown relation, i.e. $(R_{\text{MESA}} - R_{\text{brown}})/R_{\text{brown}}$. The **horizontal dashed line** is the target radius inflation for MESA models, of 4.5% over the Brown relation. **Crosses** correspond to MESA models at an age of 2 Gyrs.

neault (2015), based on work by Spruit & Weiss (1986). This implementation was done as a collaboration with Meridith Joyce⁸ and Marc Pinsonneault⁹.

Under this spot treatment, two effects are considered: the photosphere is made inhomogeneous by the presence of spots, and convection is inhibited by the presence of a strong magnetic field. In the Somers & Pinsonneault (2015) model, the former effect is enforced by altering the effective temperature to a surface-weighted average of the spotted and unspotted surface, and the latter by augmenting the radiative gradient of the star.

The spots cover a fraction of the stellar surface, f_{spot} , and a temperature contrast of $x_{\text{spot}} = T_{\text{spot}}/T_{\text{amb}}$, where the effective temperature of the spotted surface is T_{spot} , and the effective temperature of the ambient, unspotted surface is T_{amb} . The surface-weighted average of the star, T_{av} is then,

$$T_{\text{av}}^4 = (1 - f)T_{\text{amb}}^4 + f_{\text{spot}}T_{\text{spot}}^4 \quad (3.25)$$

And the altered luminosity, L_{av} , becomes

$$L_{\text{av}} = 4\pi R^2 \sigma_{\text{boltz}} T_{\text{amb}}^4 (1 - f_{\text{spot}} + f_{\text{spot}} \cdot x_{\text{spot}}^4) \quad (3.26)$$

$$L_{\text{av}} = 4\pi R^2 \sigma_{\text{boltz}} T_{\text{amb}}^4 \alpha_{\text{spot}} \quad (3.27)$$

$$L_{\text{av}} = L_{\text{amb}} \alpha_{\text{spot}} \quad (3.28)$$

α_{spot} , the redistribution parameter, and is what actually alters the structure of the star. α is analogous to the blocking area of perfectly black spots, or spots that are completely supported by magnetic pressure.

MESA performs a lookup for the surface pressure from T_{eff} using precalculated boundary condition tables (§3.4.1). I modify the MESA code to perform this lookup with T_{av} .

However, in MESA T_{eff} is not used in the stellar model interior - rather, it uses energies and pressures to calculate structure. Therefore, I alter Equation 3.25 to use pressure instead. Recall the ideal gas equation, for gas in the ambient, unspotted surface, this gas will have pressure and temperature $P_{\text{gas,amb}}$, $T_{\text{gas,amb}}$, density ρ , and mean molecular weight μ . Here, R denotes the gas constant.

$$P_{\text{gas,amb}} = \frac{\rho R}{\mu} T_{\text{gas,amb}} \quad (3.29)$$

⁸Space Telescope Science Institute: Baltimore, MD, US

⁹Ohio State University, OH, US

The spotted and unspotted surfaces are under pressure equilibrium, but the spotted surface pressure has a contribution from gas pressure, $P_{\text{gas,spot}}$, and some contribution from magnetic pressure, $P_{\text{mag,spot}}$. Therefore, we can write

$$P = P_{\text{gas,amb}} = P_{\text{gas,spot}} + P_{\text{mag,spot}} \quad (3.30)$$

$$\frac{\rho R}{\mu} T_{\text{amb}} = \frac{\rho R}{\mu} T_{\text{spot}} + P_{\text{mag,spot}} \quad (3.31)$$

$$P_{\text{mag,spot}} = \frac{\rho R}{\mu} (T_{\text{amb}} - T_{\text{spot}}) \quad (3.32)$$

$$P_{\text{mag,spot}} = (1 - x_{\text{spot}}) P_{\text{gas,amb}} \quad (3.33)$$

$$(3.34)$$

And therefore,

$$P_{\text{gas,spot}} = P_{\text{gas,amb}} - P_{\text{mag,spot}} \quad (3.35)$$

$$P_{\text{gas,spot}} = P_{\text{gas,amb}} - (1 - x_{\text{spot}}) P_{\text{gas,amb}} \quad (3.36)$$

$$P_{\text{gas,spot}} = x_{\text{spot}} P_{\text{gas,amb}} \quad (3.37)$$

However, star spots do not penetrate to the core of the star. To quantify this, rather than fixing x_{spot} and calculating the new pressure at each depth of the star, I calculate the gas pressure difference at the surface of the star, and fix this gas pressure difference for interior layers. As gas pressure rises with depth, a significant difference at the surface quickly becomes insignificant. Rather than directly altering the pressure profile of the star, the radiative gradient, ∇_r , at each depth is modified. MESA then uses ∇_r to compute a self-consistent pressure profile for the star.

$$\alpha_{\text{spot,i}} = 1 - f_{\text{spot}} + f_{\text{spot}} \cdot x_{\text{spot,i}}^4 \quad (3.38)$$

$$\nabla'_{r,i} = \frac{\nabla_{r,i}}{\alpha_{\text{spot,i}}} \quad (3.39)$$

This is analagous to the method employed in [Somers & Pinsonneault \(2015\)](#). Values of f_{spot} and x_{spot} can be passed to MESA as user-configured parameters to define the degree of spotting. Figure 3.7 shows the radii of main sequence stellar models at 2 Gyrs, and $0.15M_{\odot}$ with progressively more spots.

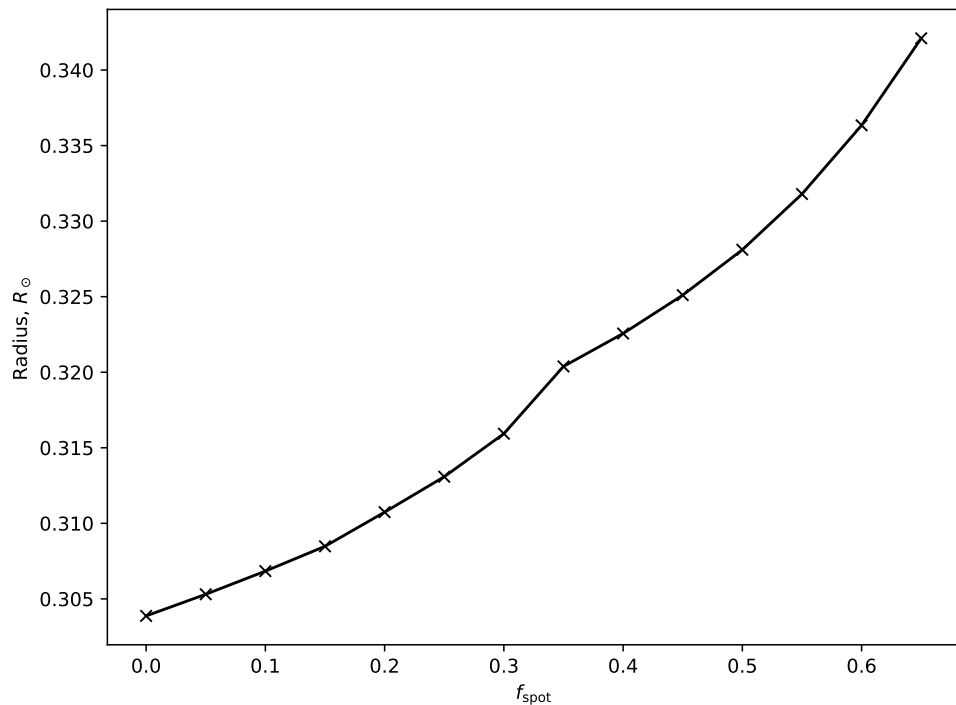


Figure 3.7: Showing how model radius varies as a function of spot coverage for a $0.15M_{\odot}$ star. Here, spots are perfectly black ($x_{\text{spot}} \equiv 0$), and the radius is extracted at 2 Gyrs. Evaluated MESA models are shown as **black crosses**, and joined by a **black line** to guide the eye.

3.4.3 Optimising mass loss rate to donor observations

The mass loss rate required to match donor observations can now be found. As the inflation of the donor increases monotonically with increasing mass loss, the bisection method is used to precisely and accurately optimise mass loss. When evaluating a proposed \dot{M} , two other key model parameters must be set. First the mass loss over a period of 1 Gyr is calculated. The initial model mass is then this expected 1 Gyr mass, in addition to the target mass. Doing this allows for some lead time before the model reaches the desired stellar mass, and gives the star time to reach both the main sequence, and settle to its equilibrium radius. The appropriate f_{spot} for the target mass is also calculated, and the model fixes f_{spot} at this value. Fixing f_{spot} this way accounts for the donor having comparable τ_{KH} and $\tau_{\dot{M}}$, which would not allow the star to properly adjust to variable spot parameters. Finally, to find the uncertainty in \dot{M} , two further combinations of donor mass and radius were evaluated for each system: ($M = \bar{M} + \sigma_M$, $R = \bar{R} + \sigma_R$), and ($M = \bar{M} - \sigma_M$, $R = \bar{R} - \sigma_R$). The donor mass and radius are highly correlated (typical cross-correlation coefficient values for the eclipse modelled systems later analysed for this work are ~ 0.9995), so this is reasonable approximation to make.

3.4.4 Determining AML rate from system parameters

Finally, the mass loss can be converted to an angular momentum loss rate. To do so, I will begin by defining the total AML from the system, \dot{J} , as the sum of the typical system AML, \dot{J}_{sys} (i.e. gravitational and magnetic braking), and CAML, \dot{J}_{CAML} ,

$$\dot{J} = \dot{J}_{\text{sys}} + \dot{J}_{\text{CAML}} \quad (3.40)$$

[King & Kolb \(1995\)](#) set a general formulation of CAML as some fraction of donor mass loss,

$$\frac{\dot{J}_{\text{CAML}}}{J} = \nu \frac{\dot{M}_{\text{donor}}}{M_{\text{donor}}} \quad (3.41)$$

where the form of ν depends on the CAML prescription being used.

The form of \dot{J}_{sys} in the presence of CAML is also given in [King & Kolb \(1995\)](#).

$$\frac{\dot{J}_{\text{sys}}}{J} = D \frac{\dot{M}_{\text{donor}}}{M_{\text{donor}}} \quad (3.42)$$

$$D = \left(\frac{5}{6} - \frac{\zeta}{2} \right) - \frac{M_{\text{donor}}}{M_{\text{wd}}} + \alpha \left(\frac{M_{\text{donor}}}{M_{\text{wd}}} - \frac{1}{3} \frac{M_{\text{donor}}}{M_{\text{wd}} + M_{\text{donor}}} \right) - \nu \quad (3.43)$$

α is the mass retention factor, $\dot{M}_{\text{total}}/\dot{M}_{\text{donor}}$. Following the findings of [McAllister et al. \(2019\)](#), there is no growth of the white dwarf over time and thus $\alpha \equiv 1$. ζ is the mass-radius exponent of the donor star, $\frac{d(\ln R_{\text{donor}})}{d(\ln M_{\text{donor}})}$.

The final equation needed is for the total J of the binary. This is simply given by

$$J_{\text{tot}} = M_{\text{wd}} M_{\text{donor}} \sqrt{\frac{Ga}{M_{\text{wd}} + M_{\text{donor}}}} \quad (3.44)$$

After substituting $\alpha = 1$, \dot{J} as a function of component masses, a , \dot{M}_{donor} , and ζ , is found

$$\dot{J} = J \frac{\dot{M}_{\text{donor}}}{M_{\text{donor}}} \cdot (D + \nu) \quad (3.45)$$

$$\dot{J} = M_{\text{wd}} \dot{M}_{\text{donor}} \sqrt{\frac{Ga}{M_{\text{wd}} + M_{\text{donor}}}} \left(\left(\frac{5}{6} - \frac{\zeta}{2} \right) - \frac{1}{3} \frac{M_{\text{donor}}}{M_{\text{wd}} + M_{\text{donor}}} \right) \quad (3.46)$$

As a product of the eclipse modelling and MESA modelling, all the necessary quantities for Equation 3.46 are known. Therefore, the secular AML rate for the modelled CV systems can be deduced.

Chapter 4

Three CVs with peculiar white dwarf colours

Table 4.1: Summary of observational information for the 3 CVs of this chapter.

System name	RA	Dec	g'	T_0 , BMJD, UTC	Period, days
ASASSN-16kr	22:05:59.48	-34:14:33.9	18.0	57658.22013(1)	0.061285933(1)
ASASSN-17jf	20:29:17.13	-43:40:19.8	20.2	58754.12003(3)	0.0567904(7)
SSS111126	05:22:10.00	-35:05:30.0	18.9	58755.36437(1)	0.06219343(1)

The work presented in this chapter was published as [Wild et al. \(2021\)](#), in the Monthly Notices of the Royal Astronomical Society under the title *System parameters of three short period cataclysmic variable stars* by Wild, Littlefair, Ashley, Breedt, Brown, Dhillon, Dyer, Green, Kerry, Marsh, Parsons, and Sahman. The following is my own work, unless otherwise cited.

This chapter concerns the three systems, ASASSN-16kr, ASASSN-17jf, and CRTS SSSJ0522–3505 J052210-350530 (hereafter SSSJ0522–3505), which proved challenging to model. Table 4.1 summarises the right ascension, declination, magnitude, and ephemeris of each CV.

4.1 Prior observations

New data were observed for each of these three systems, detailed in §2.4. Table 2.7 describes the ASASSN-16kr observations, Table 2.9 describes ASASSN-17jf, and Table 2.17 describes SSSJ0522–3505. However, in each case there were prior observations, described here.

ASASSN-16kr

ASASSN-16kr (a.k.a. MASTER J220559.40-341434.9) was discovered by the All-Sky Automated Survey for Supernovae (ASASSN) on 11 September 2016, and observed by the MASTER network on the 19th (ATel #9509 and #9510), both at $\sim 14^{\text{th}}$ magnitude. Initially classified as an SS Cyg type object due to its low outburst amplitude (vsnet alert #20189), subsequent observations confirmed eclipses and superhumping behaviour (vsnet alerts #20190, #20196, #20206; [Kato et al. 2017](#)).

Time-resolved photometry detected superhumps and eclipses, and [Kato et al. \(2017\)](#) calculated an orbital period of 0.0612858 ± 0.0000003 days, and a superhump period of 0.061999 ± 0.000067 days. [Kato et al. \(2009\)](#) demonstrated that

superhump periods vary systematically, and can be categorised into stages: stage A, an initial growth stage with a long period; stage B, a developed stage with a varying period; and stage C, with a shorter and more constant period. This system is noted by [Kato et al. \(2017\)](#) as being in the transition from stage B to stage C, though this is suggested to possibly be due to a suspect measurement at the start of the outburst they observed.

ASASSN-17jf

ASASSN-17jf was confirmed as eclipsing by Berto Monard (vsnet alert #21257) between 14 and 17 July 2017. The system was initially observed with a mean unfiltered magnitude of ~ 15.5 outside eclipse, with an eclipse depth of ~ 1 magnitude. From these observations, an orbital period of 0.0578 ± 0.0003 days, and a rough superhump period of 0.0565 days was derived.

SSSJ0522-3505

SSSJ0522–3505 was first observed by the CRTS on 28 February 2005, and as recently as 11 November 2019 ([Drake et al., 2008](#)). These data show high variability, and outbursts ~ 6 months apart. High time resolution light curves taken by [Paterson et al. \(2019\)](#) show an eclipse depth of ~ 1.5 magnitudes and an orbital period of 0.0622 ± 0.0005 days.

4.2 Eclipse modelling

The observations were reduced, analysed for system ephemerides c.f. §3.2, and phase folded for eclipse modelling following §3.3.1.

Phase-folded eclipse modelling gave good results in all three systems, each light curve being well-modelled with small residuals; the final optimisations are shown here in Figures 4.1 - 4.13. The Gaussian processes describing flickering in the systems were consistent with little to no variability, indicating that almost all the scatter in the flux residuals could be fully described by the uncertainty in flux measurement. However, when fitting white dwarf model atmospheres to the observed white dwarf fluxes, the resulting fits were not satisfactory. The bulk of this chapter discusses this poor fit, its possible causes, and its implications.

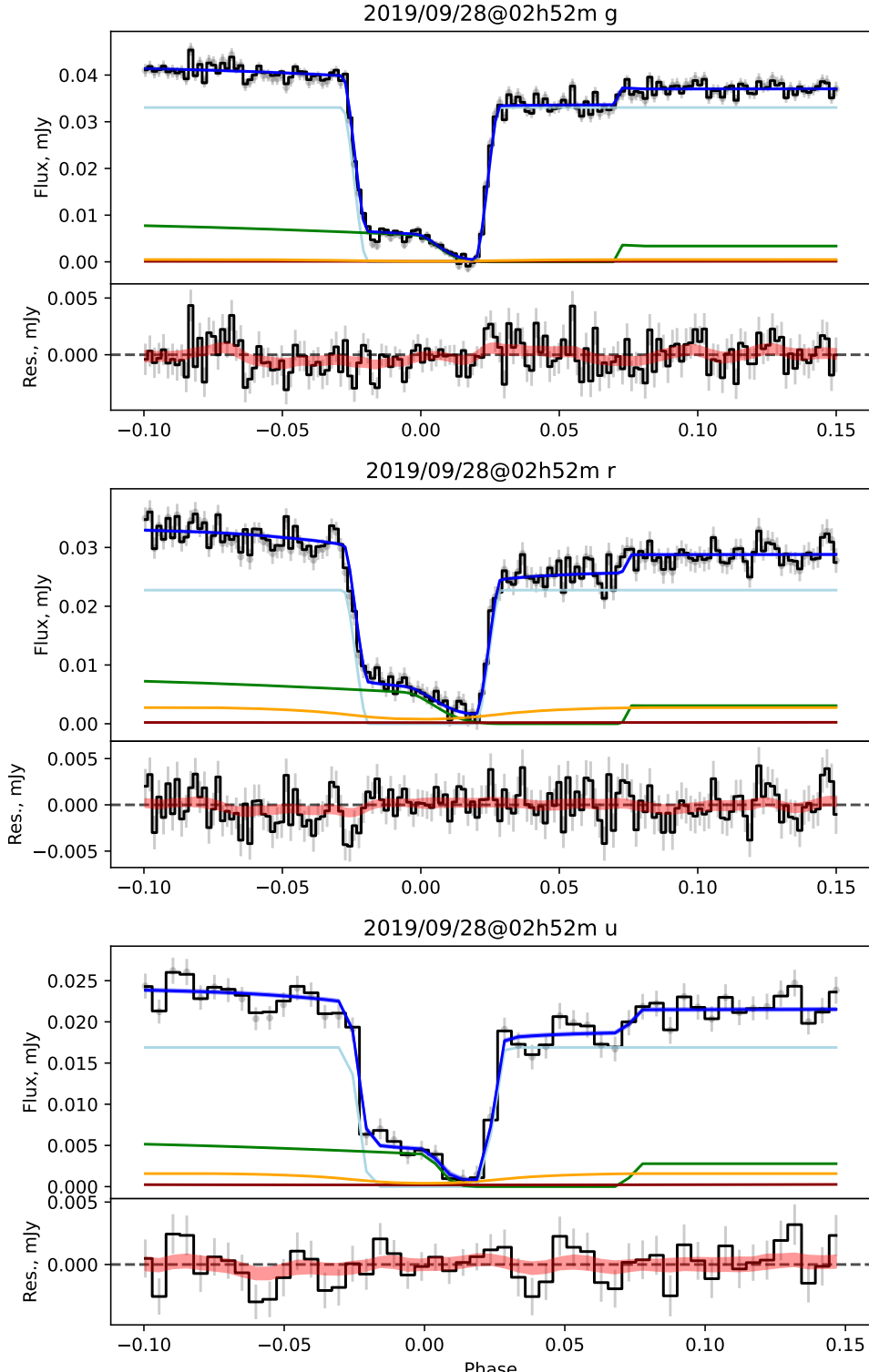


Figure 4.1: ASASSN-17jf light curve models. *Top:* grey points are the observed flux, and note that the photometric system is the SDSS as per §2.3.4; black line is the observed flux, with the mean Gaussian process sample subtracted; the dark blue line is the mean light curve model, and the blue band is the standard deviation on this in the MCMC chain. The components of the model are also shown: the light blue line is the white dwarf flux, green line is the bright spot, orange line is the disc, and the red line is the donor. *Bottom:* The residuals between the data and model are plotted as the black line, with grey error bars. The Gaussian process 1-sigma region is shown as a red band.

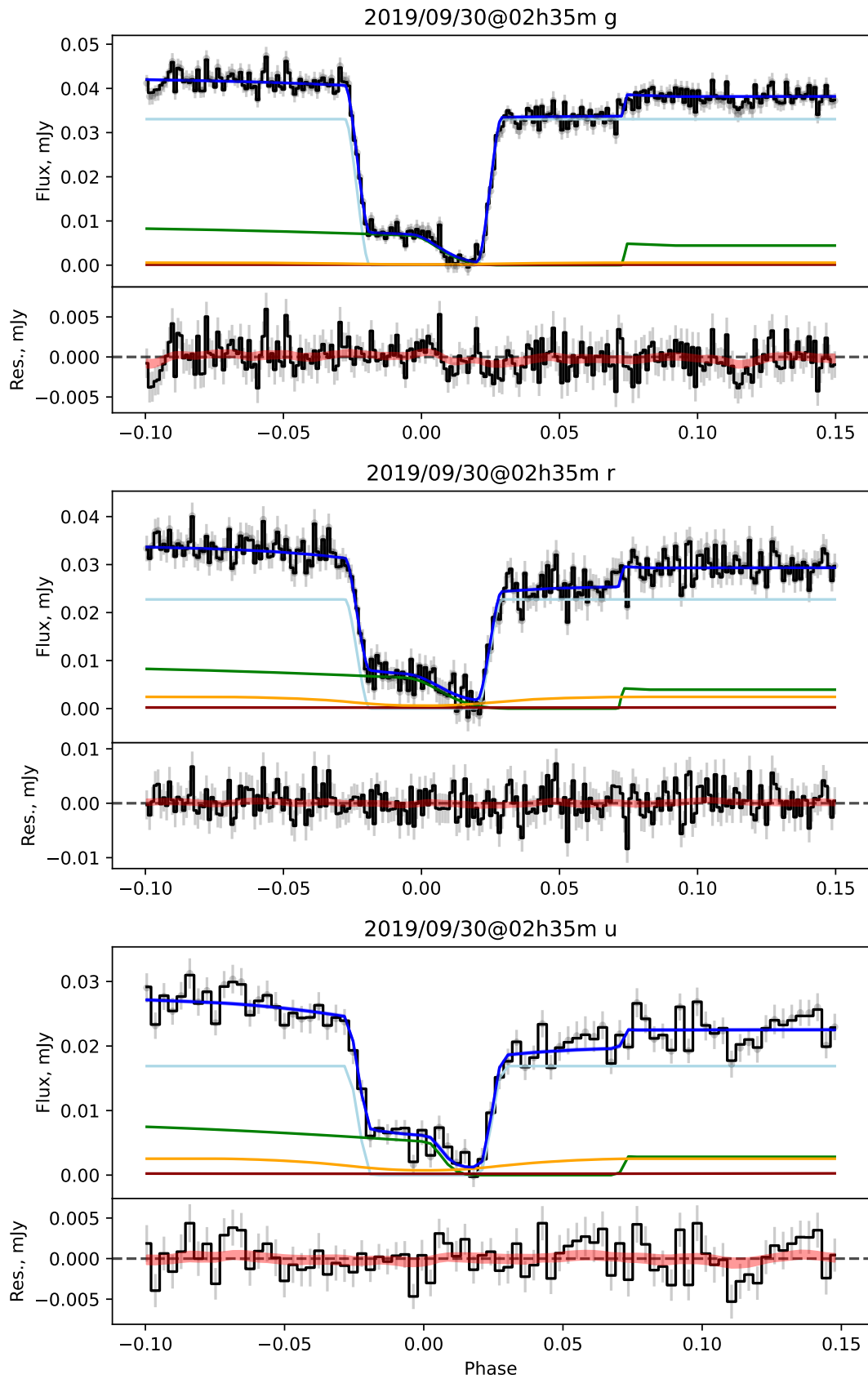


Figure 4.2: ASASSN-17jf light curve models (cont.)

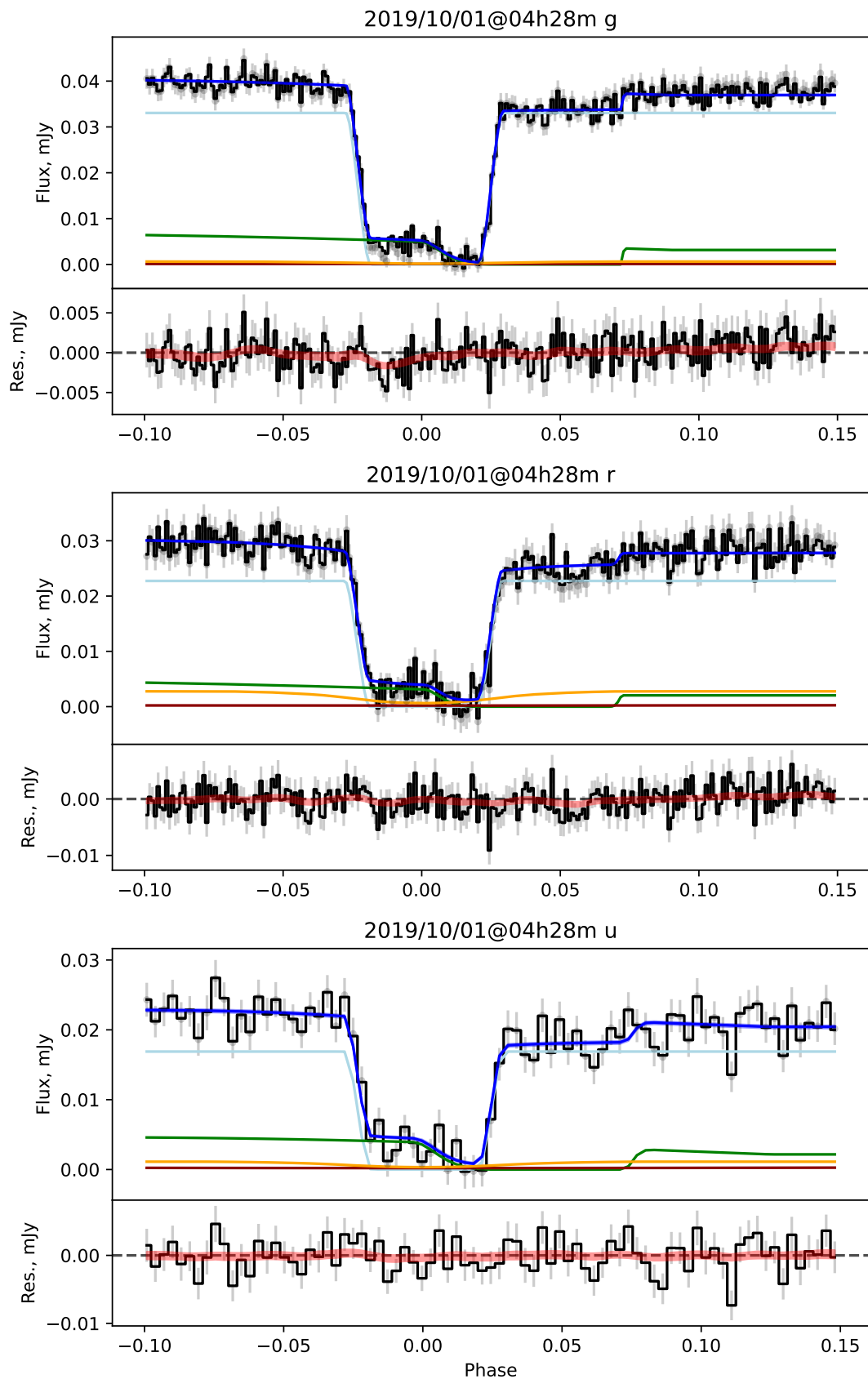


Figure 4.3: ASASSN-17jf light curve models (cont.)

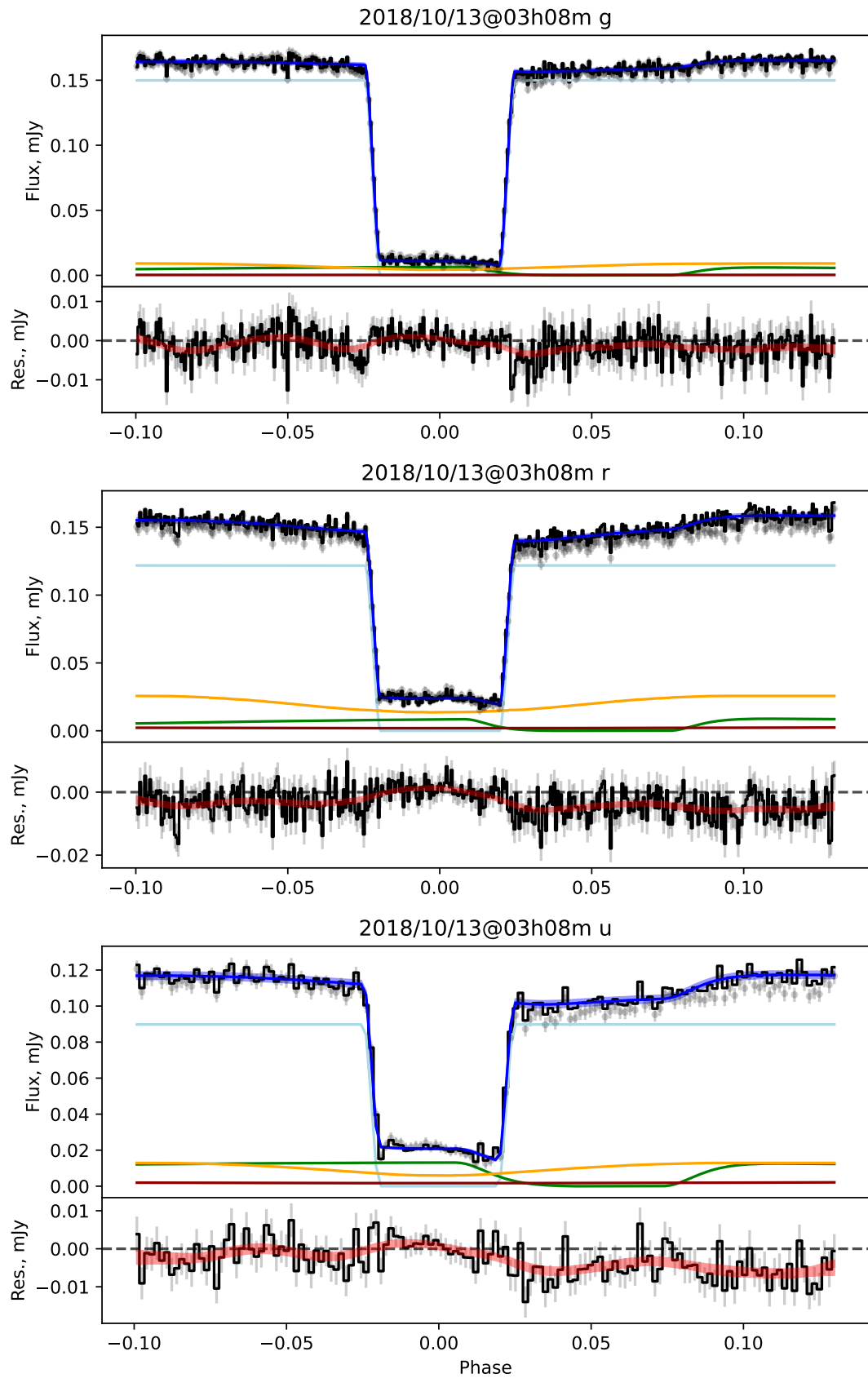


Figure 4.4: ASASSN-16kr light curve models. Symbols are the same as Figure 4.1

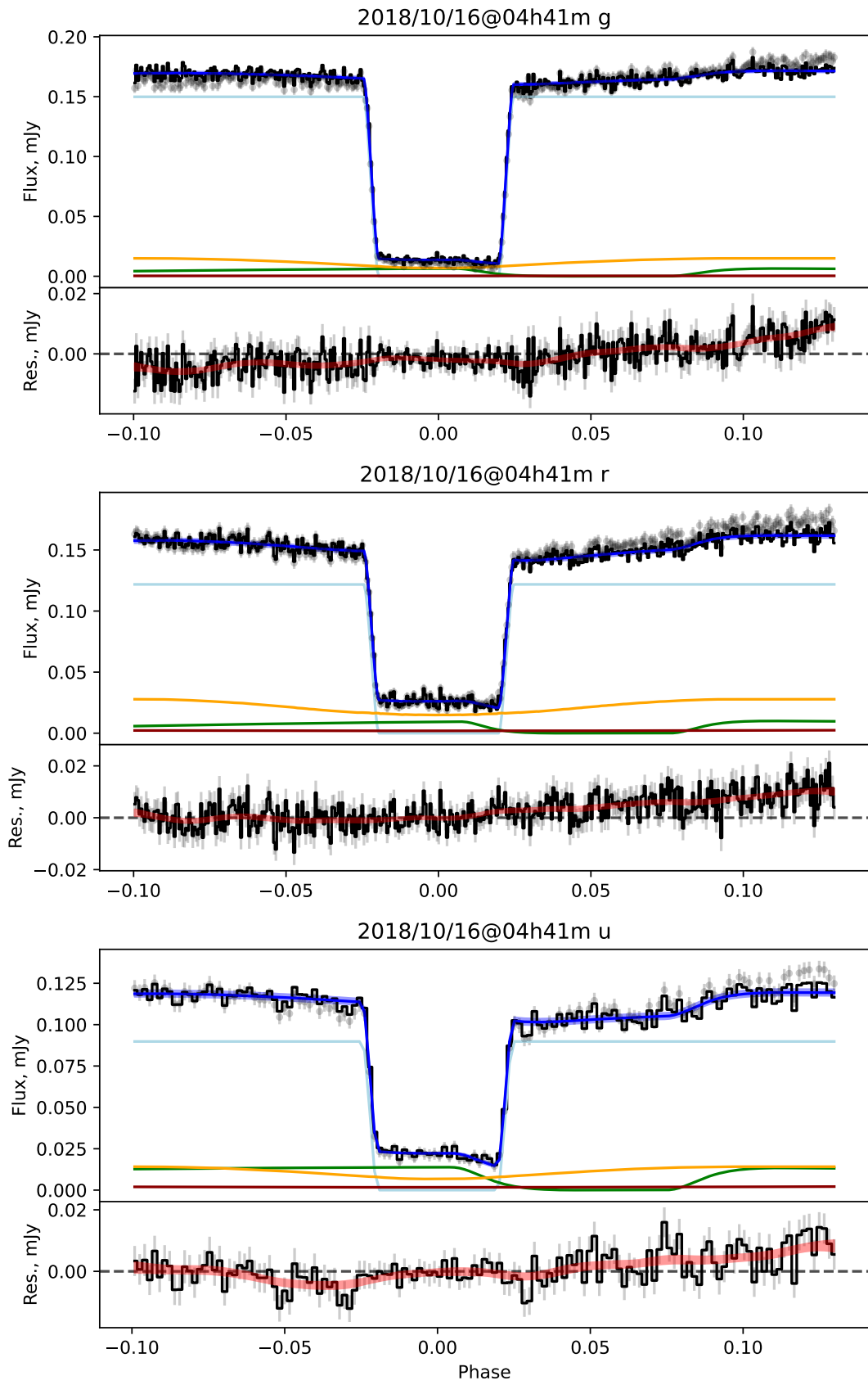


Figure 4.5: ASASSN-16kr light curve models (cont.)

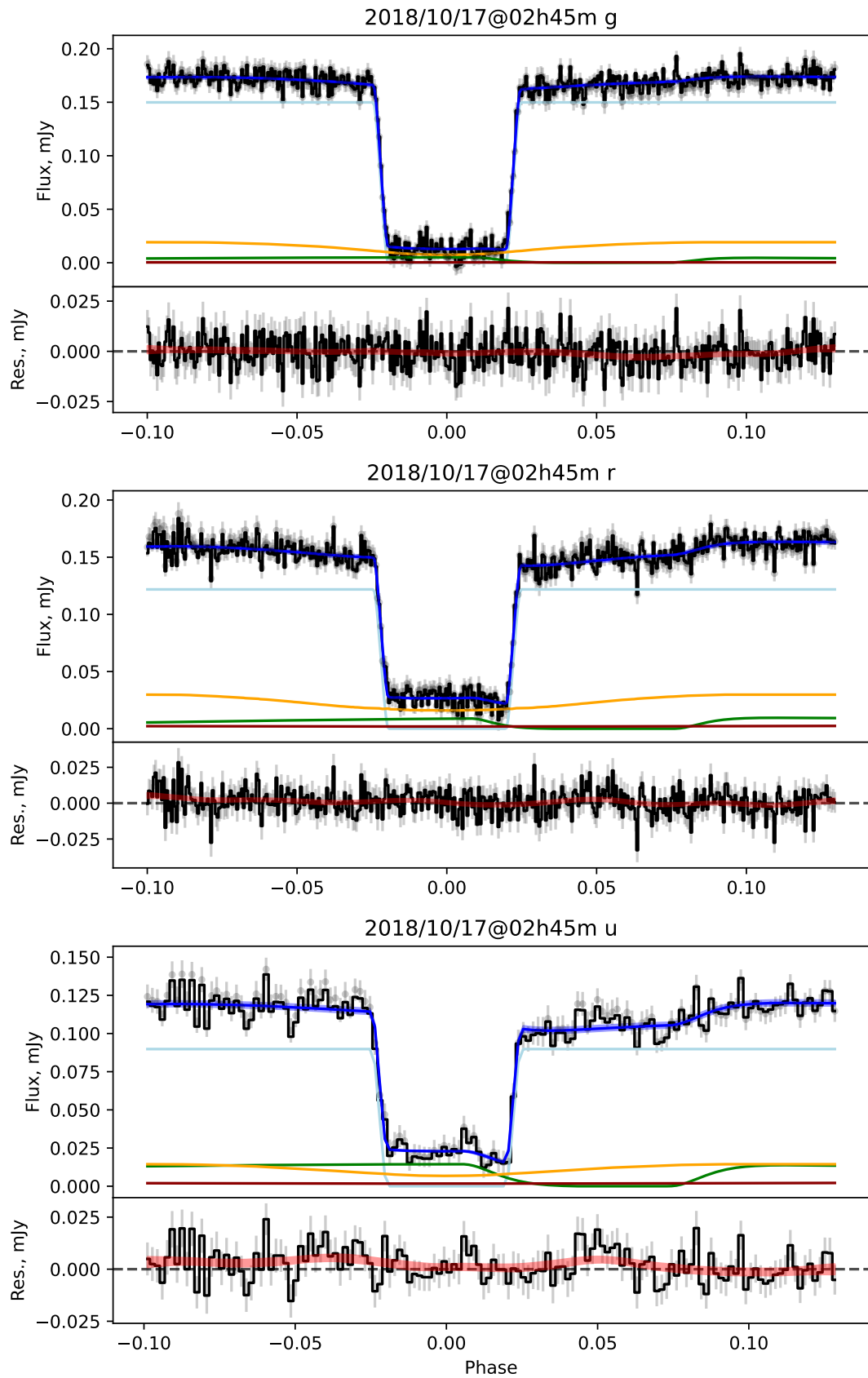


Figure 4.6: ASASSN-16kr light curve models (cont.)

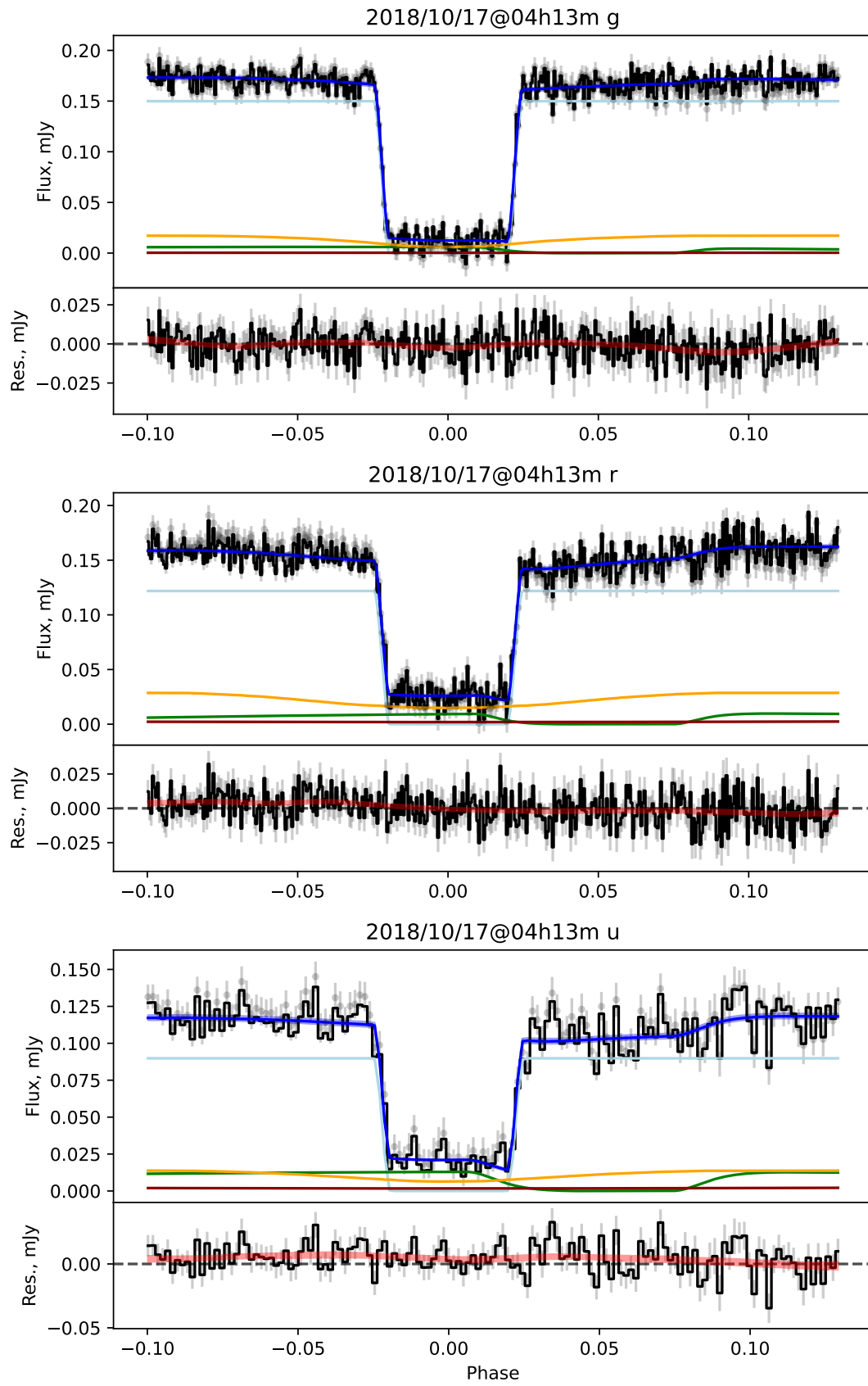


Figure 4.7: ASASSN-16kr light curve models (cont.)

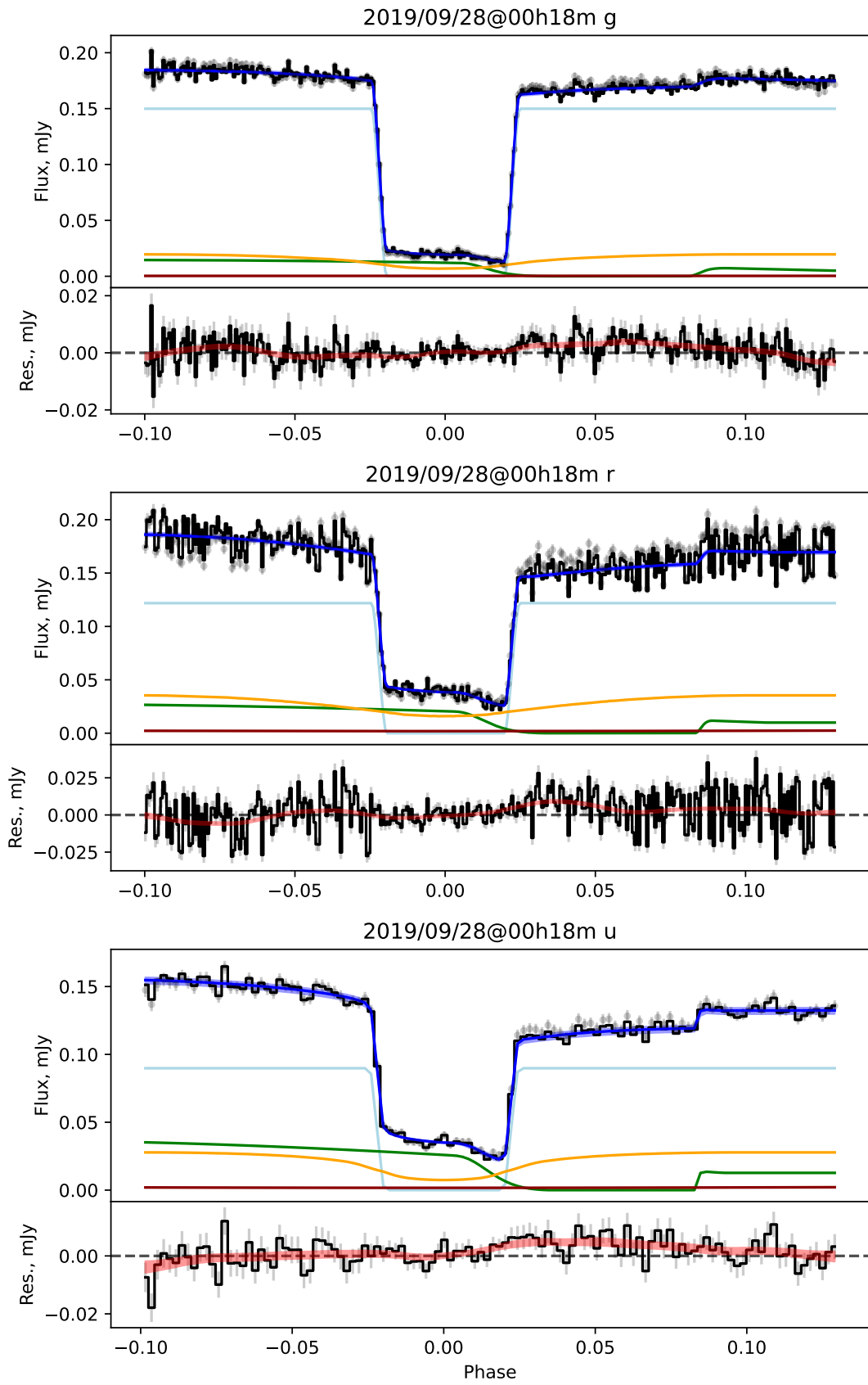


Figure 4.8: ASASSN-16kr light curve models (cont.)

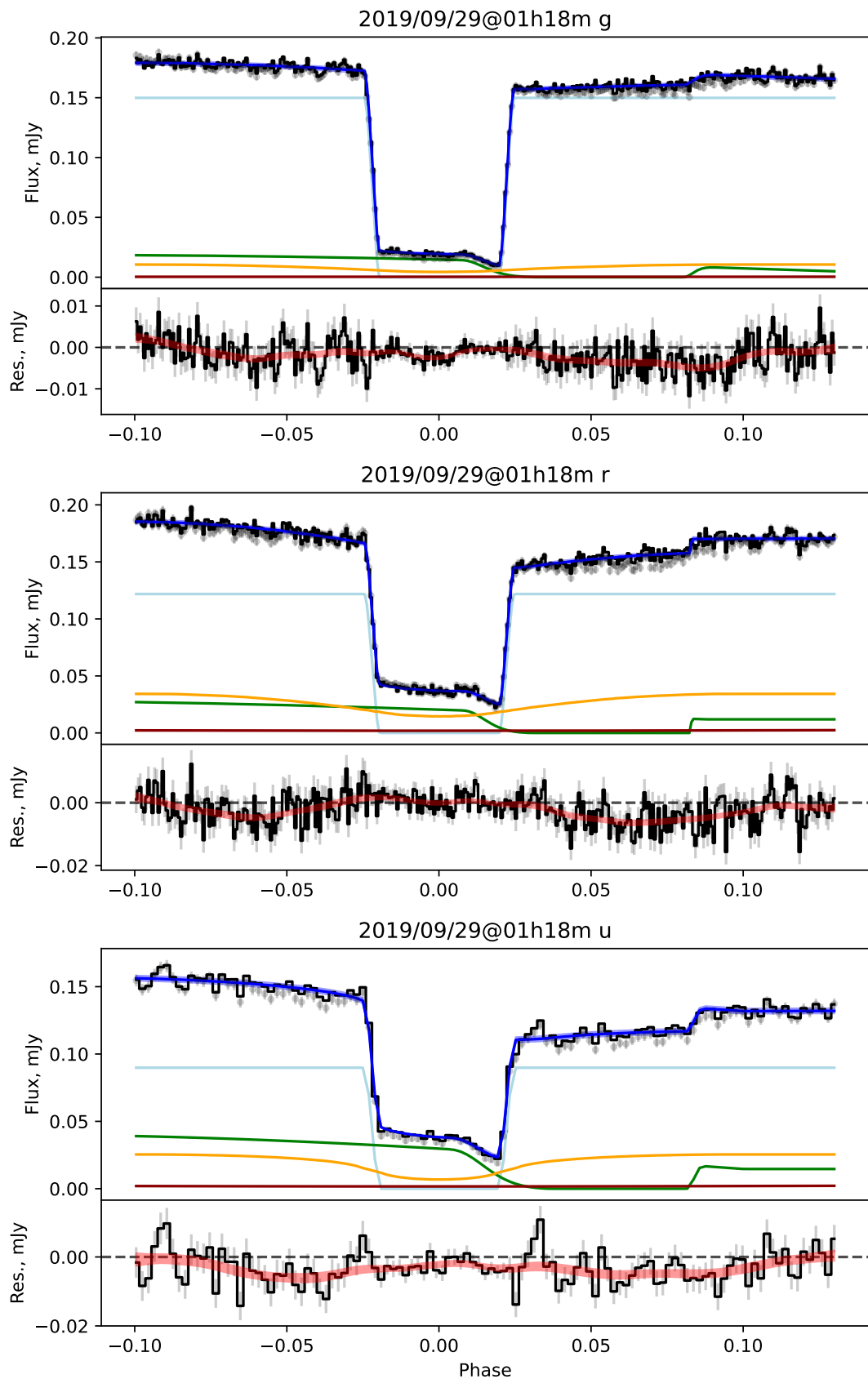


Figure 4.9: ASASSN-16kr light curve models (cont.)

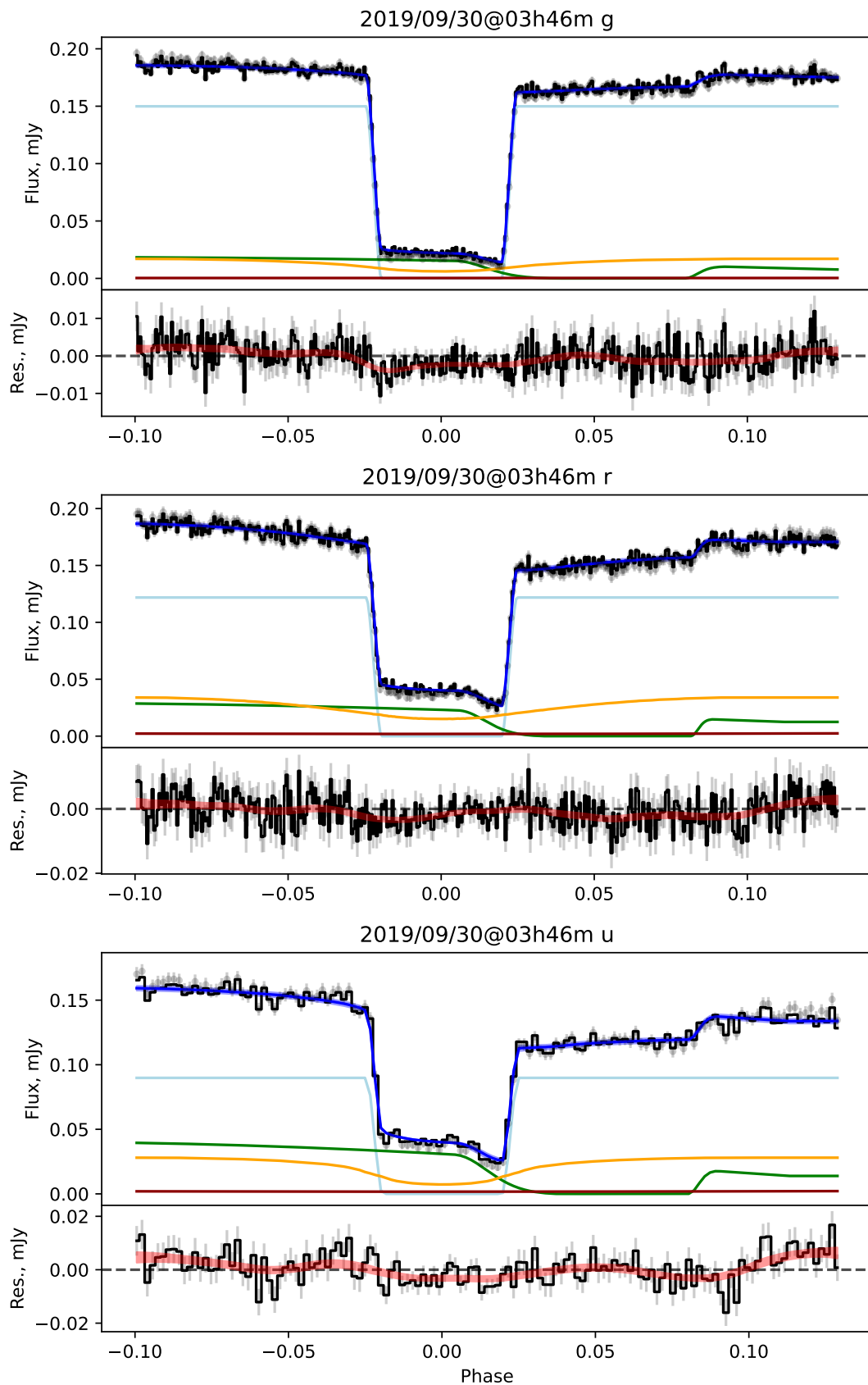


Figure 4.10: ASASSN-16kr light curve models (cont.)

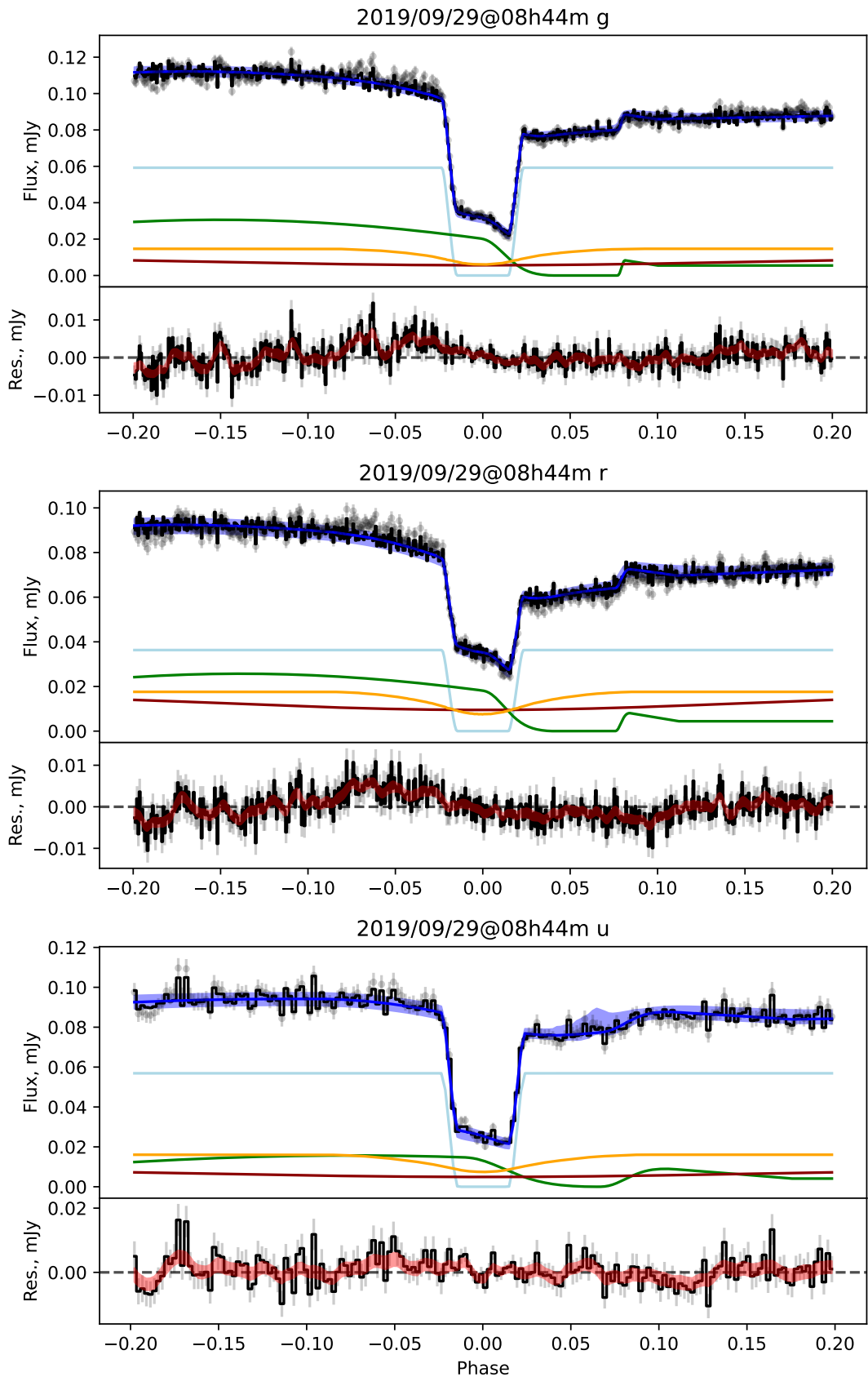


Figure 4.11: SSSJ0522–3505 light curve models. Symbols are the same as Figure 4.1

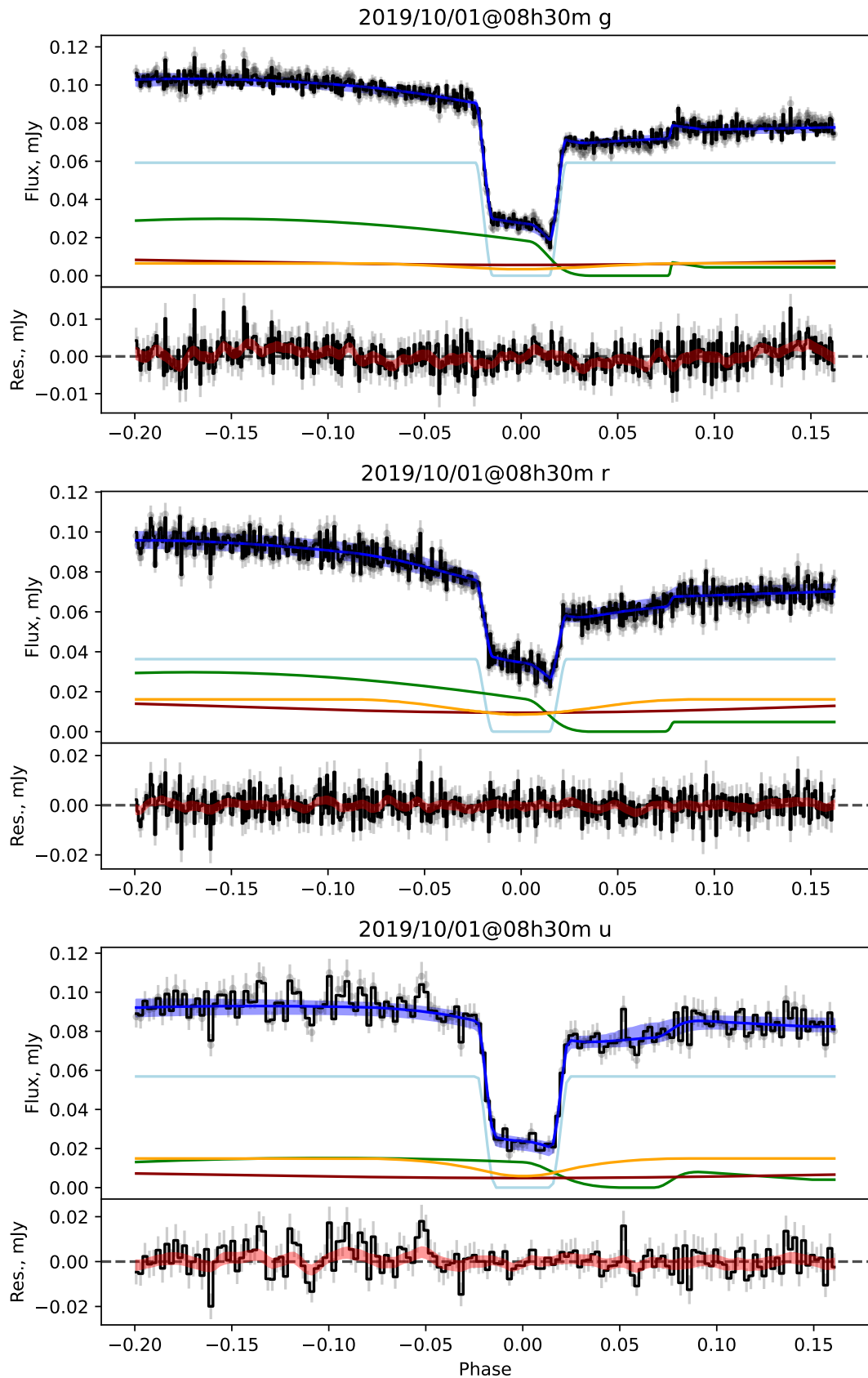


Figure 4.12: SSSJ0522-3505 light curve models (cont.)

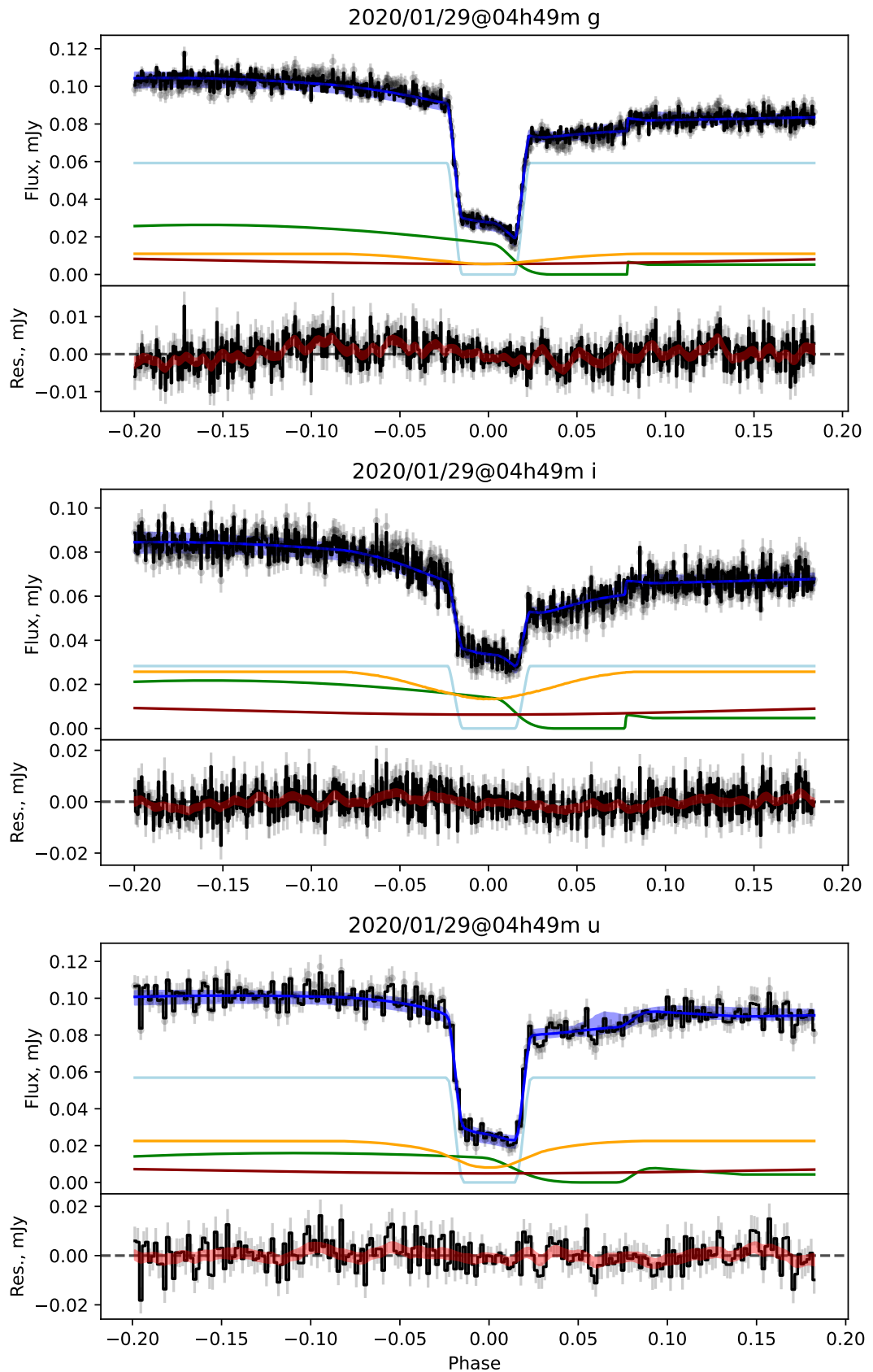


Figure 4.13: SSSJ0522-3505 light curve models (cont.)

4.3 White dwarf atmosphere fits

The two values of $\log(g)$ produced by modelling – the first from fitting the white dwarf fluxes to model atmospheres, and the second from combining T_{eff} and P with the light curve parameters – did not fall within 1σ of each other in any of these three systems. In ASASSN-17jf and SSSJ0522–3505, the white dwarf atmosphere fit converged close to the minimum surface gravity allowed by the coverage of our models, $\log(g) = 7.0$. The second $\log(g)$, from light curve fitting, indicated values for each system of 8.10 ± 0.04 and 8.30 ± 0.03 , respectively. When analysing ASASSN-16kr, flux fitting gave a more reasonable $\log(g) = 8.21 \pm 0.13$, but the second $\log(g)$ still gave a significantly higher $\log(g) = 8.59 \pm 0.03$, a difference of $\sim 3\sigma$.

This is concerning, as the two $\log(g)$ should be consistent with one another for each system. Comparison of the measured white dwarf colours to the [Bergeron et al. \(1995\)](#) model grids in Figures 4.14, 4.15, and 4.16, reveals that the measured colours of the white dwarfs lie outside the colour space of the models. This is the origin of the discrepancies in $\log(g)$ obtained with the two methods for ASASSN-17jf and SSSJ0522–3505, but ASASSN-16kr is loosely consistent with the rightmost cooling track. However, the observed flux of a white dwarf of this radius is too high for the observed Gaia parallax, pushing the model fits to smaller, higher gravity model atmospheres.

A likely cause for this issue would be an error in photometric calibration, causing a corresponding error in white dwarf fluxes. However, this is unlikely to be the source of the problem, for the reasons explained in §2.3.4, and inspection of the figures above also rules out poor light curve fits as the cause of this problem. The most plausible explanation for the fact that our measured white dwarf fluxes do not lie inside the model grids, is that the change in brightness during white dwarf ingress/egress is contaminated by an additional source of light – for example a boundary layer close to the white dwarf surface. The implications of this for our system parameters is explored in §4.5.1.

That the white dwarf colours do not lie on the model grids also raises questions about the accuracy of the white dwarf temperatures. To try and quantify the impact on T_{eff} , two additional optimisations of model parameters to the white dwarf fluxes were performed. In one approach, a Gaussian prior on $\log(g)$ using the estimate from the light curve modelling was used, and all available flux measurements were fit simultaneously. In a second approach I fit the white dwarf flux in

each band independently using the same prior on $\log(g)$ and the Gaia prior on π . Since these independent fits use no colour information, E(B-V) is only constrained by the prior, but is retained as a nuisance parameter and T_{eff} is marginalised over E(B-V). Figure 4.17 shows the T_{eff} posteriors from the individual fits for the three systems.

Figure 4.17 shows little sign of a consistent discrepancy over the three observed CVs. The u' band in ASASSN-16kr and SSSJ0522–3505 suggests a cooler temperature than the other bands, but lies in between the r' and g' in ASASSN-17jf.

Each approach gives a different distribution for T_{eff} . To avoid confusion, results of each individual fit are not reported, instead the overall temperature ranges for each system are given. ASASSN-16kr T_{eff} estimates ranged from 10200K to 12150K, and ASASSN-17jf estimates from 8330K to 12710K. The SSSJ0522–3505 fits that used all four observed fluxes both converged on ~ 22700 K, but the single-flux fits all resulted in wide posterior distributions covering 25000 – 90000K, with very weak peaks in the ~ 30000 – 50000K range, seen in Figure 4.17.

In all three systems, the figures reported in Table 4.2 are the T_{eff} produced by the constrained $\log(g)$ fit with all fluxes simultaneously. The $\log(g)$ reported are the values found from the light curve parameters.

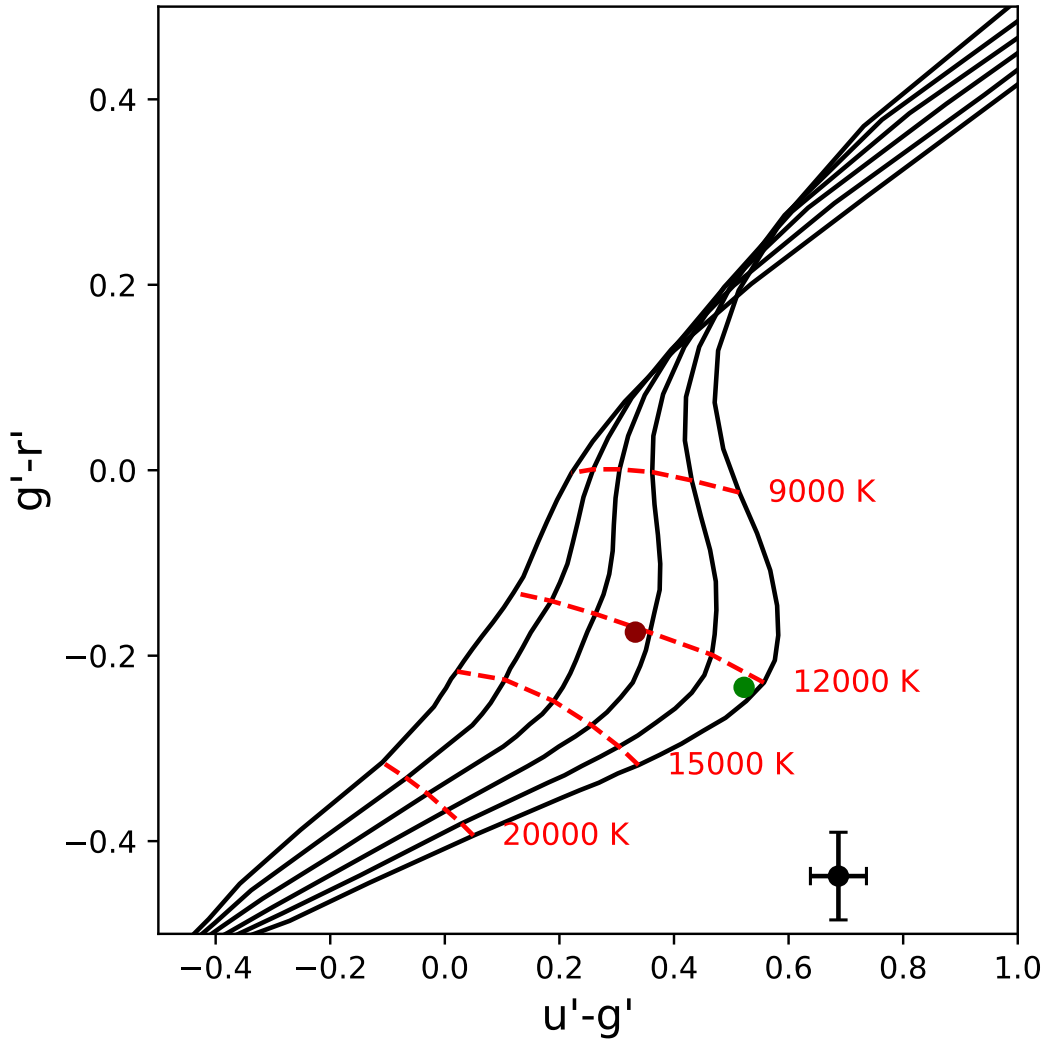


Figure 4.14: The white dwarf model atmosphere fits for ASASSN-17jf. **Green circle:** Best fit with uniform prior on $\log(g)$. **Red circle:** Best fit with the prior $\log(g) = 8.10 \pm 0.04$. The observations are shown as the **black point and error bars**. **Solid black lines** are white dwarf model cooling tracks, increasing in $\log(g)$ to the left. **Red dashed lines** are isothermal tracks for different $\log(g)$.

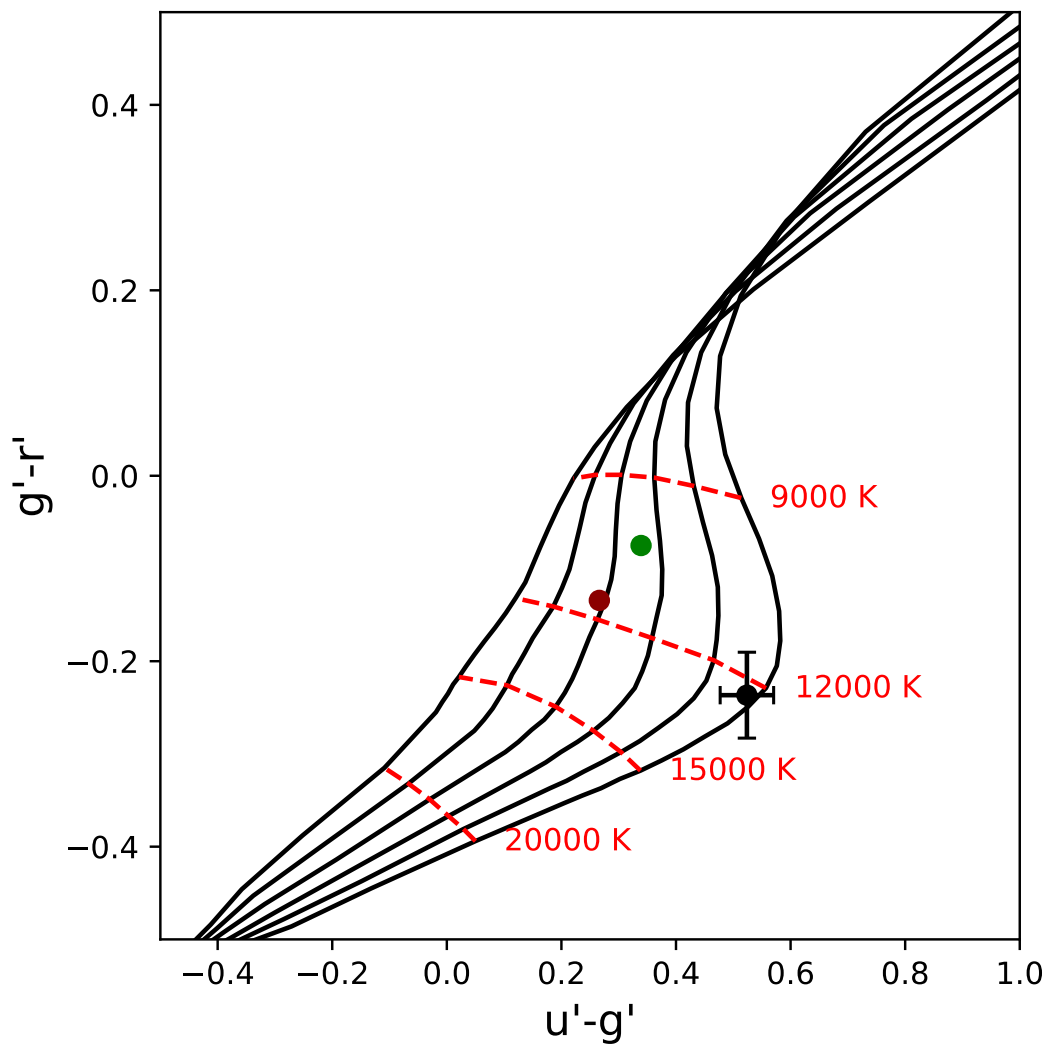


Figure 4.15: The white dwarf model atmosphere fits for ASASSN-16kr. The **red circle** is the best fit with a prior of $\log(g) = 8.52 \pm 0.02$. Symbols are the same as Figure 4.14.

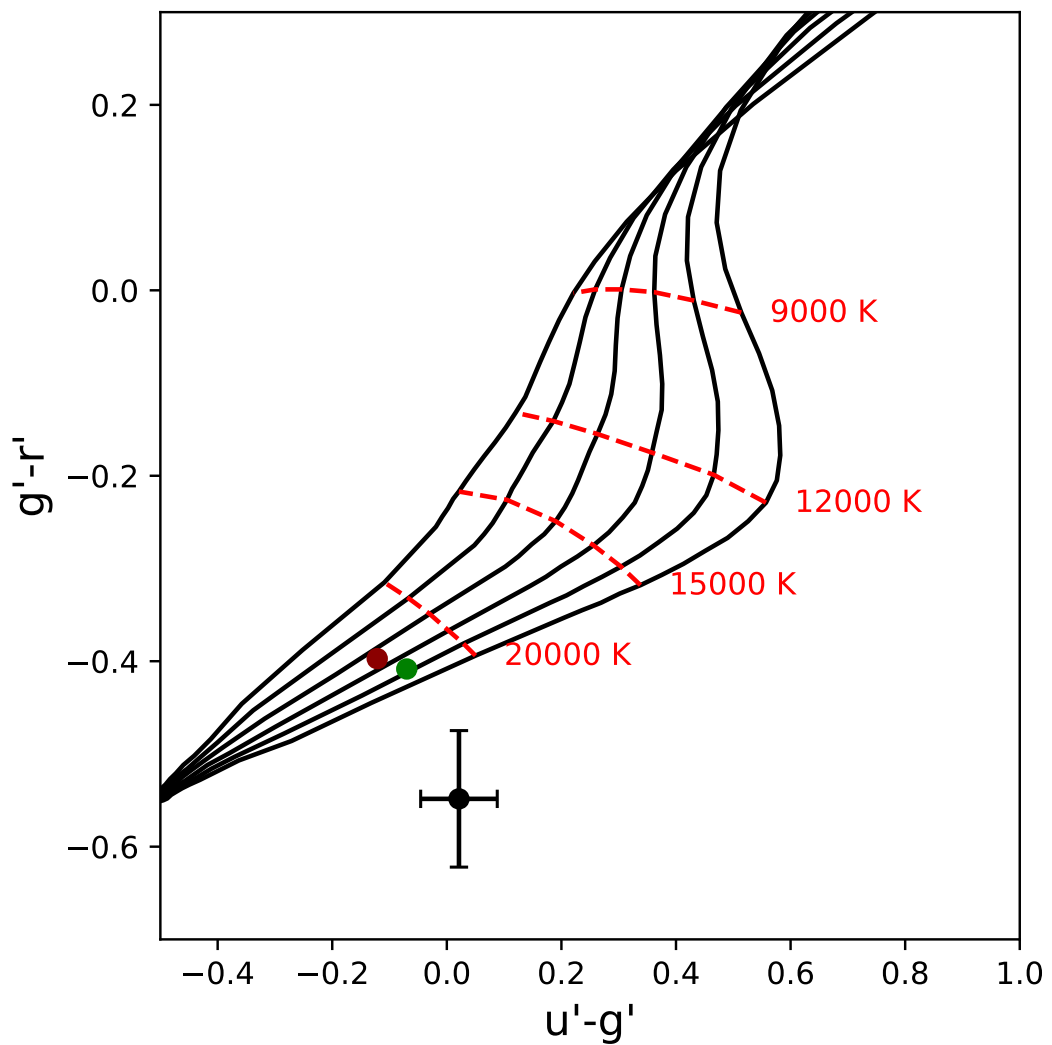


Figure 4.16: The white dwarf model atmosphere fits for SSSJ0522–3505. The **red circle** is the best fit with a prior of $\log(g) = 8.28 \pm 0.04$. Symbols are the same as Figure 4.14.

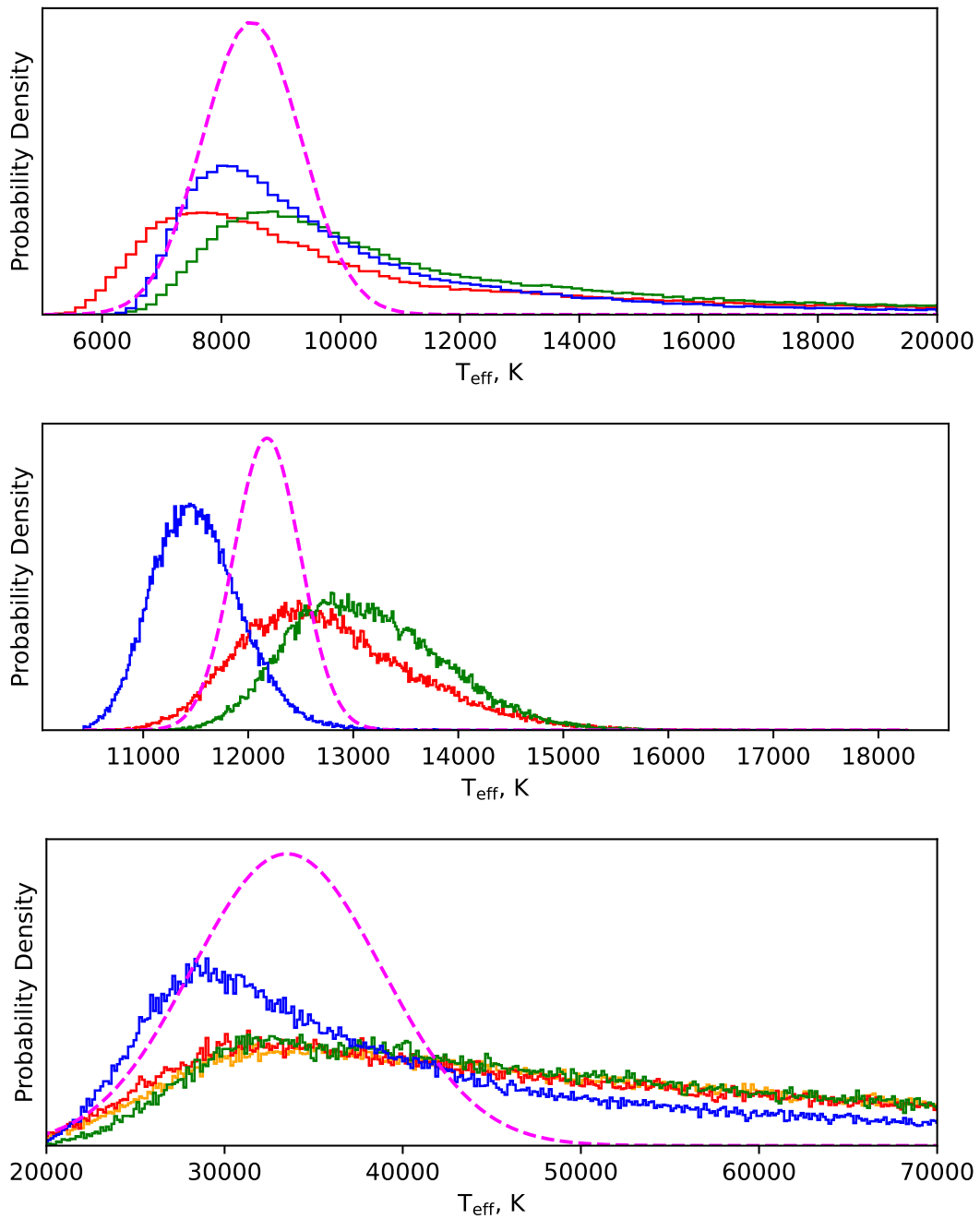


Figure 4.17: The result of fitting white dwarf model atmospheres to each photometric band independently. **Blue solid line:** u' band, **Green solid line:** g' band, **Red solid line:** r' band. The joint distribution between all bands is characterised in each case by the best fit Gaussian (**magenta dashed lines**). *Top:* ASASSN-17jf, joint $T_{\text{eff}} = 8330 \pm 780 \text{ K}$; *Middle:* ASASSN-16kr, joint $T_{\text{eff}} = 12150 \pm 300 \text{ K}$; *Bottom:* SSSJ0522-3505, joint $T_{\text{eff}} = 33300 \pm 5200 \text{ K}$.

4.4 System Parameters

A poorly constrained white dwarf model might reasonably be expected to cast doubt on the final system parameters, as the white dwarf temperature in particular is used to find the correct white dwarf mass-radius relationship. Fortunately, the effect of the uncertain white dwarf temperatures on the system parameters, most importantly on M_{wd} , is mostly negligible. For example, increasing T_{eff} for ASASSN-17jf from 8000K to 12000K only changes M_{wd} by $0.001M_{\odot}$, compared to our statistical uncertainty of $0.031M_{\odot}$. Even a large uncertainty in T_{eff} only has a minor impact on the system parameters; for example a change in the white dwarf temperature for SSSJ0522–3505 from 10000K to 20000K only changes M_{wd} by $0.02M_{\odot}$, comparable with the measurement uncertainty. The system parameters are reported in Table 4.2.

ASASSN-16kr has a recorded superhump period, and now also a q measurement. It can therefore be used to calibrate the superhump period excess, ϵ vs. q relationship, as done in [McAllister et al. \(2019\)](#), though with a more extreme mass ratio system than was previously available. The system was not confidently classed as exhibiting stage B or C stage superhumps, so the results for both stages are given. Assuming the CV was in stage B, $q_B = 0.059 \pm 0.007$; assuming stage C and using the relevant relation from [McAllister et al. \(2019\)](#), $q_C = 0.068 \pm 0.012$. In both cases, the estimated $q_{B,C}$ is $\sim 2\sigma$ higher than the observed value of $q = 0.044 \pm 0.002$. Whilst a 2σ difference is not a highly significant discrepancy, this could be preliminary evidence that the $\epsilon - q$ relation may over estimate q for CVs at short periods, which has been suspected for some time ([Pearson, 2007](#); [Knigge et al., 2011](#)).

Table 4.2: The system parameters found for the three CVs with peculiar white dwarf colours. Here, the reported π is the posterior distribution from fitting the white dwarf fluxes, c.f. §3.3.2.

System Name:	ASASSN-16kr	ASASSN-17jf	SSSJ0522–3505
M_{wd}/M_{\odot}	0.952 ± 0.018	0.669 ± 0.031	0.760 ± 0.023
R_{wd}/R_{\odot}	0.0083 ± 0.0002	0.0120 ± 0.0004	0.0112 ± 0.0003
$M_{\text{donor}}/M_{\odot}$	0.042 ± 0.001	0.060 ± 0.008	0.042 ± 0.004
$R_{\text{donor}}/R_{\odot}$	0.105 ± 0.002	0.112 ± 0.004	0.105 ± 0.004
q	0.044 ± 0.002	0.085 ± 0.006	0.055 ± 0.003
P , hours	$1.470862368(2)$	$1.36297(2)$	$1.492642(2)$
a/R_{\odot} ,	0.653 ± 0.005	0.567 ± 0.009	0.614 ± 0.007
i	86.4 ± 0.4	83.7 ± 0.5	83.8 ± 0.3
K_{wd} , km/s	22.7 ± 1.5	39.5 ± 4.2	26.0 ± 1.8
K_{donor} , km/s	515 ± 3	462 ± 5	470 ± 4
π , mas	6.58 ± 0.22	2.09 ± 0.19	1.81 ± 0.11
T_{eff} , kK	$10 - 12$	$8 - 13$	~ 25
$\log(g)$, cgs	8.55 ± 0.03	8.15 ± 0.05	8.22 ± 0.04

4.5 Implications of results

All three systems were candidate post-period minimum systems based on their periods and preliminary eclipse data; none show a prominent bright spot (indicative of a low mass transfer rate), or significant donor flux (implying a dim donor). As a result of this work, ASASSN-16kr and SSSJ0522–3505 are confirmed as having evolved through the period minimum and now have sub-stellar donors, and ASASSN-17jf lies in the period minimum region of Figure 4.18. All three CVs are strongly consistent with the ‘optimal’ Knigge et al. (2011) donor track. Additionally, despite the difficulty in white dwarf modelling, all three white dwarf masses derived in this analysis fall within the range of CV white dwarf masses observed by Pala et al. (2020), of $\langle M_{\text{wd}} \rangle = 0.83 \pm 0.17 M_{\odot}$, and are significantly higher than the pre-CV DA white dwarf mass of only $0.66 \pm 0.15 M_{\odot}$ (McCleery et al., 2020).

4.5.1 Is it correct to assume an unobscured white dwarf?

As mentioned in §4.3, the white dwarf colours may differ from model grids because the white dwarf ingress/egress is contaminated by an additional source of light,

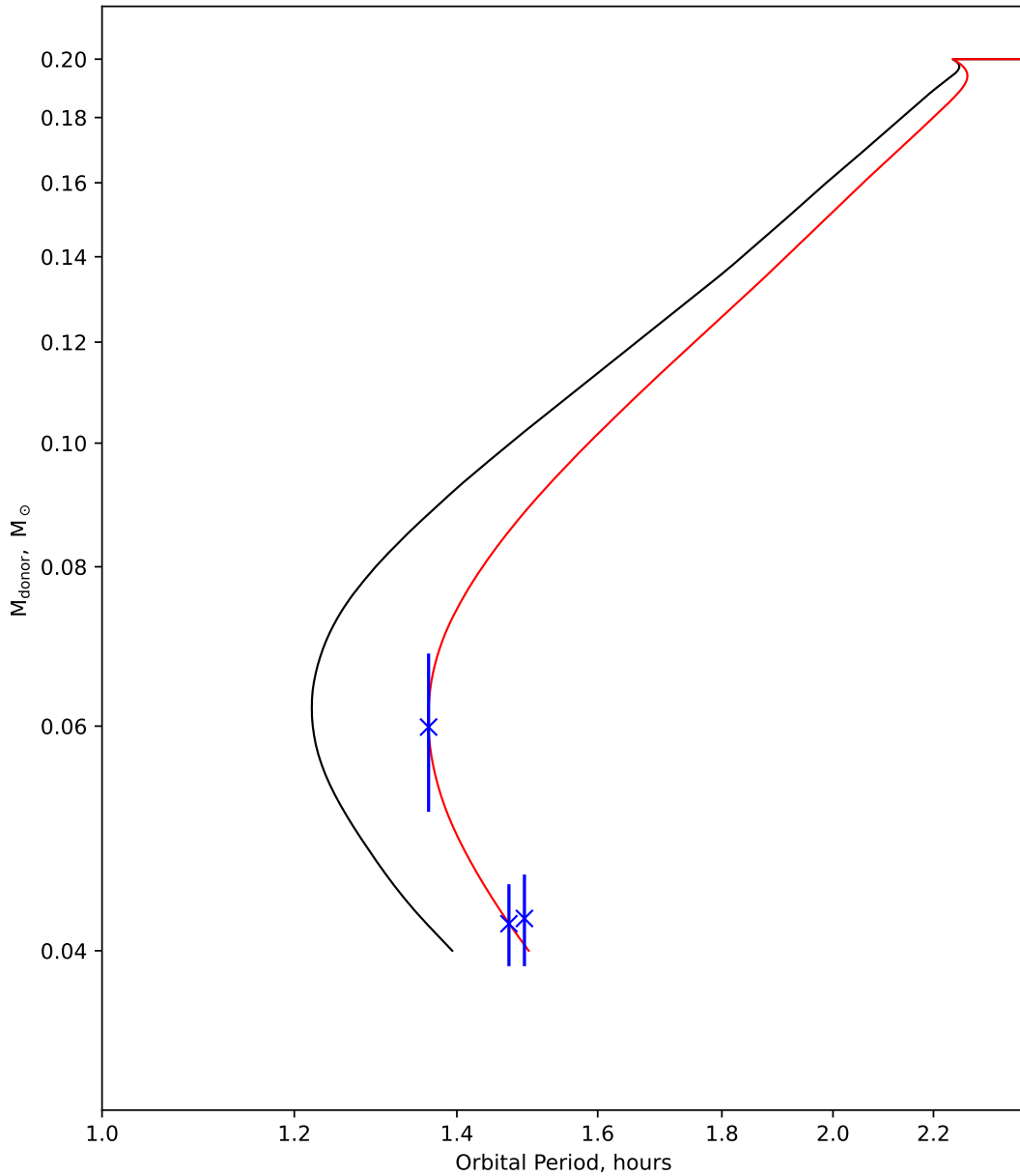


Figure 4.18: Donor evolution tracks compared with these observations – note that both axes are scaled logarithmically. **Solid black line:** the standard donor sequence from Knigge et al. (2011), **solid red line:** the ‘optimal’ donor track from Knigge et al. (2011). The three systems characterised in this chapter are shown as **blue crosses**.

such as a boundary layer close to the surface. If the eclipse is polluted by some other feature, phase-folded eclipse modelling will be wrong in two key elements: comparing colours to model atmospheres may be inaccurate, and the ingress and egress durations that constrain the white dwarf radius will not be correct. [Spark & O'Donoghue \(2015\)](#) conducted a study into the validity of assuming a pure white dwarf, comparing CV eclipse observations with white dwarfs with and without a few types of surface features such as boundary layers on the white dwarf, hot spots, or an optically thick or thin equatorial belt. These features are revealed by a departure from symmetry between the white dwarf ingress and egress, but care must be taken not to confuse the flickering component of the CV with the signature of surface features.

Unfortunately, detecting a surface layer or hot spot on the white dwarf requires both a high time resolution and high signal-to-noise ratios. [Spark & O'Donoghue \(2015\)](#) make use of SALTICAM data at a cadence of 0.15s, but the observations available here have a \sim 3-4s exposure time and lower signal-to-noise. Measuring the eclipse precisely enough to make claims about the nature of the white dwarf's surface is therefore not possible with present observations. The three systems of this work are prime candidates to search for white dwarf eclipse asymmetries, as the issue of flickering corrupting the white dwarf ingress/egress derivative is largely mitigated; all three have little to no flickering present. Future observations at higher cadence would open the possibility of examining the surfaces of these white dwarfs, though a large telescope will necessary due to the faintness of the systems; HiPERCAM on the GTC is an ideal candidate.

4.5.2 The hot white dwarf of SSSJ0522–3505

The effective temperature of white dwarfs in short period CVs is typically \sim 10000K ([Pala et al., 2017](#)), but the observed colours of SSSJ0522–3505 indicate a much hotter T_{eff} of \sim 25000K. This is likely to be accurate, as the system's observations are clearly dominated by the white dwarf flux, and show roughly the same eclipse depth in the r' , g' , and u' bands, which would not be consistent with a lower white dwarf temperature.

The measured effective temperature could be wrong, either as a result of poor flux calibration (see §2.3.4 for reasons this is unlikely) or because the ingress/egress fluxes do not represent the fluxes of the white dwarf photosphere, as discussed in section 4.5.1. However, the measured temperature is \sim 10000 K

hotter than expected, and these effects are unlikely to have introduced an error of this magnitude. As support for this, note that [Pala et al. \(2017\)](#) find that white dwarf temperatures from UV spectroscopy typically agree with those measured from eclipse light curves to within ~ 1000 K. Reasons why the white dwarf temperature in SSSJ0522–3505 might be unusually hot are explored here, but UV spectroscopy to confirm the white dwarf temperature is highly desirable.

The white dwarf in a CV is thought to settle at an equilibrium temperature, where radiative heat loss is balanced with two energy sources: energy released by infalling material, and a low level of “simmering” nuclear fusion in the white dwarf envelope ([Townsley & Bildsten, 2003, 2004](#)), but there are several reasons that this white dwarf may be temporarily out of equilibrium. There is no reason, though it is unlikely, that a CV cannot form from a main sequence star with a brown dwarf companion, to produce a young CV with a low-mass donor and a white dwarf still cooling from its formation temperature. Once the donor has reconnected with its Roche lobe, it would rejoin the normal CV evolution track and otherwise behave as a normal CV, with a normal accretion rate but a younger, hotter white dwarf than is typical.

A recent dwarf nova outburst was observed in this system in 2011, and could have produced a temporary boost to T_{eff} . During these events, the disc enters a hot, optically thick state, and the infall rate onto the white dwarf is greatly increased ([Osaki, 1996](#)), releasing a significant amount of energy and heating the white dwarf surface. This is only the most recent *observed* outburst, as there is a gap in observations between 2013 and 2019 during which any outburst events would have gone unrecorded. This may be important, as recent X-ray observations of another post period minimum system, OV Bootis ([Schwope et al., 2021](#)), shows that the white dwarf temperature is increased to 23000K 5 months after outburst, 9000K hotter than its T_{eff} prior to outburst. The increase in temperature can be somewhat long-lasting; detailed observations of GW Lib have shown its white dwarf is still 3000K hotter than equilibrium 8 years post-outburst([Szkody et al., 2016](#)). Another possibility is a recent classical nova – thermonuclear runaway in an accreted surface layer on the white dwarf – which would temporarily heat the white dwarf beyond its equilibrium temperature ([Starrfield et al., 2016](#)), giving the impression of a hotter white dwarf than expected, though a classical nova resulting in such a strong heating effect would be surprising.

However, assuming the white dwarf is in thermal equilibrium, T_{eff} can be used

to estimate the long-term accretion rate of the system (Townsley & Gänsicke, 2009). If the modelled T_{eff} of SSSJ0522–3505 is both accurate and driven by accretion, it would correspond to $\dot{M}_{\text{wd}} = 6 \pm 2 \times 10^{-10} M_{\odot} \text{yr}^{-1}$, compared to accretion rates of $\sim 10^{-10} - 10^{-11} M_{\odot} \text{yr}^{-1}$ expected for CVs in the post-period minimum regime (Pala et al., 2017). Unfortunately, the MESA-based method to find \dot{M} that is outlined in §3.4 cannot be reliably applied to this system, as the M_{donor} is too low. Although this is somewhat high, a mass accretion rate of $10^{-10} M_{\odot} \text{yr}^{-1}$ is not incompatible with the presence of dwarf nova outbursts in SSSJ0522–3505, since a hot, optically thick accretion disc that would forbid such outbursts would require an accretion rate of order $10^{-8} M_{\odot} \text{yr}^{-1}$ (Hameury et al., 1998) to be stable on long timescales.

4.6 Summarising remarks

The original paper (Wild et al., 2021) examined the period excess as a qualitative diagnostic for excess AML, but this analysis is deferred to the end of Chapter 5 where it repeated with an expanded data set – though note that the conclusions are unchanged from the original paper.

I contribute the component masses and radii, separations, white dwarf temperatures and surface gravities of three new short-period CVs to the population of well-characterised CV observations, two of which have extremely low-mass donor stars, and one which appears to be in the process of evolving through the period minimum. I measure the T_{eff} of the white dwarf in SSSJ0522–3505 to be $\sim 10000\text{K}$ higher than is typical for a CV. I note that the derived temperature is quite uncertain, but cannot confidently determine the origin of the discrepancy and summarise possible causes. All three of the newly modelled systems lie within 1σ of the ‘optimal’ model mass-radius evolutionary tracks from Knigge et al. (2011).

Chapter 5

Eclipse modelling results of 12 CVs

A modest backlog of observed CV eclipse light curve data was reduced, calibrated, and modelled following the procedure outlined in §3.3.1, and the results are presented here.

The systems modelled in this chapter were chosen largely based on their short periods, targeting the donor mass range for which mass loss rates could be inferred ($0.08M_{\odot} < M_{\text{donor}} < 0.20M_{\odot}$, shown in §6.2). They range in period from 1.4–2.2 hours, and were drawn from a few sources. The All-Sky Automated Survey for Supernovae (ASASSN) (Shappee et al., 2014) is sensitive to transients, and is a valuable tool to identify CVs by their outbursts for follow-up once they re-enter quiescence; such systems are recognised by their ASASSN moniker. Other candidate systems were gathered from a variety of sources, which are cited below. The modelled systems in this thesis were:

- ASASSN-14hq
- ASASSN-14kb (a.k.a OGLE-LMC529.30.114)
- ASASSN-15pb
- ASASSN-17fo
- AY For (a.k.a H α 0242-2802) (Woudt et al., 2004)
- CSS090622 J215636+193242 (hereafter CSS090622) (Kato et al., 2012; Thorstensen et al., 2016)
- CSS090102 J132536+210037 (hereafter CSS090102) (Kato et al., 2012)
- CSS090419 J162620-125557 (hereafter CSS090419) (Kato et al., 2012)
- MASTER OT J001400.25-561735.0 (hereafter MAS0014) (Woudt, private communication)
- OGLE BLG-ECL-000082 (a.k.a BLG510.16.126296, hereafter OGLE82) (Soszynski et al., 2016)
- SDSS J074859.6+312512.7 (hereafter SDSS J0748) (Kato et al., 2016)
- SDSS J152419.33+220920.0 (hereafter SDSS J1524) (Southworth et al., 2010; Michel et al., 2013)

ASASSN-14hq and ASASSN-15pb were observed by [Paterson et al. \(2019\)](#) and had their periods measured, though the observations used in this thesis pre-date this publication and I make my own independent measurement of the period. These two systems were also noted to be in outburst in late 2014 in the case of ASASSN-14hq, and 2015 in the case of ASASSN-15pb. Table 4.1 summarises the right ascension, declination, magnitude, and ephemeris of the CVs observed here.

Table 5.1: Summary of observational information for the 12 CVs of this chapter.

System name	RA	Dec	g'	T_0 , BMJD, UTC	Period, days
ASASSN-14hq	06:38:19.59	-48:59:16.1	18.1	57701.27140(2)	0.074326999(3)
ASASSN-14kb	04:46:50.01	-71:22:56.0	18.6	58143.16048(2)	0.0681057(4)
ASASSN-15pb	20:14:22.92	-63:37:58.6	19.5	57626.14278(3)	0.093290(6)
ASASSN-17fo	11:38:35.70	+04:44:54.5	19.6	58143.24296(2)	0.061548(1)
AY For	02:42:34.82	-28:02:44.0	18.2	57701.10964(1)	0.07461485(4)
CSS090102	13:25:36.06	+21:00:36.8	19.8	55943.12147(2)	0.062384910(2)
CSS090419	16:26:19.83	-12:55:56.5	20.5	56498.92855(3)	0.075442759(3)
CSS090622	21:56:36.34	+19:32:41.5	19.3	56874.20195(4)	0.0709293(7)
MAS0014	00:14:00.25	-56:17:35.0	18.3	57626.08355(1)	0.07152949(1)
OGLE82	17:54:16.19	-35:26:39.5	18.0	57623.03460(2)	0.071930828(3)
SDSS J0748	07:48:59.56	+31:25:12.7	17.8	57808.63030(1)	0.058311083(3)
SDSS J1524	15:24:19.33	+22:09:20.1	19.1	56486.91456(1)	0.065318733(1)

5.1 Results

All eclipses presented are well-described by their fits, with small residuals. The light curves are shown below, along with the white dwarf flux distributions their best-fit white dwarf model atmospheres, and notes on the modelling of each system. Table 5.2 details the physical parameters of these 12 new systems.

In a few cases, the GP appears as a flat line along a residual of 0 despite some obvious scatter, e.g. ASASSN-14hq, seen in Figure 5.2. This is expected, as in these cases the residuals are fully described by the error in flux and the GP likelihood becomes dominated by the priors, sampling small values of GP amplitude.

None of these systems presented the issues with their characterisations that was seen in Chapter 4. The modelled white dwarf colours were described by cooling tracks well in most cases, with the exceptions of CSS090419 and CSS090622. Spectroscopic follow-up in these cases is desirable to probe these systems more deeply.

Some results are particularly good demonstrations of the ability of the hierarchical GP modelling approach to usefully model poorer quality light curves in tandem with higher quality data. An example of this is seen in the case of MAS0014, the light curves of which are seen in Figures 5.25, 5.26, and 5.27, where the high-quality binned data help a subtle bright spot egress to be confidently constrained in the eclipse of 2016/11/07 even in the presence of significant

flickering. A more extreme example is that of SDSS J0748, which has the white dwarf and bright spot ingresses blended together for the majority of observations, but clearly distinct ingresses on the night of 2018/02/05 and somewhat distinct ingresses on 2018/02/07, seen in Figure 5.32. Using the hierarchical structure to share information between observations constrains the parameter space, and makes characterisation possible in a system that would otherwise be extremely difficult to model.

When optimising the eclipse model to the data, some systems had their eclipses binned together where appropriate to reduce the complexity of the parameter space, and the observing logs in §2.4 details which eclipses were combined. However, in the interests of readability, the dates of the data that are binned for a given light curve are also noted in the figure caption. For unbinned data, the date and approximate mid-eclipse time is given in the axis title. The majority of observations were made with ULTRACAM, though some systems are supported by ULTRASPEC data.

5.1.1 ASASSN-14hq

The period of this system was measured by [Paterson et al. \(2019\)](#) to be $0.074327(9)$ days, consistent with my own measurement of $0.074326999(3)$ days. These observations fell into two binning categories: the 2016 and 2017 data, and the January 2018 data – specific observation logs are given in Table 2.4. Eclipse modelling indicates that the disc radius fell in brightness by $\sim 20\%$ in the g' and $\sim 50\%$ in the u' between these two batches, suggesting the disc may have been in a phase of dumping material onto the white dwarf faster than material enters it from the donor during this period. As this system was observed in outburst only two years prior to these observations, this is not unexpected.

For this system, the white dwarf fluxes were well-described by the model cooling tracks, with the white dwarf fitting phase producing a value of π that agrees with Gaia (3.40 ± 0.07 mas and 3.40 ± 0.08 mas, respectively). Fitting found a somewhat low mass white dwarf, $0.67 \pm 0.07 M_{\odot}$, though this falls just over 1σ outside the intrinsic scatter of the [Pala et al. \(2020\)](#) population measurement of $0.83 \pm 0.13 M_{\odot}$ so is well within the expected range. Models converged on a donor mass of $0.097 \pm 0.002 M_{\odot}$, consistent with the pre-period minimum CV track that amplifies gravitational braking by a factor of ~ 2.5 .

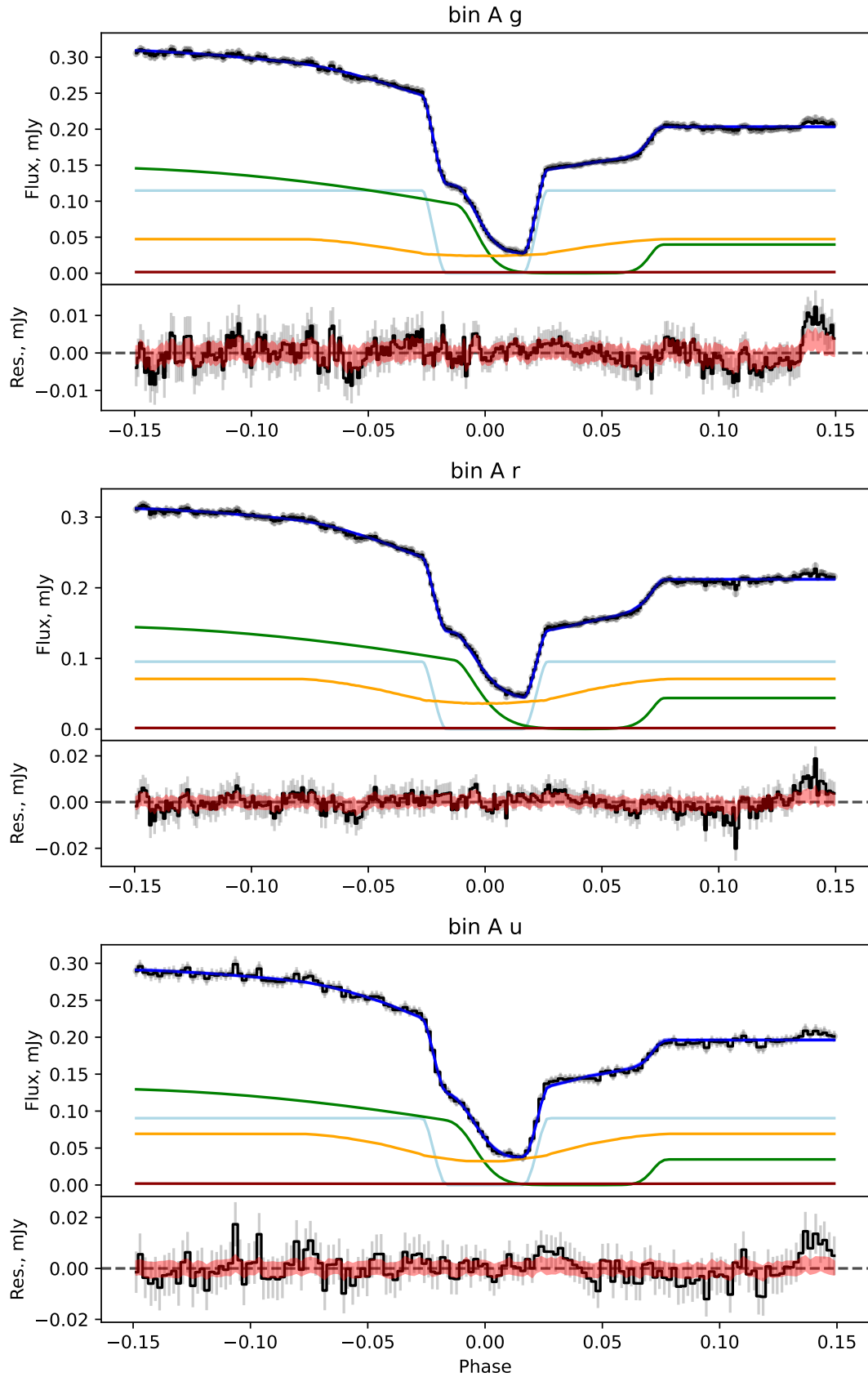


Figure 5.1: ASASSN-14hq light curve models. Symbols are the same as Figure 4.1. Data are the result of binning the following nights: 2016/11/9, 2016/11/11, 2017/3/19, 2017/3/21.

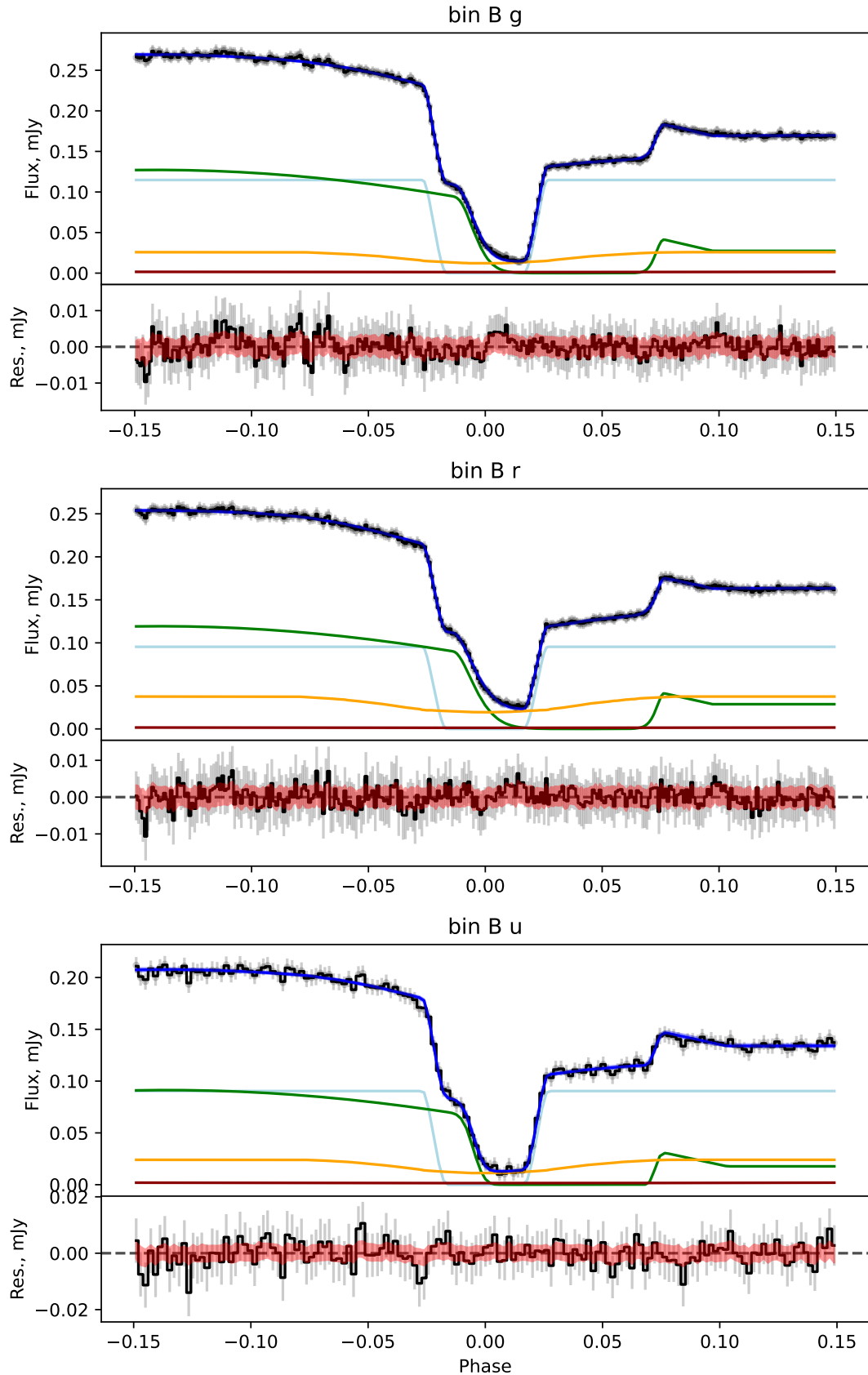


Figure 5.2: ASASSN-14hq light curve models (cont.). Data are the result of binning the following nights: 2018/1/23, 2018/1/25, both 2018/1/28 observations, 2018/1/30.

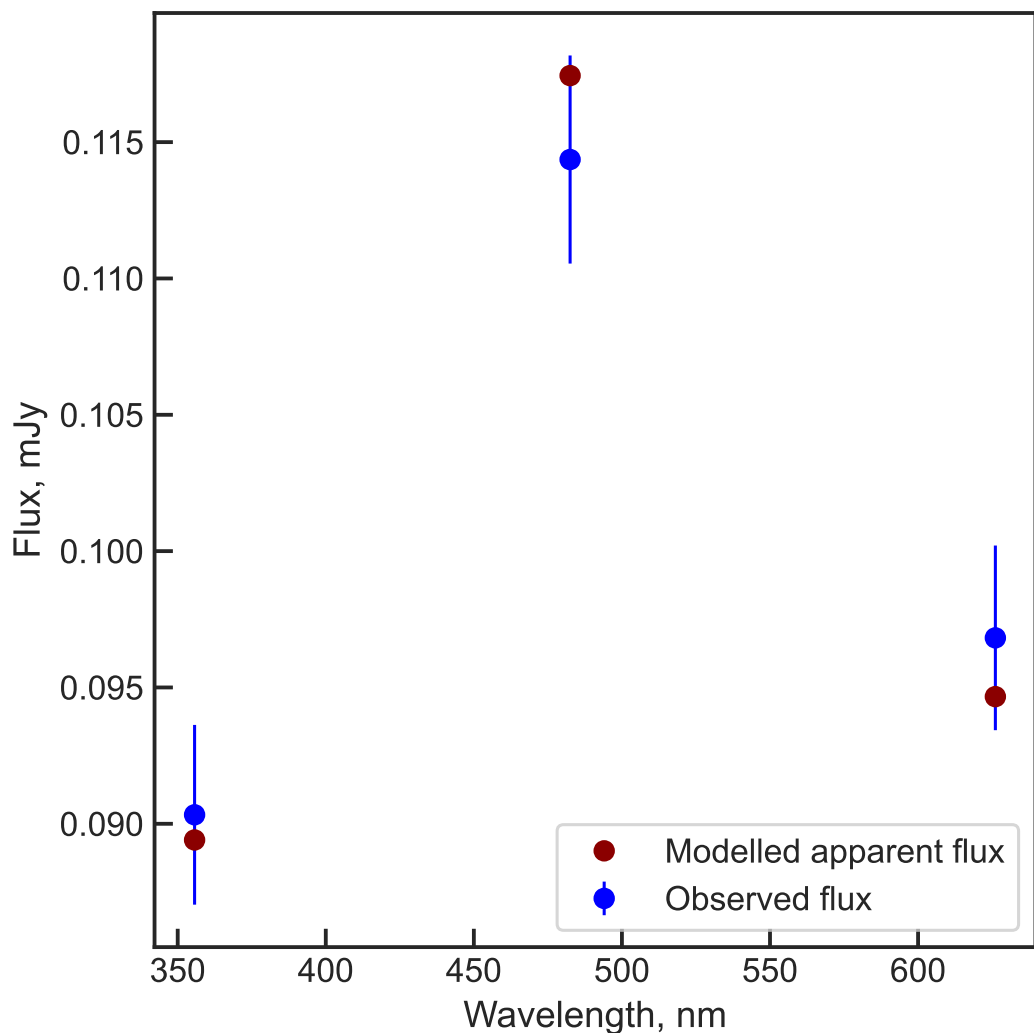


Figure 5.3: ASASSN-14hq observed white dwarf fluxes, compared to the best-fit model atmosphere.

5.1.2 ASASSN-14kb

ASASSN-14kb has very distinct modelling features, making it an easily characterised system. The 4 observations showed little variance between them, and the binned light curves seen in Figure 5.4 show remarkably little residual flickering. Additionally, the white dwarf spectral energy distribution was well-described by the cooling tracks and exactly reproduces the Gaia π distribution of 2.78 ± 0.11 . The resulting donor mass of this CV appears to be significantly high for the observed period, sitting $\sim 3\sigma$ above the purely gravitational wave driven MESA donor track.

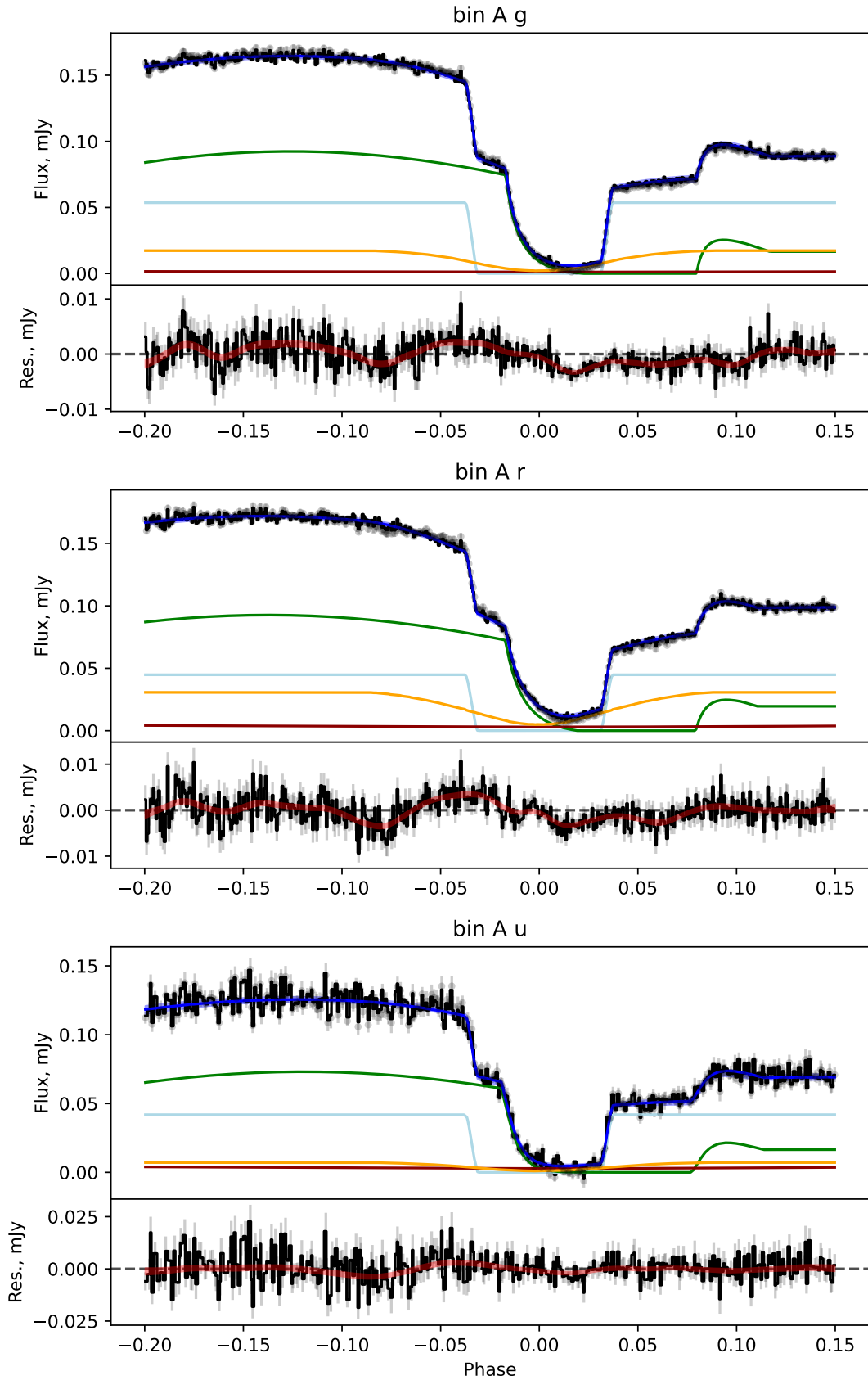


Figure 5.4: ASASSN-14kb light curve models. Symbols are the same as Figure 4.1

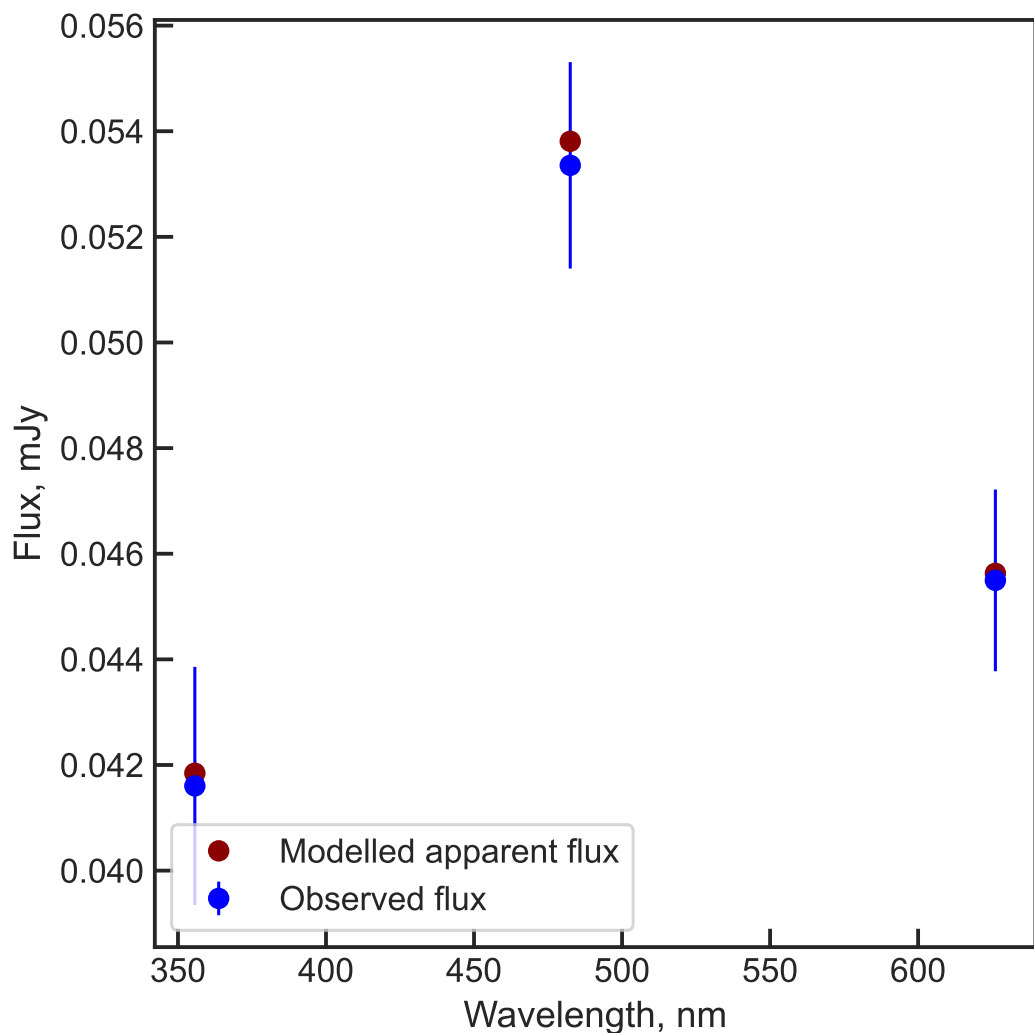


Figure 5.5: ASASSN-14kb observed white dwarf fluxes, compared to the best-fit model atmosphere.

5.1.3 ASASSN-15pb

ASASSN-15pb was an ideal candidate for modelling. The data in all bands were consistent enough to be comfortably binned together, aided by the 6 observations spanning only 6 days. The observations of this system take place in August 2016, only a year after the system was observed in outburst, but the system appears to have quickly returned to a reasonably well-behaved state and is suitable for modelling. The bright spot and white dwarf ingresses are mildly blended in the u' , g' , and r' observations, and slightly more strongly blended in the i' band. Whilst this did not prevent the optimisation from strongly constraining the white dwarf fluxes (with the exception of the loosely constrained i' band flux), this blending makes constraining the eclipse width, $\Delta\phi$, and white dwarf radius more challenging. Despite this, by drawing on information from all eclipses the quantities are well-constrained, and the white dwarf fluxes are well-described by the model cooling tracks, so the resulting system parameters can be considered sound.

[Paterson et al. \(2019\)](#) measure the period of this system to be 0.09329(2) days, which is consistent with my measurement of 0.093290(6) days. This is the longest period CV in this new sample, lying in the region defined as the period gap by the [Knigge et al. \(2011\)](#) donor tracks. However, the donor mass is significantly lower than the $0.20M_\odot$ period gap mass assumed by [Knigge et al. \(2011\)](#), at $0.148 \pm 0.008M_\odot$.

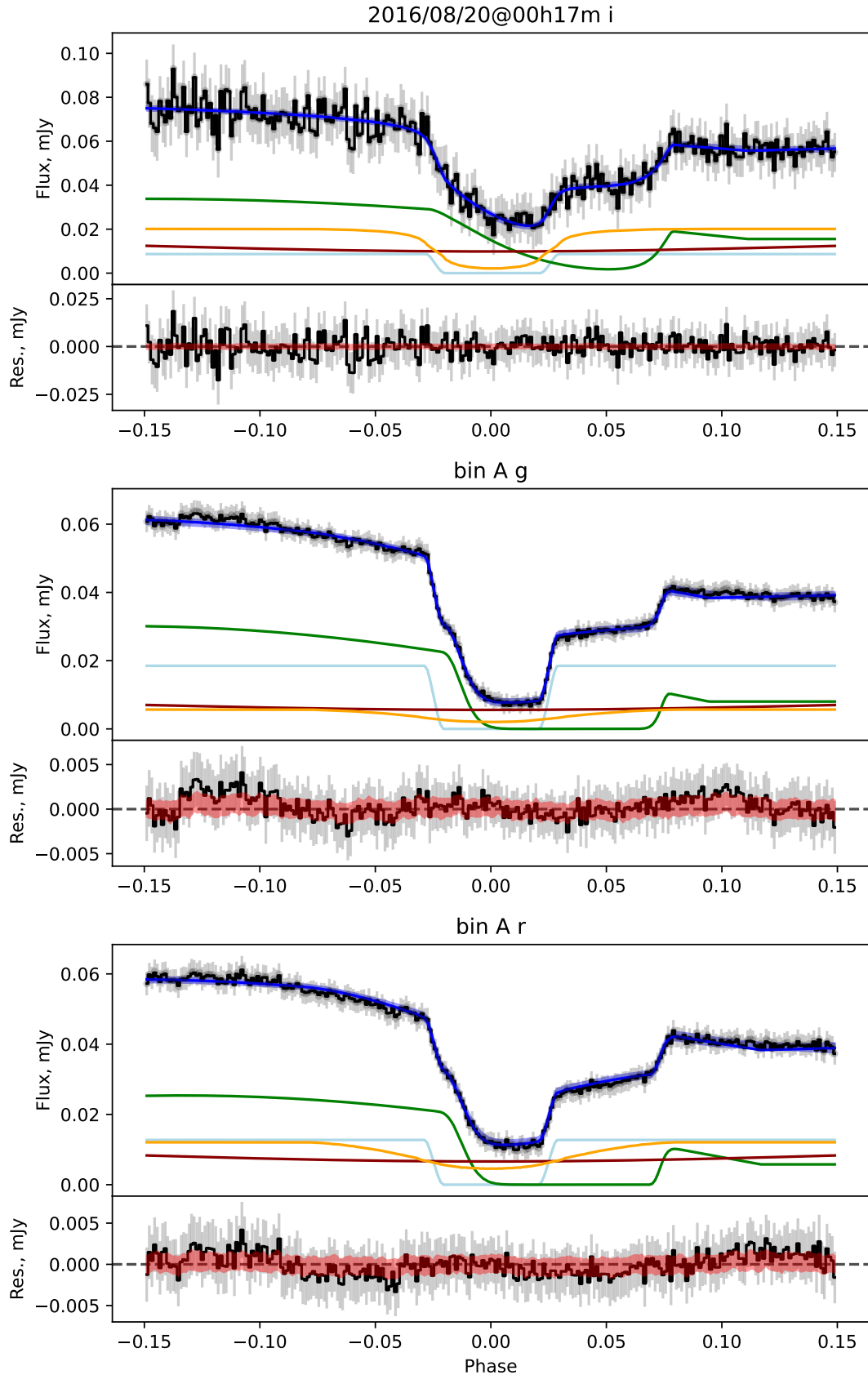


Figure 5.6: ASASSN-15pb light curve models. Symbols are the same as Figure 4.1. u' , g' , and r' data are the result of binning together all observations.

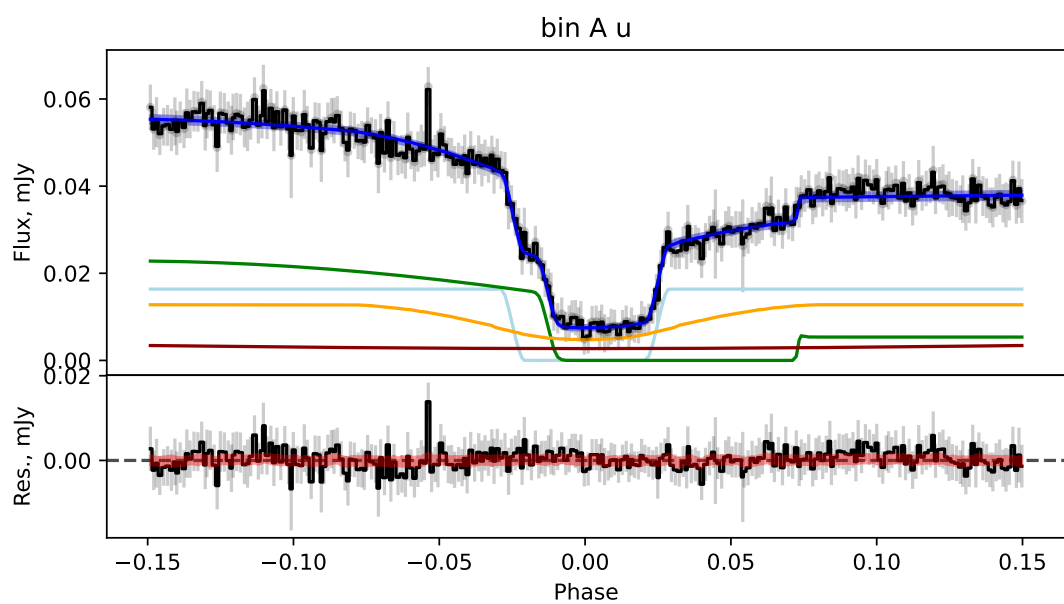


Figure 5.7: ASASSN-15pb light curve models (cont.)

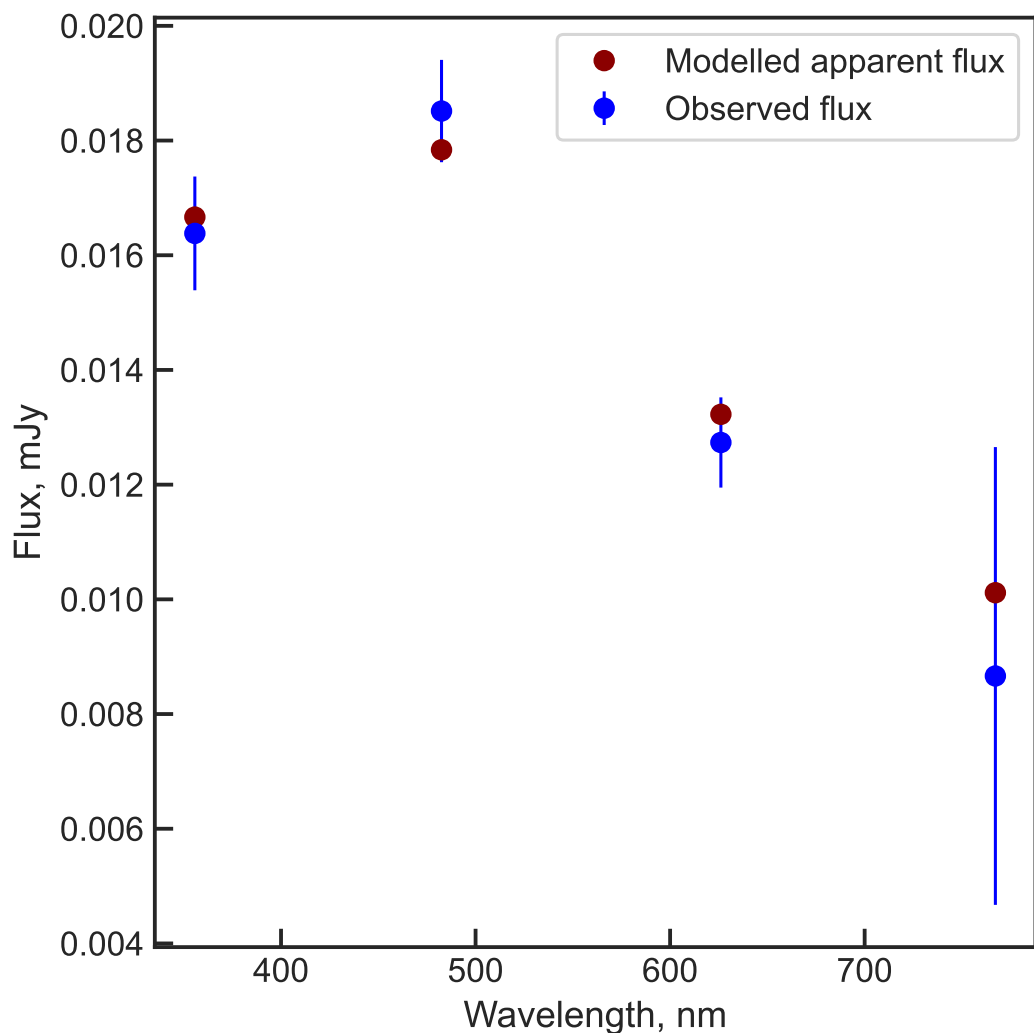


Figure 5.8: ASASSN-15pb observed white dwarf fluxes, compared to the best-fit model atmosphere.

5.1.4 ASASSN-17fo

ASASSN-17fo was observed in early 2018, and whilst the three eclipses were not suitably concordant to allow them to be binned together, the relevant eclipse features for modelling are impressively distinct with little flickering present. The resulting eclipse model described the data well, and the white dwarf fluxes find a good solution to models with $M_{\text{wd}} = 0.85 \pm 0.01 M_{\odot}$ and a parallax of 1.79 ± 0.20 mas, in strong agreement with the Gaia π of 1.96 ± 0.20 mas. However, the donor mass and period place this system well above the ‘standard’ [Knigge et al. \(2011\)](#) donor track in Figure 5.41.

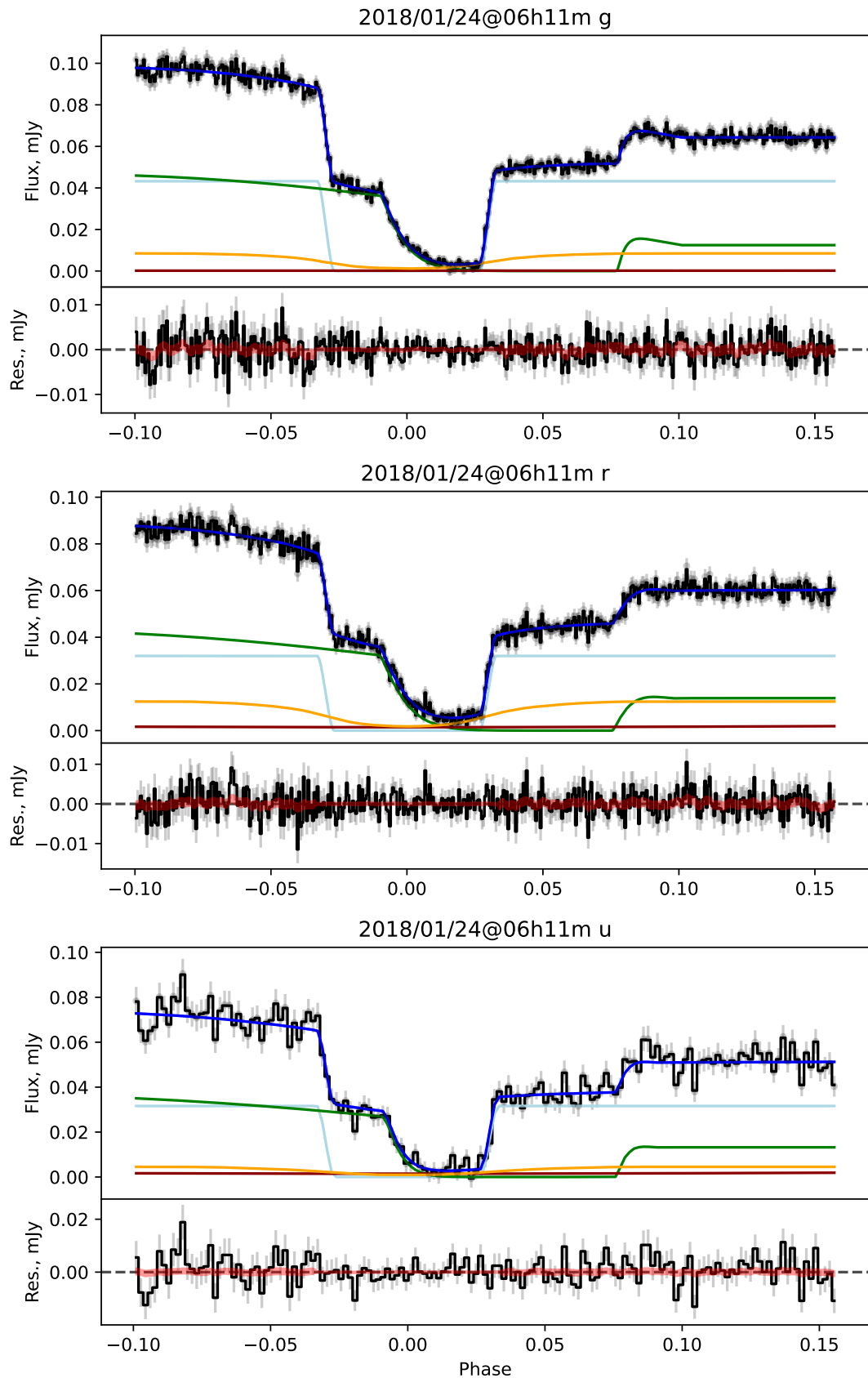


Figure 5.9: ASASSN-17fo light curve models. Symbols are the same as Figure 4.1

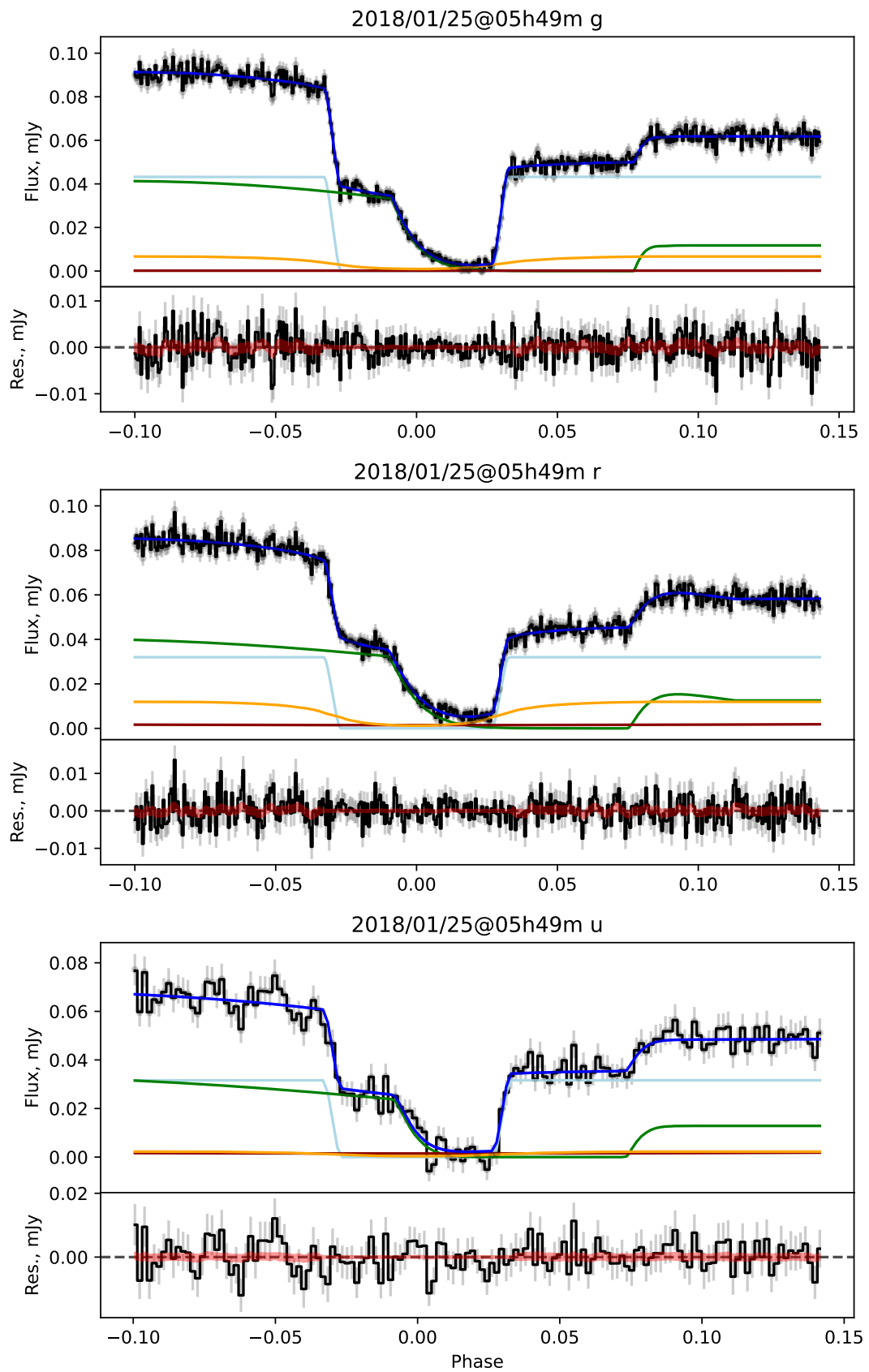


Figure 5.10: ASASSN-17fo light curve models (cont.)

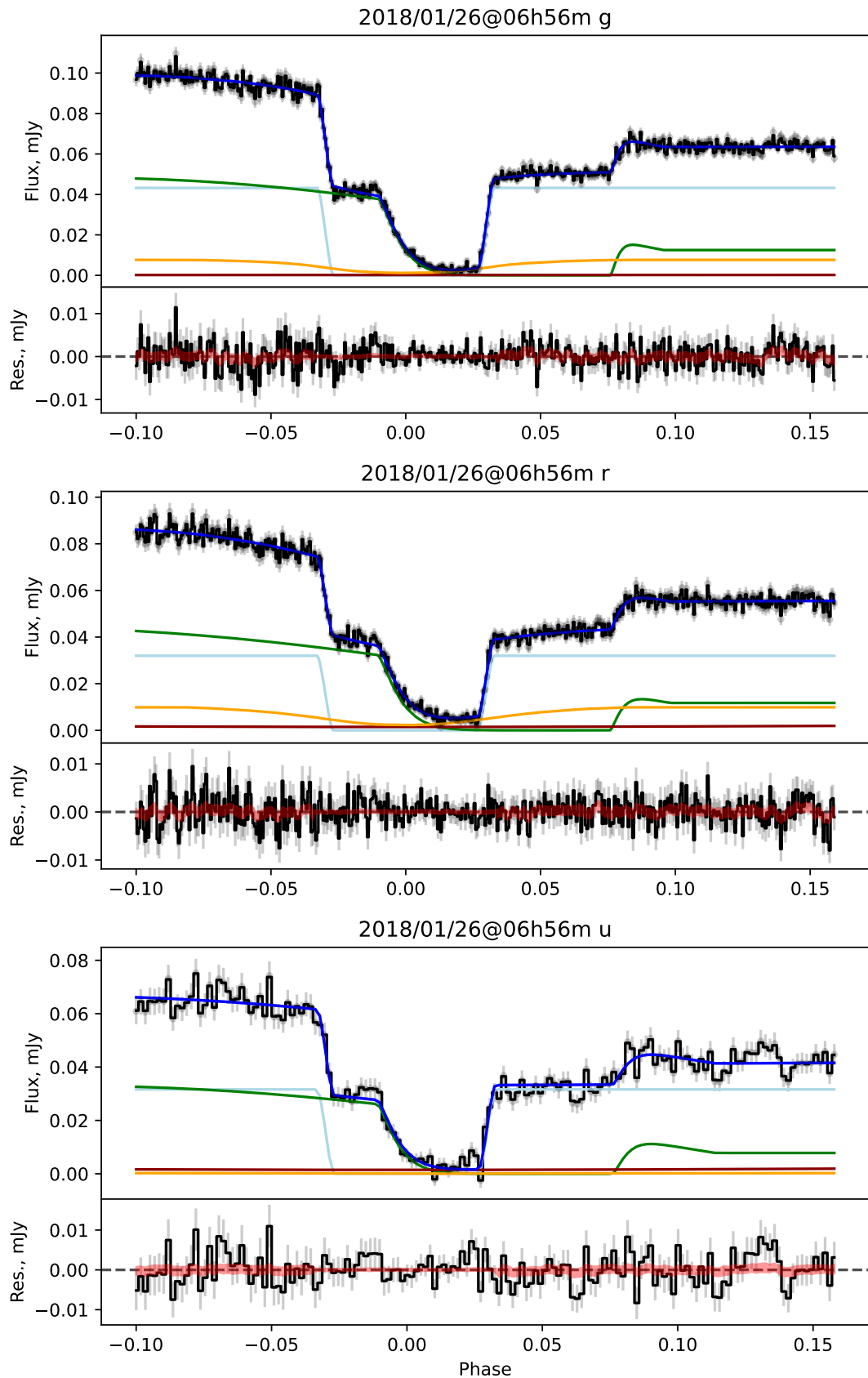


Figure 5.11: ASASSN-17fo light curve models (cont.)

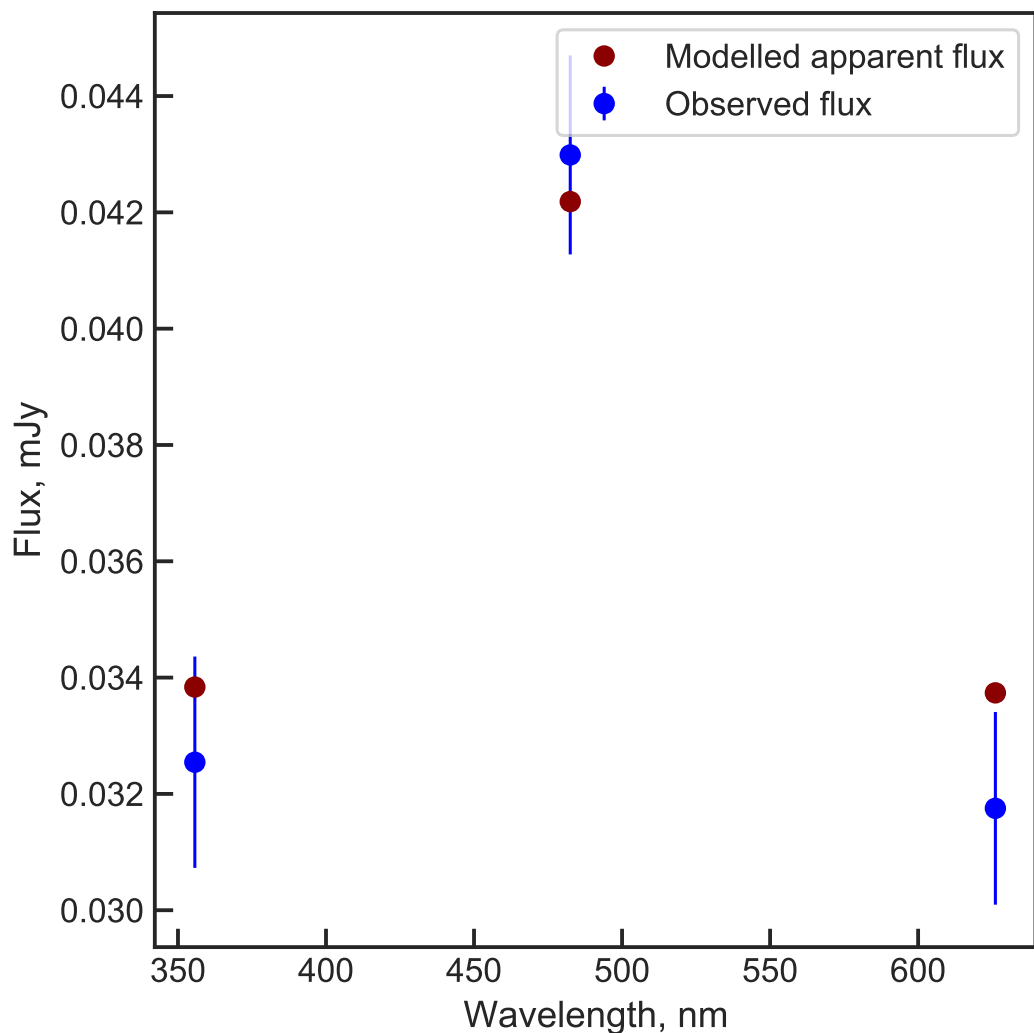


Figure 5.12: ASASSN-17fo observed white dwarf fluxes, compared to the best-fit model atmosphere.

5.1.5 AY For

AY For had the white dwarf and donor stars' masses estimated spectroscopically in [Mason & Howell \(2005\)](#) to be $M_{\text{wd}} \sim 0.64M_{\odot}$ and $M_{\text{donor}} \sim 0.17M_{\odot}$, with no error reported. These values are not consistent with my findings of $M_{\text{wd}} = 0.78 \pm 0.02M_{\odot}$ and $M_{\text{donor}} = 0.106 \pm 0.006M_{\odot}$. The previous measurement is highly dubious; it is based on inferring a donor mass and radius from the period using the model $M_{\text{donor}} - P$ relation presented in [Howell & Skidmore \(2002\)](#), which is then used to calculate a white dwarf mass from a spectroscopic q . This relies heavily on a poorly understood relationship, and extrapolates that further when giving a white dwarf mass. AY For is also claimed by [Mason & Howell \(2005\)](#) to be a pre-period minimum system, which is corroborated by this more rigorous analysis.

The white dwarf fluxes of AY For were not well-described by the white dwarf cooling tracks, similarly to the systems in §4.3. There is high confidence that this is a real effect rather than a poor calibration, as the field about AY For was observed by the PANSTARRS survey, and the comparison star SDSS magnitudes are reported, which can be used to flux-calibrate the data independently of the standard star method typically used. Comparing these two calibrations finds comparison star fluxes that are within 2% of each other. Rather, this system possibly suffers from a similar corrupting effect to that seen in the three CVs of Chapter 4, though the disagreement here is not as severe as the extreme case of SSSJ0522–3505. Modelling error is similarly unlikely, as the light curve fits generally show distinct ingress and egress features that are replicated in the models. However, based on the in-depth analysis of Chapter 4, the system parameters of AY For can still be considered robust.

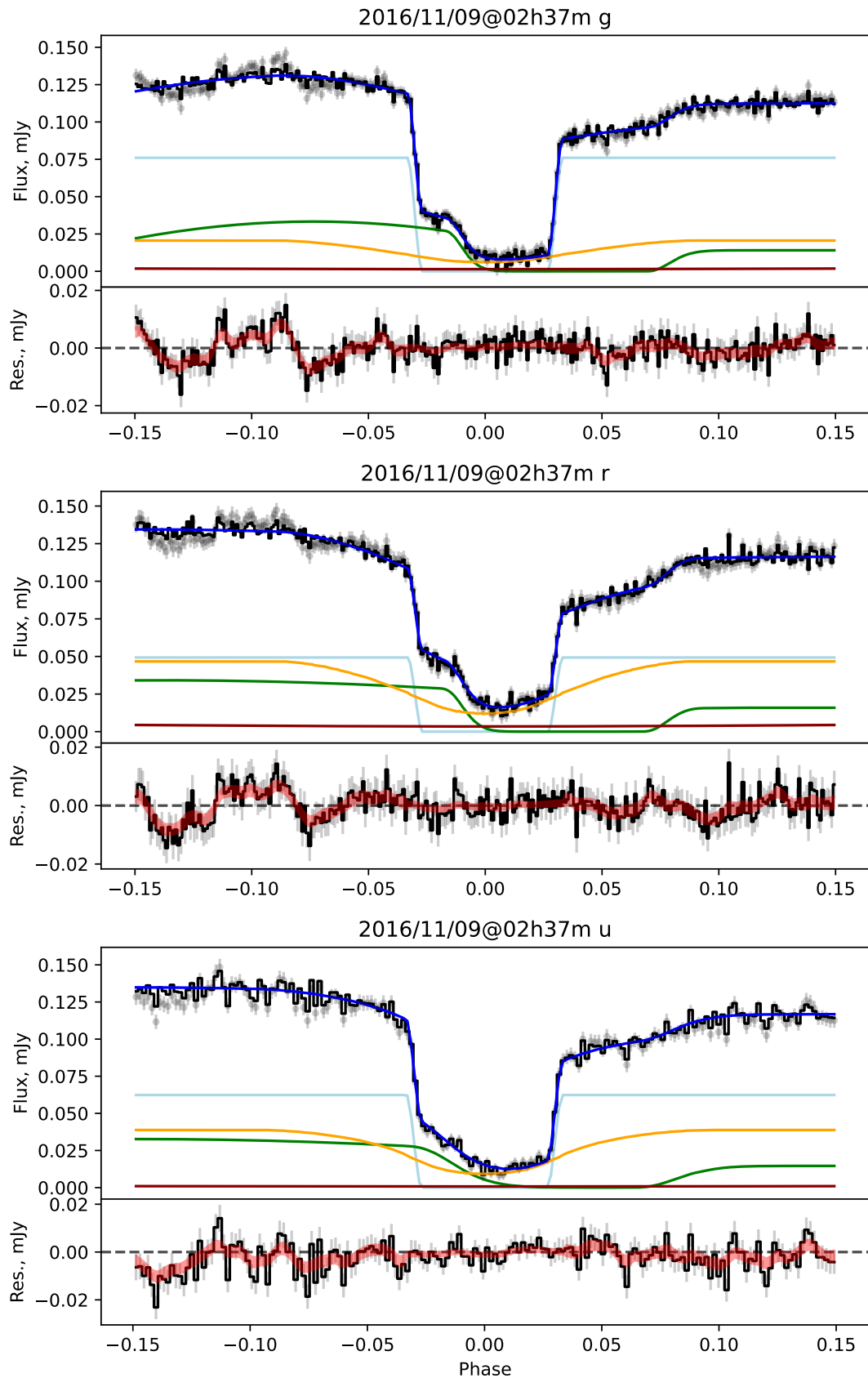


Figure 5.13: AY For light curve models. Symbols are the same as Figure 4.1

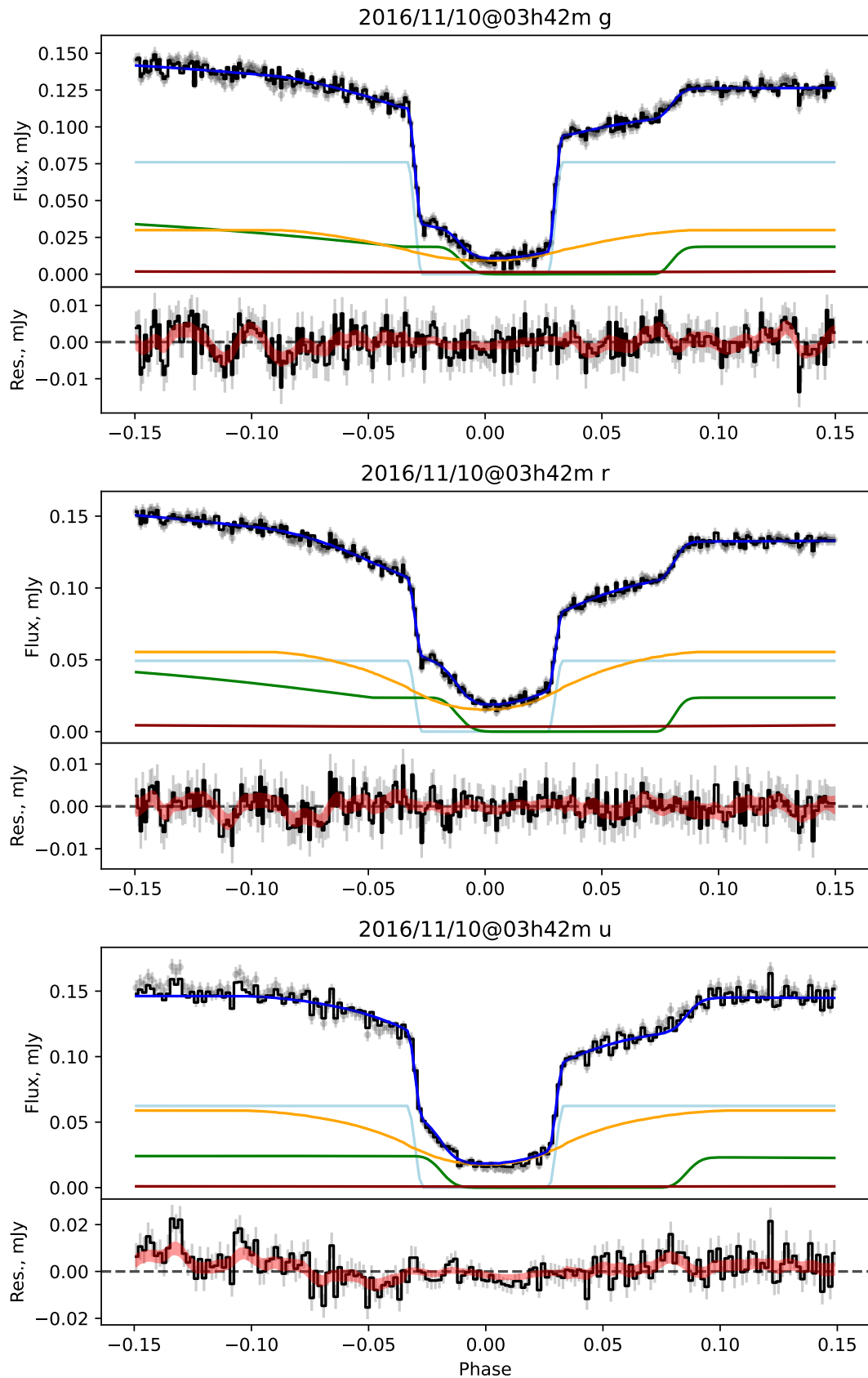


Figure 5.14: AY For light curve models (cont.)

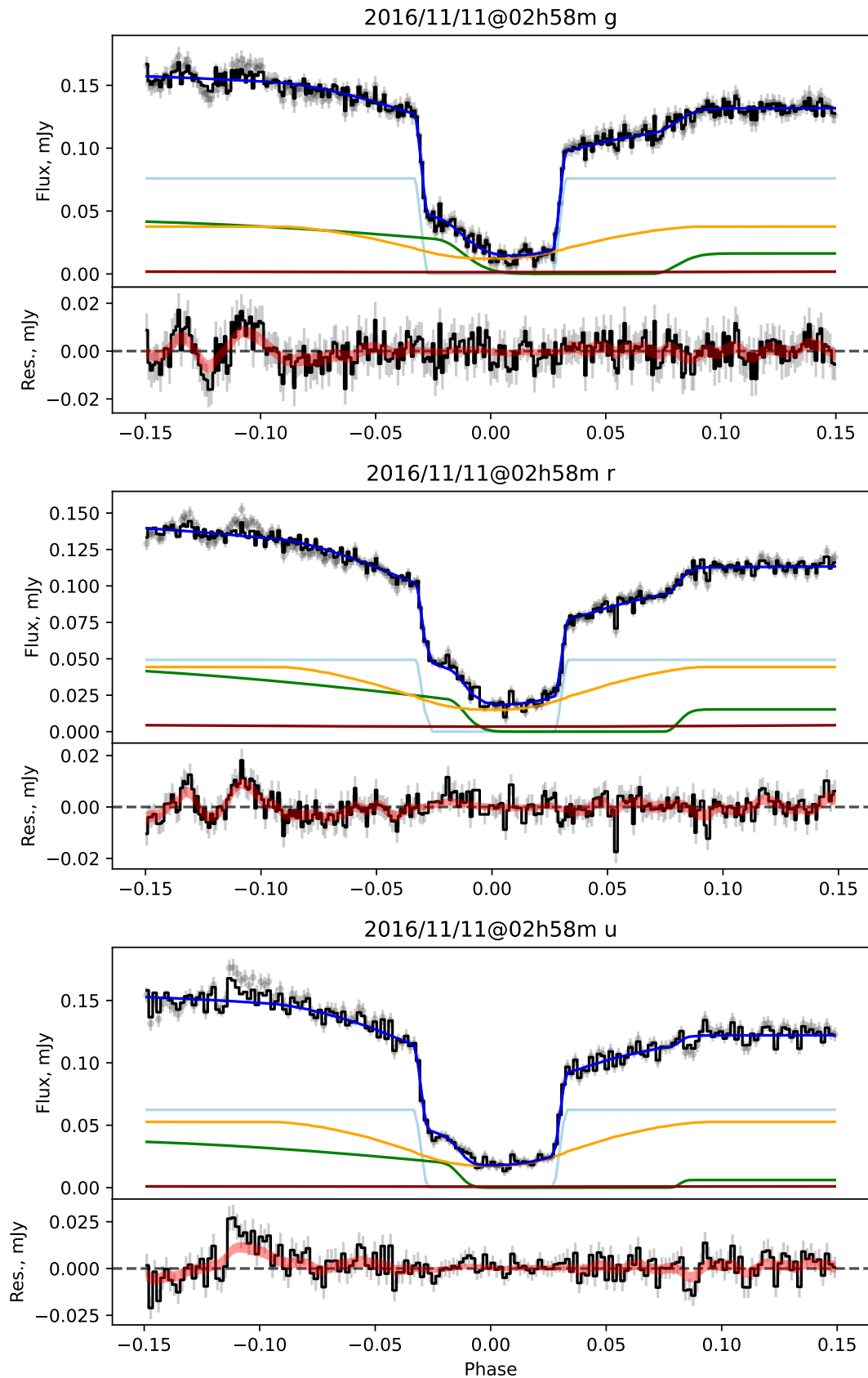


Figure 5.15: AY For light curve models (cont.)

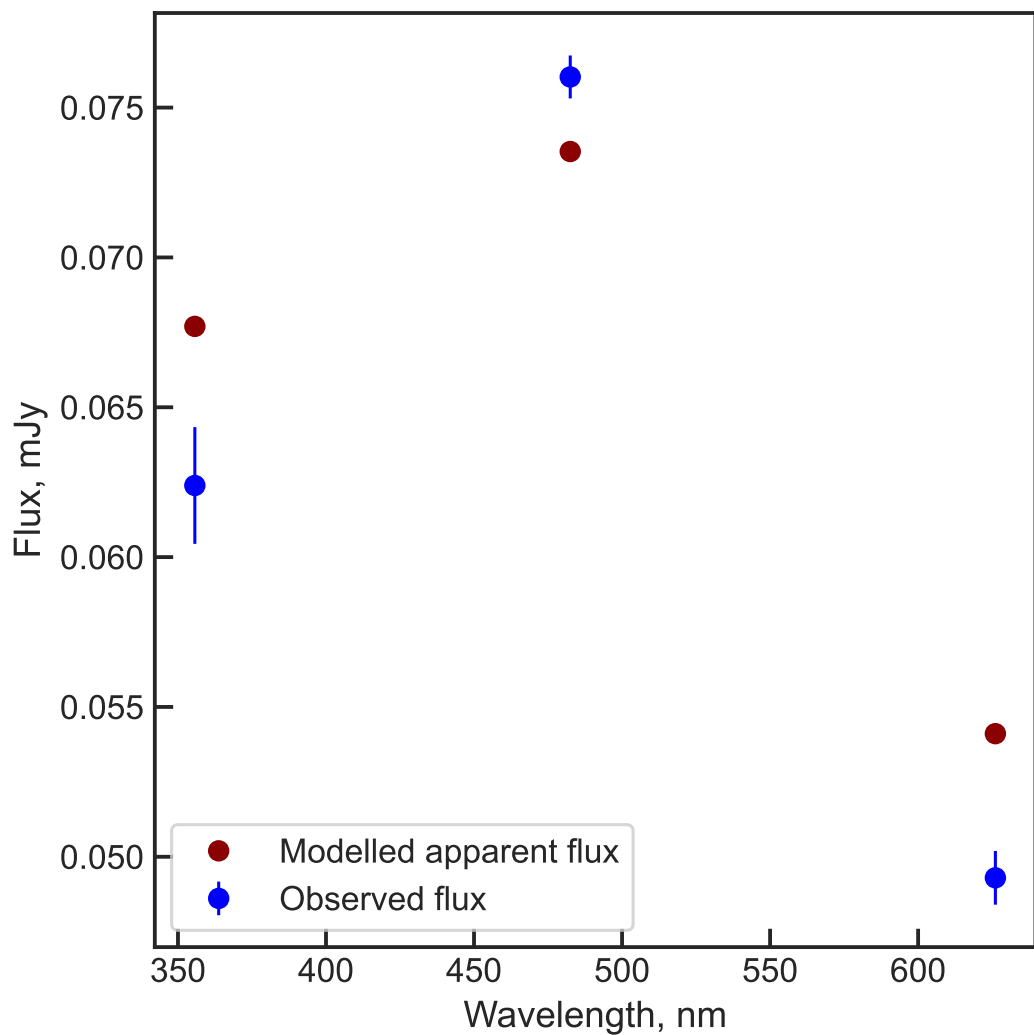


Figure 5.16: AY For observed white dwarf fluxes, compared to the best-fit model atmosphere.

5.1.6 CSS090102

Despite these observations spanning three years, from May 2011 to August 2014, the eclipses were concordant enough to be binned together. The resulting data have somewhat weak bright spot egress features, but the optimised eclipse model reproduces the observation well, with very little residual scatter about the model. The white dwarf fluxes are again well-described by cooling tracks, producing a relatively low but reasonable $M_{\text{wd}} = 0.62 \pm 0.03 M_{\odot}$ and the best-fit parallax of 1.41 ± 0.30 mas again agrees well with the Gaia observation of $\pi = 1.51 \pm 0.32$ mas.

The best-fit system parameters place this CV at the donor mass at which the direction of period evolution begins to reverse. However, the observed period is significantly longer than the canonical period minimum, possibly indicating a significantly higher mass loss rate than is typical. Unfortunately, the donor mass is just below the threshold for the methodology of §3.4 at $M_{\text{donor}} = 0.060 \pm 0.003 M_{\odot}$, so this currently cannot be verified.

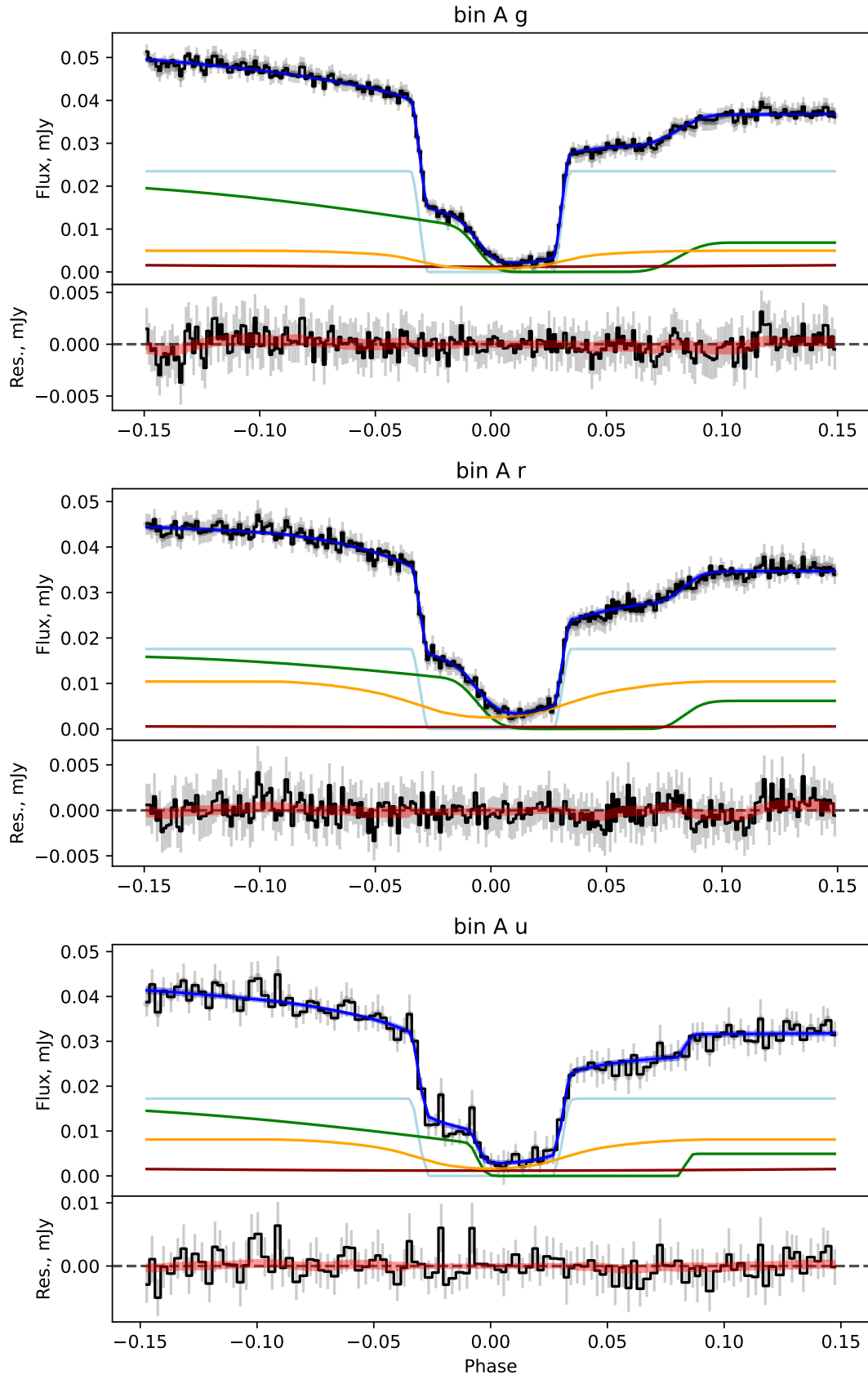


Figure 5.17: CSS090102 light curve models. Symbols are the same as Figure 4.1. Data are the results of binning all available eclipses.

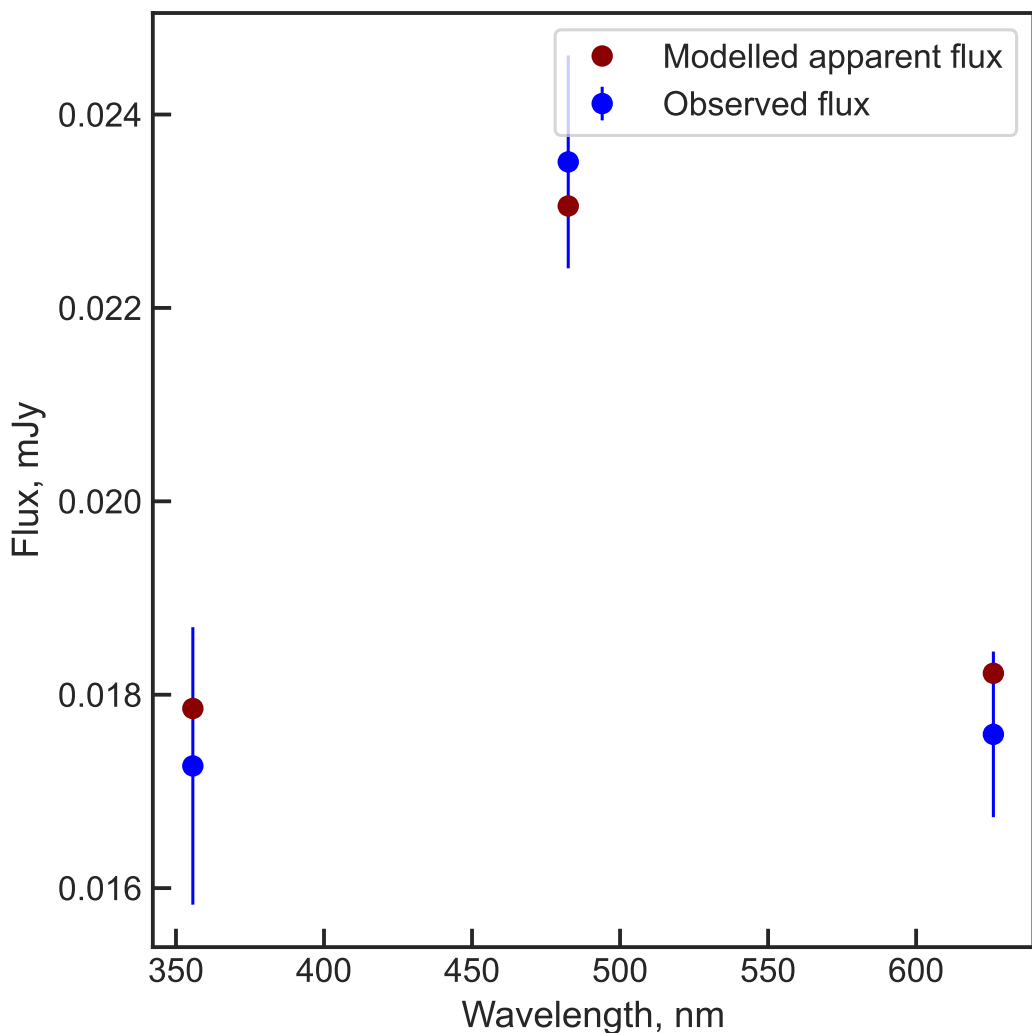


Figure 5.18: CSS090102 observed white dwarf fluxes, compared to the best-fit model atmosphere.

5.1.7 CSS090419

The white dwarf of CSS090419 significantly brightens in the i' band, compared to the r' band. This is unlikely to be calibration error in the i' band, as calibration has otherwise proven to be robust. In addition, this brightening is not seen in the ASASSN-15pb i' band observations, suggesting it is not a systematic issue.

The resulting fit appears to be acceptable, with little residual flux. These fits are given in Figures 5.19 and 5.20, and show that the eclipse model does a good job of describing the data. However, the white dwarf and bright spot ingresses are somewhat blended in the r' and i' , and whilst the egresses are distinct enough to resolve a white dwarf flux, the key parameters of R_{wd} and $\Delta\phi$ are more difficult to constrain. In addition, inspecting the light curves shows that there is some level of degeneracy between the disc flux and white dwarf flux, particularly in the r' band, exacerbating the difficulty in modelling. These blended features are reflected in large uncertainty in white dwarf flux. Indeed, the standard deviations on all four white dwarf fluxes are large enough that they are consistent with their mean – a perfectly flat spectrum.

This is not typical white dwarf behaviour, and cannot be reproduced by the white dwarf model atmospheres used here given the constraints. Whilst an extremely hot white dwarf is able to produce a flat spectrum in the optical range, the luminosity of such an object is forbidden by the Gaia distance measurement. This preference for a flat spectrum is reflected in the high, and highly uncertain, best fit $T_{\text{eff}} = 18200 \pm 9000\text{K}$, though the posterior π distribution is consistent with the Gaia measurement of 1.41 ± 0.78 mas, with slightly reduced uncertainty. Also note that this system appears to have the lowest white dwarf mass of the sample, of only $0.59 \pm 0.08M_{\odot}$. Despite these issues with the white dwarf fitting, as demonstrated in Chapter 4 the uncertain white dwarf model has little impact on the system parameters, and the resulting characterisation can still be considered valid.

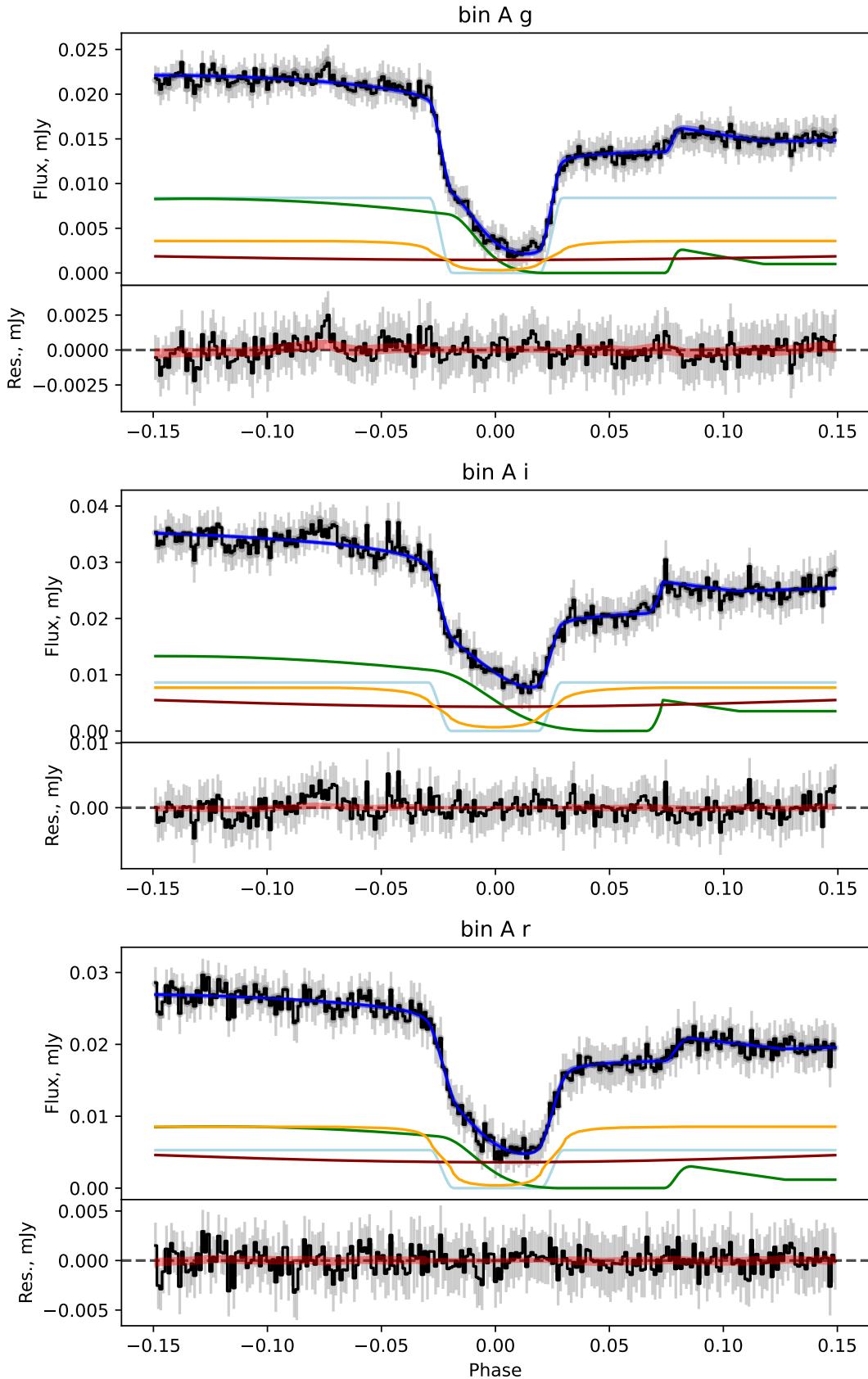


Figure 5.19: CSS090419 light curve models. Symbols are the same as Figure 4.1. Data are the results of binning all available eclipses.

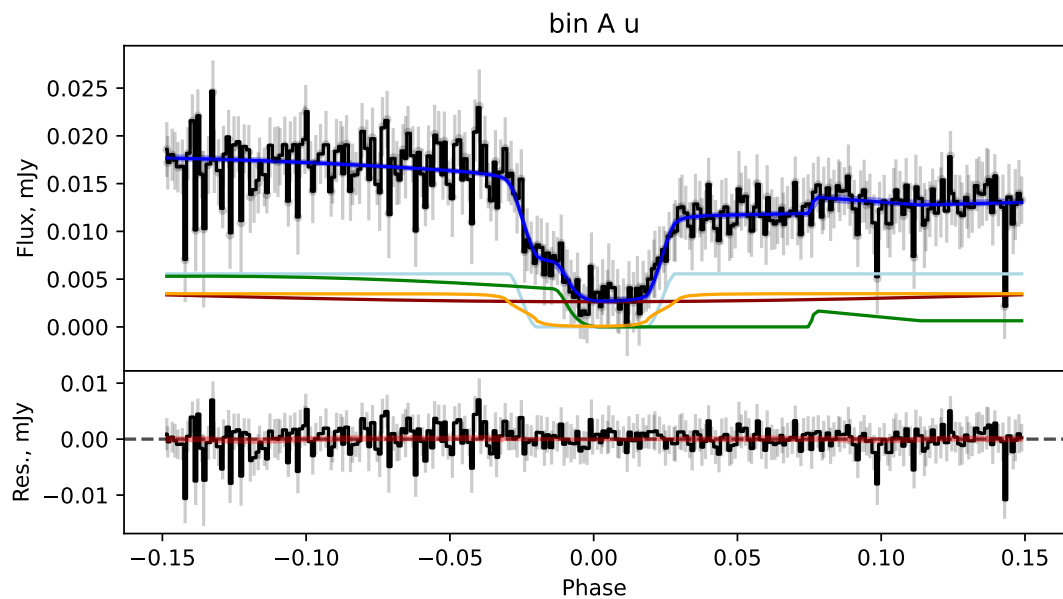


Figure 5.20: CSS090419 light curve models (cont.). Data are the results of binning all available eclipses.

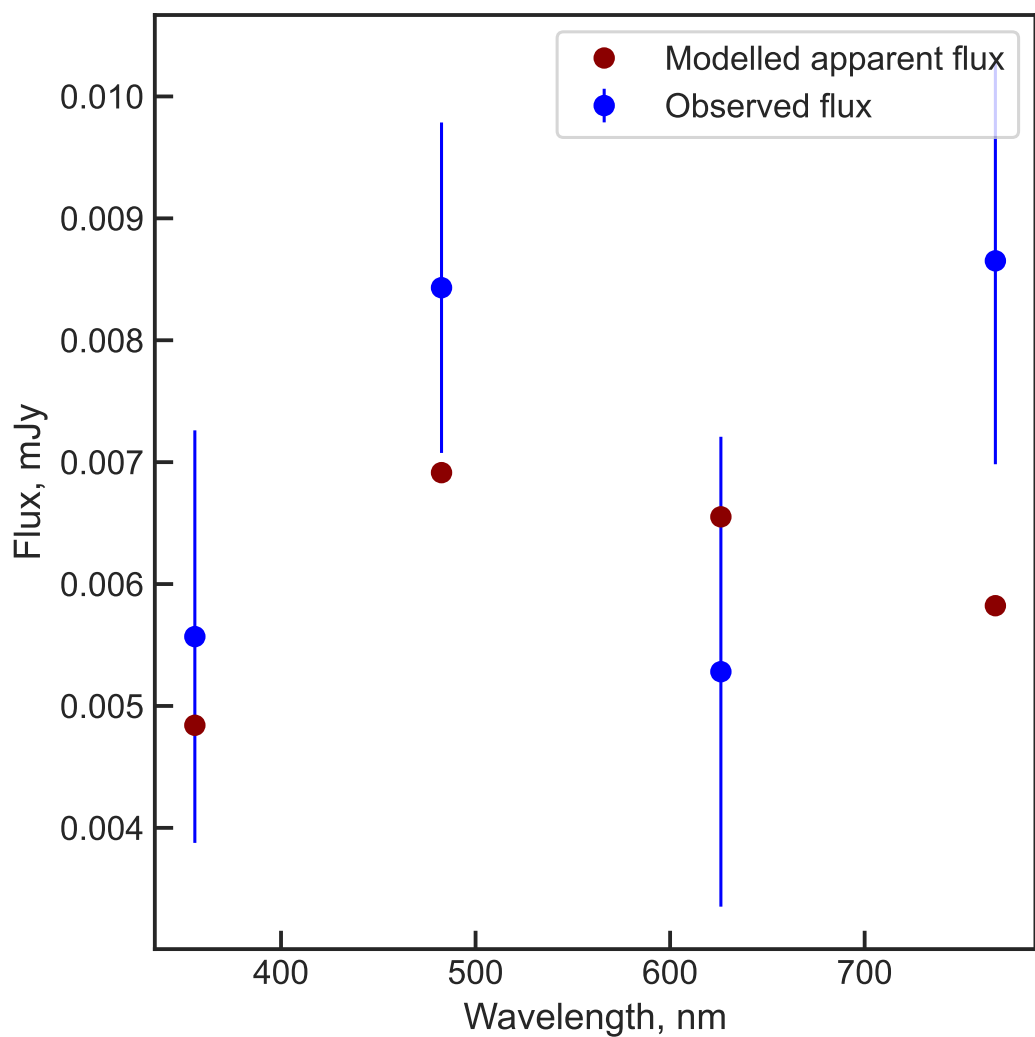


Figure 5.21: CSS090419 observed white dwarf fluxes, compared to the best-fit model atmosphere.

5.1.8 CSS090622

These observations fell into two binning categories, due to a significant dimming of the disc by a factor of ~ 3 between 2014/8/5 and 2014/8/8. Note that all eclipses (except the bin A u' eclipse) show a slight dip in flux before white dwarf ingress, possibly due to some absorbing feature in the disc. Whilst both data sets are suitable for modelling, with eclipse features that are distinct enough to characterise, the post-disc-dimming data are significantly improved, with clear, sharp ingresses and egresses. Without the improved feature resolution, this system would be significantly more challenging to model due to the severely blended u' band eclipse in the bin A eclipses.

The resulting white dwarf flux fit is acceptable, converging on $\pi = 2.02 \pm 0.27$ mas to agree with the Gaia $\pi = 2.08 \pm 0.27$ mas, and finding a white dwarf mass of $0.67 \pm 0.06 M_{\odot}$. The period and donor mass are consistent with the ‘optimal’ Knigge et al. (2011) donor track.

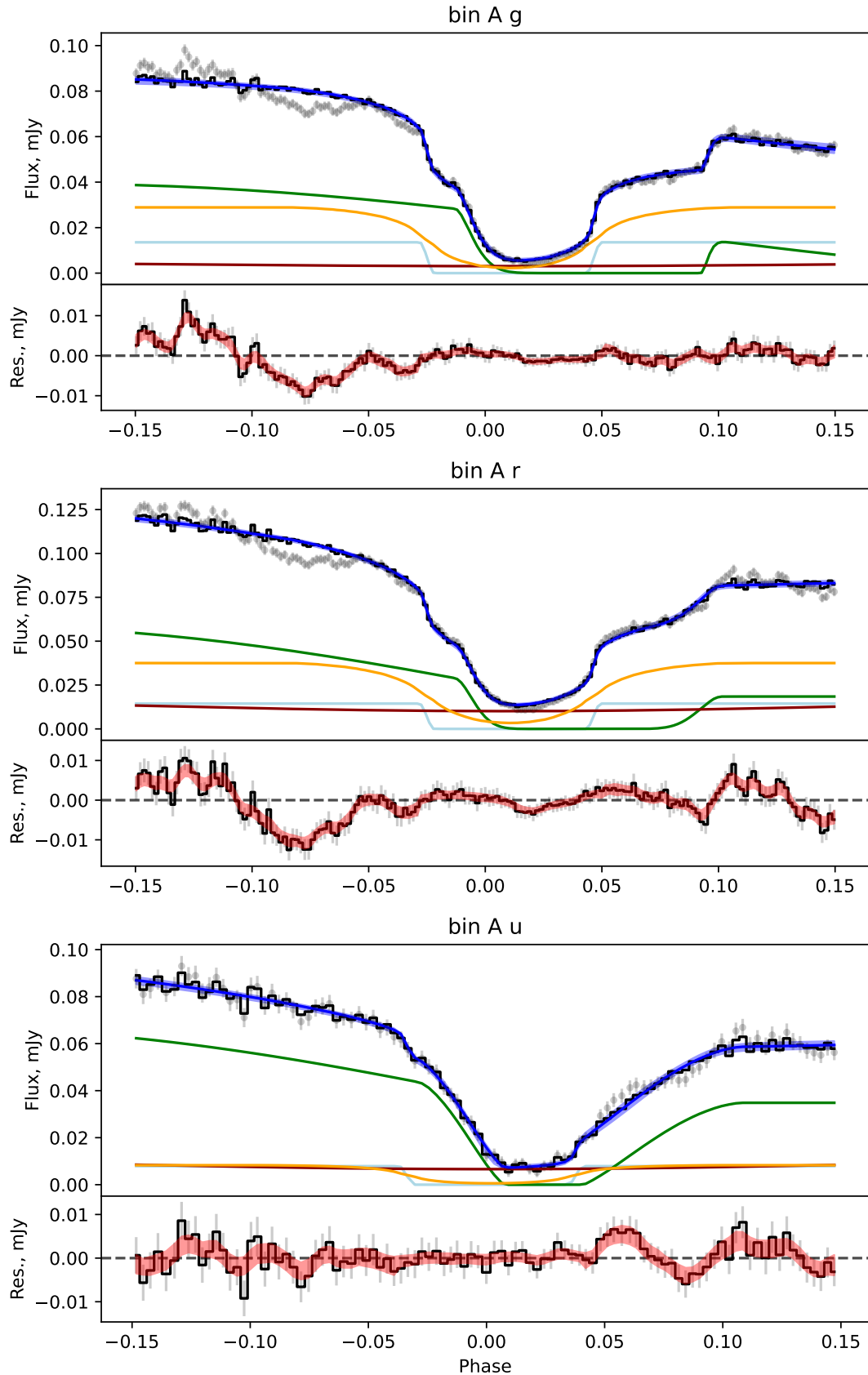


Figure 5.22: CSS090622 light curve models. Symbols are the same as Figure 4.1. Data are the result of binning together the three eclipses of 2014/8/5.

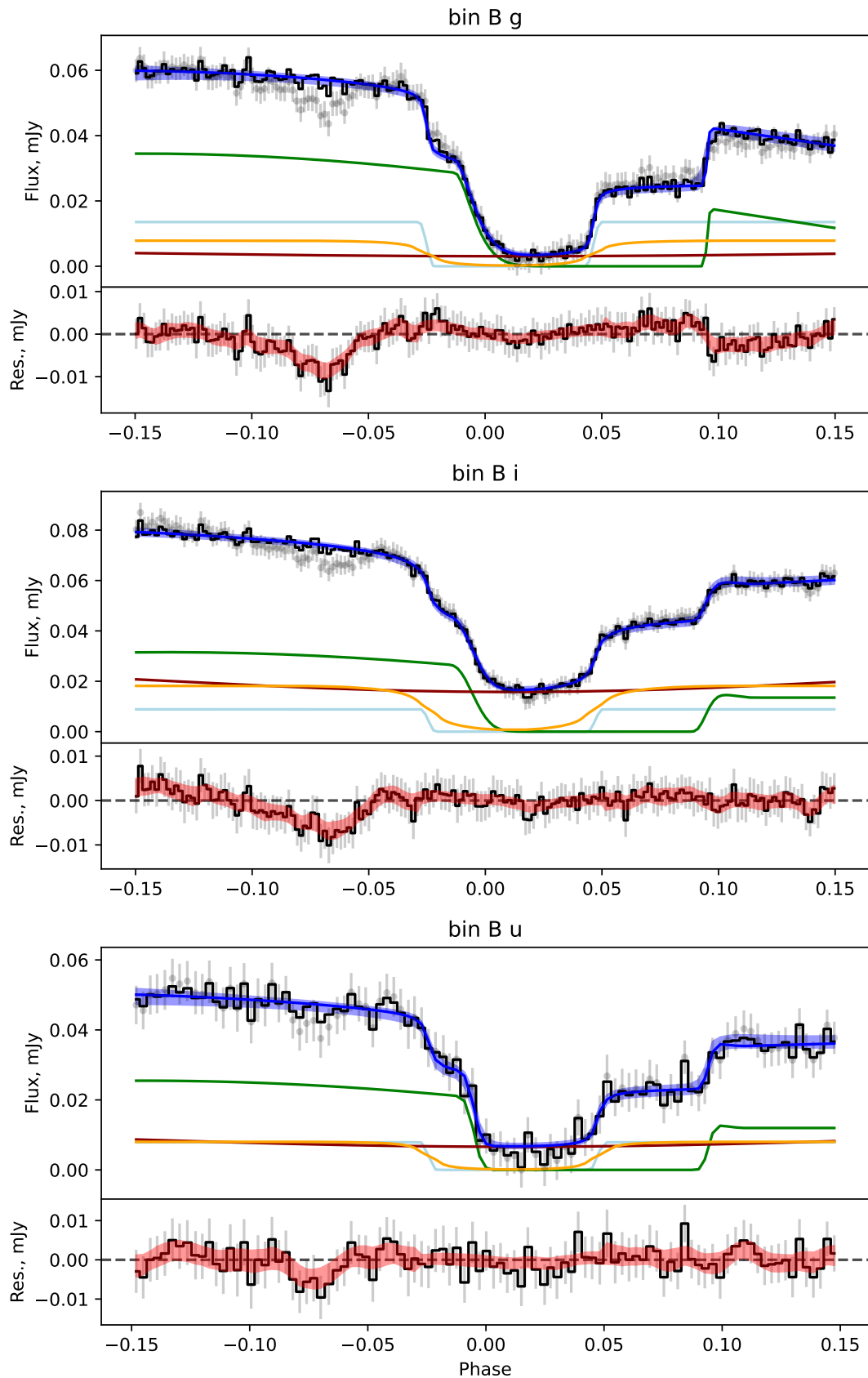


Figure 5.23: CSS090622 light curve models (cont.). Data are the result of binning together the eclipses of 2014/8/8, 2014/8/9, 2014/8/11.

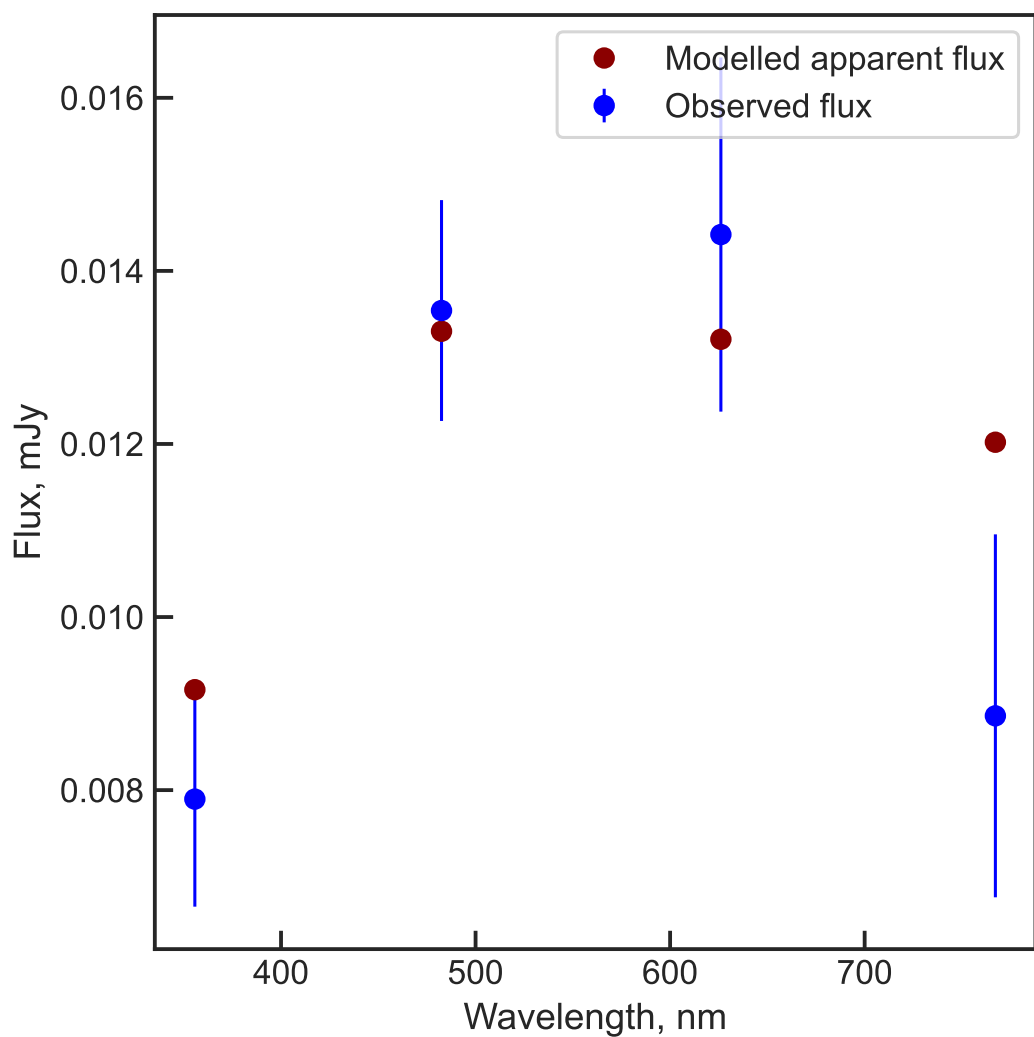


Figure 5.24: CSS090622 observed white dwarf fluxes, compared to the best-fit model atmosphere.

5.1.9 MASOT0014

As this system has strong disc features and significant flickering, modelling was challenging. Flickering during white dwarf ingress and egress resulted in uncertain white dwarf flux measurements, and the weak bright spot egress was similarly masked, though the severity of this was reduced somewhat by the hierarchical model. In addition, this system is host to a significant disc, which can obscure the fainter bright spot features. Despite this, the white dwarf fluxes are well-described by the cooling tracks, and Figure 5.41 shows this system as consistent with the ‘standard’ donor evolution track. Further supporting the model fitting is the Gaia $\pi = 2.31 \pm 0.13$ mas, closely agreeing with the white dwarf atmosphere fitting value of 2.42 ± 0.11 mas.

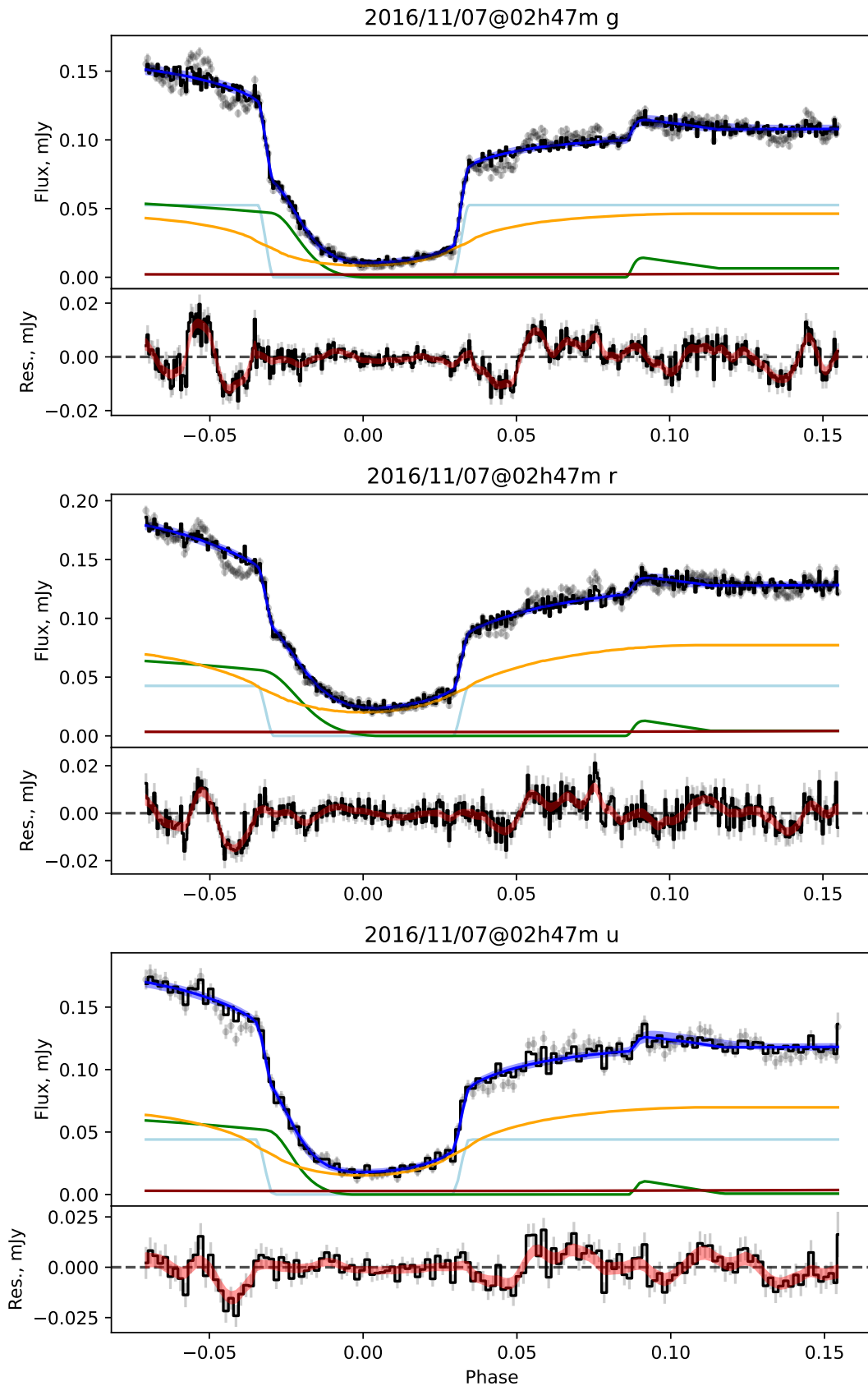


Figure 5.25: MAS0014 light curve models. Symbols are the same as Figure 4.1.

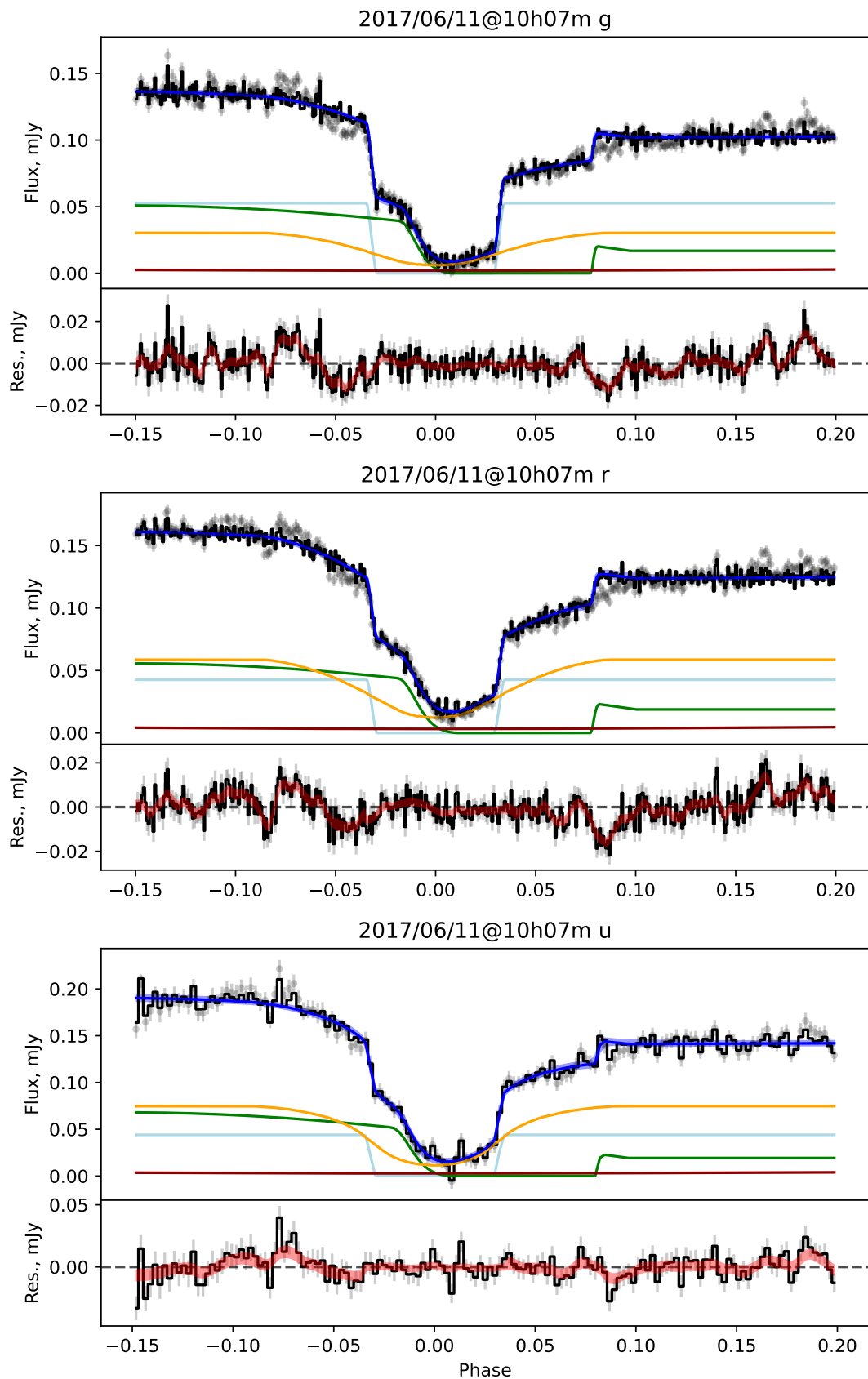


Figure 5.26: MAS0014 light curve models (cont.)

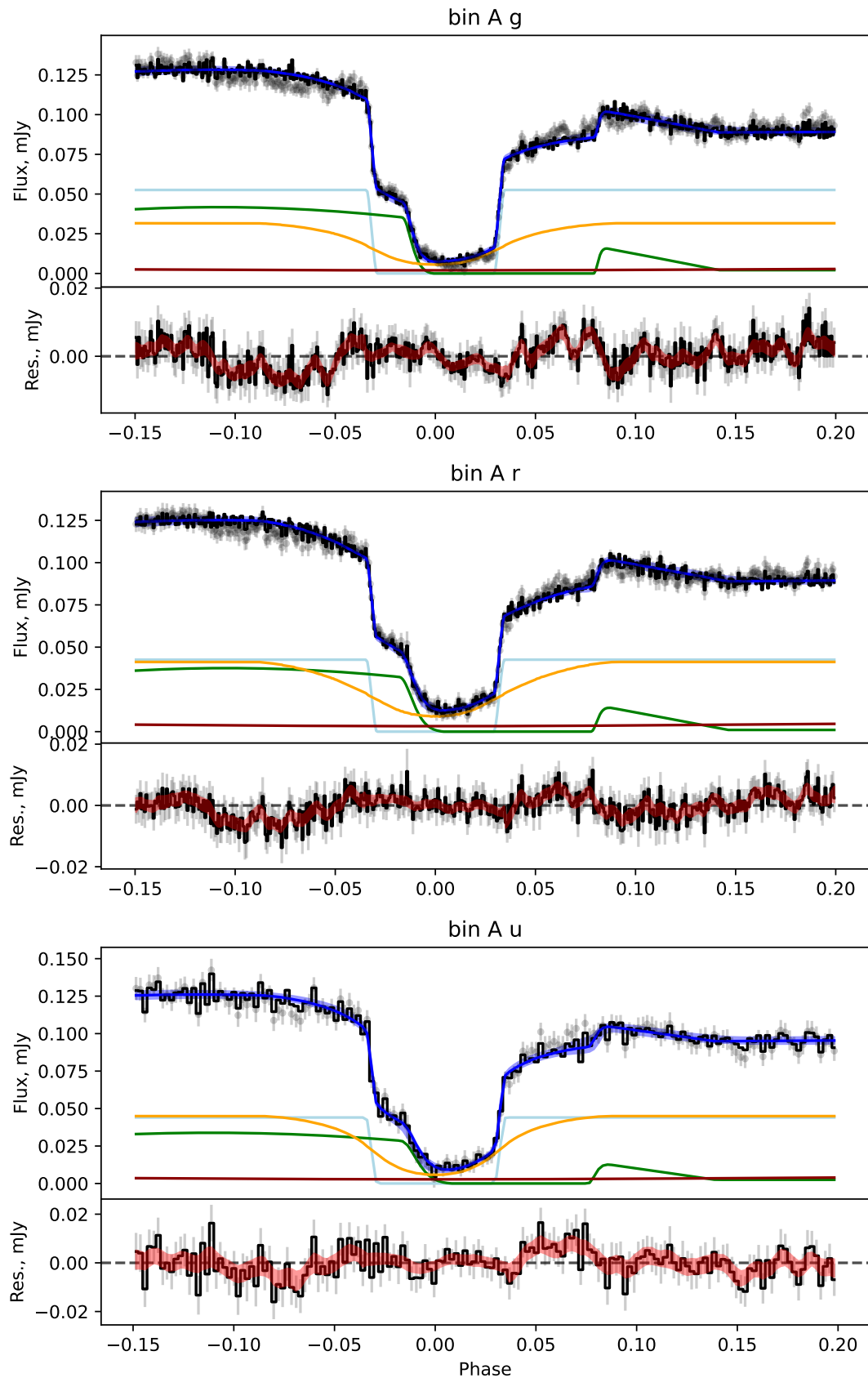


Figure 5.27: MAS0014 light curve models (cont.). Data are the result of binning together the eclipses of 2016/8/25 and 2016/8/26.

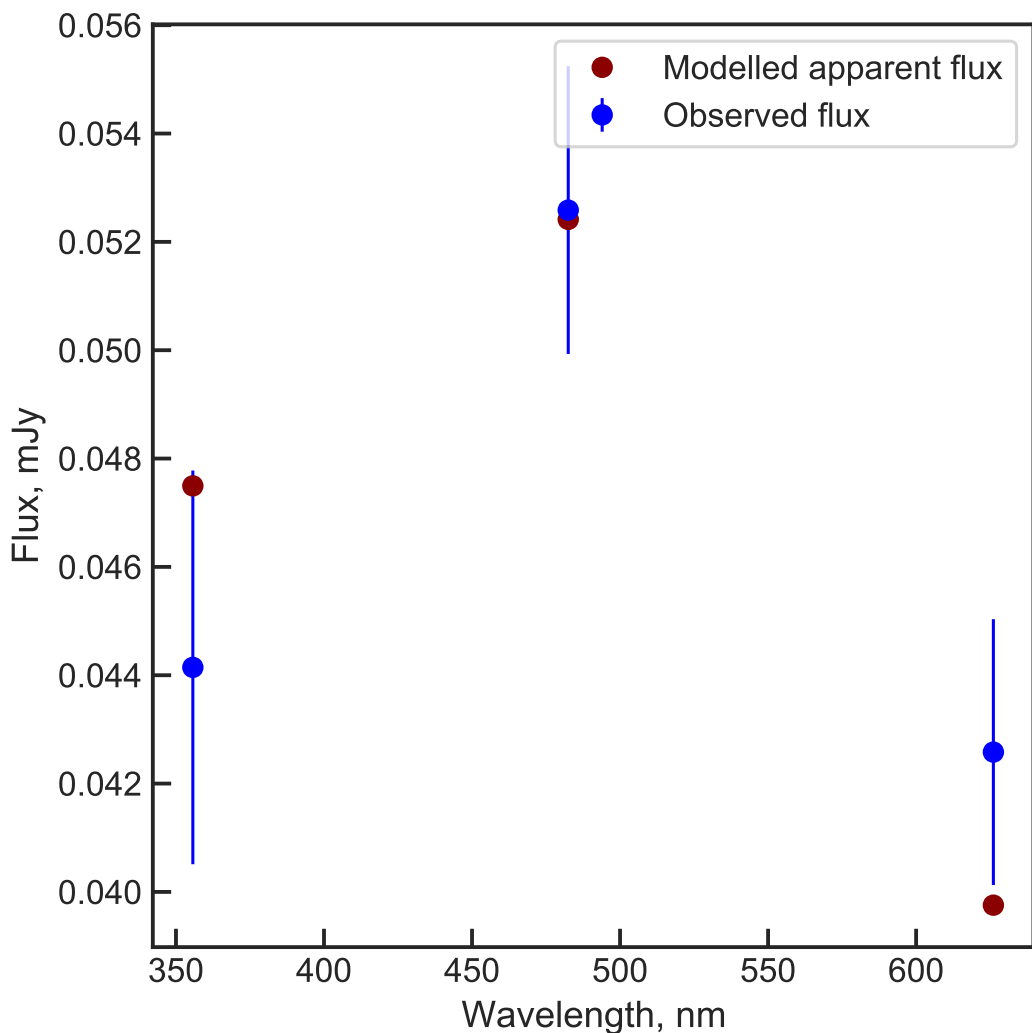


Figure 5.28: MAS0014 observed white dwarf fluxes, compared to the best-fit model atmosphere.

5.1.10 OGLE82

This system has only two observations, and 5 of the 6 resulting eclipses have distinct key eclipse features that make modelling significantly easier. The exception to this is the 2016/8/23 u' band eclipse, which has a weak bright spot and so an obfuscated bright spot egress. Most eclipses have significant flickering visible, which reduces as expected during the white dwarf eclipse, and appears to be generally less severe in the eclipse of 2016/8/23. System parameters are well-constrained and sensible, with white dwarf fluxes that are reproduced by model cooling tracks and a donor mass that places this CV approximately 1σ above the ‘standard’ donor track.

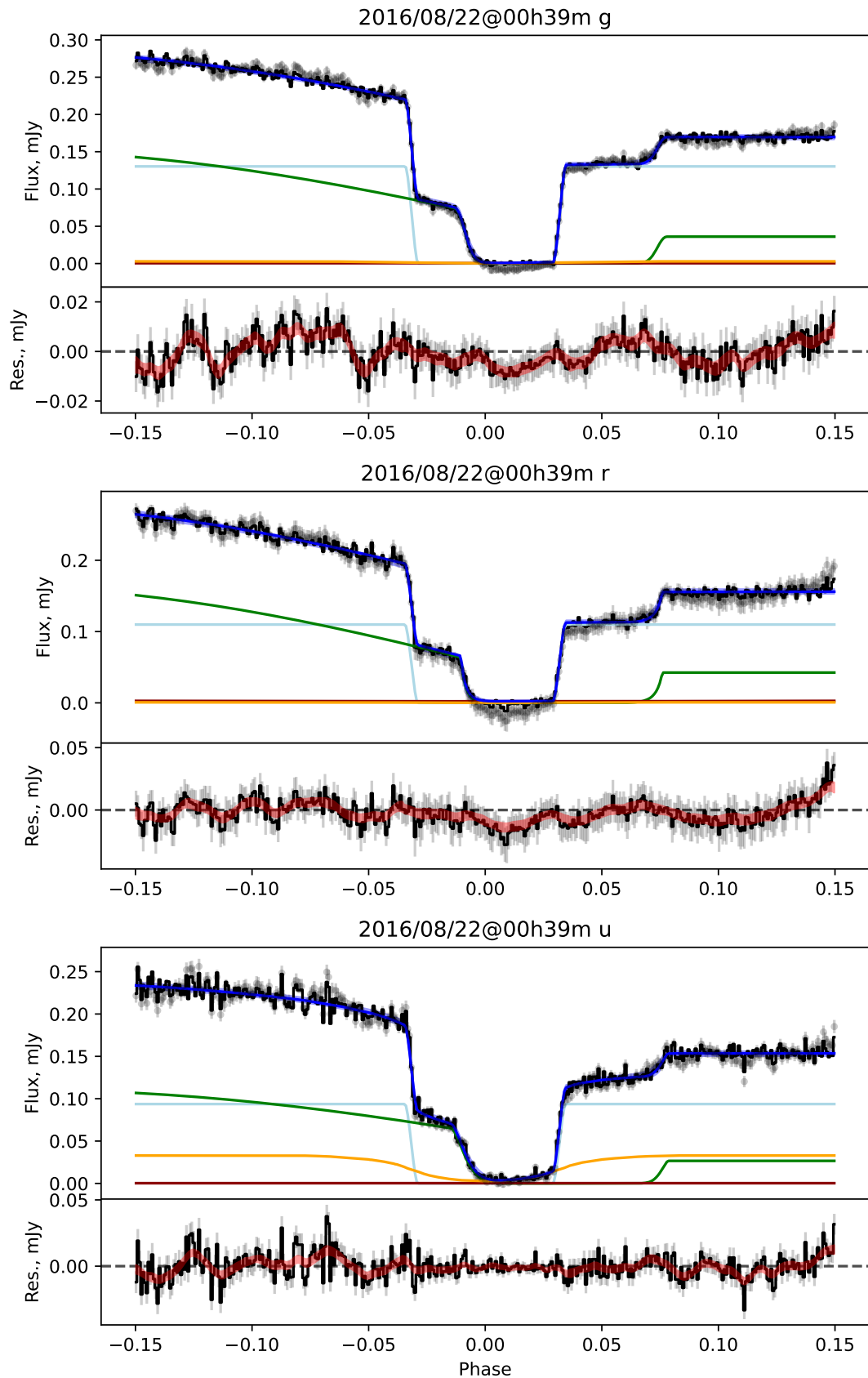


Figure 5.29: OGLE82 light curve models. Symbols are the same as Figure 4.1

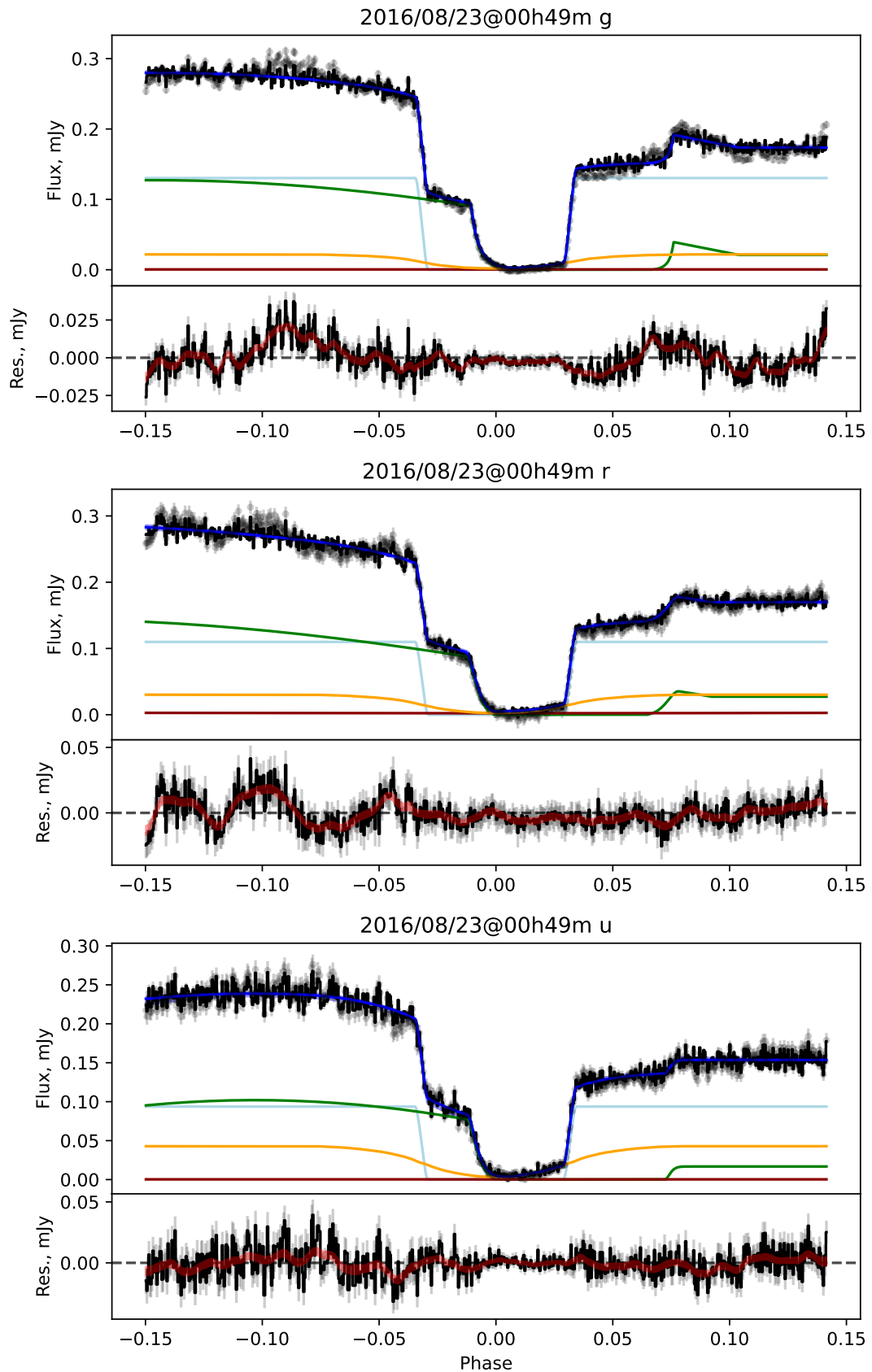


Figure 5.30: OGLE82 light curve models (cont.)

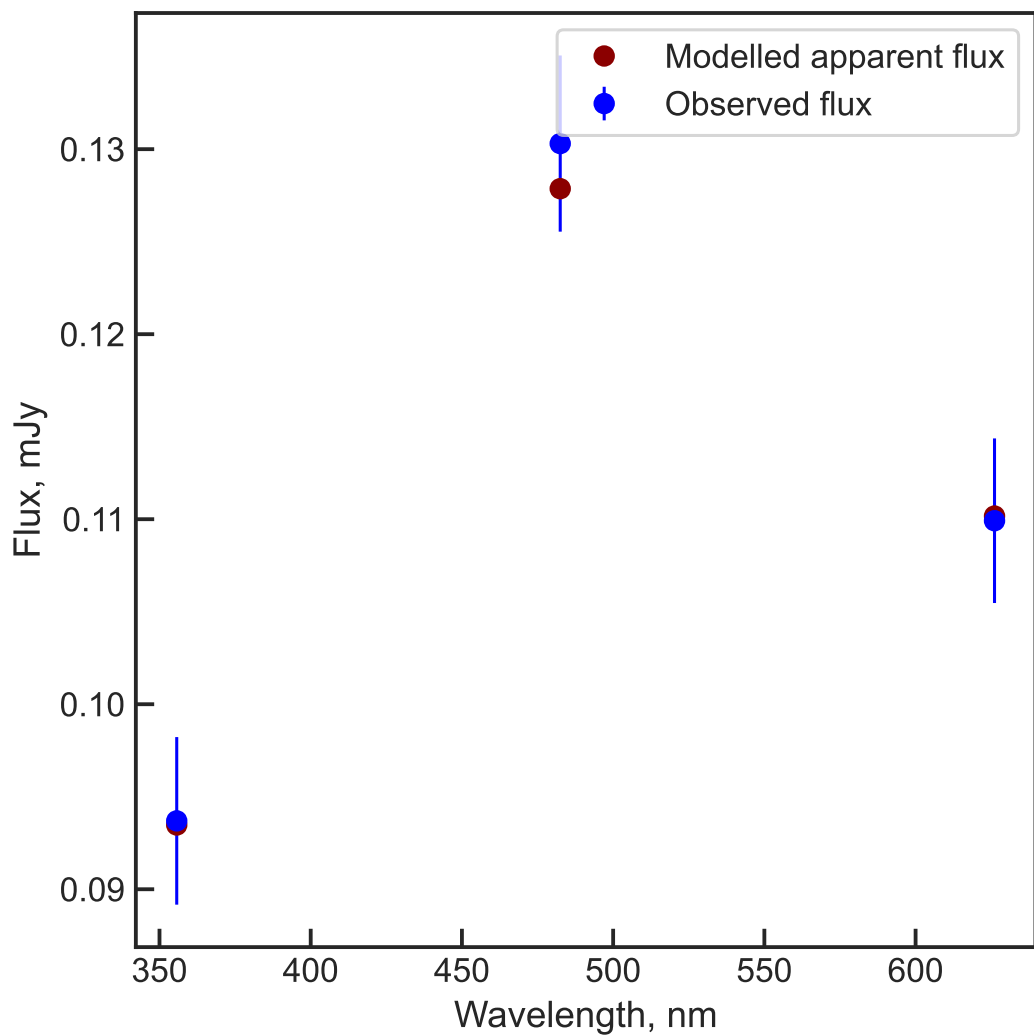


Figure 5.31: OGLE82 observed white dwarf fluxes, compared to the best-fit model atmosphere.

5.1.11 SDSS J0748

For this system, several KG5 eclipses were recorded over the course of the observations. Whilst it is possible to use KG5 data in modelling, this was not done for this analysis. Rather, the KG5 eclipses were used to constrain the period, then discarded. The KG5 eclipses are still reported in Table 2.16.

SDSS J0748 has only two u' band observations, one ULTRACAM observation, and one ULTRASPEC observation. These data have heavily blended white dwarf and bright spot ingresses, which are challenging to model. The poor u' band data are reflected in the large uncertainty in white dwarf flux, since other important parameters such as $\Delta\phi$ and R_{wd} could be constrained by other eclipses. Importantly, the two eclipses from 2018/2/5 and 2018/2/7 have distinct features, that enable modelling, though interestingly the phase offset between the white dwarf eclipse and bright spot is significant enough that the white dwarf *ingress* is blended with the bright spot *egress* in the case of the former, which is not seen in any other eclipse presented here.

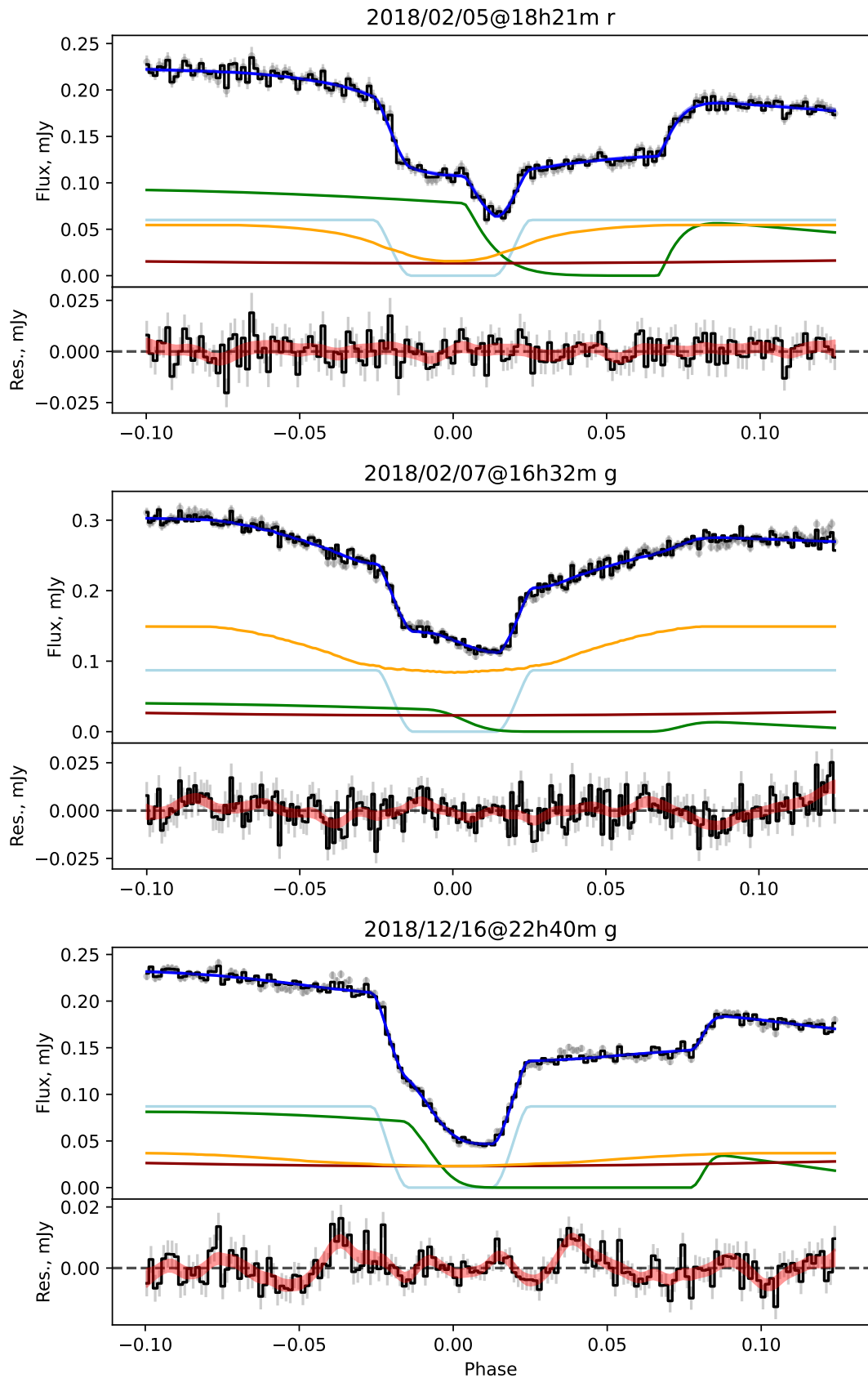


Figure 5.32: SDSS J0748 light curve models. Symbols are the same as Figure 4.1

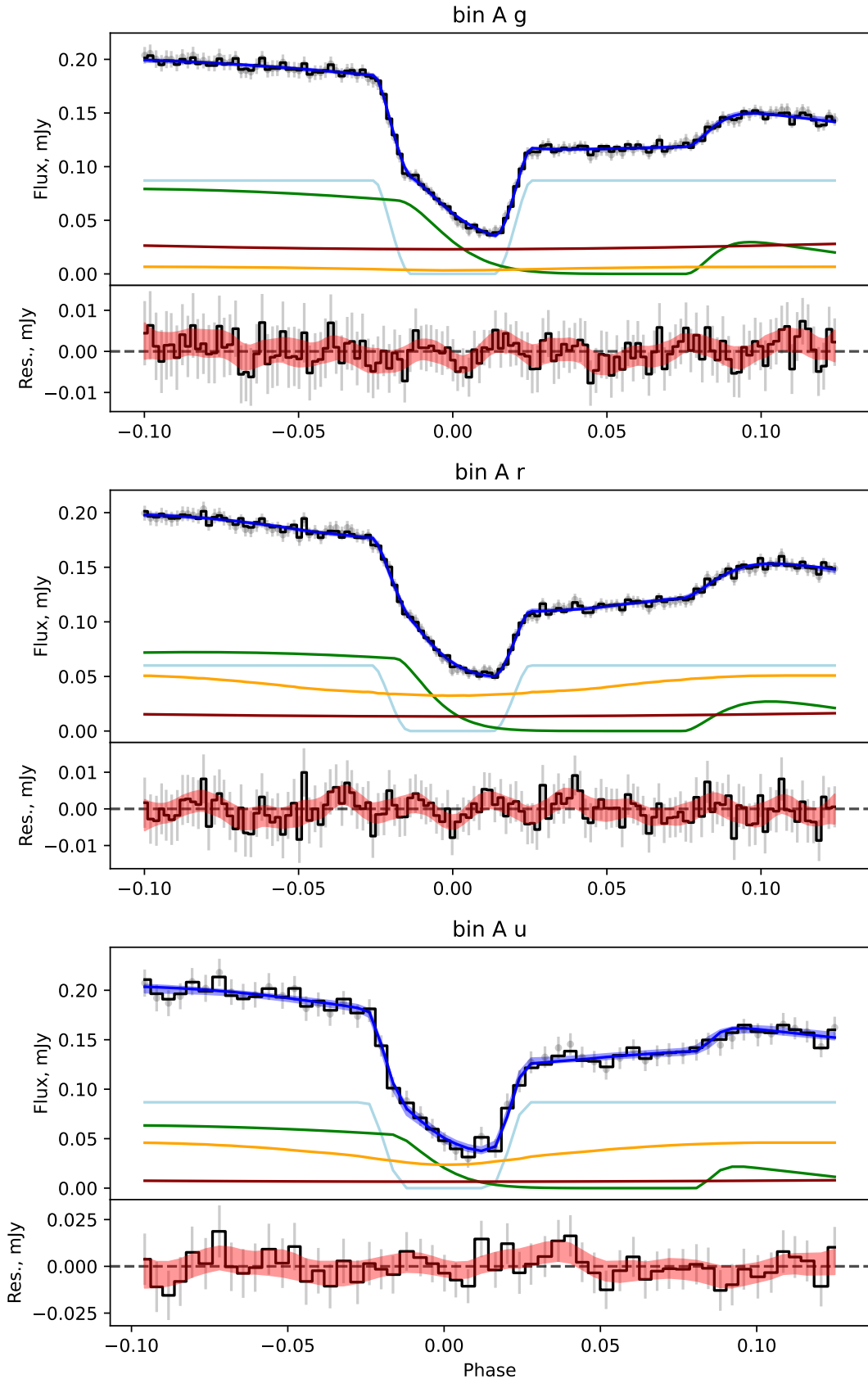


Figure 5.33: SDSS J0748 light curve models (cont.). Data are the result of binning the following eclipses: both eclipses of 2017/2/14, 2017/2/24, 2017/3/20, 2018/12/17.

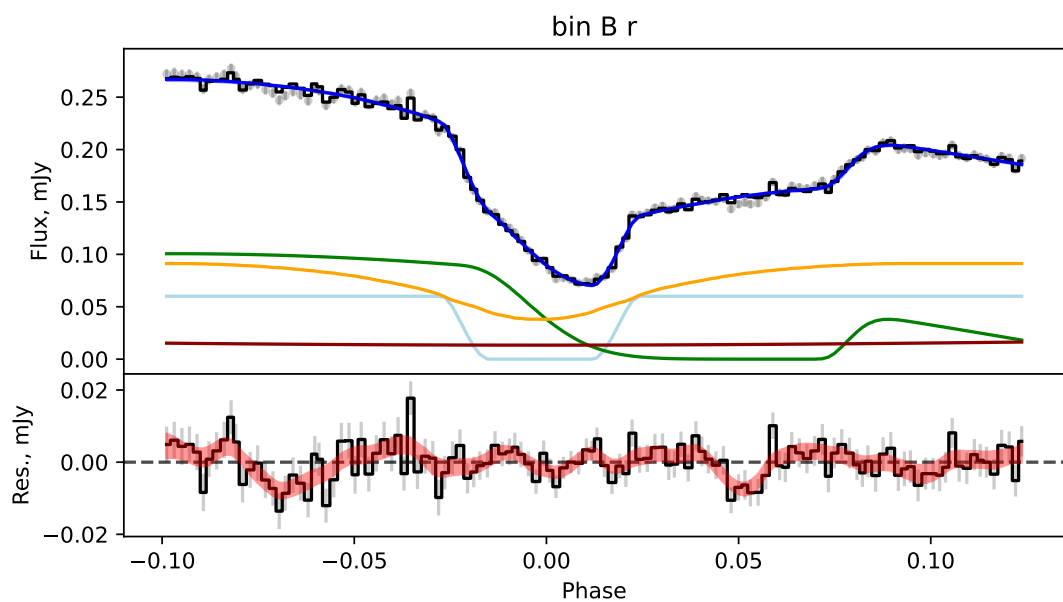


Figure 5.34: SDSS J0748 light curve models (cont.). Data are the result of combining the eclipse of 2018/2/4 with the two r' band eclipses observed on 2018/12/17.

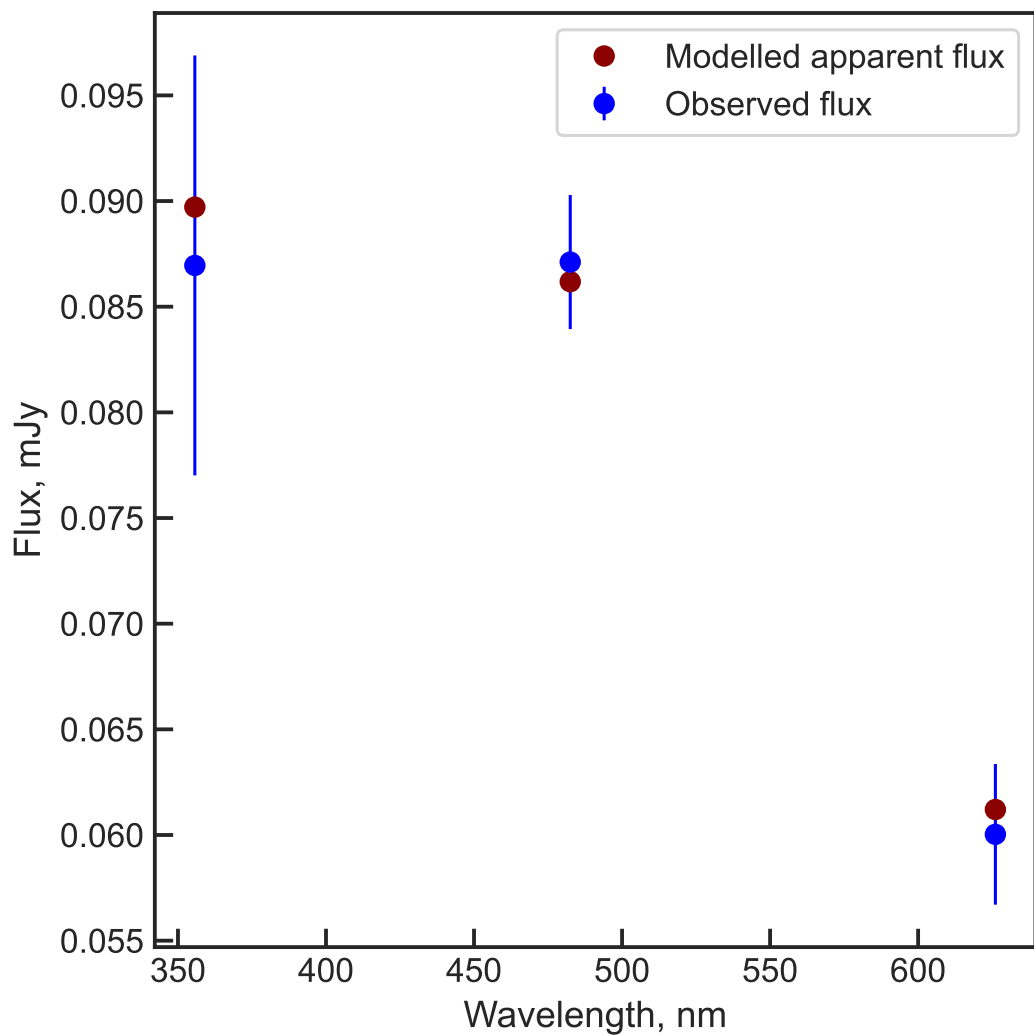


Figure 5.35: SDSS J0748 observed white dwarf fluxes, compared to the best-fit model atmosphere.

5.1.12 SDSS J1524

The binning of this system was somewhat non-standard, as the three filters on the eclipse of 2014/3/3 were not all equally consistent. The g_{reg} eclipse was consistent with the A binning group, but the u_{reg} and r_{reg} eclipses were not. As such, the u_{reg} and r_{reg} eclipses of this observation were fit individually, and the g_{reg} light curve was binned with the other relevant data. The resulting fits are broadly satisfactory, though some eclipses (namely the g_{reg} and r_{reg} eclipses of the A binning group) appear to have fairly poor white dwarf ingresses and egresses. However, the resulting fits give a well-constrained donor mass that agrees strongly with the ‘optimal’ [Knigge et al. \(2011\)](#) donor track, suggesting the results are reasonable. The white dwarf fits are not ideal, but do not diverge from models by enough to cause concern.

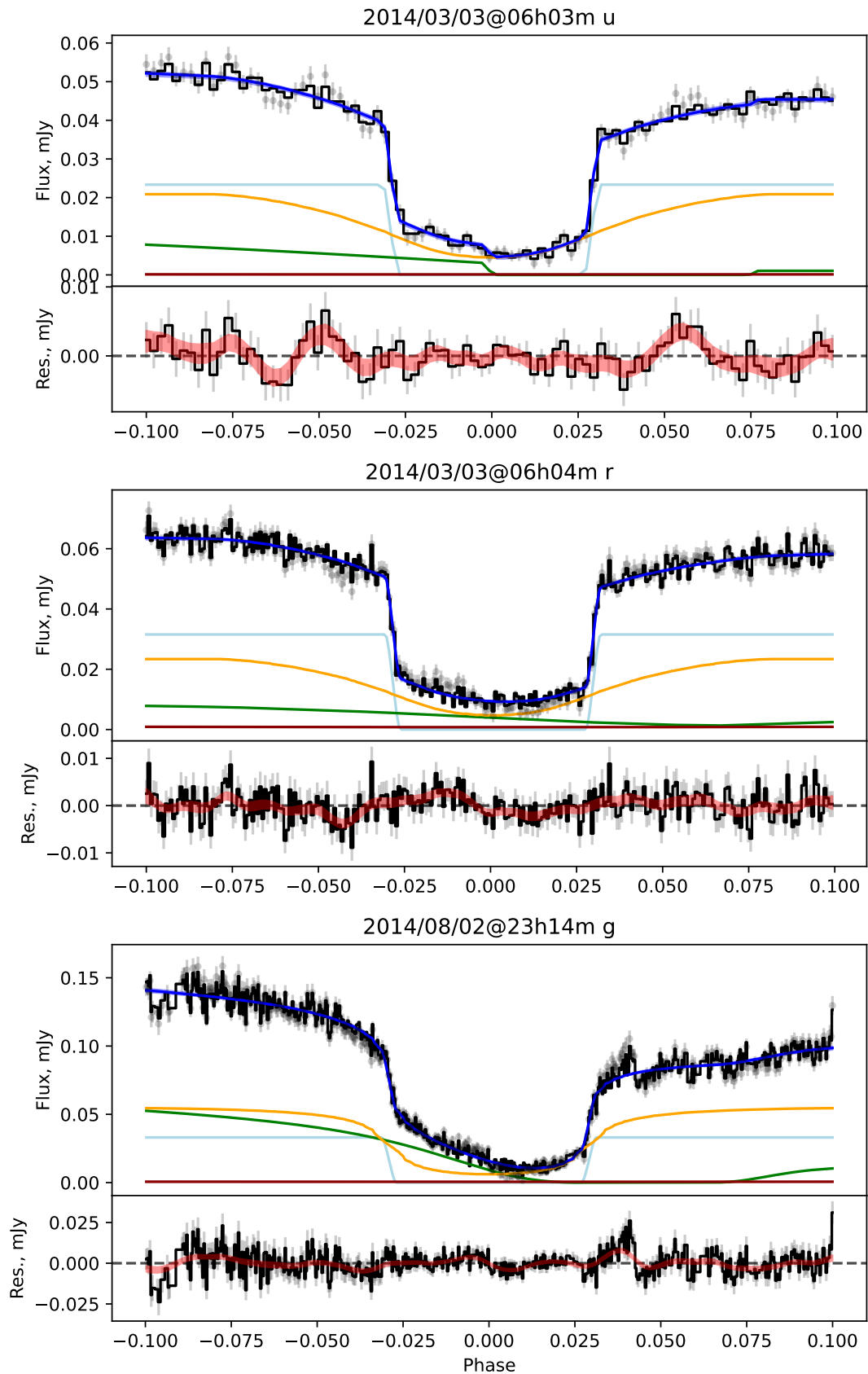


Figure 5.36: SDSS J1524 light curve models. Symbols are the same as Figure 4.1

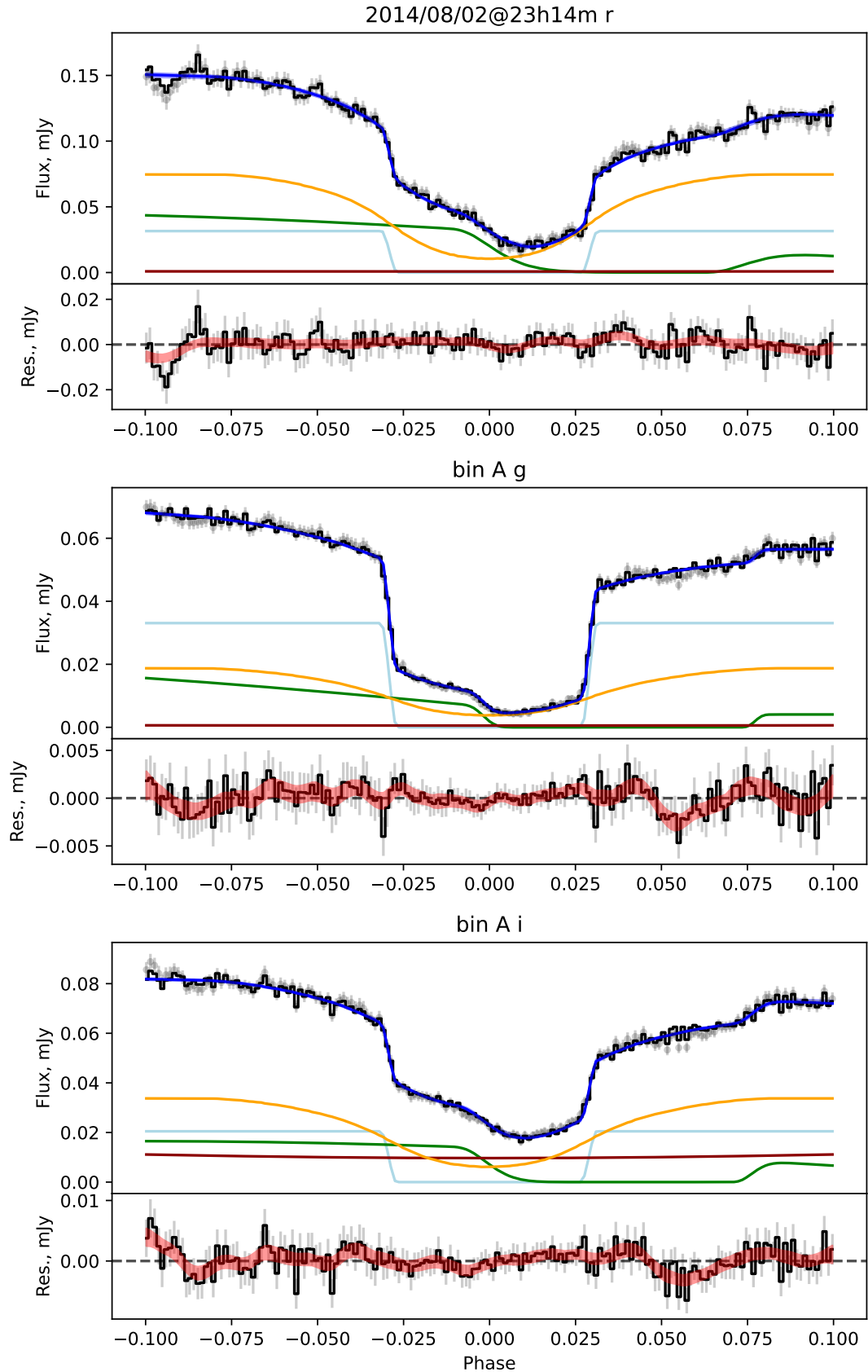


Figure 5.37: SDSS J1524 light curve models (cont.). Binned data are the result of combining eclipses from 2011/5/28, 2011/5/31, 2011/6/2, 2013/7/13, 2013/7/21, 2013/7/30, and, in the case of the *g'* band, 2014/3/3.

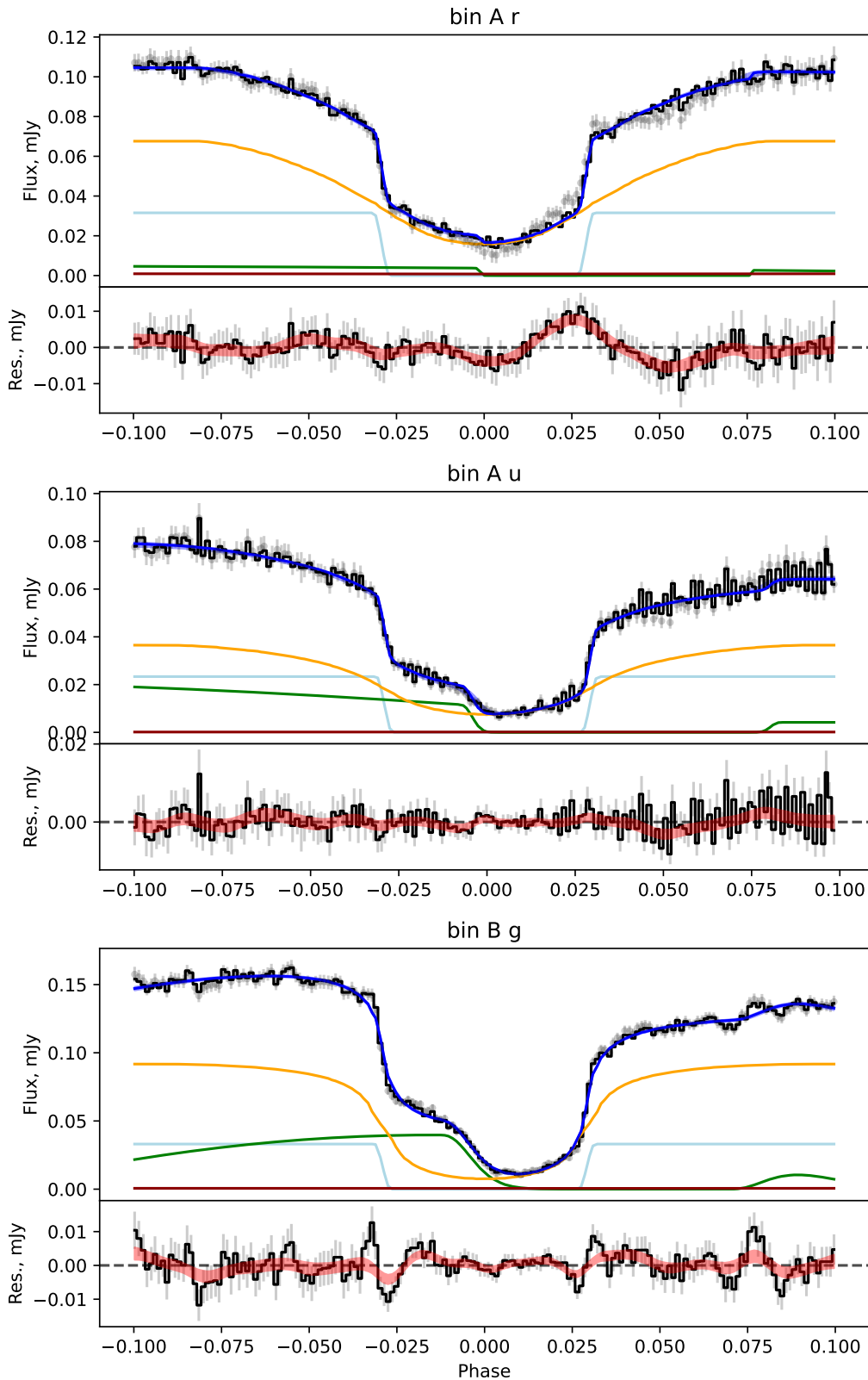


Figure 5.38: SDSS J1524 light curve models (cont.). Data labelled ‘bin A’ are a combination of the eclipses from the nights of Binned data are the result of combining eclipses from 2011/5/28, 2011/5/31, 2011/6/2, 2013/7/13, 2013/7/21, and 2013/7/30. Data labelled ‘bin B’ are the combination of 2012/4/29, 2012/4/29, and 2013/8/5.

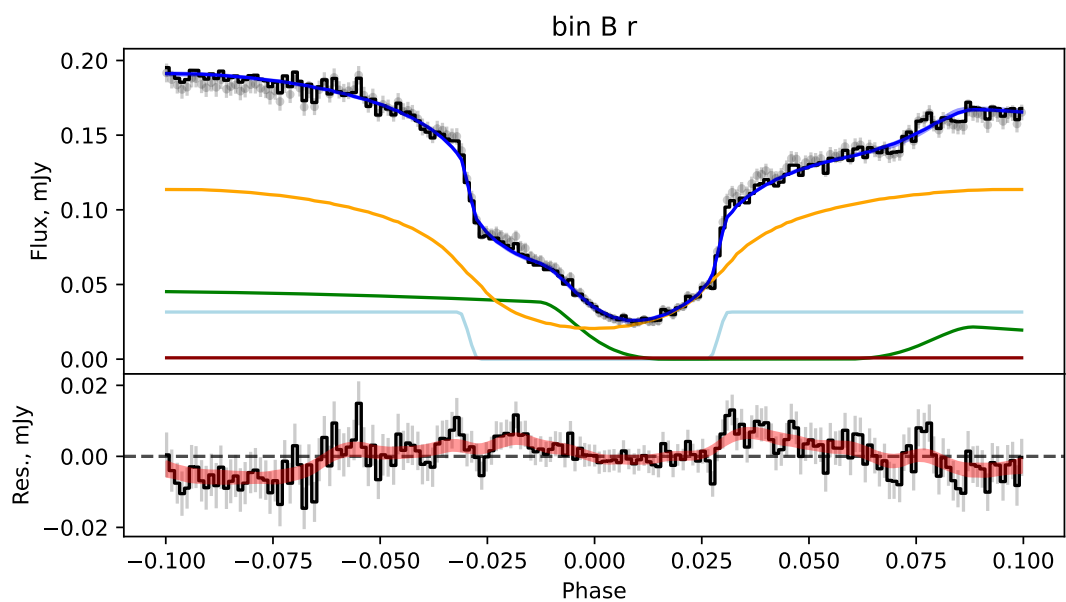


Figure 5.39: SDSS J1524 light curve models (cont.). Data are the combination of 2012/4/29, 2012/4/29, and 2013/8/5.

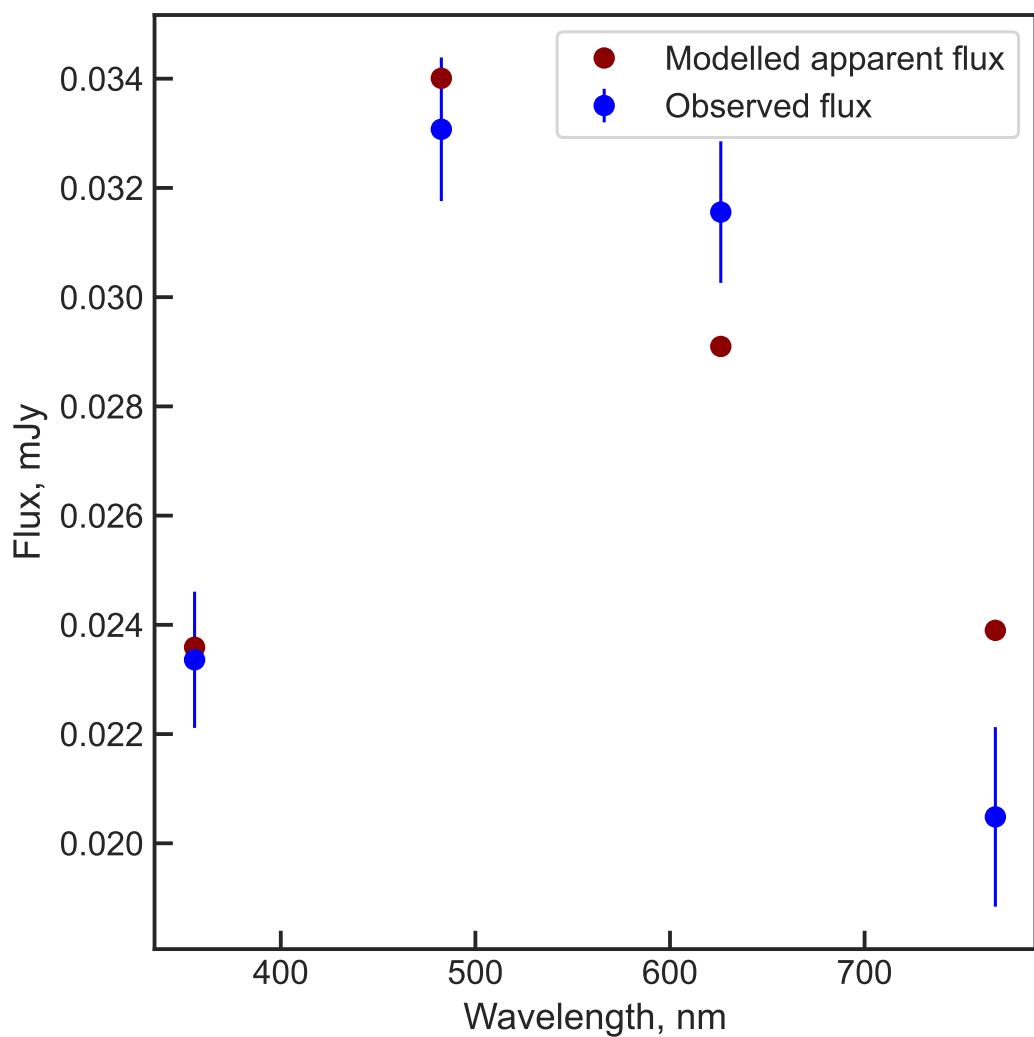


Figure 5.40: SDSS1524 observed white dwarf fluxes, compared to the best-fit model atmosphere.

Table 5.2: The system parameters found for the CVs analysed here. The reported parallax, π , is the posterior distribution from fitting the white dwarf fluxes, c.f. §3.3.2.

System Name:	ASASSN-14hq	ASASSN-14kb	ASASSN-15pb
M_{wd}/M_{\odot}	0.67 ± 0.01	0.74 ± 0.02	0.72 ± 0.03
R_{wd}/R_{\odot}	0.0119 ± 0.0001	0.0113 ± 0.0002	0.0115 ± 0.0005
$M_{\text{donor}}/M_{\odot}$	0.097 ± 0.002	0.134 ± 0.003	0.148 ± 0.008
$R_{\text{donor}}/R_{\odot}$	0.157 ± 0.001	0.164 ± 0.001	0.210 ± 0.004
q	0.145 ± 0.002	0.182 ± 0.002	0.206 ± 0.004
P , hours	$1.78384800(7)$	$1.63453(1)$	$2.23896(3)$
a/R_{\odot}	0.681 ± 0.004	0.670 ± 0.005	0.824 ± 0.014
i	80.35 ± 0.06	84.4 ± 0.1	79.4 ± 0.1
K_{wd} , km/s	58.0 ± 0.9	76.2 ± 1	75 ± 2
K_{donor} , km/s	399 ± 2	419 ± 3	364 ± 6
π , mas	3.40 ± 0.07	2.78 ± 0.11	1.0 ± 0.2
T_{eff} , K	14819 ± 800	17700 ± 1000	19200 ± 1600
$\log(g)$, cgs	8.11 ± 0.02	8.21 ± 0.03	8.17 ± 0.06

System Name:	ASASSN-17fo	AY For	CSS090102
M_{wd}/M_{\odot}	0.85 ± 0.01	0.78 ± 0.02	0.62 ± 0.03
R_{wd}/R_{\odot}	0.0099 ± 0.0001	0.0106 ± 0.0003	0.0126 ± 0.0004
$M_{\text{donor}}/M_{\odot}$	0.109 ± 0.002	0.106 ± 0.006	0.060 ± 0.003
$R_{\text{donor}}/R_{\odot}$	0.1436 ± 0.0007	0.162 ± 0.003	0.119 ± 0.002
q	0.1267 ± 0.0005	0.136 ± 0.004	0.094 ± 0.002
P , hours	$1.477147(2)$	$1.790756(1)$	$1.49723786(5)$
a/R_{\odot}	0.646 ± 0.003	0.717 ± 0.007	0.582 ± 0.008
i	84.23 ± 0.03	84.0 ± 0.2	88.7 ± 0.6
K_{wd} , km/s	60.2 ± 0.4	57.8 ± 2.0	40.9 ± 1.2
K_{donor} , km/s	468 ± 2	425 ± 4	431 ± 6
π , mas	1.79 ± 0.36	2.12 ± 0.16	1.41 ± 0.30
T_{eff} , K	14800 ± 600	18100 ± 500	14800 ± 1200
$\log(g)$, cgs	8.37 ± 0.02	8.28 ± 0.04	8.00 ± 0.33

Table 5.3: Table 5.2, continued.

System Name:	CSS090419	CSS090622	MASOT0014
M_{wd}/M_{\odot}	0.59 ± 0.08	0.67 ± 0.06	0.86 ± 0.03
R_{wd}/R_{\odot}	0.0122 ± 0.0009	0.0112 ± 0.0007	0.0097 ± 0.0003
$M_{\text{donor}}/M_{\odot}$	0.087 ± 0.011	0.104 ± 0.009	0.122 ± 0.007
$R_{\text{donor}}/R_{\odot}$	0.152 ± 0.007	0.155 ± 0.005	0.165 ± 0.003
q	0.146 ± 0.003	0.159 ± 0.008	0.142 ± 0.004
P , hours	$1.81062621(6)$	$1.702302(6)$	$1.7167077(5)$
a/R_{\odot}	0.660 ± 0.030	0.661 ± 0.020	0.722 ± 0.008
i	80.9 ± 0.1	88.2 ± 0.6	84.8 ± 0.3
K_{wd} , km/s	56.0 ± 2.7	63.7 ± 2.5	63.2 ± 2.0
K_{donor} , km/s	381 ± 16	408 ± 12	445 ± 5
π , mas	1.42 ± 0.69	2.02 ± 0.27	2.42 ± 0.11
T_{eff} , K	18200 ± 9000	9800 ± 1500	17300 ± 1000
$\log(g)$, cgs	8.04 ± 0.12	8.16 ± 0.08	8.37 ± 0.04

System Name:	OGLE82	SDSS J0748	SDSS J1524
M_{wd}/M_{\odot}	0.83 ± 0.01	0.68 ± 0.02	0.99 ± 0.01
R_{wd}/R_{\odot}	0.0099 ± 0.0002	0.0121 ± 0.0004	0.0082 ± 0.0003
$M_{\text{donor}}/M_{\odot}$	0.131 ± 0.004	0.066 ± 0.004	0.097 ± 0.003
$R_{\text{donor}}/R_{\odot}$	0.170 ± 0.002	0.117 ± 0.002	0.144 ± 0.001
q	0.157 ± 0.002	0.095 ± 0.004	0.099 ± 0.001
P , hours	$1.7263398(6)$	$1.39947(1)$	$1.56764953(2)$
a/R_{\odot} ,	0.720 ± 0.006	0.575 ± 0.007	0.701 ± 0.006
i	83.9 ± 0.1	81.7 ± 0.2	85.8 ± 0.1
K_{wd} , km/s	68.5 ± 1.0	42.2 ± 1.8	48.6 ± 0.8
K_{donor} , km/s	435 ± 3	450 ± 5	493 ± 5
π , mas	3.82 ± 0.12	1.83 ± 0.14	1.95 ± 0.18
T_{eff} , K	18000 ± 4000	22500 ± 3000	12500 ± 900
$\log(g)$, cgs	8.37 ± 0.03	8.11 ± 0.03	8.61 ± 0.04

5.2 Comparing observations with model donor tracks

The observed donor properties can be compared to the [Knigge et al. \(2011\)](#)-like MESA donor tracks. Figure 5.41 shows the full sample of short-period eclipse modelled CVs (a catalogue of these systems is given in Appendix A.1) plotted with the ‘standard’ donor track that includes only gravitational braking below the gap and the disagreement between model and data indeed persists.

There is a large scatter in the observations, but new data continue to lie systematically to the right of the ‘standard’ model track (shown by the blue line), and the need for extra AML continues to be supported by observations. The new data appear to have a significant scatter about the canonical donor evolutionary tracks. Typically, scatter in CV donor tracks is explained as being due to different white dwarf masses, but the effect of this on P is thought to be relatively small, on the order of a few minutes ([Goliasch & Nelson, 2015](#)), and falls significantly short of explaining these new results. Further discrediting this as the source of scatter is Figure 5.41, which illustrates that whilst the average white dwarf mass of this sample is indeed slightly lower than the canonical [Pala et al. \(2020\)](#) value, the difference is small and its effects are unlikely to be significant.

There are then two possibilities for this scatter: either the parameter estimations of this thesis are somehow flawed, or CV donor evolution is not as unified as believed; at this time, it is difficult to rule out either option. The majority of the eclipse model fits do not give significant cause for concern about their validity. In theory, the new hierarchical model only requires a single example of distinct egresses to constrain the mass ratio, with other eclipses only needed to constrain the white dwarf fluxes. However, I have not included a thorough study into the hierarchical model’s ability to recover parameters from blended eclipse features. Such a study would be desirable, to better understand the capabilities of the new model. If, however, these results are to be believed (and there is little cause not to), this may indicate that the canonical idea of a unified track does not account for possibly significant effects, such as variation in the age or formation metallicity of the donor, or variations in the degree of excess AML that is known to be present in these CVs.

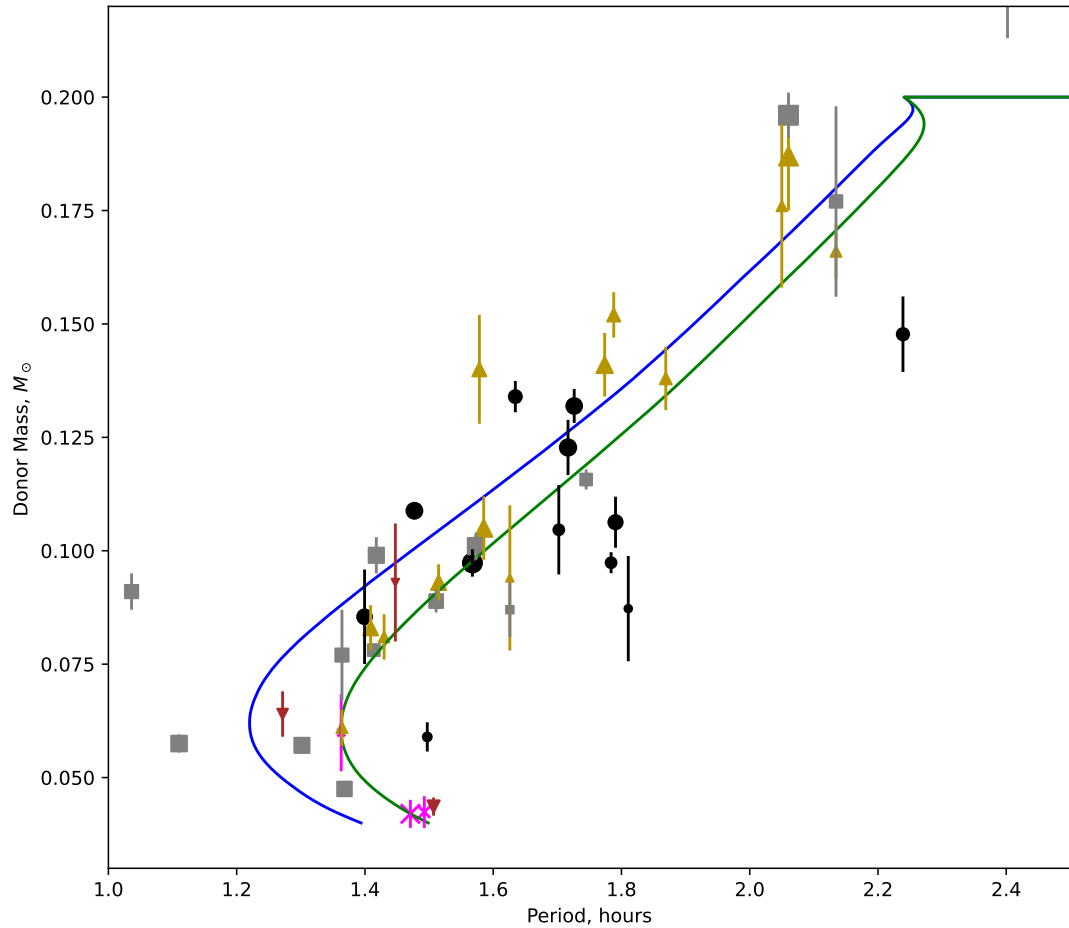


Figure 5.41: Showing how eclipse modelled observations compare with evolutionary models in the short period regime. The **solid blue line** is the ‘standard’ Knigge et al. (2011) donor track with only gravitational braking below the period gap, and the **solid green line** is the ‘optimal’ track with $2.47\times$ amplified gravitational braking. Data points are scaled based on their white dwarf masses. The **magenta crosses** are the 3 CVs with peculiar colours from Chapter 4, **black circles** are the 12 systems of Chapter 5, **gold upright triangles** are data from McAllister et al. (2019), **grey squares** are from Savoury et al. (2011), and the **brown inverted triangles** are the supplementary systems from Gänsicke et al. (2010); McAllister et al. (2015); McAllister et al. (2017a); McAllister et al. (2017b).

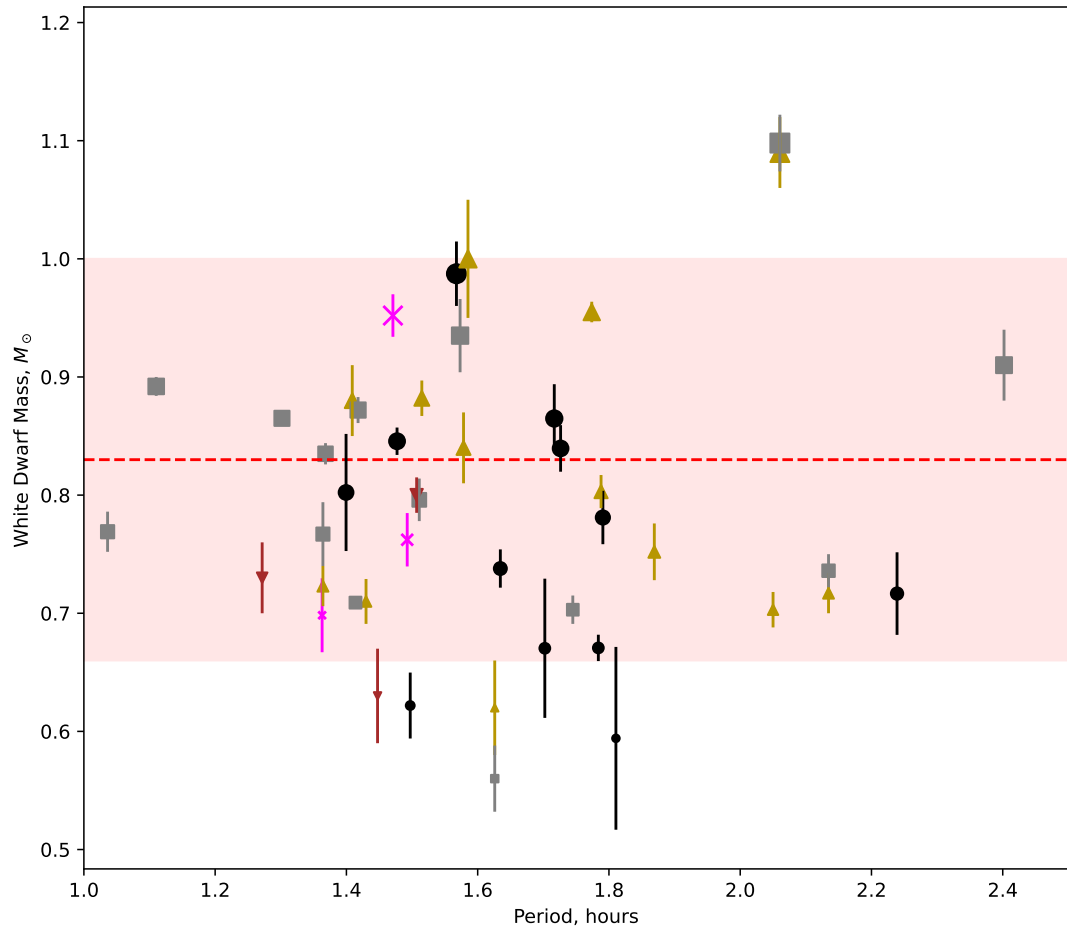


Figure 5.42: Showing how the modelled observations compare with the average white dwarf mass found by Pala et al. (2020), $0.83 \pm 0.17 M_{\odot}$, which is shown by the **red dashed line** and **red shaded area**. Data symbols are similar to Figure 5.41, and the data points are similarly scaled to aid understanding of the correlation between datum size and M_{wd} .

5.2.1 A preliminary look at AML in CVs

The published results and analysis of the three CVs in Chapter 4 (Wild et al., 2021) pre-date the more fully developed method to infer a donor mass loss rate described in §3.4.3. However, that preliminary analysis remains of interest, and motivates Chapter 6. As such, the preliminary AML analysis method of Wild et al. (2021) was repeated using the new data presented here, significantly increasing the population of well-characterised CVs compared to what was available at publication. The core findings of that work persist with the new data set, lending further credence to the results.

In order to qualitatively evaluate missing AML, the period *excess* was examined, $P_{\text{ex}} = P_{\text{obs}} - P_{\text{std}}$. Here, P_{obs} is the observed period, and P_{std} is the period predicted by the Knigge et al. (2011) CV donor track with only $1\times$ gravitational braking below the period gap, interpolated across M_{donor} . To determine P_{ex} from a measured ($P_{\text{obs}}, M_{\text{donor}}$) pair, mass samples are drawn from the modelled posterior distribution of M_{donor} , and period is interpolated at each mass from the evolutionary tracks to give a corresponding P_{std} distribution. As P_{std} is very sensitive to M_{donor} , the P_{std} error dominates the uncertainty in P_{ex} . A positive P_{ex} indicates that the model is missing AML, and a negative P_{ex} indicates a model that has too much AML, relative to an observation. The validity of P_{ex} is vulnerable to two key systematic biases; the validity of P_{std} (itself contingent on the accuracy of a variety of model assumptions and biases), and the inherent physical variation of the CV population.

CVs may follow inherently different evolutionary tracks due to differences in donor metallicity (Stehle et al., 1997; Harrison, 2016), white dwarf mass (Knigge, 2006), and the age of the donor when it first contacts the Roche lobe (Howell, 2001). A population-wide scatter in this parameter space is not captured in the Knigge et al. (2011) model, which uses fixed values for these variables, but justification for the adopted values are given (Knigge et al., 2011; Knigge, 2006). If any individual system deviates from the adopted values in the models of Knigge et al. (2011) then P_{ex} for that system will be influenced by these differences as well as any extra AML. However, conclusions about P_{ex} drawn from the population at large should remain robust, as long as the population doesn't differ systematically from the values adopted in the models. The white dwarf mass used by Knigge et al. (2011) is somewhat lower than more recent observations suggest, using $M_{\text{wd}} = 0.75M_{\odot}$ versus the more recent value of $M_{\text{wd}} = 0.83 \pm 0.17M_{\odot}$ (Pala

et al., 2020). An updated version of Knigge’s modelling is necessary to properly characterise the effect of this change on the donor evolutionary tracks, as this will affect both the size of the Roche lobes, and the rate of gravitational wave AML. Other CV models suggest that the effect of correcting M_{wd} will be small, at most around 2 minutes (Goliasch & Nelson, 2015). This analysis is not rigorous enough for this to become an issue, and the effects of using an incorrect white dwarf mass is considered acceptable.

More seriously, P_{ex} is only an accurate proxy of additional AML if the underlying donor physics in the model are correct. For example, if the models incorrectly predict the mass of systems in the period gap, this can have a large effect on P_{ex} . In the models of Knigge et al. (2011) this mass is fixed at the empirically derived value of $0.2M_{\odot}$, as observations of superhumping and eclipsing CVs suggest that period gap occurs at donor masses of $0.20 \pm 0.02M_{\odot}$ (Knigge, 2006). Using model tracks with lower or higher masses for the donor mass of the period gap would alter P_{ex} , though in this case the broad trend in P_{ex} will again be unchanged.

The result is plotted in Figure 5.43. These data are fit with a straight line, and as the data have significant uncertainty in both axes, the sum orthogonal distance (weighted by uncertainty) from the data is minimised to find the best fit (Hogg et al., 2010). Python’s SciPy package, `ODR` was used to perform this fitting.

The best-fit lines to the two data sets are $P_{\text{ex}}/\text{hours} = -(4.07 \pm 0.83)M_{\text{donor}}/M_{\odot} + (0.32 \pm 0.06)$ and $P_{\text{ex}}/\text{hours} = -(1.62 \pm 0.27)M_{\text{wd}}/M_{\odot} + (1.34 \pm 0.21)$. The best-fit slope of P_{ex} as a function of both M_{donor} and M_{wd} is significantly correlated: 5σ from the null hypothesis of 0 in the case of M_{wd} , and $\sim 3\sigma$ for M_{donor} . However, note that the best-fit line for M_{donor} does *not* pass through $P_{\text{ex}} = 0$ at $M_{\text{donor}} = 0.20M_{\odot}$ as expected, unless $> 3\sigma$ confidence on the gradient and intercept are considered.

Again, it is stressed that the only robust product of this analysis is the *sign of the gradient* of the $M - P_{\text{ex}}$ relationship, and that its steepness and y-intercept are both subject to systematic errors that are not captured in the statistical errors given above. Despite this, the clear and statistically significant increase in P_{ex} towards low masses implies that additional AML has a larger effect on the donor at lower component masses.

Note that P_{ex} considers a changing gravitational braking strength, which declines as the total system mass falls. There are then three cases to describe the trend in P_{ex} : the excess AML also declines in strength but more slowly than

gravitational losses; excess AML is roughly constant across the range of M_{donor} or M_{wd} ; or excess AML actually increases in strength towards lower M_{donor} or M_{wd} . Note that none of these options translate to the “optimal” [Knigge et al. \(2011\)](#) models which adopt additional AML of the same form as GWB, but are compatible with the eCAML solution for excess AML.

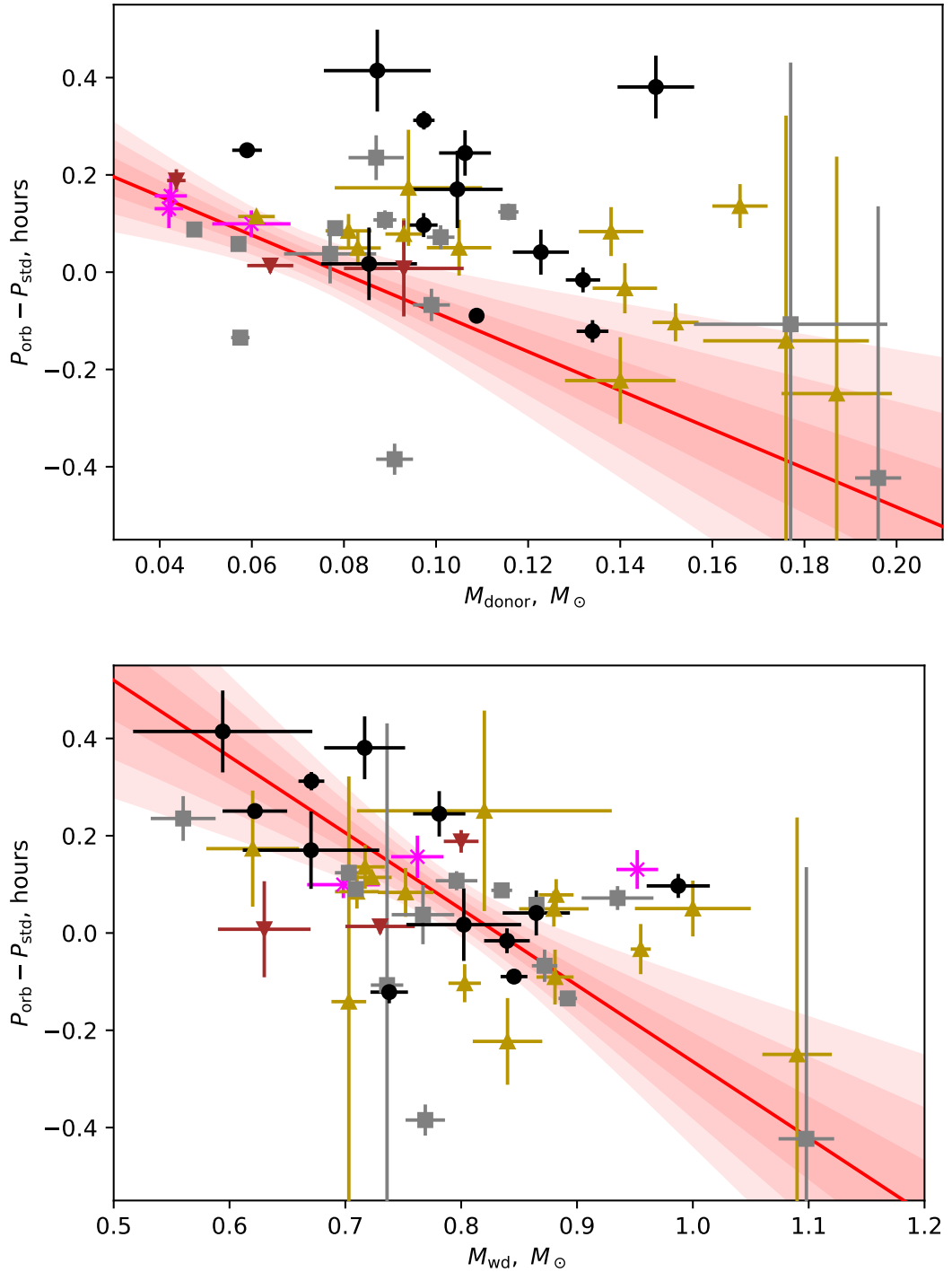


Figure 5.43: The relation between the two body masses, and the period excess, P_{ex} is shown. The observed data are keyed the same as Figure 5.41, and the **solid red line** shows the best-fit solution to the data. **Shaded red regions** show successively lower confidence intervals of the fit, with the darkest region being 1σ confidence, and the lightest region being 3σ confidence. The lines of best fit have the forms: $P_{\text{ex}} = -(4.07 \pm 0.83)M_{\text{donor}}/M_{\odot} + (0.32 \pm 0.06)$ and $P_{\text{ex}}/\text{hours} = -(1.62 \pm 0.27)M_{\text{wd}}/M_{\odot} + (1.34 \pm 0.21)$.

Chapter 6

Inferring mass loss rate from donor properties

The structure of this chapter is as follows: first, I demonstrate that MESA is capable of reproducing the canonical CV donor tracks of Knigge et al. (2011), and use MESA to evaluate the range of donor masses for which the method detailed in §3.4 can be reasonably applied. Then, I derive an empirical relationship for appropriate spot parameters as a function of donor mass, and use this to infer \dot{M}_{donor} and \dot{J} for the well-characterised eclipse modelled CV sample.

The analysis of this section includes eclipse modelled data from several sources: the 15 systems contained in this thesis, the 15 CVs characterised by McAllister et al. (2019), and the 14 CVs modelled by Savoury et al. (2011). An additional 4 systems from McAllister et al. (2015); McAllister et al. (2017a); McAllister et al. (2017b); and Gänsicke et al. (2010) were used, detailed in Table A.11. A full catalogue of all these data is given in Appendix A.1. There is some overlap between the CVs contained in McAllister et al. (2019) and Savoury et al. (2011), and where this is the case the more recent findings of McAllister et al. (2019) are preferred.

6.1 Reproducing the canonical CV donor tracks

MESA can closely reproduce the two Knigge et al. (2011) donor tracks. Recall from §1.5.5 that two such tracks are constructed, a ‘standard’ track with only typical gravitational braking below the period gap, and an ‘optimal’ track that amplifies gravitational braking by a factor of 2.47.

Initial work to reproduce CV evolution is outlined in Paxton et al. (2015). A subsequent reproduction of the ‘optimal’ track was undertaken by Pala et al. (2017), and I continue to refine their process. By default, MESA shuts off magnetic braking when the donor becomes fully convective, a practice which I motivate in §1.5.5 to be spurious. Instead, MESA is altered to enforce a fixed magnetic braking cut-off at $0.2M_{\odot}$, arbitrarily fixing the donor mass of the period gap in line with Knigge et al. (2011) (this is justified by observations - the mass of the period gap appears to be $0.20 \pm 0.02M_{\odot}$ (Knigge et al., 2011)). In addition, Pala et al. (2017) added a subroutine to MESA that allows for the amplification of gravitational braking below the period gap. This subroutine uses the `s% other_jdot_mb` MESA hook, and scales the calculated gravitational braking by a fixed constant below the period gap and applies it as magnetic braking. This was previously hard-coded, and I made minor changes to allow this scaling to be defined in the

MESA configuration inlist.

This was used to reproduce the ‘optimal’ track. Previous works have used entirely default MESA configuration for the donor physics, though I apply the configuration described in §3.4.1 to improve model accuracy. Beyond these settings, the model is also initialised with some additional binary configuration:

- The two objects begin at an orbital period of 12 hours, with $M_{\text{donor}} = 0.65M_{\odot}$ and $M_{\text{wd}} = 0.82$ to match the mean observed white dwarf mass. This period is chosen as the donor is not yet in contact with the Roche lobe but evolves to contact the Roche lobe relatively quickly.
- The donor mass at which the CV emerges from the period gap is dependent on spot parameters. The donor star has a fixed spot coverage $f_{\text{spot}} = 0.10$ and contrast ratio of $x_{\text{spot}} = 0$, chosen to approximately match the period at which the donor emerges from the period gap.
- The white dwarf is not allowed to retain any accreted material,
 - `mass_transfer_beta = 1.0, limit_retention_by_mdot_edd = .false.`
- The white dwarf is considered as a point mass, with no evolution over time,
 - `evolve_both_stars = .false.`

These changes are enough to reproduce the [Knigge et al. \(2011\)](#) tracks to a reasonable degree; Figure 6.1 shows the four model tracks in the short period regime. Note that the small deviation at $\sim 0.13M_{\odot}$ in the MESA models are due to MESA transitioning do a different equation of state, and is expected. The small difference in gradient between the MESA models and the [Knigge et al. \(2011\)](#) models is due to the donor having a differing mass-radius relationship; this model does not use variable star spot physics as the donor mass falls. With a more tailored donor configuration this could likely be improved without introducing the star spot physics at all – specifically, the period minimum occurs at a significantly lower donor mass in the MESA models due to the differing equations of state and atmosphere tables used, but an exact reproduction of [Knigge et al. \(2011\)](#) is not the focus of this study and this agreement is considered acceptable.

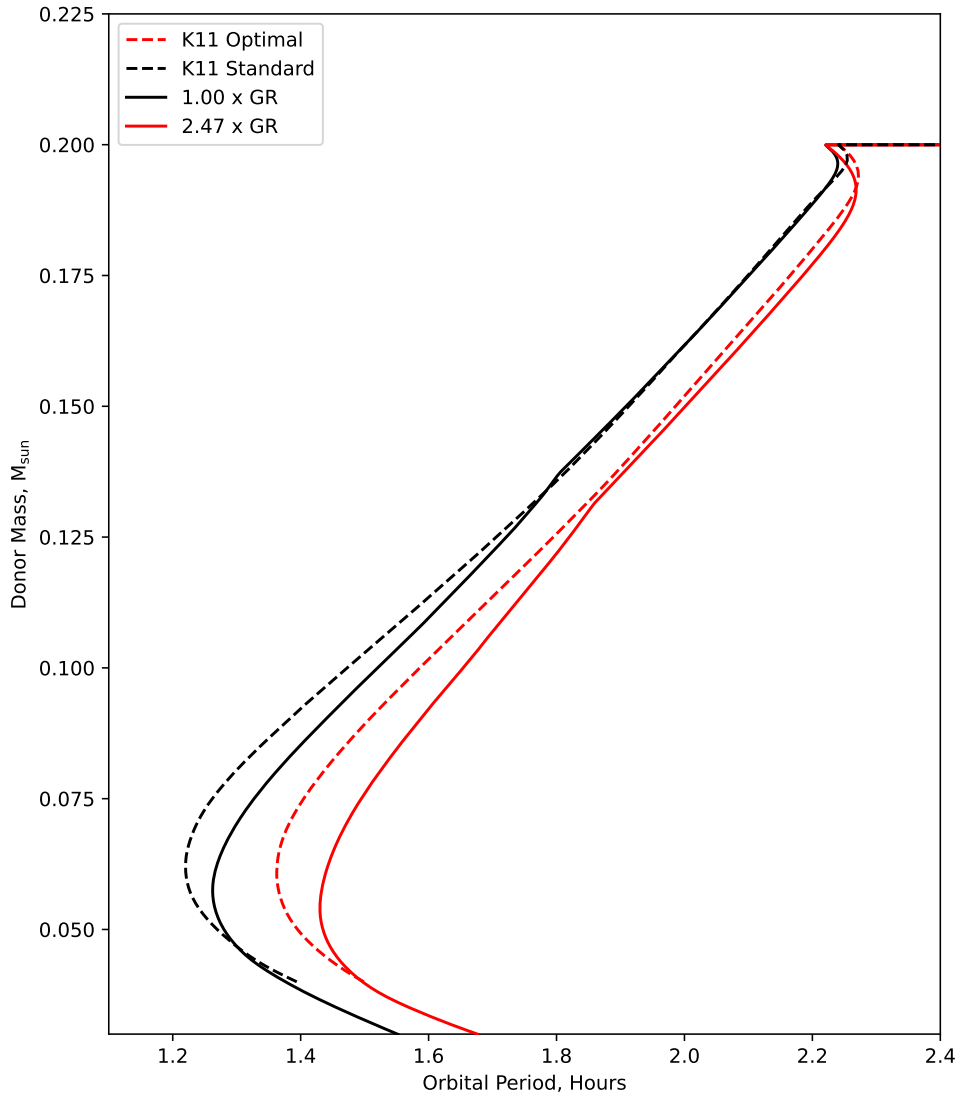


Figure 6.1: Showing how well MESA can reproduce the canonical [Knigge et al. \(2011\)](#) donor tracks. **Solid lines** are MESA tracks, and **dotted lines** are the [Knigge et al. \(2011\)](#) tracks. **Black** lines have only gravitational braking below the period gap, and **red** lines gave gravitational braking at $2.47 \times$ strength below the period gap.

6.2 For what range of masses can mass loss rates be extracted?

Note that the analysis of this section does not include any star spots, i.e. $f_{\text{spot}} = 0$ for these models.

Recall from §1.5.3 the two timescales that govern the response of the donor to mass loss: τ_{KH} and $\tau_{\dot{M}}$. These timescales are calculated by

$$\tau_{\text{KH}} = \frac{GM_{\text{donor}}^2}{L_{\text{donor}}R_{\text{donor}}} \quad (6.1)$$

$$\tau_{\dot{M}} = \frac{\dot{M}}{M_{\text{donor}}} \quad (6.2)$$

If $\tau_{\text{KH}} \ll \tau_{\dot{M}}$, the donor is able to maintain thermal equilibrium and is indistinguishable from a singleton star of the same mass.

If $\tau_{\text{KH}} \gg \tau_{\dot{M}}$, the donor is not able to maintain equilibrium, and mass loss is fast and adiabatic. The donor is inflated by mass loss, but since the stellar structure reacts relatively slowly, the adjustment of the structure towards equilibrium can be interrupted by changes in mass loss rate. This time lag between the star beginning to experience a specific mass loss rate, and the structure adjusting to reflect it makes the degree of inflation of the donor sensitive to the mass loss *history* of the donor.

Calculating the two timescales for CVs reveals that for much of their lives, $\tau_{\text{KH}} \sim \tau_{\dot{M}}$ (Knigge et al., 2011) - meaning that most CV donors are *almost* able to maintain thermal equilibrium, but are still mildly affected by mass loss. Under this almost-equilibrium regime, mass loss induces some degree of radius inflation in the donor, but because the star adjusts on timescales comparable to $\tau_{\dot{M}}$, the degree of inflation only depends on the present-day average \dot{M} . In this regime, the mass loss history of the donor can be discarded, and the radius inflation becomes a diagnostic for the baseline mass loss rate, averaged over $\tau_{\dot{M}} \sim 1\text{Gyr}$.

Whether a donor radius is sensitive to its \dot{M} history is a function of M_{donor} . As M_{donor} falls, τ_{KH} begins to rise faster than $\tau_{\dot{M}}$. Figure 6.2 shows this trend, produced by a MESA model of a CV using the configuration provided in Paxton et al. (2015). The rise in τ_{KH} relative to $\tau_{\dot{M}}$ becomes significant at $\sim 0.1M_{\odot}$, around the mass the donor enters the adiabatic $\tau_{\text{KH}} \gg \tau_{\dot{M}}$ period bouncer phase c.f. §1.5.3.

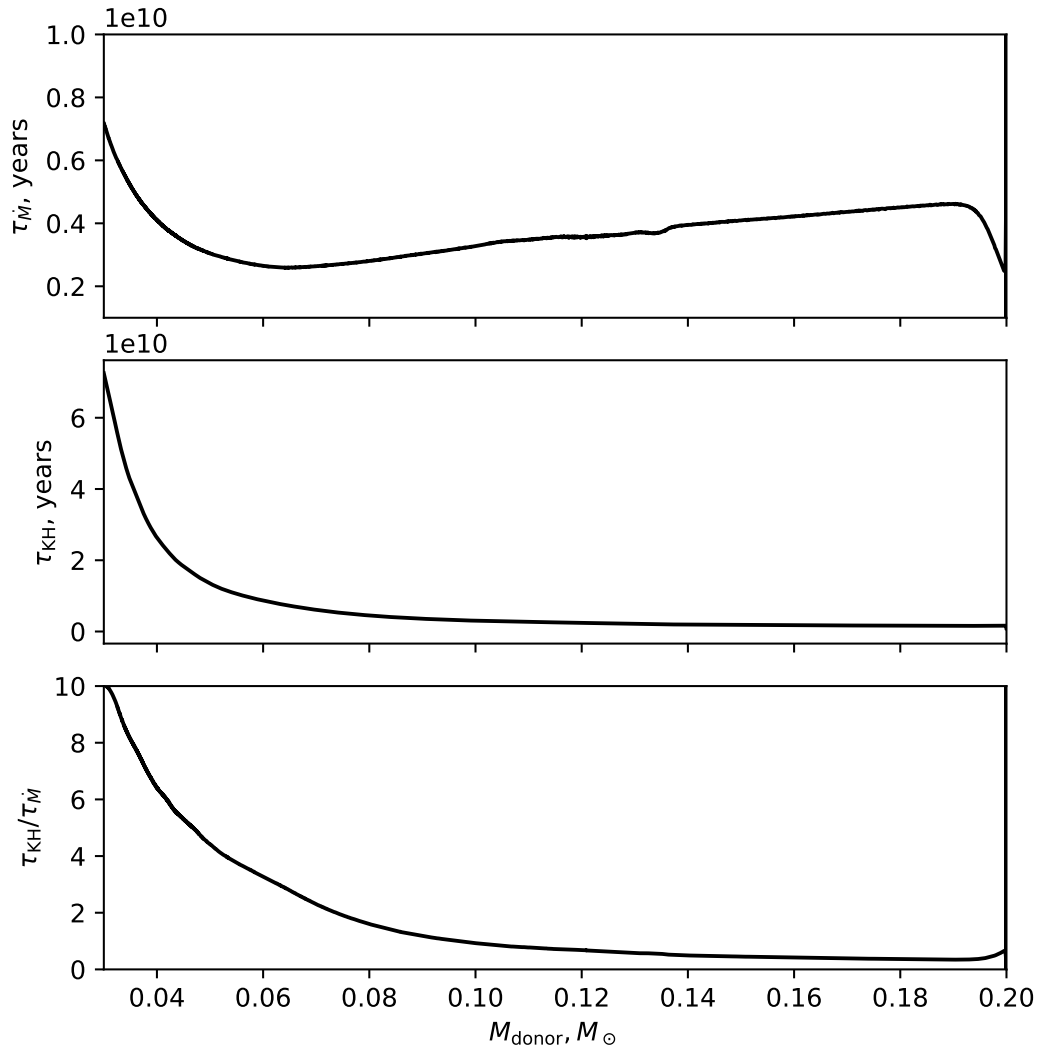


Figure 6.2: Showing how the two timescales, τ_{KH} and τ_M vary with donor mass below the period gap in CV donors, as modelled by MESA ([Paxton et al., 2015](#); [Pala et al., 2017](#)).

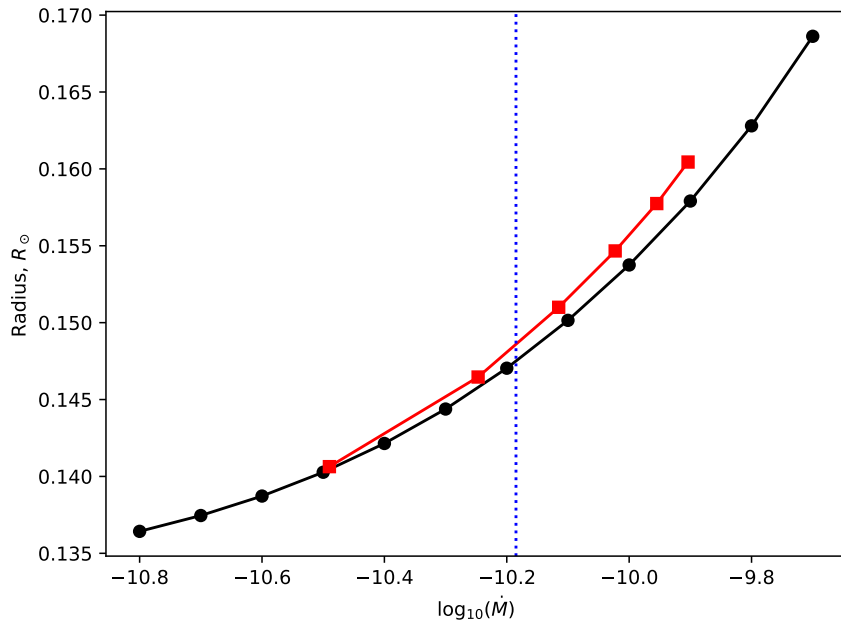


Figure 6.3: Showing the radius and mass loss extracted from MESA models at $0.1M_\odot$. The **black** line is a series of singleton models with constant mass loss, and the **red** line is a series of CV models with gravitational AML amplified by $x = 1 \rightarrow 6$, with the lowest AML rate on the left. The **blue dotted line** shows \dot{M} for a CV with $2.47\times$ gravitational braking strength as predicted by a MESA CV model.

The range of donor masses for which $\tau_{\text{KH}} \sim \tau_{\dot{M}}$ can be determined using MESA models. First, a series of singleton models (this time using the MESA configuration given in §3.4.1) were evaluated with varying amounts of fixed mass loss rates, uniformly spaced between $\log(\dot{M}, M_\odot \text{yr}^{-1}) = -9.9 \rightarrow -10.8$. Then, a series of MESA CV models were run with gravitational losses amplified by $x = 1 \rightarrow 6$, using the configuration and AML amplification in §6.1. Finally, each model has its radius, R , and \dot{M} extracted at $0.1M_\odot$. Since the CV models have varying \dot{M} and the singleton models do not, if \dot{M} history does not affect radius inflation the radii between the two sets of models will match, and a disagreement indicates that history plays a significant role in radius inflation. Figure 6.3 shows this, and little divergence between the two sets of radii is visible. Note that higher \dot{M} show a small but increasing degree of divergence, as might be expected since higher \dot{M} corresponds to lower $\tau_{\dot{M}}$.

Now, by looking at what level of divergence historical changes in \dot{M} induces at various donor masses, the allowable mass range can be evaluated. By instead

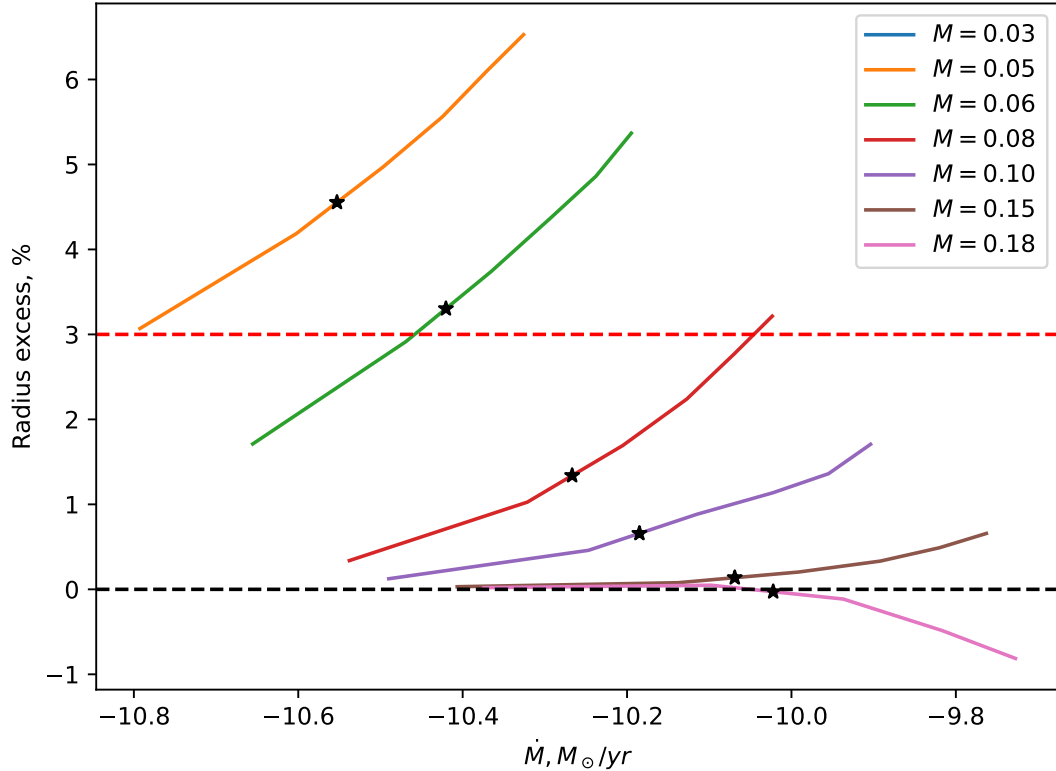


Figure 6.4: The inflation of CV model radii, R_{CV} (whose \dot{M} is time-dependent), over singleton model radii, R_S (whose \dot{M} is constant), from Figure 6.3, for a range of masses. The **stars** on each line show the \dot{M} and inflation for a model with gravitational braking at $2.47\times$ strength, mirroring the [Knigge et al. \(2011\)](#) optimal track. The **red dashed line** shows the upper limit for acceptable disagreement, and the **black dashed line** shows perfect agreement.

plotting the difference between the two sets of models, and repeating the same process for a range of masses, Figure 6.4 is produced. The upper limit on mass must be $0.2M_{\odot}$, as this is the enforced mass of the period gap, and for a lower limit I impose an acceptable level of disagreement of 3%. It can be seen that the minimum acceptable mass is then $0.08M_{\odot}$.

6.3 Tuning star spot parameters to observations

With star spots implemented in MESA in §3.4.2, the Brown relation can now be reproduced. For simplicity, x_{spot} is fixed at 0 and f_{spot} is varied. Since radius increases monotonically with f_{spot} , a binary chop is performed (see §??), optimising for $\Delta R = R_{\text{MESA}} - (1.045 \times R_{\text{Brown}}) = 0$ at a stellar age of 2 Gyrs for a range of masses. The 4.5% radius increase is to compensate for the non-spherical Roche geometry of the donor, c.f. Knigge et al. (2011). The resulting $M-f_{\text{spot}}$ relation is shown in Figure 6.5.

Below masses of $\sim 0.12M_{\odot}$, the required f_{spot} becomes slightly negative, i.e. default MESA models are larger than observations plus the 4.5% non-spherical correction. Since a negative coverage fraction is unphysical, negative values of f_{spot} are set equal to 0 and it should be emphasised that derived mass loss rates may become somewhat unreliable below this mass. However, the clear trend in f_{spot} towards 0 prior to this, and the close proximity to $f_{\text{spot}} = 0$ below $0.12M_{\odot}$ suggests that the MESA radius calibration given here is still valid.

There is significant scatter in the Brown mass-radius relation that is not captured in these models. The inherent scatter in radius for the observations is $\sim 3\%$ between 0.1 and $0.2 M_{\odot}$, which adds to the uncertainty in modelled radius inflation, and thus mass loss rate. Below $\sim 0.1M_{\odot}$, the scatter is not able to be characterised. Whilst this may skew an individual system, on average the inferred mass loss from model radius should be accurate. Therefore, this effect should not corrupt the \dot{M} results with a large enough sample size. Since the uncertainties I report here do not include the effects of the scatter in the Brown mass-radius relation, they are underestimates of the true uncertainty. However, due to the very poor constraints on the scatter, this effect is ignored until more information is available.

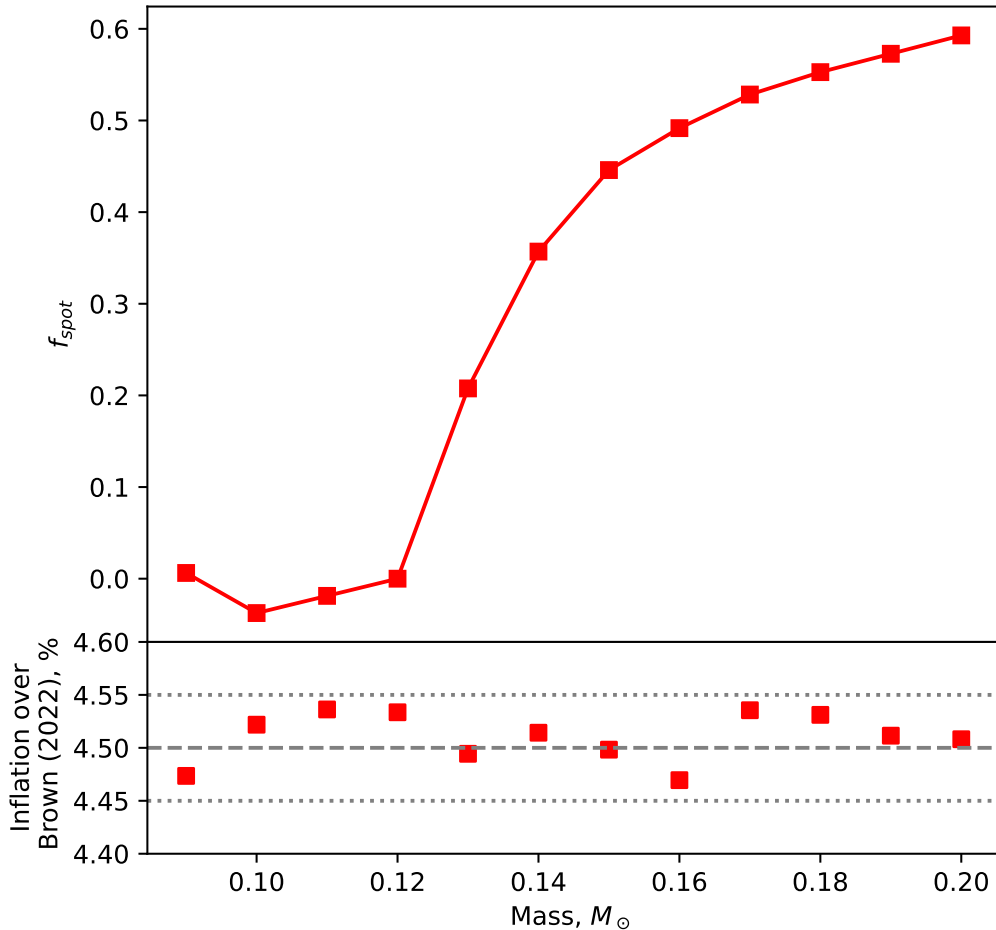


Figure 6.5: *Top:* The required f_{spot} that is applied to tune M dwarf MESA models to match the Brown relation, plus an added 4.5% inflation due to non-spherical Roche geometry. *Bottom:* the residuals from the best-fit value of f_{spot} . The **dotted lines** show the acceptable deviation from perfect agreement in order to terminate the binary chop, and the **dashed line** shows the target inflation. Note that when finding the necessary value of f_{spot} to match the Brown relation $x_{\text{spot}} \equiv 0$, and negative values of f_{spot} were allowed. However, in all subsequent modelling, negative f_{spot} were set to 0. **Red squares** show evaluated MESA models.

6.4 Inferred mass and angular momentum loss rates from CV donors

Overall, there are 33 systems with eclipse-modelled characterisations available with donors in the correct mass range of $0.08M_{\odot} < M_{\text{donor}} < 0.20M_{\odot}$, catalogued in Table 6.1.

Table 6.2 shows the AML rates, \dot{J} , calculated using Equation 3.46 for the systems for which \dot{M} could be calculated from donor properties. Also shown is the AML expected from gravitational losses alone for that system, and the ratio between the observed and expected values.

Two systems appear to have less AML than is predicted by gravitational losses: ASASSN-17fo (from Chapter 5) and SDSS J0903 ([Savoury et al., 2011](#)), and an erroneous eclipse model result can be eliminated in each case. ASASSN-17fo is confidently eclipse modelled, with distinct, well modelled eclipse features and a good white dwarf flux fit, so is unlikely to be unreliable. SDSS J0903 also has a confident eclipse model fit. Whilst the bright spot features of this system are less distinct, the fitting results are satisfactory. However, the inferred \dot{M} is contingent on a chain of assumptions all holding true; the eclipse modelling must be robust, the MESA configuration must be accurate *for the specific donor being considered*, and the equilibrium radius of the donor in question must be well-described by the Brown relation. A failure in any of these steps will produce incorrect values of \dot{M} and \dot{J} , and the consequences of the breakdown of these assumptions is discussed in §6.4.1.

Aside from these two cases the inferred \dot{M} are generally physically reasonable, suggesting that the general data set is acceptable for preliminary analysis. In the interests of honest analysis, the two sub-gravitational loss CVs are still included in the following examination of the data.

6.4.1 Systematic issues with mass loss estimation

It is critical to treat these mass loss rates with caution. The sample as given here is subject to systematic bias as a result of the sparse nature of the data used to calibrate the Brown relation, and the validity of \dot{M} and \dot{J} is sensitive to the validity of the MESA configuration for the donor model. Whilst the majority of CV donors are probably well-described by my MESA configuration, it cannot be assumed that *all* donors will be; the configuration could easily be invalidated by,

Table 6.1: The inferred \dot{M} for eclipse-modelled CVs. For the Source column, ‘W22’ are from Chapter 5, ‘M19’ are systems modelled by McAllister et al. (2019), ‘M17b’ is from McAllister et al. (2017b), ‘S11’ are from Savoury et al. (2011)

System Name:	Source	$M_{\text{donor}}, M_{\odot}$	$R_{\text{donor}}, R_{\odot}$	$\log_{10}(\dot{M}, M_{\odot}/\text{yr})$
ASASSN-14hq	W22	0.097 ± 0.002	0.157 ± 0.001	-9.897 ± 0.008
ASASSN-15pb	W22	0.148 ± 0.008	0.209 ± 0.003	-9.997 ± 0.164
ASASSN-17fo	W22	0.109 ± 0.001	0.144 ± 0.001	-10.859 ± 0.137
AY For	W22	0.106 ± 0.005	0.162 ± 0.002	-9.918 ± 0.024
CSS090419	W22	0.087 ± 0.016	0.152 ± 0.006	-9.859 ± 0.003
CSS090622	W22	0.105 ± 0.009	0.155 ± 0.004	-10.046 ± 0.074
MASTER OT J0014	W22	0.123 ± 0.006	0.165 ± 0.002	-10.279 ± 0.328
OGLE82	W22	0.132 ± 0.003	0.170 ± 0.001	-11.686 ± 1.078
SDSS J0748	W22	0.085 ± 0.010	0.128 ± 0.005	-10.438 ± 0.152
SDSS J1524	W22	0.097 ± 0.003	0.144 ± 0.001	-10.210 ± 0.030
CSS080623	M19	0.081 ± 0.005	0.128 ± 0.002	-10.343 ± 0.041
CSS110113	M19	0.105 ± 0.007	0.149 ± 0.003	-10.272 ± 0.129
OY Car	M19	0.093 ± 0.004	0.139 ± 0.001	-10.278 ± 0.046
SDSS J0901	M19	0.138 ± 0.007	0.182 ± 0.003	-10.547 ± 0.368
SDSS J1152	M19	0.094 ± 0.016	0.147 ± 0.006	-10.062 ± 0.156
SSS100615	M19	0.083 ± 0.005	0.128 ± 0.002	-10.384 ± 0.038
ASASSN-14ag	M17b	0.093 ± 0.010	0.135 ± 0.007	-10.416 ± 0.211
CTCV J2354-4700	S11	0.101 ± 0.003	0.146 ± 0.001	-10.245 ± 0.030
OU Vir	S11	0.116 ± 0.002	0.163 ± 0.001	-10.067 ± 0.026
XZ Eri	S11	0.091 ± 0.004	0.135 ± 0.001	-10.352 ± 0.054
SDSS J0903	S11	0.099 ± 0.004	0.136 ± 0.002	-10.677 ± 0.155
SDSS J1227	S11	0.089 ± 0.002	0.137 ± 0.001	-10.243 ± 0.017
SDSS J1502	S11	0.078 ± 0.001	0.124 ± 0.001	-10.377 ± 0.008
ASASSN-14kb	W22	0.134 ± 0.003	0.164 ± 0.001	-
CTCV 1300-3052	M19	0.166 ± 0.006	0.211 ± 0.002	-
DV UMa	M19	0.187 ± 0.012	0.215 ± 0.005	-
IY UMa	M19	0.141 ± 0.007	0.177 ± 0.002	-
SSS130413	M19	0.140 ± 0.012	0.163 ± 0.004	-
V713 Cep	M19	0.176 ± 0.018	0.208 ± 0.005	-
Z Cha	M19	0.152 ± 0.005	0.182 ± 0.002	-
CTCV J1300-3052	S11	0.177 ± 0.021	0.215 ± 0.008	-
DV UMa	S11	0.196 ± 0.005	0.218 ± 0.001	-

Table 6.2: The inferred AML rates for the CVs in this sample. \dot{J}_{total} is calculated from the inferred \dot{M} , and \dot{J}_{GR} is the calculated gravitational AML rate. Sources are keyed the same as Table 6.1.

System Name:	Source	$\log(\dot{J}_{\text{total}}, J)$	$\log(\dot{J}_{\text{GR}}, J)$	$\dot{J}_{\text{total}}/\dot{J}_{\text{GR}}$
ASASSN-14hq	W22	27.157 ± 0.009	26.681 ± 0.007	2.996 ± 0.081
ASASSN-15pb	W22	27.091 ± 0.162	26.796 ± 0.013	2.115 ± 0.818
ASASSN-17fo	W22	26.240 ± 0.137	26.711 ± 0.004	0.355 ± 0.114
AY For	W22	27.184 ± 0.026	26.705 ± 0.015	3.021 ± 0.204
CSS090419	W22	27.158 ± 0.039	26.634 ± 0.058	3.381 ± 0.548
CSS090622	W22	26.994 ± 0.078	26.699 ± 0.028	2.011 ± 0.388
MASTER OT J0014	W22	26.842 ± 0.325	26.745 ± 0.014	1.661 ± 1.488
OGLE82	W22	25.428 ± 1.083	26.767 ± 0.009	0.980 ± 8.280
SDSS J0748	W22	26.645 ± 0.156	26.629 ± 0.053	1.116 ± 0.442
SDSS J1524	W22	27.027 ± 0.031	26.723 ± 0.043	2.027 ± 0.234
CSS080623	M19	26.705 ± 0.042	26.615 ± 0.026	1.238 ± 0.141
CSS110113	M19	26.895 ± 0.128	26.701 ± 0.019	1.633 ± 0.502
OY Car	M19	26.844 ± 0.046	26.666 ± 0.014	1.517 ± 0.168
SDSS J0901	M19	26.536 ± 0.368	26.780 ± 0.014	0.815 ± 0.870
SDSS J1152	M19	26.954 ± 0.157	26.656 ± 0.073	2.149 ± 0.894
SSS100615	M19	26.730 ± 0.039	26.625 ± 0.024	1.282 ± 0.138
ASASSN-14ag	M17b	26.587 ± 0.215	26.657 ± 0.056	0.968 ± 0.526
CTCV J2354-4700	S11	26.899 ± 0.032	26.691 ± 0.008	1.616 ± 0.122
OU Vir	S11	26.992 ± 0.027	26.729 ± 0.005	1.837 ± 0.117
XZ Eri	S11	26.721 ± 0.054	26.659 ± 0.015	1.164 ± 0.151
SDSS J0903	S11	26.427 ± 0.154	26.685 ± 0.012	0.587 ± 0.217
SDSS J1227	S11	26.848 ± 0.018	26.652 ± 0.010	1.572 ± 0.075
SDSS J1502	S11	26.669 ± 0.009	26.602 ± 0.005	1.169 ± 0.026

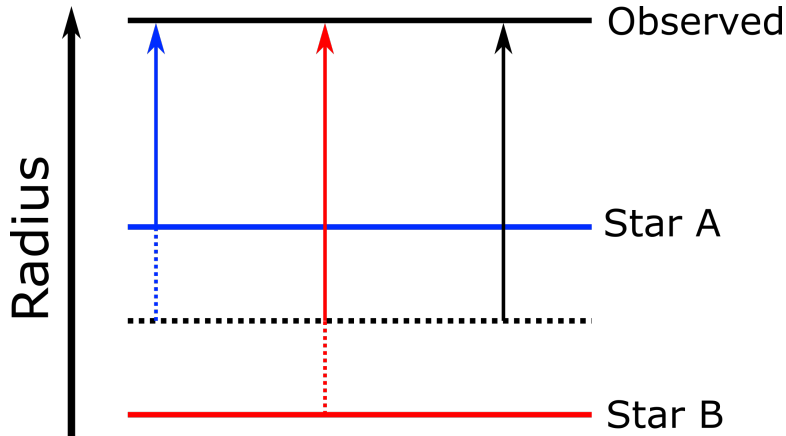


Figure 6.6: Illustrating how scatter about the Brown relation can corrupt inferred \dot{M} rates. The upper solid black line shows the observed radius of a donor, and the lower three lines show possible zero \dot{M} radii. The dotted black line shows the radius predicted by the Brown relation. The arrows show the amount of inflation induced by \dot{M} , with longer arrows requiring more \dot{M} . The black arrow shows the reported value, but assumes the donor would exactly agree with the Brown relation. If the zero- \dot{M} radius of a donor corresponds to star A (blue line), some extra \dot{M} will be incorrectly attributed to the system (shown as the dotted section). If the zero- \dot{M} radius of the donor corresponds to star B (red line), some amount of \dot{M} will be ignored (again shown as the dotted section).

for example, the presence of a more evolved donor, or one with a substantially different metallicity from typical M dwarfs. This would alter the mass-radius exponent of the donor (ζ in Equation 3.46) and corrupt the inferred \dot{J} .

Beyond a potentially incorrect MESA configuration, there is a more serious problem with the unknown scatter in the Brown relation. Consider a star which lies below the Brown relation, i.e. one with a smaller zero- \dot{M} radius than its mass suggests. If this star begins to experience mass loss, and its radius is measured to be inflated beyond the Brown relation (after factoring for Roche geometry), the corresponding mass loss rate found will be *lower* than reality, as some amount of the star's inflation – the amount required to inflate it to agree with the Brown relation – is ignored. This is illustrated in Figure 6.6. This will also cause some stars to fail to have \dot{M} inferred. If the zero- \dot{M} radius is small enough, it becomes likely that the amount of inflation induced by mass loss is not sufficient to bring the star up to the radius assumed by the Brown relation. Such a donor would not be possible to reproduce using this methodology, and 9 such donors (approximately a quarter of the sample) are seen in Table 6.1.

The combination of these two effects makes our dataset as a whole systemat-

ically over-estimate \dot{M} . This is because systems with donors that scatter below the Brown relation are preferentially removed from the sample – they are more likely to have inflations that lie below the baseline radius (i.e. they lie below the dotted black line in Figure 6.6), and are systems which would have had their \dot{M} under-estimated. Donors which scatter above the Brown relation are not removed in this way, so over-estimated \dot{M} become over-represented in the sample. Some portion of systems are, for the same reasons, reported with abnormally low \dot{M} – i.e. ASASSN-17fo and SDSS J0903 – as their donors scatter below the Brown relation, but not by enough as to remove them from the sample. Finally, since our reported \dot{M} do not consider the intrinsic scatter in the M dwarf population, the uncertainties in \dot{M} reported are likely to be significantly under-estimated.

Although this bias presents a problem for quantitative analysis, the general trends that these data show can still be considered generally correct, with the caveat that these are preliminary results. A larger sample of M dwarf masses and radii in the $M < 0.2M_{\odot}$ range to give a better mass-radius relationship is highly desirable, and is likely to be provided in the near future with the release of Gaia DR3. With a proper characterisation of the intrinsic population scatter, it will be possible to marginalise over the scatter to remove the over-estimation of \dot{M} , more faithfully report uncertainties, and perform more rigorous quantitative analysis of the data.

6.5 Inferring mass loss from white dwarf properties

The white dwarf temperature also reveals information on the mass transfer rate, and the following summary is described more quantitatively by [Townsley & Gänsicke \(2009\)](#). In brief, as accreted material strikes the surface of the white dwarf its kinetic energy is converted to thermal energy, heating the white dwarf surface. The degree of this heating is related to the rate at which material falls to the surface – if more material falls in, more heating is induced. Since, in general, it can be assumed that the rate material falls onto the white dwarf is roughly equal to the rate at which material enters the accretion disc from the donor, the white dwarf T_{eff} becomes a proxy diagnostic of the donor \dot{M} . Simulations demonstrate that even through successive Nova eruptions, the core temperature of the white dwarf is stable over timescales of $\sim 10^8$ years ([Epelstain et al., 2007](#)), so

if the accretion rate falls, the white dwarf T_{eff} is able to cool to the appropriate, lower temperature and remain accurate to the present-day accretion rate.

The white dwarf temperature approach holds a major advantage over using the donor properties: measurements of white dwarf temperatures are easier to gather in large sample sizes. However, the white dwarf temperature is capable of responding to changes in \dot{M} on $\tau_{\text{Twd}} \sim 10^3 - 10^5$ yrs (Townsley & Gänsicke, 2009), as opposed to the \sim Gyr timescales of the donor-based method described in §6.4, thus the \dot{M} inferred from the white dwarf is averaged over τ_{Twd} and only provides a short-term snapshot of the \dot{M} and is susceptible to corruption from outbursts.

The short-term average mass loss rate, $\langle \dot{M} \rangle$, is ultimately a function only of white dwarf mass, and temperature, given in Equation 6.3.

$$T_{\text{eff}} = 1.7 \times 10^4 \text{ K} \left(\frac{\langle \dot{M} \rangle}{10^{-10} M_{\odot} \text{ yr}^{-1}} \right)^{1/4} \left(\frac{M_{\text{wd}}}{0.9 M_{\odot}} \right) \quad (6.3)$$

Recently, Pala et al. (2021) used spectroscopically estimated T_{eff} and M_{wd} to infer the \dot{M} of 65 CVs. One finding from this analysis was an inverse correlation between M_{wd} and \dot{M} , contrary to the prediction of gravitational wave braking that lower mass systems should have lower AML rates driving lower \dot{M} . As the eclipse modelling of CVs also produces a measure of T_{eff} , the systems analysed for this thesis can be processed with *both* techniques, and have their results compared. Table 6.3 shows the resulting \dot{M} from the white dwarf parameters.

Table 6.3: The \dot{M} found using the white dwarf properties for each system with a \dot{M} measurement from donor properties. Sources are keyed the same as Table 6.1

Name	Source	M_{wd}, M_{\odot}	T_{eff}, K	$\log(\dot{M}, M_{\odot}\text{yr}^{-1})$
ASASSN-14hq	W22	0.67 ± 0.01	14800 ± 800	-9.93 ± 0.02
ASASSN-14kb	W22	0.74 ± 0.02	17700 ± 1000	-9.90 ± 0.03
ASASSN-15pb	W22	0.72 ± 0.03	19200 ± 1600	-9.85 ± 0.04
ASASSN-17fo	W22	0.85 ± 0.01	14800 ± 600	-10.03 ± 0.02
AY For	W22	0.78 ± 0.02	18200 ± 500	-9.91 ± 0.02
CSS090102	W22	0.62 ± 0.03	14800 ± 1200	-9.90 ± 0.04
CSS090419	W22	0.59 ± 0.08	18200 ± 9000	-9.79 ± 0.28
CSS090622	W22	0.67 ± 0.06	9800 ± 1500	-10.11 ± 0.08
MAS0014	W22	0.86 ± 0.03	17300 ± 1000	-9.97 ± 0.03
OGLE82	W22	0.84 ± 0.02	18000 ± 4400	-9.95 ± 0.12
SDSS J0748	W22	0.80 ± 0.05	28400 ± 3300	-9.73 ± 0.06
SDSS J1524	W22	0.99 ± 0.01	12500 ± 900	-10.17 ± 0.03
ASASSN-16kr	W20	0.95 ± 0.02	11500 ± 300	-10.19 ± 0.01
ASASSN-17jf	W20	0.70 ± 0.03	12020 ± 850	-10.03 ± 0.04
SSSJ1502-3505	W20	0.76 ± 0.02	22800 ± 1500	-9.80 ± 0.03
CSS080623	M19	0.71 ± 0.02	15500 ± 1700	-9.94 ± 0.05
CSS110113	M19	1.00 ± 0.05	14500 ± 2200	-10.11 ± 0.07
CTCV 1300-3052	M19	0.72 ± 0.02	11000 ± 1000	-10.09 ± 0.04
DV UMa	M19	1.09 ± 0.03	17400 ± 1900	-10.07 ± 0.05
GY Cnc	M19	0.88 ± 0.02	25900 ± 2300	-9.81 ± 0.04
IY UMa	M19	0.96 ± 0.01	18000 ± 1000	-10.00 ± 0.02
OY Car	M19	0.88 ± 0.02	18600 ± 2800	-9.95 ± 0.07
SDSS J0901	M19	0.75 ± 0.02	14900 ± 2000	-9.98 ± 0.06
SDSS J1006	M19	0.82 ± 0.11	16500 ± 2000	-9.97 ± 0.08
SDSS J1152	M19	0.62 ± 0.04	15900 ± 2000	-9.87 ± 0.06
SDSS J1501	M19	0.72 ± 0.02	14900 ± 1000	-9.96 ± 0.03
SSS100615	M19	0.88 ± 0.03	13600 ± 1500	-10.09 ± 0.05
SSS130413	M19	0.84 ± 0.03	24000 ± 3000	-9.82 ± 0.06
V713 Cep	M19	0.70 ± 0.02	17000 ± 6000	-9.89 ± 0.19
Z Cha	M19	0.80 ± 0.01	16300 ± 1400	-9.97 ± 0.04
SDSS J1057	M17a	0.80 ± 0.02	13300 ± 1100	-10.06 ± 0.04
ASASSN-14ag	M17b	0.63 ± 0.04	14000 ± 2100	-9.93 ± 0.07
PHL 1445	M15	0.73 ± 0.03	13200 ± 700	-10.02 ± 0.03

Table 6.4: Table 6.3, continued

Name	Source	M_{wd}, M_{\odot}	T_{eff}, K	$\log(\dot{M}, M_{\odot}\text{yr}^{-1})$
CTCV J1300-3052	S11	0.74 ± 0.01	11100 ± 800	-10.10 ± 0.03
CTCV J2354-4700	S11	0.94 ± 0.03	14800 ± 700	-10.08 ± 0.02
SDSS J1152	S11	0.56 ± 0.03	12400 ± 1400	-9.93 ± 0.06
OU Vir	S11	0.70 ± 0.01	22300 ± 2100	-9.77 ± 0.04
XZ Eri	S11	0.77 ± 0.02	15300 ± 1900	-9.98 ± 0.06
SDSS J1702	S11	0.91 ± 0.03	15200 ± 1200	-10.05 ± 0.04
SDSS J1035	S11	0.84 ± 0.01	10000 ± 1100	-10.20 ± 0.05
SDSS J1507	S11	0.89 ± 0.01	11300 ± 1000	-10.17 ± 0.04
SDSS J0903	S11	0.87 ± 0.01	13300 ± 1700	-10.09 ± 0.06
SDSS J1227	S11	0.80 ± 0.02	15900 ± 1400	-9.98 ± 0.04
SDSS J1433	S11	0.87 ± 0.01	12700 ± 1500	-10.11 ± 0.05
SDSS J1502	S11	0.709 ± 0.004	11800 ± 1200	-10.05 ± 0.04
IP Peg	C10	1.16 ± 0.02	12500 ± 2500	-10.24 ± 0.09

Chapter 7

Discussion

This chapter concerns the implications of the data gathered in previous chapters, as well as in other studies. As discussed in Chapter 1, the different explanations for the apparent excess AML in short period CVs may be discriminated by correlations with each of the component masses; eCAML expects a correlation with the white dwarf mass, whilst the residual magnetic braking prescriptions expect a correlation with donor mass and period.

First, however, the mass loss rates of the \dot{M} inferred from donor properties are compared with the mass loss rates inferred from the white dwarf properties. Figure 7.1 plots the \dot{M} from each method as a function of period – note that this figure plots all the white dwarf based \dot{M} regardless of if they were able to have donor based \dot{M} found, so not every CV has two data points plotted.

It is immediately obvious that the white dwarf properties indicate a generally higher \dot{M} than the donor properties, and do not follow the modelled donor tracks as the CV ages. Conversely, the donor-derived \dot{M} closely follows the ‘optimal’ MESA model with gravitational braking amplified by a factor of 2.47, even appearing to follow the period bounce regime though this is unlikely to be a real effect and is discussed later. Interestingly, the white dwarf properties also suggest a much more *consistent* mass loss rate across the CV population, with little scatter about $\sim 10^{-10} M_{\odot} \text{ yr}^{-1}$ across the full period range.

This result is somewhat surprising given the expectation for the donor properties to over-estimate \dot{M} (§6.4.1), but Figure 7.1 shows little indication of this. Further, an explicit assumption in the white dwarf based \dot{M} to be the total system \dot{M} is that all material lost by the donor is accreted onto the white dwarf – this is unlikely to be a robust assumption, as some material will be lost from the system without being accreted and would cause the white dwarf properties to indicate a lower system-wide \dot{M} than reality. Despite these factors, generally *higher* \dot{M} are observed with the white dwarf properties than with the donor.

The white dwarf indicating a higher mass loss rate may be a result of recent dwarf novae (i.e. periods of intense accretion onto the white dwarf), which cause the surface to temporarily heat up. After a dwarf nova has subsided, the white dwarf will take some time to readjust its temperature to the lower accretion rate, and for that period will appear to have an exaggerated accretion rate. OV Bootis (Schwope et al., 2021) was observed to be $\sim 9000\text{K}$ hotter than equilibrium 5 months after an outburst, and observations of GW Lib (Szkody et al., 2016) show that the white dwarf is $\sim 3000\text{K}$ hotter than equilibrium 8 years after an outburst.

Whilst such outburst could feasibly inflate the inferred \dot{M} , this would require a very recent outburst and would be extremely unlikely to affect every system in the sample. Further, the measurement uncertainty of the white dwarf T_{eff} in this sample is, on average, $\sim 2000\text{K}$ - comparable to what one might reasonably expect from a recent dwarf nova. Assuming a recent nova heats a white dwarf by 5000K , the apparent \dot{M} would be increased only by $\log(\dot{M}, M_{\odot} \text{ yr}^{-1}) \lesssim 0.2$ and should not radically alter the conclusions drawn from these data. At this time, the source of this discrepancy is unknown and more work is necessary to understand the tension between the two methods.

A system can be categorised as a period bouncer based on either the observed M_{donor} , or the observed \dot{M} . Despite this sample explicitly removing donors with masses typical of the post period minimum regime, three CVs have donor-inferred \dot{M} that are consistent with the \dot{M} of a period bounce CV: SDSS J0903, ASASSN-17fo, and OGLE82, though OGLE82 has an extremely uncertain \dot{M} measurement of $\log(\dot{M}, M_{\odot} \text{ yr}^{-1}) = -11.686 \pm 1.078$. This raises the question of an exceptionally poor understanding of the period minimum and period bounce regimes, but it must be noted that SDSS J0903 and ASASSN-17fo are peculiar systems for reasons previously mentioned in §6.4, and later revisited in §7.2. These two systems are instead more likely an artefact of systematic bias, discussed in §6.4.1, and only coincidentally lie on the period bounce donor track.

Hereafter, when values of \dot{M} are used they are the values derived from the donor properties.

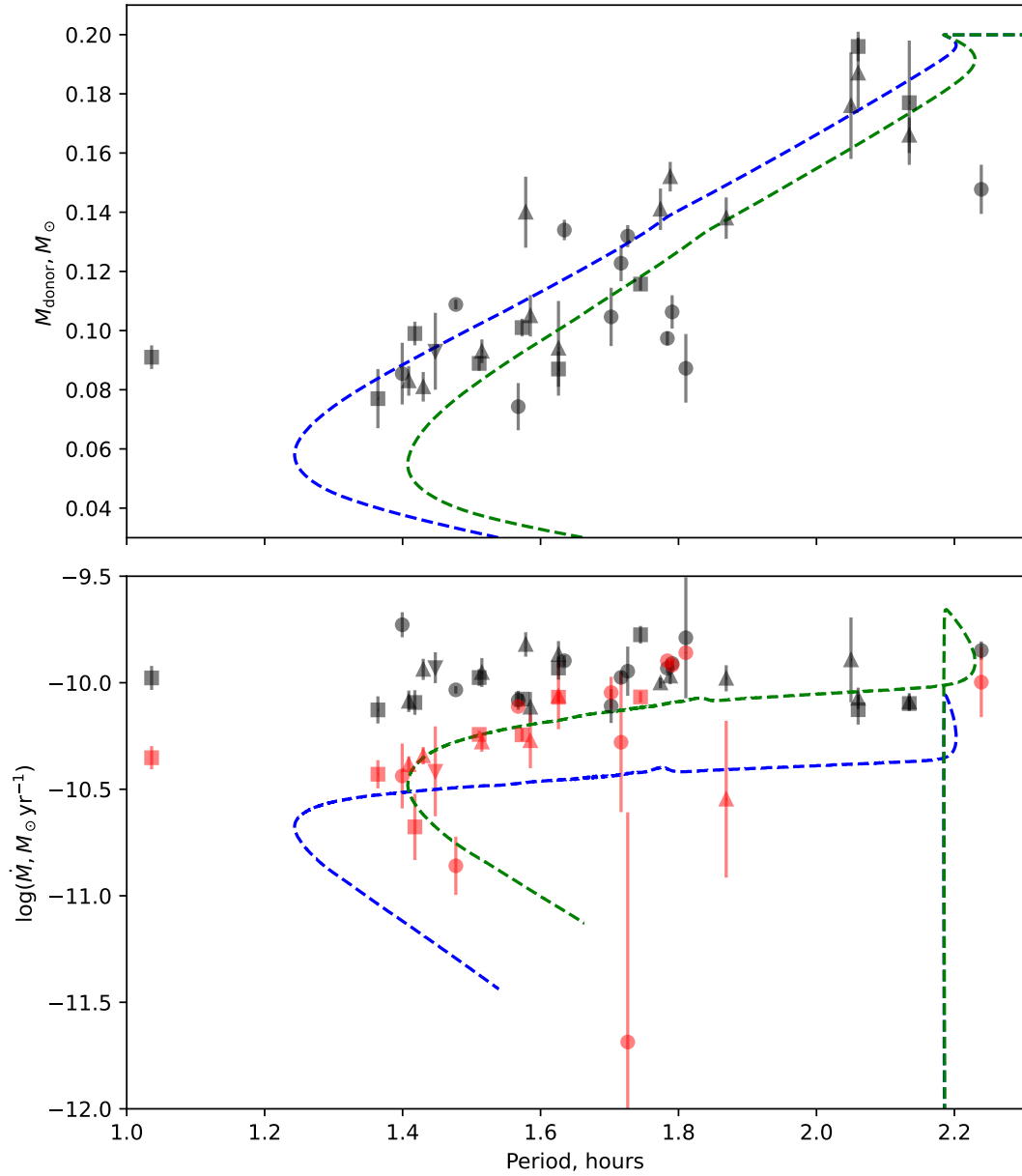


Figure 7.1: *Top:* Plotting the Period - M_{donor} relationship for the systems for which the white dwarf mass was determined. The MESA donor tracks are also plotted; the **blue dashed line** shows the purely gravitational wave driven model, and the **green dashed line** shows the model with gravitational braking amplified by a factor of 2.47. The symbols denote the source of the data: **circles** are the systems from Chapter 5, **upright triangles** are data from McAllister et al. (2019), **squares** are from Savoury et al. (2011), and the **inverted triangle** is the supplementary system from McAllister et al. (2017b). *Bottom:* Comparing the mass loss rates inferred from the donor properties (**red data**) with those inferred from the white dwarf properties (**black data**). Symbols are similar to the top panel.

7.1 Mass loss rate correlations

Recall from the discussion in §1.5.7 that if the missing AML from CV models is rooted in residual magnetic braking, *and these prescriptions correctly describe how magnetism scales with stellar properties*, one would expect to see a correlation between M_{donor} and \dot{M} , and see no such correlation with M_{wd} . This is because both magnetic braking prescriptions considered are dependent on the Rossby number, a function of the rotational period, which itself is a function of donor mass for short period CVs. Note that the allowed mass range of the method used here forces us to omit period bouncer systems. If, however, the CAML or eCAML model is correct, and the missing AML arises from white dwarf ejecta, (refer to §1.5.6), one would expect a correlation between M_{wd} and \dot{M} , as in both cases there is a dependence of AML on the total system mass, which is dominated by M_{wd} . Of course, the two sources of extra AML are not mutually exclusive and may co-exist.

To probe for these correlations the χ^2 test is insufficient, since both axes have significant uncertainty. The orthogonal distance between the line and data is minimised, similar to §5.2.1. Pearson correlation coefficients and their associated p values are reported, computed based on the *means* of the data, and do not consider the uncertainty in the measurements. Since uncertainty is ignored, these correlation coefficients are not technically correct, however, these values serve as a useful rough guide and are often easily corroborated by inspection of the relevant plots¹.

Figure 7.3 shows the data for $\dot{M}(M_{\text{wd}})$, and Figure 7.4 shows $\dot{M}(M_{\text{donor}})$. The correlation between M_{wd} and \dot{M} , is reasonably confident; ignoring errors, these data have a Pearson rank correlation coefficient of -0.502 and a p value of 0.012 , indicating a high likelihood of a mild correlation. Fitting a straight line to these data supports this, finding a best-fit gradient that is 4.5σ from the null-hypothesis of 0 . However, no correlation is found between \dot{M} and M_{donor} . These data have a Pearson coefficient of 0.089 with a p value of 0.68 , and attempting to fit a straight line to the data results in an unconstrained gradient.

The relationship between M_{wd} and \dot{M} has been previously observed, and justified theoretically by Pala et al. (2021). The luminosity of the white dwarf is

¹Pearson correlation coefficients range from -1 (perfect negative correlation), to $+1$ (perfect positive correlation), with 0 indicating no correlation between the data. The p value is the probability of the null hypothesis, i.e. that the data are uncorrelated, and values of $p < 0.05$ are generally accepted to indicate confidence in a correlation.

related to both the radius and temperature, and the mass and mass loss rate,

$$L \propto R_{\text{wd}}^2 T_{\text{eff}}^4 \propto \dot{M} M_{\text{wd}}^{0.4} \quad (7.1)$$

By disregarding the weak mass relationship on the right side of this equation,

$$\dot{M} \propto R_{\text{wd}}^2 T_{\text{eff}}^4 \quad (7.2)$$

R_{wd} as a function of M_{wd} can be retrieved from the Bergeron et al. (1995) cooling tracks for a given T_{eff} . Pala et al. (2021) demonstrate that there is no observable correlation between white dwarf temperature, and white dwarf mass, so T_{eff} can be assumed to be the mean of the Pala et al. (2021) sample, $\sim 15000\text{K}$. Note that whilst the gradient is weakly dependent on the chosen value of T_{eff} , the difference within the range of reasonable CV temperatures ($\sim 5000 - 30000\text{K}$) is negligible. The constant of proportionality is chosen by Pala et al. (2021) to reflect $\dot{M} = 7 \times 10^{-10} M_{\odot}\text{yr}^{-1}$ at $M_{\text{wd}} = 0.8M_{\odot}$, and this is mirrored here.

Thus, a prediction for approximate typical mass loss rates is found from the white dwarf sample in Pala et al. (2021). Figure 13 from Pala et al. (2021) is reproduced in Figure 7.2, and shows both the lack of correlation between M_{wd} and T_{eff} , and the loose agreement between observations and Equation 7.2. Similarly, Equation 7.2 is compared in Figure 7.3 alongside the best fit straight line, where it can be seen that this relationship agrees with the 3σ threshold of the best fit but appears less steep than the data suggests. The mass loss rates found from donor properties are loosely consistent with the recent findings of Pala et al. (2021) – specifically, that mass loss rates estimated from donor radii show a similar trend with WD mass as those estimated from WD temperatures. However, as discussed, the mass loss rates from the donor are slightly lower and show a stronger trend with M_{wd} .

Figure 7.1 shows a reasonably tight agreement between the model MESA donor tracks and observed \dot{M} and P . One might expect to see this reflected in a plot of M_{donor} vs. \dot{M} given the strong dependence of M_{donor} on P , but the agreement is more ambiguous with many data lying between the two model tracks. This is likely related to the scatter about the models in Figure 5.41. As the mass-period relationship is synonymous with the mass-radius relationship, the scatter in Figure 5.41 propagates forward.

Based on these results, it appears unlikely that residual magnetic braking (in

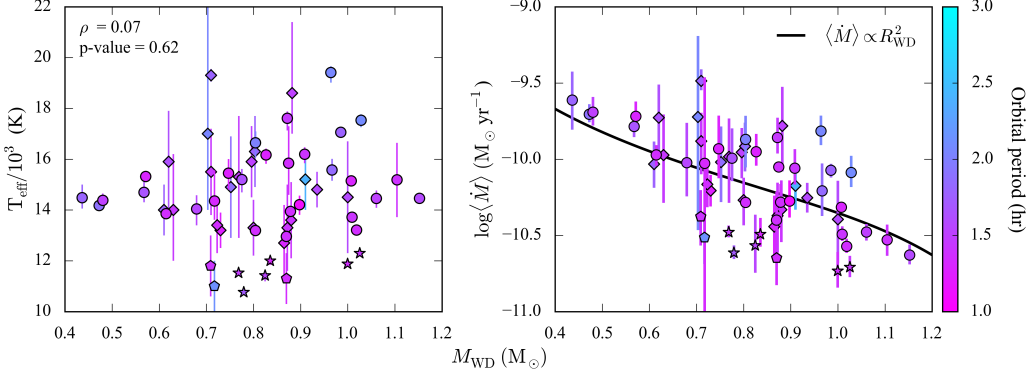


Figure 7.2: Reproduced from [Pala et al. \(2021\)](#), Figure 13. The subset of modelled systems, with $P < 3\text{hr}$ are shown. **Circles** and **stars** are pre- and post-period bounce systems derived by [Pala et al. \(2021\)](#), and **diamonds** and **pentagons** are pre- and post-period bounce systems taken from the literature. *Left:* The T_{eff} is plotted against M_{wd} , and no correlation can be seen. *Right:* $\log\langle\dot{M}\rangle$ is plotted against M_{wd} , though now the data are correlated along the white dwarf mass-radius relationship outlined by [Pala et al. \(2021\)](#), $M_{\text{wd}} \propto R_{\text{wd}}^2$, shown by the **black line**.

the forms given in §1.5.7) is responsible for the excess AML in CVs, but still possible that the drag imposed by nova material is the cause. However, there are a few factors to consider when deciding how convincing these findings are, beyond the important factors mentioned in §6.4.1. The sample size is still small, only 24 systems, and the uncertainty in these measurements is significant. More importantly, the parameter space between $0.12M_{\odot} < M_{\text{donor}} < 0.20M_{\odot}$ is sparsely populated, and has particularly large uncertainties. This makes the search for correlation dominated by data in the narrow range of $0.08M_{\odot} < M_{\text{donor}} < 0.12M_{\odot}$, and thus less robust; gathering more data for short period CVs with higher M_{donor} may yet reveal a correlation between donor mass and mass loss rate. Also, the lack of correlation with M_{donor} may be a consequence of even the amplified ‘optimal’ model \dot{M} not varying by much across the donor mass range, a problem that may similarly be solved by expanding the available sample.

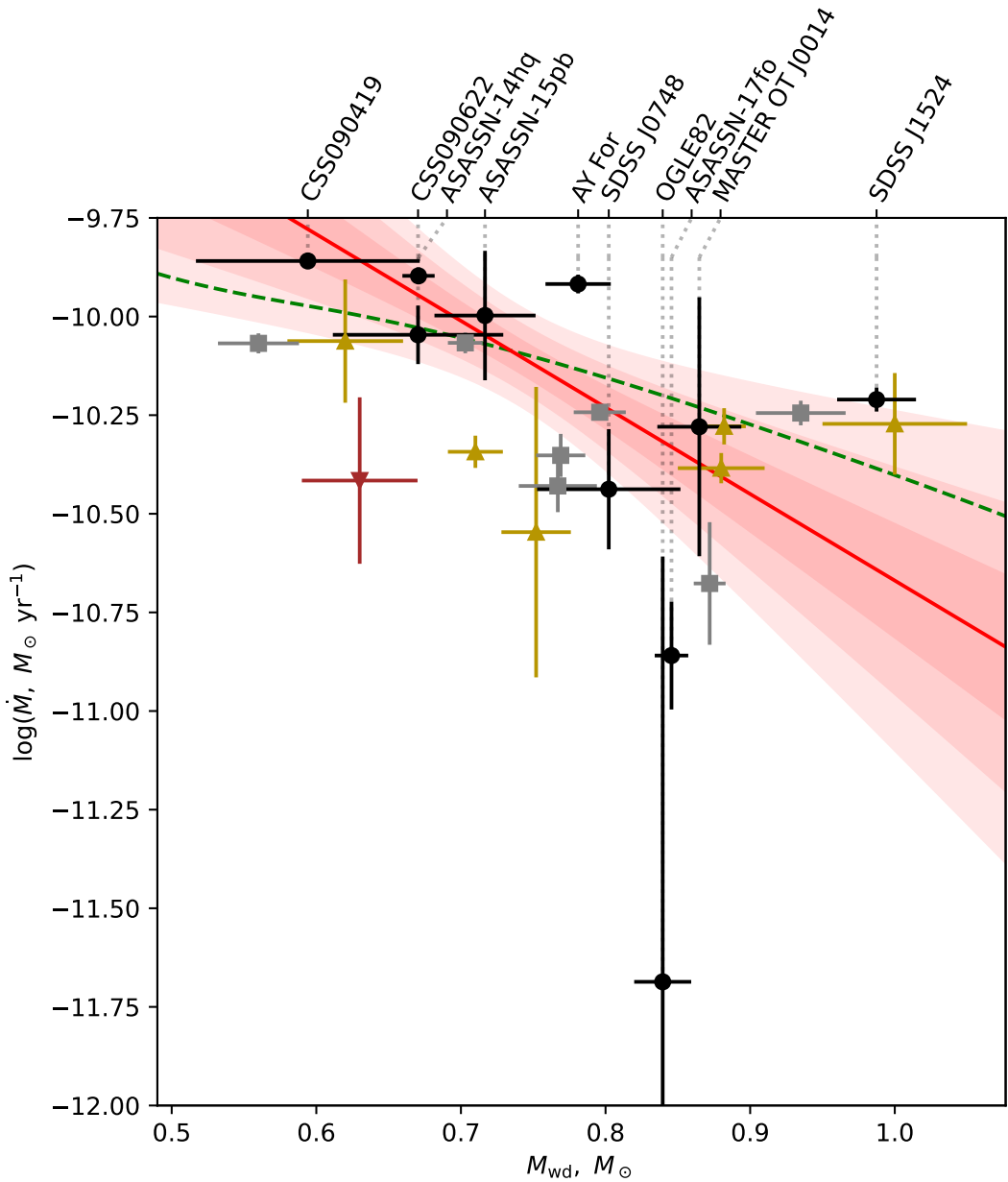


Figure 7.3: Showing the correlation between the white dwarf mass and mass loss rate. The **black circles** are the systems from Chapter 5 and have their system names labelled, **gold upright triangles** are data from McAllister et al. (2019), **grey squares** are from Savoury et al. (2011), and the **brown inverted triangle** is the supplementary system from McAllister et al. (2017b). The **red line** shows the best fit to the data, with the **shaded red region** showing the coverage of the uncertainty in the line parameters. The darkest region is 1σ , the middle region is 2σ , and the lightest region shows 3σ . The best fit line has the form $\log(\dot{M}, M_{\odot} \text{ yr}^{-1}) = (-2.62 \pm 0.60)(M_{\text{wd}}, M_{\odot}) - (8.18 \pm 0.44)$. Also shown as the **dashed green line** is the mass loss expected corresponding to a typical CV white dwarf T_{eff} , following the relationship described in Equation 7.2

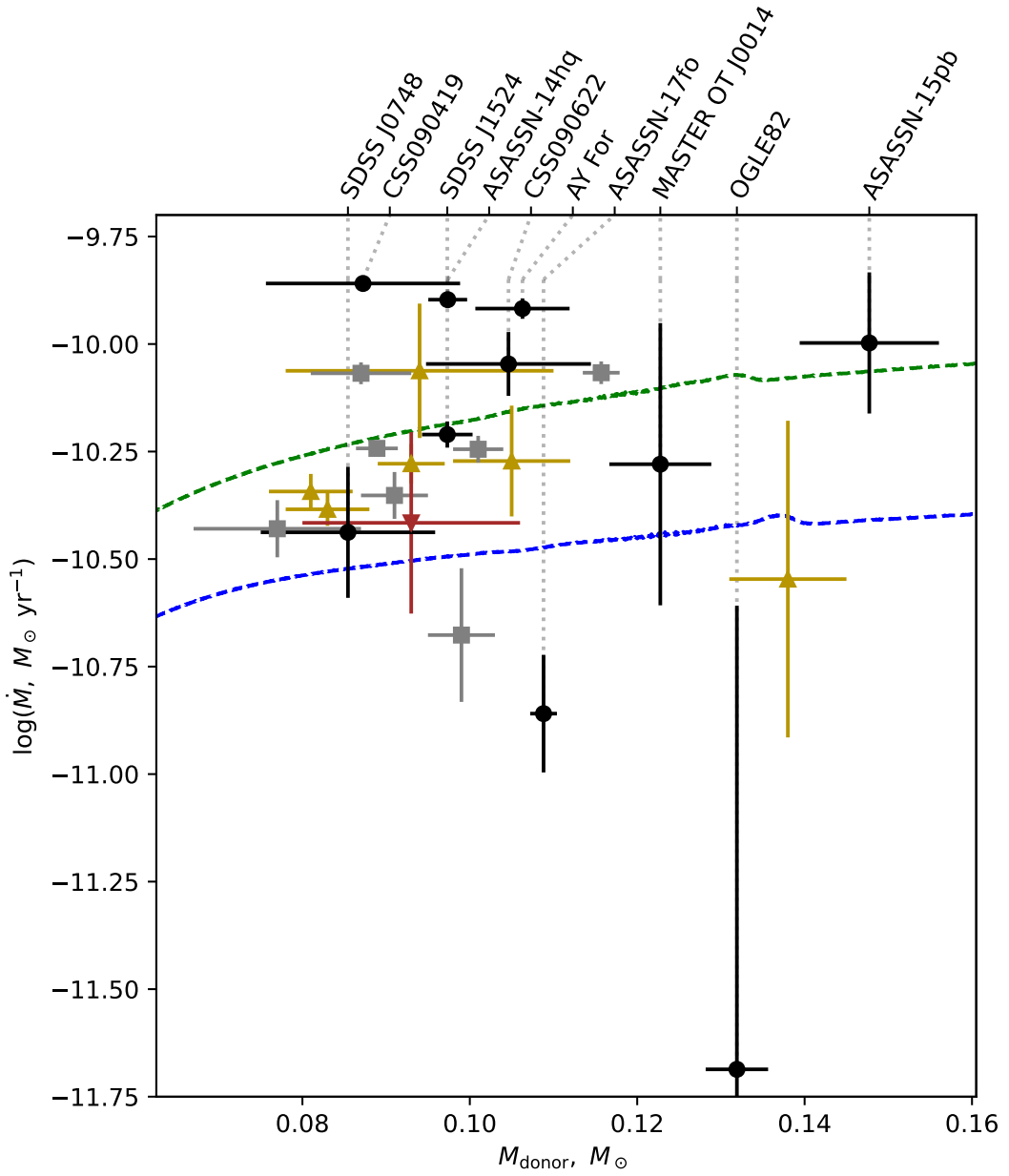


Figure 7.4: Showing the donor masses and mass loss rates. Observations are styled similarly to Figure 7.3. The **dashed blue line** shows the value predicted by the ‘standard’ MESA CV model, and the **dashed green line** is the ‘optimal’ MESA CV track.

7.2 Measured angular momentum loss

It is possible to more directly probe the AML of the CVs – Equation 3.46 shows how the AML can be calculated from M_{wd} , M_{donor} , \dot{M} , and a . Figures 7.5 and 7.6 show the \dot{J} excess, \dot{J}_{ex} , which has had \dot{J}_{GR} subtracted, against the two component masses.

Note that there are two peculiar systems in the sample, ASASSN-17fo and SDSS J0903, which were raised in §6.4 as having exceptionally low \dot{M} and \dot{J} estimates and are likely the result of the systematic bias described in §6.4.1. Here, it can be seen that these systems appear to have sub-GR angular momentum loss, which is unphysical. Whilst there remains serious doubt on the validity of these systems, they are still considered in the following analysis.

The M_{wd} and \dot{J}_{ex} data appear to be loosely correlated, with a Pearson correlation of -0.514 and a p-value of 0.010 . Fitting a straight line to the data finds $(\dot{J}_{\text{obs}} - \dot{J}_{\text{MESA}}) = (-8.3 \pm 1.6) \times 10^{27} (M_{\text{wd}}, M_{\odot}) + (6.9 \pm 1.3) \times 10^{27}$ Joules.

However, similarly to the $\log(\dot{M})$ data, there is no sign of correlation between M_{donor} and \dot{J}_{ex} – these data have a correlation coefficient of 0.032 and a p-value of 0.884 , strongly indicating that the data are uncorrelated and again suggesting that the magnetic braking prescriptions outlined in §1.5.7 do not cause excess AML in short period CVs.

Based on period excess, three possibilities for the form of excess AML were suggested in §5.2.1: the excess AML declines in strength, but more slowly than gravitational losses; excess AML is roughly constant across the range of M_{wd} or M_{donor} ; or excess AML increases in strength towards lower M_{donor} or M_{wd} . The evidence suggests that excess AML appears to increase in strength towards lower M_{wd} , and is uncorrelated with M_{donor} .

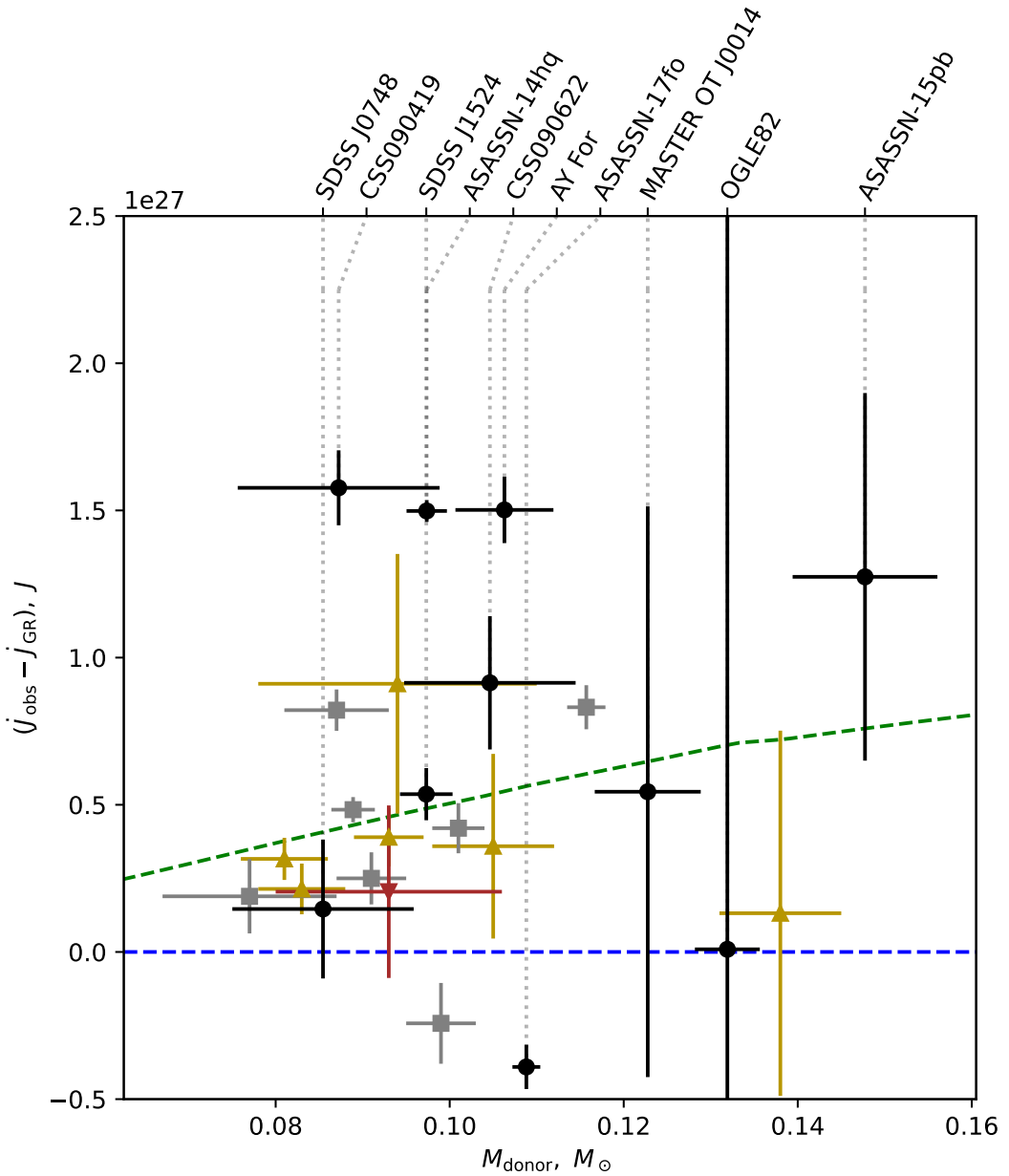


Figure 7.5: Showing the correlation between the donor mass and angular momentum loss rate, \dot{J} . Observations are keyed similarly to Figure 7.3, though here the **dashed blue line** shows perfect agreement between observations and gravitational angular momentum loss. The **dashed green line** shows the $2.47 \times$ donor track.

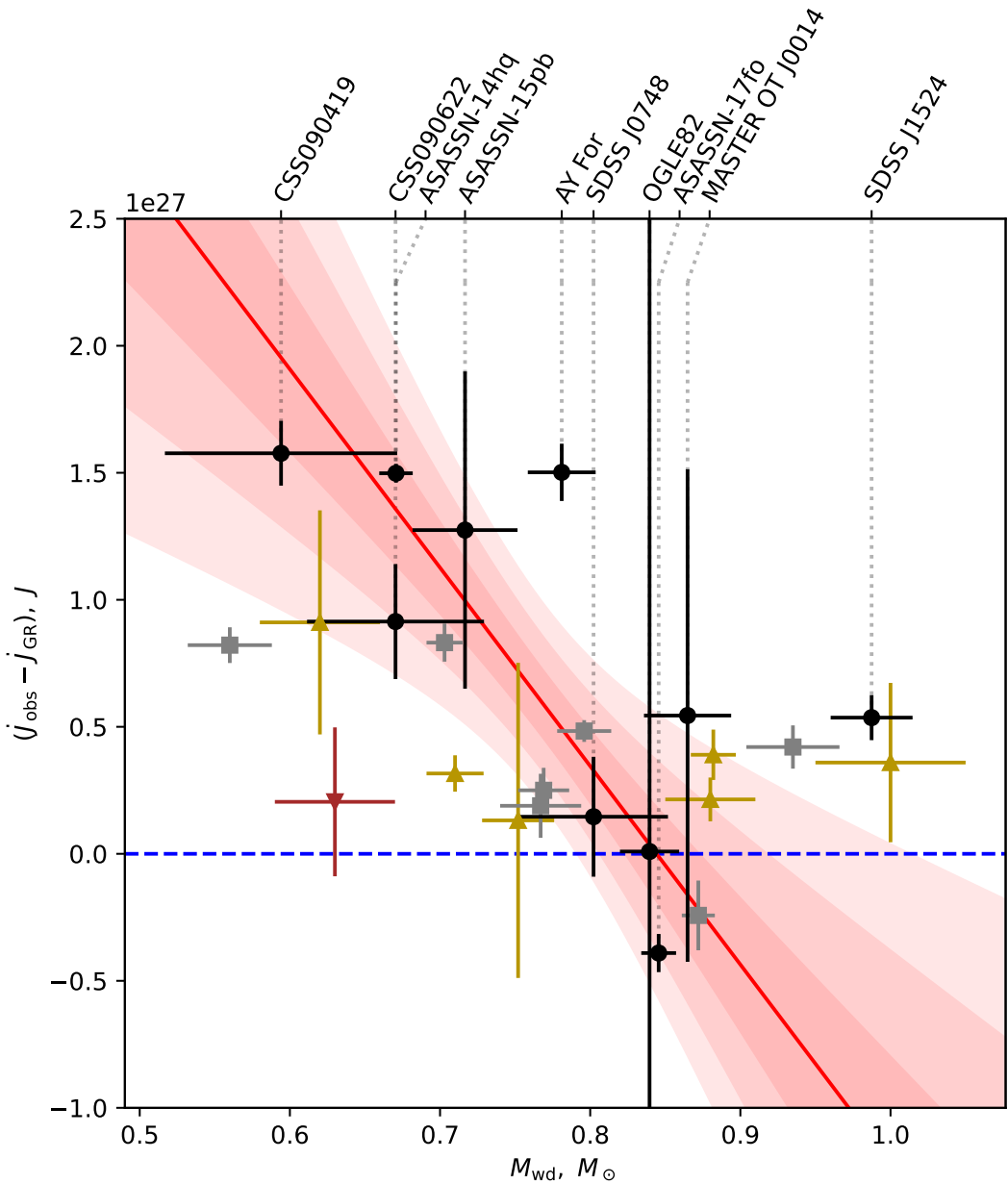


Figure 7.6: Showing the correlation between the white dwarf mass and angular momentum loss rate, \dot{J} . Observations are keyed similarly to Figure 7.3, and the best fit line has the form $(\dot{J}_{\text{obs}} - \dot{J}_{\text{MES}}), J = (-8.3 \pm 1.6) \times 10^{27} (M_{\text{wd}}, M_{\odot}) + (6.9 \pm 1.3) \times 10^{27}$.

7.3 A closer look at CAML

Recall from §1.5.6 that under eCAML, the efficiency parameter ν is given by C/M_{wd} , and typical values of C are roughly chosen to be $0.3 - 0.4$ to reproduce the observed CV population distribution ([Schreiber et al., 2016](#)).

$$\frac{\dot{J}_{\text{ex}}}{J} = \nu \frac{\dot{M}_{\text{donor}}}{M_{\text{donor}}} \quad (7.3)$$

$$\frac{\dot{J}_{\text{ex}}}{J} = C \frac{\dot{M}_{\text{donor}}}{M_{\text{donor}} M_{\text{wd}}} \quad (7.4)$$

C can be fit to the measured excess AML, again minimising the orthogonal distance. Doing so finds a best-fit $C = 0.59 \pm 0.02$, shown in Figure 7.7, much higher than the previously estimated range of $0.3 - 0.4$, which is also plotted.

Such a high value of C is incompatible with the existence of short-period CVs, as this degree of CAML would render all short period systems dynamically unstable, which is clearly not the case. Whilst the sample size is small and the uncertainty in these measurements remains large, these preliminary results might be interpreted as a tension between the eCAML calibrated from population synthesis models by [Schreiber et al. \(2016\)](#), and the calibration reported here. However, such an interpretation is premature. As discussed in §6.4.1, the values reported here are subject to uncharacterised systematic bias, which likely causes an over-estimation of \dot{M} and thus likely an over-estimation of C . Using the sample to calculate C is therefore unwise, but the general trend present in these data remains promising. The measured \dot{J}_{ex}/J clearly lie on a straight line, C is only a factor of 2 higher than expected, and the data are clearly strongly correlated with the quantities predicted by eCAML, implying that the theory is likely to be supported by a future, more robust dataset.

A further comparison with the previous eCAML calibration is possible by calculating ν for each system. The ν values are plotted as a function of white dwarf mass in Figure 7.8, alongside the predicted ν for eCAML, $\nu = C/M_{\text{wd}}$. As the uncertainties in both \dot{J}/J_{tot} and \dot{M}/M_{donor} are large, the uncertainty in the calculated ν is too large to draw confident conclusions; however, it still provides a useful indication of what might be expected from future results. Whilst some data are consistent with the [Schreiber et al. \(2016\)](#) eCAML calibration, it appears to generally under-estimate the mass loss from short period CVs with a significant portion of the data consistent with $\nu \sim 0.9$.

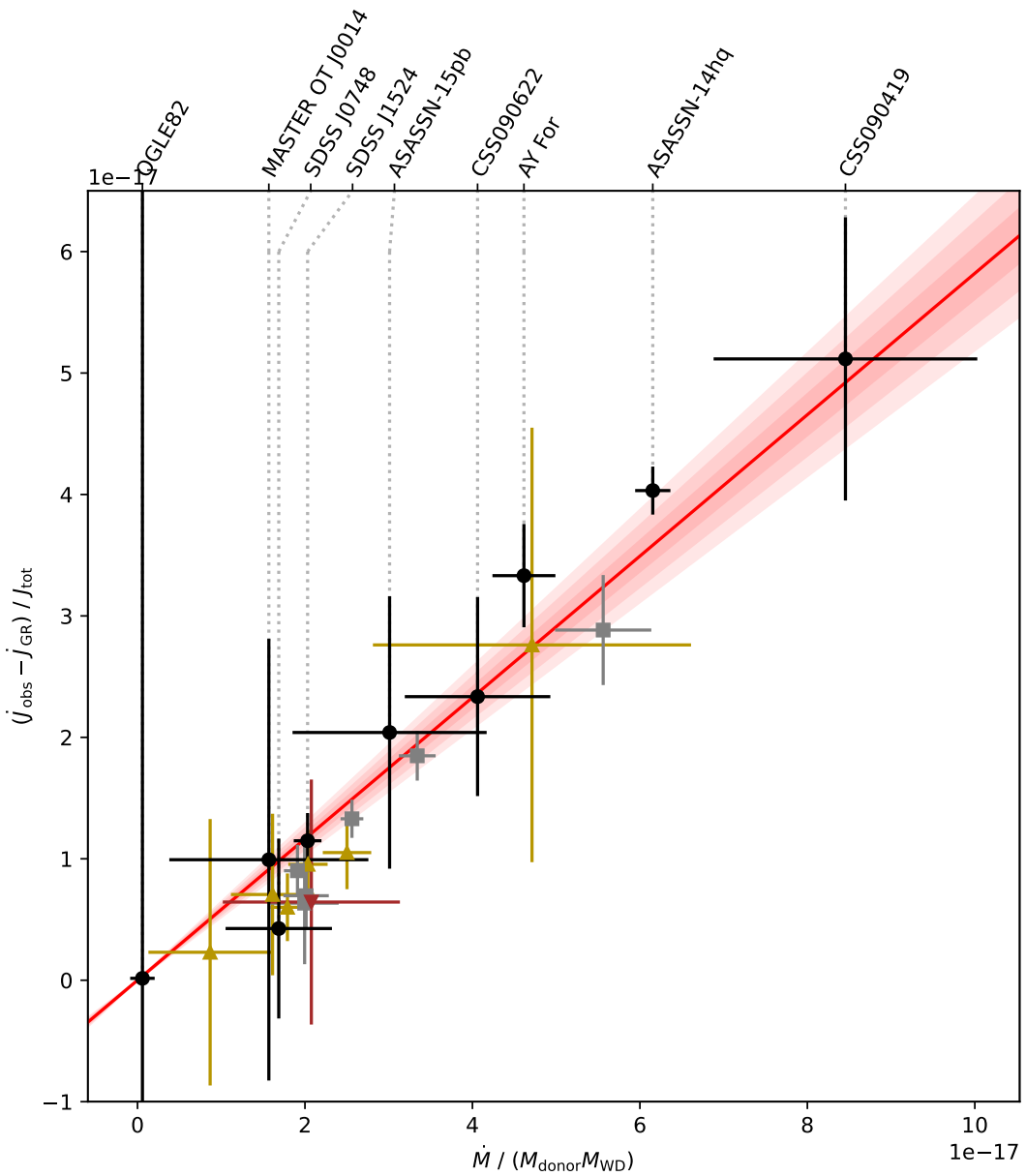


Figure 7.7: Showing the observed quantities relevant to Equation 7.4 and the best-fit value of C for short period CVs, based on donor properties. Symbols are as in Figure 7.3, and the **dashed blue line** shows the relationship for $C = 0.35$.

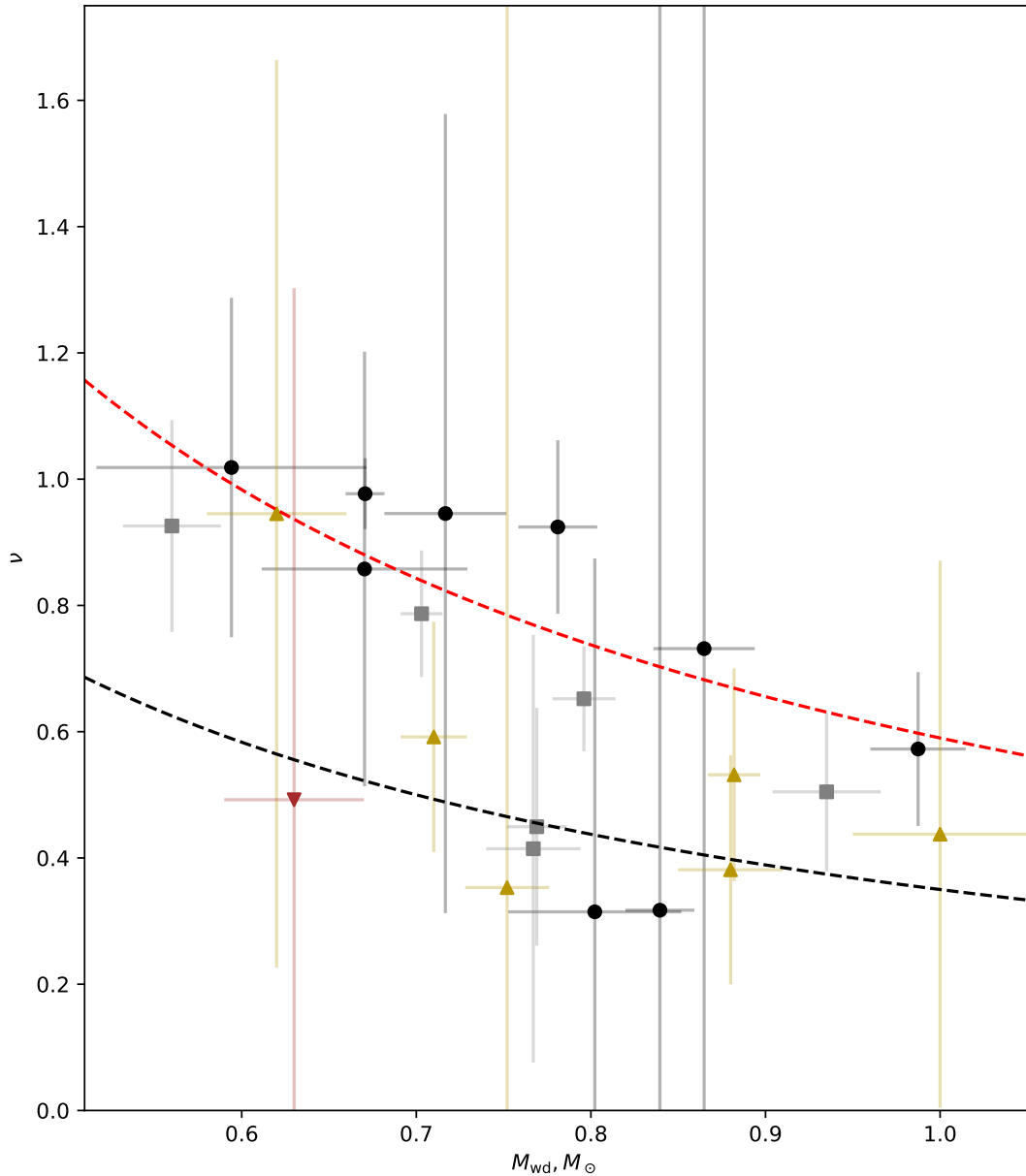


Figure 7.8: Showing the calculated values of ν for each short period CV in this sample. Symbols are as in Figure 7.3, though note that for clarity the error bars here are partially transparent. The **dashed black line** shows the eCAML prescription for $\nu = 0.35/M_{\text{wd}}$, and the **red dashed line** shows $\nu = 0.59/M_{\text{wd}}$.

Chapter 8

Conclusion and future work

I have extended the CV eclipse model to allow for a tiered structure of shared eclipse parameters as a logical progression of the work by [McAllister \(2017\)](#). Using this new hierarchical eclipse model I characterise the component masses and radii, separations, white dwarf temperatures and surface gravities of 15 new short-period CVs. Future work should be directed to improving the optimisation of the eclipse light curve modelling – the Affine invariant sampler with parallel tempering that is employed here is inefficient for problems with more than ~ 5 parameters, and the model frequently has more than 100 free parameters. While the optimisation works, it is likely sub-optimal. Unfortunately, the optimisation of expensive, non-differentiable models with many free parameters is inherently difficult, and it remains to be seen how significant an improvement is possible.

Some issues were encountered during the modelling of a handful of systems, which are recommended for UV spectroscopic follow-up studies to probe them in more detail: T_{eff} of the white dwarf in SSSJ0522–3505 appears to be $\sim 10000\text{K}$ higher than is typical for a CV, and the white dwarfs of CSS090419 and CSS090622 appear to *brighten* in the i' band, contrary to models. However, I justify the assertion that these problems do not significantly impact the final results of modelling.

The newly extended sample of eclipse modelled CVs follows the canonical CV donor evolutionary tracks, though with significant scatter that suggests the possibility of a less unified donor track than is typically thought. A significantly larger sample is necessary before more concrete claims can be made.

I demonstrate the effectiveness of MESA in modelling CV evolution, and produce a configuration that replicates the canonical CV donor evolutionary sequence. I also note that with some additional work, MESA should be capable of even closer agreement. Instead, I focus on an empirical reproduction of the observed M dwarf mass-radius relationship of [Brown et al. \(2022\)](#) by introducing star spots to MESA. By adjusting the star spot parameters, I am able to exactly reproduce the Brown mass-radius relation.

Based on prior work by [Knigge \(2006\)](#); [Knigge et al. \(2011\)](#), I use these MESA M dwarf models to deduce the mass loss rates of the M dwarf donors of eclipse modelled CVs by comparing their measured masses and radii with those of MESA models with varying degrees of mass loss. As such, I present the first sample of donor-derived secular mass loss rate estimates for CVs, and use these data to interrogate the source of the long-standing excess AML implied by CV prior observations. The data are preliminary, and are contingent on the validity of the

M dwarf masses and radii to calibrate the MESA models. The best available M dwarf mass-radius sample is sparsely populated below $\sim 0.12M_{\odot}$, so I cannot marginalise over the intrinsic scatter in the M dwarf mass-radius relationship, biasing the sample towards higher \dot{M} while also polluting it with some unphysically low \dot{M} systems. Future observations of low mass M dwarf masses and radii should be able to rectify this shortfall.

The results here are considered preliminary for a few reasons. Primarily, the mass-radius relationship used to calibrate the MESA model radii at zero mass loss is poorly sampled and incomplete, reverting to theoretical models at $0.121M_{\odot}$ – the majority of my data lie in this poorly understood mass range. In addition, significant further work is needed to grow the population of eclipse modelled low- M_{donor} CVs and improve these statistics, and continued eclipse modelling targeting short period CVs will be invaluable to confidently determining the source of excess AML. Specific effort should be targeted towards confident characterisation of CVs at slightly higher M_{donor} of ~ 0.15 (i.e. a period of $\sim 1.8 - 2.2$ hours), where existing data are somewhat sparse and have large uncertainties. The clustering of confident data at lower masses leaves the current sample subject to an over-reliance on data with donor masses below $\sim 0.12M_{\odot}$.

These results suggest that magnetic braking is a poor description of the excess AML inferred from eclipse modelling of CVs, and indicate that eCAML continues to be a better descriptor of the data. The basic prediction of eCAML – that the relationship between \dot{J}/J and $\dot{M}/(M_{\text{donor}}M_{\text{wd}})$ follows a straight line – is seen in the data, though I suggest in §6.4.1 that my \dot{M} are systematically over-estimated so cannot yet be used to calibrate eCAML. It must be reiterated, however, that the data presented here are themselves *not* well-described by eCAML. Calibrating the eCAML free parameter from these data results in a higher constant of proportionality and concludes that virtually all CVs are dynamically unstable, which is not self-consistent.

Bibliography

- Allard F., Homeier D., Freytag B., 2012, in Richards M. T., Hubeny I., eds, IAU Symposium Vol. 282, From Interacting Binaries to Exoplanets: Essential Modeling Tools. pp 235–242, [doi:10.1017/S1743921311027438](https://doi.org/10.1017/S1743921311027438)
- Andronov N., Pinsonneault M., Sills A., 2003, [ApJ, 582, 358](#)
- Argiroff C., Caramazza M., Micela G., Sciortino S., Moraux E., Bouvier J., Flaccomio E., 2016, [A&A, 589, A113](#)
- Asplund M., Grevesse N., Sauval A. J., Scott P., 2009, [ARA&A, 47, 481](#)
- Bailey J., 1979, Monthly Notices of the Royal Astronomical Society, 187, 645
- Baraffe I., Homeier D., Allard F., Chabrier G., 2015, [A&A, 577, A42](#)
- Belloni D., Schreiber M. R., Zorotovic M., Ilkiewicz K., Hurley J. R., Giersz M., Lagos F., 2018, [Monthly Notices of the Royal Astronomical Society, 478, 5639](#)
- Belloni D., Schreiber M. R., Pala A. F., Gänsicke B. T., Zorotovic M., Rodrigues C. V., 2020, [MNRAS, 491, 5717](#)
- Bergeron P., Wesemael F., Beauchamp A., 1995, [Publications of the Astronomical Society of the Pacific, 107, 1047](#)
- Bradshaw P., 1974, [Nature, 249, 135](#)
- Brown A. J., et al., 2022, [MNRAS,](#)
- Bruch A., 2000, [A&A, 359, 998](#)
- Bruch A., Beele D., Baptista R., 1996, [A&A, 306, 151](#)
- Cannizzo J. K., 1993, [ApJ, 419, 318](#)
- Castelli F., Kurucz R., 2004, Proceedings of the International Astronomical Union
- Choi J., Dotter A., Conroy C., Cantiello M., Paxton B., Johnson B. D., 2016, [The Astrophysical Journal, 823, 102](#)

Copperwheat C. M., et al., 2012, *Monthly Notices of the Royal Astronomical Society*, 421, 149

Cyburt R. H., et al., 2010, *ApJS*, 189, 240

Davis P. J., Kolb U., Willems B., Gänsicke B. T., 2008, *Monthly Notices of the Royal Astronomical Society*, 389, 1563

De Marco O., Passy J.-C., Moe M., Herwig F., Mac Low M.-M., Paxton B., 2011, *MNRAS*, 411, 2277

Dhillon V. S., et al., 2007, *MNRAS*, 378, 825

Dhillon V. S., et al., 2014, *MNRAS*, 444, 4009

Dhillon V. S., et al., 2021, *MNRAS*, 507, 350

Donati J. F., Landstreet J. D., 2009, *ARA&A*, 47, 333

Dotter A., 2016, *The Astrophysical Journal Supplement Series*, 222, 8

Drake A. J., et al., 2008, *Astrophysical Journal*, 696, 870

Dubus G., Otulakowska-Hypka M., Lasota J.-P., 2018, *A&A*, 617, A26

Earl D. J., Deem M. W., 2005, *Phys. Chem. Chem. Phys.*, 7, 3910

Eggleton P. P., 1983, *The Astrophysical Journal*, 268, 368

Einstein A., 1918, *Sitzungsberichte der Königlich Preußischen Akademie der Wissenschaften* (Berlin, pp 154–167)

Epelstain N., Yaron O., Kovetz A., Prialnik D., 2007, *MNRAS*, 374, 1449

Foreman-Mackey D., Hogg D. W., Lang D., Goodman J., 2013, *Publications of the Astronomical Society of the Pacific*, 125, 306

Fukugita M., Ichikawa T., Gunn J. E., Doi M., Shimasaku K., Schneider D. P., 1996, *AJ*, 111, 1748

Gaia Collaboration et al., 2016, *A&A*, 595, A1

Gaia Collaboration et al., 2018, *A&A*, 616, A1

Gallet F., Bouvier J., 2013, *A&A*, 556, A36

Gänsicke B., et al., 2009, *MNRAS*, 397, 2170

Gänsicke B. T., Southworth J., Hickman R., Marsh T. R., Copperwheat C. M., Littlefair S. P., Dhillon V. S., 2010, *Monthly Notices of the Royal Astronomical Society*, 402, 1824

- Garraffo C., Drake J. J., Cohen O., 2015, [ApJ](#), **813**, 40
- Garraffo C., Drake J. J., Cohen O., 2016, [ApJL](#), **833**, L4
- Garraffo C., et al., 2018a, [ApJ](#), **862**, 90
- Garraffo C., Drake J. J., Alvarado-Gomez J. D., Moschou S. P., Cohen O., 2018b, [ApJ](#), **868**, 60
- Gibson N. P., Aigrain S., Roberts S., Evans T. M., Osborne M., Pont F., 2012, [MNRAS](#), **419**, 2683
- Goliasch J., Nelson L., 2015, [ApJ](#), **809**, 80
- Goodman J., Weare J., 2010, [Communications in Applied Mathematics and Computational Science](#), **5**, 65
- Gossage S., Dotter A., Garraffo C., Drake J. J., Douglas S., Conroy C., 2021, [ApJ](#), **912**, 65
- Hamada T., Salpeter E., 1961, [ApJ](#), **134**, 683
- Hameury J. M., 2002, in Gänsicke B. T., Beuermann K., Reinsch K., eds, Astronomical Society of the Pacific Conference Series Vol. 261, The Physics of Cataclysmic Variables and Related Objects. p. 377
- Hameury J.-M., Menou K., Dubus G., Lasota J.-P., Hure J.-M., 1998, [MNRAS](#), **298**, 1048
- Harrison T. E., 2016, [ApJ](#), **833**, 14
- Harrison T. E., 2018, [ApJ](#), **861**, 102
- Hauschildt J., Weiß J., Beck C., Grebenhchikov S. Y., Düren R., Schinke R., Koput J., 1999, [Chemical Physics Letters](#), **300**, 569
- Hauschildt P., Allard F., Barman T., Schweitzer A., Baron E., Leggett S. K., 2001, in Woodward C. E., Bicay M. D., Shull J. M., eds, Astronomical Society of the Pacific Conference Series Vol. 231, Tetons 4: Galactic Structure, Stars and the Interstellar Medium. p. 427
- Hellier C., 2001, Cataclysmic variable stars: how and why they vary. Springer
- Henyey L., Vardya M. S., Bodenheimer P., 1965, [ApJ](#), **142**, 841
- Hoffmann S. M., Vogt N., 2022, [New Astronomy](#), **92**, 101722
- Hogg D. W., Bovy J., Lang D., 2010, arXiv e-prints, p. [arXiv:1008.4686](#)
- Horne K., Stiening R. F., 1985, [MNRAS](#), **216**, 933

- Howell S. B., 2001, *PASJ*, **53**, 675
- Howell S. B., Skidmore W., 2002, *New Astron. Rev.*, **46**, 801
- Hurley J. R., Tout C. A., Pols O. R., 2002, *MNRAS*, **329**, 897
- Ivanova N., et al., 2013, *A&ARv*, **21**, 59
- Ivanova N., Justham S., Ricker P., 2020, Common Envelope Evolution, doi:10.1088/2514-3433/abb6f0.
- James D. J., Jardine M. M., Jeffries R. D., Randich S., Collier Cameron A., Ferreira M., 2000, *Monthly Notices of the Royal Astronomical Society*, **318**, 1217
- Jeffries R. D., Jackson R. J., Briggs K. R., Evans P. A., Pye J. P., 2011, *MNRAS*, **411**, 2099
- Kato T., 2022, arXiv e-prints, p. arXiv:2201.02945
- Kato T., et al., 2009, *Publications of the Astronomical Society of Japan*, **61**, S395
- Kato T., Maehara H., Uemura M., 2012, *PASJ*, **64**, 63
- Kato T., et al., 2016, *PASJ*, **68**, 65
- Kato T., et al., 2017, *PASJ*, **69**, 75
- King A., Kolb U., 1995, *ApJ*, **439**, 330
- Knigge C., 2006, *Monthly Notices of the Royal Astronomical Society*, **373**, 484
- Knigge C., 2011, arXiv e-prints, p. arXiv:1101.1538
- Knigge C., Baraffe I., Patterson J., 2011, *ApJS*, **194**, 28
- Kochukhov O., 2021, *A&ARv*, **29**, 1
- Koester D., 2010, *Mem. Soc. Astron. Italiana*, **81**, 921
- Kolb U., 1993, *A&A*, **271**, 149
- Kolb U., 2002, in Gänsicke B., Beuermann K., Reinsch K., eds, Astronomical Society of the Pacific Conference Series Vol. 261, The Physics of Cataclysmic Variables and Related Objects. p. 180
- Kolb U., Baraffe I., 1999, in Hellier C., Mukai K., eds, Astronomical Society of the Pacific Conference Series Vol. 157, Annapolis Workshop on Magnetic Cataclysmic Variables. p. 273 ([arXiv:astro-ph/9810315](https://arxiv.org/abs/astro-ph/9810315))
- Kolb U., de Kool M., 1993, *A&A*, **279**, L5

- Kolb U., King A., Ritter H., 1998, [MNRAS](#), 298, L29
- Lindegren L., et al., 2018, [A&A](#), 616, A2
- Littlefair S. P., Dhillon V. S., Marsh T. R., Gänsicke B. T., Baraffe I., Watson C. A., 2007, [MNRAS](#), 381, 827
- Littlefair S. P., Dhillon V. S., Marsh T. R., Gänsicke B. T., Southworth J., Baraffe I., Watson C. A., Copperwheat C., 2008, [MNRAS](#), 388, 1582
- Littlefair S., Dhillon V., Gänsicke B., Bours M., Copperwheat C., Marsh T., 2014, [MNRAS](#), 443, 718
- Livio M., Pringle J. E., 1994, [ApJ](#), 427, 956
- López-Morales M., Ribas I., 2005, [ApJ](#), 631, 1120
- Lubow S. H., Shu F. H., 1975, [The Astrophysical Journal](#), 198, 383
- Luri X., et al., 2018, [A&A](#), 616, A9
- Marsden S. C., et al., 2011, [MNRAS](#), 413, 1922
- Mason E., Howell S. B., 2005, [A&A](#), 439, 301
- Matt S. P., Brun A. S., Baraffe I., Bouvier J., Chabrier G., 2015, [ApJL](#), 799, L23
- McAllister M., 2017, PhD thesis, The University of Sheffield
- McAllister M. J., et al., 2015, [MNRAS](#), 451, 114
- McAllister M. J., et al., 2017a, [MNRAS](#), 464, 1353
- McAllister M. J., et al., 2017b, [MNRAS](#), 467, 1024
- McAllister M., et al., 2019, [Monthly Notices of the Royal Astronomical Society](#), 486, 5535
- McCleery J., et al., 2020, [MNRAS](#), 499, 1890
- Meibom S., Mathieu R. D., Stassun K. G., 2007, [ApJL](#), 665, L155
- Michel R., Echevarría J., Hernández Santisteban J. V., 2013, [A&A](#), 554, A25
- Moraux E., et al., 2013, [A&A](#), 560, A13
- Morrell S., Naylor T., 2019, [MNRAS](#), 489, 2615
- Murphy S. J., Joyce M., Bedding T. R., White T. R., Kama M., 2021, [MNRAS](#), 502, 1633
- Naylor T., 1998, [MNRAS](#), 296, 339

- Osaki Y., 1996, [PASP](#), **108**, 39
- Paczyński B., 1965, [Acta Astron.](#), **15**, 89
- Paczyński B., 1967, [Acta Astronomica](#), **17**, 287
- Paczyński B., 1971, [ARAA](#), **9**, 183
- Paczynski B., 1976, in Eggleton P., Mitton S., Whelan J., eds, Vol. 73, Structure and Evolution of Close Binary Systems. p. 75
- Pala A. F., et al., 2017, [MNRAS](#), **466**, 2855
- Pala A. F., et al., 2020, [MNRAS](#), **494**, 3799
- Pala A. F., et al., 2021, [MNRAS](#),
- Panei J., Althaus L., Benvenuto O., 2000, [A&A](#), **353**, 970
- Parsons S. G., et al., 2017, [MNRAS](#), **470**, 4473
- Passy J.-C., 2013, PhD thesis, University of Victoria (Canada)
- Passy J. C., et al., 2011, in Schmidtbreick L., Schreiber M. R., Tappert C., eds, Astronomical Society of the Pacific Conference Series Vol. 447, Evolution of Compact Binaries. p. 107
- Paterson K., Woudt P. A., Warner B., Breytenbach H., Gilligan C. K., Motsoaledi M., Thorstensen J. R., Worters H. L., 2019, [Monthly Notices of the Royal Astronomical Society](#), **486**, 2422
- Patterson J., 1998, [PASP](#), **110**, 1132
- Patterson J., 2001, [PASP](#), **113**, 736
- Patterson J., et al., 2005, [PASP](#), **117**, 1204
- Paxton B., Bildsten L., Dotter A., Herwig F., Lesaffre P., Timmes F., 2010, MESA: Modules for Experiments in Stellar Astrophysics (ascl:1010.083)
- Paxton B., Bildsten L., Dotter A., Herwig F., Lesaffre P., Timmes F., 2011, [ApJS](#), **192**, 3
- Paxton B., et al., 2013, [ApJS](#), **208**, 4
- Paxton B., et al., 2015, [The Astrophysical Journal Supplement Series](#), **220**, 15
- Paxton B., et al., 2019, [The Astrophysical Journal Supplement Series](#), **243**, 10
- Pearson K. J., 2007, [MNRAS](#), **379**, 183

- Petit P., Donati J. F., Espadons Project Team 2003, in Arnaud J., Meunier N., eds, EAS Publications Series Vol. 9, EAS Publications Series. p. 97 ([arXiv:astro-ph/0403118](https://arxiv.org/abs/astro-ph/0403118))
- Politano M., 1996, [ApJ](#), 465, 338
- Politano M., 2002, in American Astronomical Society Meeting Abstracts. p. 120.06
- Politano M., 2004, [ApJ](#), 604, 817
- Politano M., Weiler K. P., 2007, [ApJ](#), 665, 663
- Prandtl L., 1925, ZAMM-Journal of Applied Mathematics and Mechanics/Zeitschrift für Angewandte Mathematik und Mechanik, 5, 136
- Rappaport S., Joss P. C., Webbink R. F., 1982, [The Astrophysical Journal](#), 254, 616
- Rappaport S., Verbunt F., Joss P., 1983, [ApJ](#), 275, 713
- Rasmussen C. E., Williams C. K. I., 2006, Gaussian Processes for Machine Learning
- Reiners A., Mohanty S., 2012, [ApJ](#), 746, 43
- Reiners A., Basri G., Browning M., 2009, [ApJ](#), 692, 538
- Renvoizé V., Baraffe I., Kolb U., Ritter H., 2002, [A&A](#), 389, 485
- Renzini A., 1981, in Chiosi C., Stalio R., eds, Astrophysics and Space Science Library Vol. 89, IAU Colloq. 59: Effects of Mass Loss on Stellar Evolution. pp 319–336, [doi:10.1007/978-94-009-8500-1_48](https://doi.org/10.1007/978-94-009-8500-1_48)
- Rezzolla L., Uryū K. ō., Yoshida S., 2001, [MNRAS](#), 327, 888
- Ritter H., 1985, [A&A](#), 145, 227
- Ritter H., 2010b, Memorie della Società Astronomica Italiana, [81](#), 849
- Ritter H., 2010a, Mem. Soc. Astron. Italiana, [81](#), 849
- Ritter H., 2012, Memorie della Società Astronomica Italiana, 83, 505
- Ritter H., Kolb U., 1998, [A&A Suppl.](#), 129, 83
- Ritter, H. Kolb, U. 2003, [A&A](#), 404, 301
- Roberts S., Osborne M., Ebden M., Reece S., Gibson N., Aigrain S., 2012, [Philosophical Transactions of the Royal Society of London Series A](#), 371, 20110550

- Savoury C. D. J., et al., 2011, *Monthly Notices of the Royal Astronomical Society*, 415, 2025
- Savoury C. D., Littlefair S. P., Marsh T. R., Dhillon V. S., Parsons S. G., Copperwheat C. M., Steeghs D., 2012, *Monthly Notices of the Royal Astronomical Society*, 422, 469
- Schaefer B. E., 2010, *ApJS*, 187, 275
- Schenker K., Kolb U., Ritter H., 1998, *MNRAS*, 297, 633
- Schönberg M., Chandrasekhar S., 1942, *ApJ*, 96, 161
- Schreiber M. R., Zorotovic M., Wijnen T. P. G., 2015, arXiv e-prints, p. arXiv:1512.03310
- Schreiber M. R., Zorotovic M., Wijnen T. P. G., 2016, *Monthly Notices of the Royal Astronomical Society*, 455, L16
- Schwpo A., Worpel H., Traulsen I., 2021, *A&A*, 646, A181
- Shafter A. W., Holland J. N., 2003, *PASP*, 115, 1105
- Shakura N., Sunyaev R., 1973, *Astronomy and Astrophysics*, 24, 337
- Shappee B. J., et al., 2014, *ApJ*, 788, 48
- Sharma S., 2017, *ARAA*, 55, 213
- Simonsen M., et al., 2014, *J. Am. Ass. of Variable Star Observers*, 42, 177
- Sion E. M., Godon P., 2022, *Galaxies*, 10, 43
- Skumanich A., 1972, *ApJ*, 171, 565
- Smith N., 2014, *ARAA*, 52, 487
- Smith J. A., et al., 2002, *The Astronomical Journal*, 123, 2121
- Solheim J. E., 2010, *PASP*, 122, 1133
- Somers G., Pinsonneault M. H., 2015, *ApJ*, 807, 174
- Soszynski I., et al., 2016, *VizieR Online Data Catalog*, p. J/AcA/65/39
- Southworth J., Copperwheat C. M., Gänsicke B. T., Pyrzas S., 2010, *A&A*, 510, A100
- Southworth J., Tappert C., Gänsicke B. T., Copperwheat C. M., 2015, *A&A*, 573, A61

- Spada F., Lanzafame A. C., Lanza A. F., Messina S., Collier Cameron A., 2011, [MNRAS, 416, 447](#)
- Spark M. K., O'Donoghue D., 2015, [MNRAS, 449, 175](#)
- Sparks W. M., Sion E. M., 2021, [ApJ, 914, 5](#)
- Spruit H. C., Ritter H., 1983, [A&A, 124, 267](#)
- Spruit H. C., Weiss A., 1986, [A&A, 166, 167](#)
- Starrfield S., Iliadis C., Hix W. R., 2016, [PASP, 128, 051001](#)
- Stehle R., Kolb U., Ritter H., 1997, [A&A, 320, 136](#)
- Szkody P., et al., 2016, [AJ, 152, 48](#)
- Taam R. E., Bodenheimer P., Ostriker J. P., 1978, [ApJ, 222, 269](#)
- Thorstensen J. R., Alper E. H., Weil K. E., 2016, [AJ, 152, 226](#)
- Townsley D. M., Bildsten L., 2003, [ApJL, 596, L227](#)
- Townsley D. M., Bildsten L., 2004, [ApJ, 600, 390](#)
- Townsley D. M., Gänsicke B. T., 2009, [ApJ, 693, 1007](#)
- Tremblay P. E., Bergeron P., 2009, [ApJ, 696, 1755](#)
- Tulloch S. M., Rodríguez-Gil P., Dhillon V. S., 2009, [Monthly Notices of the Royal Astronomical Society: Letters, 397](#)
- Uthas H., Knigge C., Long K. S., Patterson J., Thorstensen J., 2011, [MNRAS, 414, L85](#)
- Verbunt F., Zwaan C., 1981, [A&A, 100, L7](#)
- Waite I. A., Marsden S. C., Carter B. D., Hart R., Donati J. F., Ramírez Vélez J. C., Semel M., Dunstone N., 2011, [MNRAS, 413, 1949](#)
- Waite I. A., Marsden S. C., Carter B. D., Petit P., Donati J. F., Jeffers S. V., Boro Saikia S., 2015, [MNRAS, 449, 8](#)
- Warner B., 1995, [Astrophysics and Space Science, 232, 89](#)
- Warner B., O'Donoghue D., 1988, [MNRAS, 233, 705](#)
- Watson C. L., Henden A. A., Price A., 2006, [Society for Astronomical Sciences Annual Symposium, 25, 47](#)
- Webbink R. F., 1984, [ApJ, 277, 355](#)

- Wickramasinghe D., Li J., Wu K., 1996, [PASA](#), 13, 81
- Wijnen T., Zorotovic M., Schreiber M., 2015, [A&A](#), 577, A143
- Wild J. F., et al., 2021, [MNRAS](#),
- Wood M. A., 1995, in Koester D., Werner K., eds, White Dwarfs. Springer Berlin Heidelberg, Berlin, Heidelberg, pp 41–45
- Wood J., Crawford C., 1986, [MNRAS](#), 222, 645
- Woudt P. A., Warner B., Pretorius M. L., 2004, [MNRAS](#), 351, 1015
- Wright N. J., Drake J. J., 2016, [Nature](#), 535, 526
- Wright N. J., Drake J. J., Mamajek E. E., Henry G. W., 2011, [The Astrophysical Journal](#), 743, 48
- Wu K., Wickramasinghe D. T., Warner B., 1995, [PASA](#), 12, 60
- Zorotovic M., Schreiber M., 2010, in Kalogera V., van der Sluys M., eds, American Institute of Physics Conference Series Vol. 1314, American Institute of Physics Conference Series. pp 19–21, [doi:10.1063/1.3536366](https://doi.org/10.1063/1.3536366)
- Zorotovic M., Schreiber M. R., 2017, [MNRAS](#), 466, L63
- Zorotovic M., Schreiber M., Gänsicke B., 2011, [A&A](#), 536, A42
- van Saders J. L., Ceillier T., Metcalfe T. S., Silva Aguirre V., Pinsonneault M. H., García R. A., Mathur S., Davies G. R., 2016, [Nature](#), 529, 181

Appendix A

Appendix

A.1 Eclipse modelled CV sample

The following data are also available in machine-readable format upon reasonable request to the author.

Table A.1: The system parameters found for the 12 CVs analysed in Chapter 5. The reported parallax, π , is the posterior distribution from fitting the white dwarf fluxes, c.f. §3.3.2.

	ASASSN-14hq	ASASSN-14kb	ASASSN-15pb	ASASSN-17fo	AY For
M_{wd}/M_{\odot}	0.67 ± 0.01	0.74 ± 0.02	0.72 ± 0.03	0.85 ± 0.01	0.78 ± 0.02
R_{wd}/R_{\odot}	0.0119 ± 0.0001	0.0113 ± 0.0002	0.0115 ± 0.0005	0.0099 ± 0.0001	0.0106 ± 0.0003
$M_{\text{donor}}/M_{\odot}$	0.097 ± 0.002	0.134 ± 0.003	0.148 ± 0.008	0.109 ± 0.002	0.106 ± 0.006
$R_{\text{donor}}/R_{\odot}$	0.157 ± 0.001	0.164 ± 0.001	0.210 ± 0.004	0.1436 ± 0.0007	0.162 ± 0.003
q	0.145 ± 0.002	0.182 ± 0.002	0.206 ± 0.004	0.1267 ± 0.0005	0.136 ± 0.004
P , hours	$1.78384800(7)$	$1.63453(1)$	$2.23896(3)$	$1.477147(2)$	$1.790756(1)$
a/R_{\odot} ,	0.681 ± 0.004	0.670 ± 0.005	0.824 ± 0.014	0.646 ± 0.003	0.717 ± 0.007
$i, {}^{\circ}$	80.35 ± 0.06	84.4 ± 0.1	79.4 ± 0.1	84.23 ± 0.03	84.0 ± 0.2
K_{wd} , km/s	58.0 ± 0.9	76.2 ± 1	75 ± 2	60.2 ± 0.4	57.8 ± 2.0
K_{donor} , km/s	399 ± 2	419 ± 3	364 ± 6	468 ± 2	425 ± 4
π , mas	3.40 ± 0.07	2.78 ± 0.11	1.0 ± 0.2	1.79 ± 0.36	2.12 ± 0.16
T_{eff} , K	14819 ± 800	17700 ± 1000	19200 ± 1600	14800 ± 600	18100 ± 500
$\log(g)$, cgs	8.11 ± 0.02	8.21 ± 0.03	8.17 ± 0.06	8.37 ± 0.02	8.28 ± 0.04

Table A.2: Table A.1, continued.

	CSS090102	CSS090419	CSS090622	OGLE82	SDSS J0748
M_{wd}/M_{\odot}	0.62 ± 0.03	0.59 ± 0.08	0.67 ± 0.06	0.83 ± 0.01	0.68 ± 0.02
R_{wd}/R_{\odot}	0.0126 ± 0.0004	0.0122 ± 0.0009	0.0112 ± 0.0007	0.0099 ± 0.0002	0.0121 ± 0.0004
$M_{\text{donor}}/M_{\odot}$	0.060 ± 0.003	0.087 ± 0.011	0.104 ± 0.009	0.131 ± 0.004	0.066 ± 0.004
$R_{\text{donor}}/R_{\odot}$	0.119 ± 0.002	0.152 ± 0.007	0.155 ± 0.005	0.170 ± 0.002	0.117 ± 0.002
q	0.094 ± 0.002	0.146 ± 0.003	0.159 ± 0.008	0.157 ± 0.002	0.095 ± 0.004
P , hours	$1.49723786(5)$	$1.81062621(6)$	$1.702302(6)$	$1.7263398(6)$	$1.39947(1)$
a/R_{\odot} ,	0.582 ± 0.008	0.660 ± 0.030	0.661 ± 0.020	0.720 ± 0.006	0.575 ± 0.007
$i, {}^{\circ}$	88.7 ± 0.6	80.9 ± 0.1	88.2 ± 0.6	83.9 ± 0.1	81.7 ± 0.2
K_{wd} , km/s	40.9 ± 1.2	56.0 ± 2.7	63.7 ± 2.5	68.5 ± 1.0	42.2 ± 1.8
K_{donor} , km/s	431 ± 6	381 ± 16	408 ± 12	435 ± 3	450 ± 5
π , mas	1.41 ± 0.30	1.42 ± 0.69	2.02 ± 0.27	3.82 ± 0.12	1.83 ± 0.14
T_{eff} , K	14800 ± 1200	18200 ± 9000	9800 ± 1500	18000 ± 4000	22500 ± 3000
$\log(g)$, cgs	8.00 ± 0.33	8.04 ± 0.12	8.16 ± 0.08	8.37 ± 0.03	8.11 ± 0.03

Table A.3: Table A.1, continued.

	MASOT0014	SDSS J1524
M_{wd}/M_{\odot}	0.86 ± 0.03	0.80 ± 0.04
R_{wd}/R_{\odot}	0.0097 ± 0.0003	0.0103 ± 0.0005
$M_{\text{donor}}/M_{\odot}$	0.122 ± 0.007	0.074 ± 0.008
$R_{\text{donor}}/R_{\odot}$	0.165 ± 0.003	0.132 ± 0.005
q	0.142 ± 0.004	0.093 ± 0.007
P , hours	$1.7167077(5)$	$1.56764953(2)$
a/R_{\odot} ,	0.722 ± 0.008	0.652 ± 0.01197
$i, {}^{\circ}$	84.8 ± 0.3	86.7 ± 1.1
K_{wd} , km/s	63.2 ± 2.0	42.9 ± 3.4
K_{donor} , km/s	445 ± 5	461 ± 7
π , mas	2.42 ± 0.11	1.92 ± 0.19
T_{eff} , K	17300 ± 1000	12500 ± 1100
$\log(g)$, cgs	8.37 ± 0.04	8.32 ± 0.06

Table A.4: The system parameters found for the three CVs with peculiar white dwarf colours. Here, the reported π is the posterior distribution from fitting the white dwarf fluxes, c.f. §3.3.2.

	ASASSN-16kr	ASASSN-17jf	SSSJ0522–3505
M_{wd}/M_{\odot}	0.952 ± 0.018	0.669 ± 0.031	0.760 ± 0.023
R_{wd}/R_{\odot}	0.0083 ± 0.0002	0.0120 ± 0.0004	0.0112 ± 0.0003
$M_{\text{donor}}/M_{\odot}$	0.042 ± 0.001	0.060 ± 0.008	0.042 ± 0.004
$R_{\text{donor}}/R_{\odot}$	0.105 ± 0.002	0.112 ± 0.004	0.105 ± 0.004
q	0.044 ± 0.002	0.085 ± 0.006	0.055 ± 0.003
P , hours	$1.470862368(2)$	$1.36297(2)$	$1.492642(2)$
a/R_{\odot} ,	0.653 ± 0.005	0.567 ± 0.009	0.614 ± 0.007
$i, {}^{\circ}$	86.4 ± 0.4	83.7 ± 0.5	83.8 ± 0.3
K_{wd} , km/s	22.7 ± 1.5	39.5 ± 4.2	26.0 ± 1.8
K_{donor} , km/s	515 ± 3	462 ± 5	470 ± 4
π , mas	6.58 ± 0.22	2.09 ± 0.19	1.81 ± 0.11
T_{eff} , kK	$10 - 12$	$8 - 13$	~ 25
$\log(g)$, cgs	8.55 ± 0.03	8.15 ± 0.05	8.22 ± 0.04

Table A.5: System parameters for 15 eclipsing systems from [McAllister et al. \(2019\)](#).

	CSS080623	CSS110113	CTCV 1300	DV UMa	GY Cnc	IY UMa
M_{wd}/M_{\odot}	0.710 ± 0.019	$1.00^{+0.04}_{-0.01}$	0.717 ± 0.017	1.09 ± 0.03	0.881 ± 0.016	$0.955^{+0.013}_{-0.028}$
R_{wd}/R_{\odot}	$0.0117^{+0.0001}_{-0.0004}$	0.0080 ± 0.0003	0.01133 ± 0.00021	0.0072 ± 0.0004	$0.00976^{+0.00021}_{-0.00018}$	$0.0087^{+0.0003}_{-0.0001}$
$M_{\text{donor}}/M_{\odot}$	0.081 ± 0.005	0.105 ± 0.007	$0.166^{+0.006}_{-0.003}$	$0.187^{+0.003}_{-0.012}$	$0.394^{+0.016}_{-0.022}$	0.141 ± 0.007
$R_{\text{donor}}/R_{\odot}$	0.1275 ± 0.0024	0.149 ± 0.003	$0.2111^{+0.0025}_{-0.0014}$	$0.215^{+0.001}_{-0.005}$	$0.446^{+0.006}_{-0.009}$	0.1770 ± 0.0028
q	0.114 ± 0.005	0.105 ± 0.006	0.233 ± 0.004	$0.172^{+0.002}_{-0.007}$	$0.448^{+0.014}_{-0.021}$	$0.146^{+0.009}_{-0.001}$
P (hours)	$1.429895304(72)$	$1.585220897(3)$	$2.134576795(41)$	$2.060463139(17)$	$4.210617576(144)$	$1.773814276(5)$
a/R_{\odot}	0.593 ± 0.005	$0.711^{+0.009}_{-0.003}$	0.805 ± 0.007	$0.889^{+0.006}_{-0.012}$	1.429 ± 0.012	$0.765^{+0.004}_{-0.009}$
$i, {}^{\circ}$	80.76 ± 0.19	79.94 ± 0.19	$86.9^{+0.5}_{-0.2}$	$83.29^{+0.29}_{-0.10}$	$77.06^{+0.29}_{-0.18}$	$84.9^{+0.1}_{-0.5}$
K_{wd} km/s	50.8 ± 2.3	$51.1^{+2.9}_{-2.4}$	86.4 ± 1.4	$76.1^{+0.9}_{-2.9}$	125 ± 4	66^{+4}_{-1}
K_{donor} km/s	449^{+1}_{-6}	487 ± 3	371 ± 3	444 ± 4	278.0 ± 2.4	453 ± 3
d , pc	550 ± 60	430 ± 60	340 ± 40	380 ± 40	320 ± 30	–
$T_{\text{eff}}(K)$	15500 ± 1700	14500 ± 2200	11000 ± 1000	17400 ± 1900	25900 ± 2300	–
$\log(g)$, cgs	$8.15^{+0.01}_{-0.04}$	8.63 ± 0.03	8.186 ± 0.019	8.77 ± 0.04	8.40 ± 0.019	8.54 ± 0.03

Table A.6: Table A.5, continued.

	OY Car	SDSS 0901	SDSS 1006	SDSS 1152	SDSS 1501	SSS100615
M_{wd}/M_{\odot}	$0.882^{+0.011}_{-0.015}$	$0.752^{+0.024}_{-0.018}$	0.82 ± 0.11	0.62 ± 0.04	$0.723^{+0.017}_{-0.013}$	0.88 ± 0.03
R_{wd}/R_{\odot}	$0.00957^{+0.00018}_{-0.00012}$	$0.01105^{+0.00022}_{-0.00029}$	0.0102 ± 0.0013	0.0129 ± 0.0006	$0.01142^{+0.00016}_{-0.00022}$	0.0095 ± 0.0003
$M_{\text{donor}}/M_{\odot}$	$0.093^{+0.004}_{-0.001}$	0.138 ± 0.007	0.37 ± 0.06	$0.094^{+0.016}_{-0.009}$	0.061 ± 0.004	0.083 ± 0.005
$R_{\text{donor}}/R_{\odot}$	$0.1388^{+0.0018}_{-0.0003}$	0.182 ± 0.003	$0.457^{+0.022}_{-0.026}$	0.147 ± 0.006	$0.1129^{+0.0025}_{-0.0016}$	$0.1276^{+0.0028}_{-0.0024}$
q	$0.1065^{+0.0009}_{-0.0029}$	$0.182^{+0.009}_{-0.004}$	0.46 ± 0.03	$0.153^{+0.015}_{-0.011}$	0.084 ± 0.004	0.095 ± 0.004
P (hours)	$1.514902211(6)$	$1.869132770(12)$	$4.461914568(312)$	$1.625992862(7)$	$1.364190385(5)$	$1.4089080(96)$
a/R_{\odot}	0.662 ± 0.003	0.739 ± 0.007	1.46 ± 0.07	0.627 ± 0.014	0.574 ± 0.004	0.628 ± 0.007
$i, {}^{\circ}$	$83.27^{+0.10}_{-0.13}$	$81.4^{+0.1}_{-0.3}$	$83.1^{+1.2}_{-0.7}$	82.6 ± 0.5	$83.89^{+0.20}_{-0.27}$	85.1 ± 0.3
K_{wd} km/s	50.4 ± 0.9	73 ± 3	124 ± 9	62 ± 5	$39.5^{+2.2}_{-1.3}$	$46.5^{+2.2}_{-1.7}$
K_{donor} km/s	475.9 ± 2.1	401 ± 3	270 ± 13	402 ± 7	468 ± 3	493 ± 5
d , pc	90 ± 5	600 ± 70	—	610 ± 80	$^{400 \pm 30 \text{ (2004)}}_{338 \pm 21 \text{ (2012)}}$	350 ± 30
$T_{\text{eff}}(K)$	18600^{+2800}_{-1600}	14900 ± 2000	—	15900 ± 2000	$^{13400 \pm 1100 \text{ (2004)}}_{14900 \pm 1000 \text{ (2012)}}$	13600 ± 1500
$\log(g)$, cgs	$8.422^{+0.017}_{-0.013}$	$8.228^{+0.022}_{-0.025}$	8.33 ± 0.13	8.01 ± 0.05	$8.182^{+0.016}_{-0.019}$	8.43 ± 0.03

Table A.7: Table A.5, continued.

	SSS130413	V713 Cep	Z Cha
M_{wd}/M_{\odot}	0.84 ± 0.03	$0.703^{+0.012}_{-0.015}$	0.803 ± 0.014
R_{wd}/R_{\odot}	$0.0102^{+0.0006}_{-0.0002}$	$0.01173^{+0.00020}_{-0.00015}$	0.01046 ± 0.00017
$M_{\text{donor}}/M_{\odot}$	$0.140^{+0.012}_{-0.008}$	$0.176^{+0.007}_{-0.018}$	0.152 ± 0.005
$R_{\text{donor}}/R_{\odot}$	0.163 ± 0.004	$0.208^{+0.002}_{-0.005}$	0.1820 ± 0.0020
q	$0.169^{+0.011}_{-0.006}$	$0.246^{+0.006}_{-0.014}$	0.189 ± 0.004
P (hours)	$1.578462967(29)$	$2.050044192(29)$	$1.787982314(7)$
a/R_{\odot}	$0.680^{+0.007}_{-0.011}$	0.781 ± 0.006	0.734 ± 0.005
$i, {}^{\circ}$	82.5 ± 0.3	81.7 ± 0.3	80.44 ± 0.11
K_{wd} km/s	75 ± 4	91^{+2}_{-5}	$78.4^{+1.4}_{-1.8}$
K_{donor} km/s	443^{+3}_{-7}	$367.6^{+2.6}_{-2.3}$	$413.2^{+2.5}_{-2.0}$
d , pc	240 ± 40	320 ± 30	103 ± 6
$T_{\text{eff}}(K)$	24000 ± 3000	17000^{+6000}_{-3000}	16300 ± 1400
$\log(g)$, cgs	8.35 ± 0.04	$8.147^{+0.017}_{-0.014}$	8.304 ± 0.016

Table A.8: System parameters derived by [Savoury et al. \(2011\)](#).

	CTCV J1300-3052	CTCV J2354-4700	SDSS J1152+4049	OU Vir
M_{wd}/M_{\odot}	0.736 ± 0.014	0.935 ± 0.031	0.560 ± 0.028	0.703 ± 0.012
R_{wd}/R_{\odot}	0.01111 ± 0.00018	0.0089 ± 0.0003	0.0135 ± 0.0004	0.01191 ± 0.00017
$M_{\text{donor}}/M_{\odot}$	0.177 ± 0.021	0.101 ± 0.003	0.087 ± 0.006	0.1157 ± 0.0022
$R_{\text{donor}}/R_{\odot}$	0.215 ± 0.008	0.1463 ± 0.0016	0.142 ± 0.003	0.1634 ± 0.0010
q	0.240 ± 0.021	0.1097 ± 0.0008	0.155 ± 0.006	0.1641 ± 0.0013
P (mins)	$128.0746325(14)$	$94.3923889(14)$	$97.518753(4)$	$104.696803(7)$
a/R_{\odot}	0.813 ± 0.011	0.692 ± 0.008	0.606 ± 0.010	0.686 ± 0.004
$i, {}^{\circ}$	86.3 ± 1.1	89.26 ± 0.28	82.38 ± 0.23	79.60 ± 0.04
K_{wd} km/s	90 ± 8	51.9 ± 0.6	60 ± 3	66.4 ± 0.6
K_{donor} km/s	372.2 ± 2.5	482 ± 6	387 ± 6	403.0 ± 2.3
d , pc	375 ± 13	674 ± 19	543 ± 21	570 ± 70
$T_{\text{eff}}(K)$	11100 ± 800	14800 ± 700	12400 ± 1400	22300 ± 2100
$\log(g)$, cgs	8.21 ± 0.02	8.51 ± 0.04	7.93 ± 0.05	8.13 ± 0.02

Table A.9: Table A.8, continued

	SDSS 1035	DV UMa	XZ Eri	SDSS 1702	SDSS 1501
M_{wd}/M_{\odot}	0.835 ± 0.009	1.098 ± 0.024	0.769 ± 0.017	0.91 ± 0.03	0.767 ± 0.027
R_{wd}/R_{\odot}	0.00991 ± 0.00010	0.00703 ± 0.00028	0.01081 ± 0.00022	0.0092 ± 0.0004	0.0107 ± 0.0003
$M_{\text{donor}}/M_{\odot}$	0.0475 ± 0.0012	0.196 ± 0.005	0.091 ± 0.004	0.223 ± 0.010	0.077 ± 0.010
$R_{\text{donor}}/R_{\odot}$	0.1047 ± 0.0008	0.2176 ± 0.0018	0.1350 ± 0.0018	0.252 ± 0.004	0.122 ± 0.005
q	0.0571 ± 0.0010	0.1778 ± 0.0022	0.118 ± 0.003	0.248 ± 0.005	0.101 ± 0.010
P (mins)	$82.08965(29)$	$123.6278190(20)$	$88.069667(7)$	$144.11821(13)$	$81.85141771(28)$
a/R_{\odot}	0.5977 ± 0.0022	0.892 ± 0.006	0.621 ± 0.005	0.945 ± 0.012	0.588 ± 0.008
$i, {}^{\circ}$	83.98 ± 0.08	82.93 ± 0.10	80.02 ± 0.12	82.55 ± 0.17	82.8 ± 0.5
K_{wd} km/s	28.5 ± 0.6	78.9 ± 1.0	53.6 ± 1.5	94.0 ± 2.2	48 ± 5
K_{donor} km/s	499.3 ± 1.5	443 ± 3	452 ± 3	380 ± 4	470.5 ± 3.2
d , pc	174 ± 12	504 ± 30	371 ± 19	270 ± 16	306 ± 21
$T_{\text{eff}}(K)$	10000 ± 1100	15500 ± 2400	15300 ± 1900	15200 ± 1200	10800 ± 1500
$\log(g)$, cgs	8.37 ± 0.01	8.78 ± 0.04	8.26 ± 0.03	8.47 ± 0.05	8.26 ± 0.04

Table A.10: Table A.8, continued

	SDSS 1507	SDSS 0903	SDSS 1227	SDSS 1433	SDSS 1502
M_{wd}/M_{\odot}	0.892 ± 0.008	0.872 ± 0.011	0.796 ± 0.018	0.865 ± 0.005	0.709 ± 0.004
R_{wd}/R_{\odot}	0.00956 ± 0.00013	0.00947 ± 0.00019	0.01052 ± 0.00022	0.00962 ± 0.00006	0.01145 ± 0.00005
$M_{\text{donor}}/M_{\odot}$	0.0575 ± 0.0020	0.099 ± 0.004	0.0889 ± 0.0025	0.0571 ± 0.0007	0.0781 ± 0.0008
$R_{\text{donor}}/R_{\odot}$	0.0969 ± 0.0011	0.1358 ± 0.0020	0.1365 ± 0.0013	0.1074 ± 0.0004	0.1241 ± 0.0003
q	0.0647 ± 0.0018	0.113 ± 0.004	0.1115 ± 0.0016	0.0661 ± 0.0007	0.1099 ± 0.0007
P (mins)	$66.61192(6)$	$85.065902(13)$	$90.661019(10)$	$78.106657(3)$	$84.82984(7)$
a/R_{\odot}	0.5329 ± 0.0019	0.632 ± 0.003	0.640 ± 0.005	0.5869 ± 0.0012	0.5844 ± 0.0013
$i, {}^{\circ}$	83.47 ± 0.12	82.09 ± 0.19	84.29 ± 0.10	84.36 ± 0.05	88.35 ± 0.17
K_{wd} km/s	35.1 ± 1.0	54.6 ± 2.0	51.3 ± 0.8	33.8 ± 0.3	50.4 ± 0.4
K_{donor} km/s	543.7 ± 1.2	481.7 ± 1.9	460 ± 3	511.1 ± 0.9	456.5 ± 0.8
d , pc	168 ± 12	299 ± 14	400 ± 13	226 ± 12	175 ± 11
$T_{\text{eff}}(K)$	11300 ± 1000	13300 ± 1700	15900 ± 1400	12700 ± 1500	11800 ± 1200
$\log(g)$, cgs	8.45 ± 0.01	8.42 ± 0.02	8.29 ± 0.02	8.41 ± 0.01	8.17 ± 0.01

Table A.11: System parameters from assorted other sources: [McAllister et al. \(2015\)](#) (M15), [McAllister et al. \(2017a\)](#) (M17a), [McAllister et al. \(2017b\)](#) (M17b), [Gänsicke et al. \(2010\)](#) (C10), [Shafter & Holland \(2003\)](#) (S03),

	PHL 1445	SDSS J1057+2759	ASASSN-14ag	IP Peg
M_{wd}/M_{\odot}	0.733 ± 0.006	0.800 ± 0.015	0.63 ± 0.04	1.16 ± 0.02
R_{wd}/R_{\odot}	0.01122 ± 0.00008	0.01040 ± 0.00017	0.0126 ± 0.0006	0.0081 ± 0.0013
$M_{\text{donor}}/M_{\odot}$	0.0637 ± 0.0007	0.0436 ± 0.0020	0.093 ± 0.013	0.55 ± 0.04
$R_{\text{donor}}/R_{\odot}$	0.1092 ± 0.0004	0.1086 ± 0.0017	0.135 ± 0.007	0.46 ± 0.02
q	0.08701 ± 0.0005	0.0546 ± 0.0020	0.149 ± 0.016	0.47 ± 0.03
P , days	$0.0529848884(13)$	$0.0627919557(6)$	$0.060310665(9)$	$0.1582061029(3)$
a/R_{\odot} ,	0.550 ± 0.011	0.629 ± 0.004	0.583 ± 0.015	1.472 ± 0.009
$i, {}^{\circ}$	85.2 ± 0.9	85.74 ± 0.21	83.4 ± 0.7	83.81 ± 0.45
K_{wd} , km/s	42 ± 3	26.2 ± 0.9	63 ± 7	151 ± 3
K_{donor} , km/s	482 ± 5	478 ± 3	422 ± 9	317 ± 2
d , pc	220 ± 50	367 ± 26	146 ± 20	151 ± 14
T_{eff} , K	13200 ± 700	13300 ± 1100	14000 ± 2100	12500 ± 2500
$\log(g)$, cgs	8.2 ± 0.3	8.307 ± 0.017	8.04 ± 0.05	-
Source	M15	M17a	M17b	C10